CHARACTERIZING, IMAGING, AND QUANTIFYING THE ENVIRONMENTAL BEHAVIOR AND BIOLOGICAL INTERACTIONS OF METAL-BASED NANOPARTICLES

A Thesis
Presented to
The Academic Faculty

By

Wen Zhang

In Partial Fulfilment
of the Requirements for the Degree
Doctor of Philosophy in Environmental Engineering
School of Civil and Environmental Engineering

Georgia Institute of Technology
August, 2011

CHARACTERIZING, IMAGING, AND QUANTIFYING THE ENVIRONMENTAL BEHAVIOR AND BIOLOGICAL INTERACTIONS OF METAL-BASED NANOPARTICLES

Approved by:

Dr. Yongsheng Chen, Advisor
School of Civil and Environmental Engineering,
Georgia Institute of Technology

Dr. John Crittenden
School of Civil and Environmental Engineering,
Georgia Institute of Technology

Dr. Ching-hua Huang
School of Civil and Environmental Engineering,
Georgia Institute of Technology

Dr. Joseph B. Hughes
School of Civil and Environmental Engineering,
Georgia Institute of Technology

Dr. Zhonglin Wang
School of Material Sciences and Engineering,
Georgia Institute of Technology

Date Approved: May 10, 2011

To my beloved families,
Ying Yao, Nathan Zhang,
my parents and parents-in-law

ACKNOWLEDGEMENTS

First and foremost, I would like to express my sincere thanks to my thesis advisor and the research project PI, Dr. Yongsheng Chen. He imparted upon me with his knowledge and insightful vision that brought me to an exciting and highly creative research field, where I gained and benefited from interdisciplinary training. He has continuously provided me guidance, insightful suggestions, and support throughout the course of my Ph.D. research. Moreover, Dr. Chen has always been supportive of the ideas I created, most of which have proven to be of great importance for the success of my research.

Special thanks go to my thesis committee members, Dr. John Crittenden, Dr. Joseph Hughes, Dr. Ching-hua Huang, and Dr. Zhonglin Wang. I want to especially thank them for finding time in their busy schedules to review this thesis and provide suggestions, constructive and critical comments. Particularly, I want to thank Dr. Crittenden for his guidance on aggregation modeling. His insight and suggestions have pushed me toward a better and deeper understanding of nanoscale physicochemical processes. Dr. Hughes provided me with helpful advice on appropriate expressions of experimental data in scientific presentations. Dr. Huang and Dr. Wang both emphasized to me the importance of a clear and well-organized presentation in scientific research communications, which is truly beneficial to me. I want to thank them all for their considerate advice, important feedback and input.

The financial support from the U.S. Environmental Protection Agency Science to Achieve Results Program Grant RD-83385601 and Engineering Research Center

(ERC)/Semiconductor Research Corporation (SRC)/ESH grant (425.025) are gratefully acknowledged.

It was my great honor to work in Dr. Bruce Rittmann's group from 2007 to 2009 at Arizona State University (ASU). As my thesis co-advisor, Dr. Rittmann deeply influenced me with his efficient, diligent, and dedicating character. He emphasized the importance of being a successful graduate student and how to achieve this goal. More importantly, he gave me rigorous but valuable training on writing scientific papers and stressed to me the importance of the "take-home lesson" of a scientific article, which is one of my great treasures from working with him.

I also want to acknowledge Dr. Paul Westerhoff and Dr. Paul Johnson for their interesting and instructive teaching on water chemistry and contaminant fate and transport. Their courses armed me with the basics of environmental engineering knowledge that has benefited my own research. They were also very warm and ready to help students. Dr. Morteza Abbaszadegan and Dr. Absar Alum are also thanked for sharing the lab equipment with me and for assisting my research from time to time. I also want to thank Dr. Andrew Stack from school of earth and atmospheric sciences at Georgia Tech for his guidance in AFM and now he is working at chemical sciences division of Oak Ridge National Laboratory.

Many thanks go to Drs. Xuezhi Zhang, Yang Zhang, and Xiaoshan Zhu for their kind help on my research experiments at ASU. Particularly, Drs. Xuezhi and Xiaoshan helped me tremendously on synthesis of nanoparticles and other instrumental operations at ASU. I also like to thank Dr. Daisuke Minakata, who helped me as senior colleague at

both ASU and Georgia Tech. Dr. Ming Xu sets a good model for me to learn from and a perfect colleague representing academic excellence and a success in academic career.

I appreciate Dr. Chunrong Wang for her assistance with nanosilver experiments. Kungang Li and Ying Huang are appreciated for their experimental support on DLS measurements. My thanks also go to Ryan Ravenelle, Wei Lin, and Zhuo Li for their kind help with my experiments. I would like to thank Hao Jiang for his help and patience during our "crazy" experiments on "vibrating" DNA molecules. During my PhD research, I have been extensively interacting with two research groups, Dr. David Capco and his group members (Madhavi Kalive and James Faust) and Dr Qingguo (Jack) Huang and his graduate student (Liwen Zhang). I want to thank them for giving me the opportunities of the collaborations and conducting joint research.

I would also like to appreciate Dr. Guangxuan Zhu for his warm help and guidance on lab maintenance and utilization of various analytical instruments. There are many more graduate students (Johana Husserl, Zakiya Seymour, Yi Qu, and Biao Chang) at Georgia Tech, postdocs, visiting scholars, and staff who supported me with their friendship and helped me grow from a less experienced student to a qualified Ph.D. candidate.

I would not succeed in this endeavor without my family's continued support, understanding, encouragement, and patience, which accompany me through all the hardship during the research adventure. My deepest gratitude is given to my wife, Ying Yao, for always being supportive and to our sons for bringing extraordinary happiness to my family.

TABLE OF CONTENTS

LIST OF TABLES

LIST OF FIGURES

LIST OF ABBREVIATIONS

AgNPs	Silver NPs
AFM	Atomic force microscopy
AC	Alternating current
CAM	Contact angle measurement
CPD	Contact potential difference
DC	Direct current
DI water	deionized water
DLS	Dynamic laser scattering
DMT	Derjaguin-Müller-Toporov
DO	Dissolved oxygen
DLVO	Derjaguin-Landau-Verwey-Overbeek
EDLVO	Extended Derjaguin-Landau-Verwey-Overbeek
EDL	Electric double layer
HOPG	Highly oriented pyrolytic graphite
ICP-MS	Inductively coupled plasma-mass spectrometry
ICP-OES	Induced coupled plasma-optical emission spectrometry
IFBL	Interfacial force boundary layer
JKR	Johnson-Kendall-Roberts
KFM	Kelvin force microscopy
KPFM	Kelvin probe force microscopy
LIA	Lock-in amplifier
LPS	lipopolysaccharides

LB medium	Luria-Bertani medium
NOM	Natural organic matter
PDI	Polydispersivity index
ROS	Reactive oxidative species
SAM	self-assembly monolayer
SEM	Scanning electron microcopy
TR-DLS	Time-resolved-dynamic laser scattering
TEER	Transepithelial electrical resistance
TEM	Transmission electron microscopy

SUMMARY

Due to the rapid expansion of nanotechnology and the increasing range of nanomaterials under production and development, it is essential evaluate the potential impacts on human health, ecosystems and environment. The ultrasmall nanoparticles (NPs) exhibit unique physicochemical properties (e.g., high surface area to volume ratio, various morphology, crystallinity, electronic properties, surface reactivity, dynamic and size-dependent dissolution, and aggregation behavior). The same unique properties have been found to have potential deleterious effects on human or other biological systems. Much work is needed to identify these adverse effects and meanwhile to link physicochemical characteristics of NP to their biological behavior.

This study is specifically focusing on the nanoparticle-cell (or bio-nano) interactions, aiming at exploration of the fundamental knowledge essentially useful in better understanding about nanotoxicity and its connections with particle properties. The nano-bio interactions are widely considered the first and initial step for NPs to approach cells and this step has important influences on the subsequent cellular adhesion, adsorption, penetration, and cell function disruption or cytotoxicity. The whole structure of this study can be divided into three levels: the first level is to quantitatively understand physicochemical properties of NPs of interest and their dynamic changes under varying environmental conditions. The overall goal is to seek the connection between the kinetics of the environmental behavior and potential toxicokinetics. The second level is to evaluate the biological interactions of representative NPs with a specific focus on the size-dependent adsorption processes, interfacial forces, cellular disruption, and membrane damages. This part together with the first part are expected to provide us a

sense of how the dynamic and heterogeneous properties of NPs will possibly be interconnected with toxicokinetics (e.g., adsorption kinetics), which essentially allows us to categorize and prioritize nanomaterials and the properties with toxicity relevance. In line with this effort, novel mathematical models were derived to quantitatively interpret and underpin the mechanisms of the bio-nano interactions and the associated key factors. The third level is to develop a potentially effective, accurate, and valid tool based on atomic force microscopy (AFM) to characterize NPs in terms of the identified key factors or parameters that are outlined in the mathematical models. Particularly, my work employed AFM to quantify the adhesion forces between the probe tip and the surface of NPs, which was then converted to the contact angle, reflecting the nanoscale hydrophobicity or wettability property of NPs. On the other hand, the surface potential of NPs at nanoscale was evaluated by Kelvin force microscopy or KFM, an electrical mode of AFM, to explore the nanoscale electric properties and its potential influences on particle stability, transport, and biological interactions of NPs in the environment.

In summary, this thesis demonstrate useful quantitative methods characterizing the kinetic environmental behavior, biological interactions, and unique nano-properties of metal-based NPs, which should be of interest to people in application research of nanotechnology (e.g., nano-enabled biomedical applications). Moreover, our findings lay out the ground work for better understanding of the environmental fate and transport of anthropogenic NPs as a new class of emerging contaminants.

CHAPTER 1

INTRODUCTION

1.1. Background of Nanotechnology

Nanotechnology is an emerging technology exploiting distinct technological advances of manufacturing the structure of materials at a reduced dimensional scale approaching individual molecules and their organized aggregates or supramolecular structures. Basically, the nanometre-length scale is creating possibilities for novel materials that can be used for the construction of devices and systems. The objective of this section is to introduce the key aspects pertaining to nanotechnology and its applications, with a particular focus on manufactured nanomaterials.

The National Nanotechnology Initiative (NNI) defines nanotechnology as a wide range of technologies that measure, manipulate, or incorporate materials and/or features with at least one dimension between approximately 1 and 100 nanometers (nm). Nanotechnology must be distinguished from the nanoscience enabling such technology. In a recently published report of The Royal Society & The Royal Academy of Engineering (2004) definitions were given for nanoscience and nanotechnology: Nanoscience is the study of phenomena and manipulation of materials at atomic, molecular and macromolecular scales, where properties differ significantly from those at larger scale. Basically, nanoscience is the study of phenomena and material properties at nanoscale, while nanotechnology is applying the resulting knowledge to design, create, produce, and apply novel materials and structures.

Nanotechnology as a whole is projected to a market of $1 trillion by 2015, with nanomaterials growing to $11 billion in 2010 *(1)*. Another market research center estimated that the sales of products incorporating nanotechnology will rise from less than

0.1% of global manufacturing output in 2004 to 15% in 2014, totaling $2.6 trillion (Lux research 2004). Although estimates of future nanotechnology industry growth may differ, they show the great potential of this emerging industry. Advances in knowledge in nanoscience and nanotechnology have led to great scientific advances, including fundamental changes in the way that materials, devices, and systems are understood and created.

Novel nanomaterials with high performance and unique properties can be produced that traditional synthesis/manufacturing methods could not create, and can exhibit extraordinary mechanical, electric, electronic, thermal, and optical properties that few materials platforms could ever match. As particle size decreases, the ratio of surface area to volume rapidly increases so that surface properties become the dominant factor. This large surface area provides various unique properties that have widespread applications in many different industrial sectors, including the composite materials, electronics, and chemical sectors. To name a few applications, carbon nanotubes (CNTs), fullerenes, carbon nanofibers, and carbon black. Small additions of nanomaterials such as carbon nanotubes can greatly improve structural properties of composite materials. Due to their electrical conductivity, CNTs also have application for the manufacture of low-cost solar cells, electronics, and anti-static composite materials. Quantum dots (semiconductor nanocrystals) possess remarkable optical and electronic properties that can be precisely tuned by changing their size and composition *(2-4).* Due to their relatively inexpensive and simple synthesis QDs have already entered the market for experimental biomedical imaging, biolabeling and anti-counterfeiting applications to create special inks, dyes and paints, light displays, and chemical sensing *(5-7).* Dendrimers (complex spherical macromolecules) have unique properties compared to traditional polymers and offer the possibility as medical nanovehicles due to the presence of internal cavities offering *(8-10).* Gold (Au) NPs less than 5 nm in diameter can be a very effective catalyst for several

chemical reactions under ambient temperature. Silver (Ag) NPs or AgNPs have been found to be very effective as an antibacterial agent and are used in many types of products. Cerium oxide (CeO_2) can be used as a diesel fuel combustion catalyst *(11)*, as well as solar cells *(12, 13)* and gas sensors *(14)*. Titanium dioxide (TiO_2) NPs have a large band gap and are used for ultraviolet (UV) protection, photocatalysts *(15)*, photovoltaics, and sensing *(16)*. As a photocatalyst, TiO_2 nanomaterials are being applied to exterior walls of buildings to provide a self-cleaning function *(17)*.

In general, nanotechnology is acknowledged to represent a new frontier in science and technology of the 21st century. Increased production results in an increased potential of release to the environment, either deliberately in discharges or accidentally in spillages, and a greater possibility of adverse environmental and human health effects. Clinical and experimental studies indicate that a small size and a large surface area induce the production of reactive oxygen species (ROS), the oxidative stress and cellular injury *(18-20)*. Thus, even if the same material is relatively inert in bulkier form (e.g., carbon black and TiO_2), there is a tendency for cytotoxicity to increase for ultrasmall NPs *(1)*. Additionally, the end-of-life impacts of nanomaterials to human and the environment are largely unknown. Many nanotechnology-based products are already available in the marketplace, including sporting goods, electronics, personal care, and automotive parts. The same unique properties of nanomaterials may cause the substantial and potential risks to both human health and the environment *(21)*. Thus, understanding the broad scope and diversity of the nanotechnology industry is an important first step in identifying potential risks that may be associated with this industry.

1.2. Current understandings of nanotoxicity

1.2.1. Route and extent of exposure

The risk that nanomaterials pose to humans and the environment is strongly affected by the route and extent of exposure to such materials. Nanomaterials can unintentionally enter the human body through three primary routes: inhalation, ingestion, and dermal penetration. In addition to humans, the environment may also be exposed to nanomaterials through deliberate or accidental releases into the water, air, and soil, during the manufacture, use, or disposal of these materials. For example, nanomaterials could enter water through discharges from production facilities. In addition, when nanomaterials are used in pharmaceuticals, cosmetics, and sunscreens, the nanomaterials could enter water via the sewage system during washing, showering, or swimming after having been applied to the skin and may eventually end up in a waste water treatment plant. These nanomaterials, if antibacterial in nature and if released in sufficient amounts, could potentially interfere with beneficial bacteria in sewage and waste water treatment plants and could also contaminate water intended for re-use, according to some of the studies that we reviewed. Thus, some researchers have raised serious concerns that antibacterial nanomaterials will pose toxicity risks to human health and to environmental systems. In addition, unused cosmetics are most likely to be disposed of in household waste, which may be incinerated, transmitted into the air, or put in a landfill and potentially leaching out into the water. In addition, nanomaterials that are currently being used to treat polluted water (e.g., iron NPs) will result in releases of the materials into water and soil.

The difficulties in studying any nanoscale material are exacerbated in natural systems because of their polydispersivity, complexity, and spatial and temporal variability. Current understanding of the nanomaterial associated risks is challenged by those above and also limited by technical factors, including a lack of tools and methods

that are effective and available for detecting nanomaterials *in situ*. As a result, predicting and assessing the potential hazards, exposures, and resulting risks from nanomaterials is difficult. Although extensive studies have advanced the knowledge in assessing the risks of nanomaterials, the studies completed to date have yielded limited risk information. Some grand challenges still remain and they may include *(21)*: (1) Studies of similar nanomaterials may not be comparable due to the insufficient characterizations or other experimental settings; (2) Some nanomaterials are over focused on, while others (e.g., nanoclays) are poorly studied; (3) Classic approaches used in aquatic ecological risk assessments may be less applicable to NPs since exposure assessments have classically depended on predicting the soluble portion of the contaminant; and (4) Difficulties measuring NPs *in situ* are related to measuring trace levels against a high background of natural colloids. As yet, no peer-reviewed literature is available on concentrations (or speciation) of NPs in natural waters or sediments *(22-24)*. Routine monitoring of concentration for regulatory purposes is still further away.

1.2.2. Toxicity mechanisms of NPs

Among the suggested toxicity mechanisms, oxidative stress, rupture of cell membrane, genetic disruption, cutting off intracellular metabolic routes, and release of heavy metals are regarded as the most acceptable mechanisms.

1.2.1.1. Damage to membrane integrity

The bacterial cell membrane is a semipermeable barrier that serves important cellular functions, such as regulation of material transport, energy transduction, and intercellular communication. While QDs smaller than 15 nm have been reported to enter bacterial cells *(25, 26)*, it is likely that larger NPs may also cross the membrane *(27, 28)*. In addition, some NPs have been shown to attach to the cell surface and compromise the integrity and functions of the cell membrane *(29-31)*. For example, silicon NPs and fullerene derivatives can embed themselves in the membranes *(32)*. Carboxyfullerene

caused puncturing of bacterial cell membrane in a gram-positive bacterial strain that resulted in cell death *(33)*. AgNPs adhered to the surface altering the membrane properties, therefore affecting the permeability and the respiration of the cell *(34)*. ZnO NPs were reported to induce membrane disorganization of *E. coli* cells *(35-37)*. Nanomaterials can also indirectly cause membrane damage through the generation of reactive oxygen species (ROS), which can oxidize double bonds on fatty acid tails of membrane phospholipids in a process known as lipid peroxidation *(38)*. This increases membrane permeability and fluidity, making cells more susceptible to osmotic stress or hindering nutrient uptake *(39, 40)*. Peroxidized fatty acids can trigger reactions that generate other free radicals, leading to more cell membrane and trans-membrane protein damage.

1.2.1.2. Protein oxidation and inhibition

Nanomaterial–protein interactions have been optimized for a variety of biomedical applications, such as bioimaging and biosensing *(41-43)*. The toxicological interactions between NMs and proteins are related to either the NM chemically binding with proteins or ROS generation or other damaging radicals from NPs. The generated ROS can damage iron–sulfur clusters that behave as cofactors in many enzymes, leading to Fenton chemistry that catalyzes the production of more ROS generation *(44)*. Reactive oxygen species can also lead to the formation of disulfide bonds between sulfur-containing amino acids, thus disturbing the structure and function of the protein. Nonlethal effects, such as inhibition of enzymatic activities, have also been found in some cases *(45-47)*.

1.2.1.3. Nucleic acid damage

Interactions of NMs with nucleic acids have applications in DNA labeling or DNA cleavage. Nucleotides can be tagged with NPs, such as QDs, which act as labeling agents for bioimaging applications *(48-50)*. Photosensitive metallic and metal oxides that generate ROS as well as fullerenes are used for photodynamic therapy, targeting cells and

DNA *(51-53)*. In contrast to the beneficial applications, fullerenes were found to bind DNA and cause deformation of the strand, adversely impacting the stability and function of the molecule *(54)*. Photosensitive fullerenes and copper complexes can cleave double stranded DNA on exposure to light *(55-57)*. QDs could cause DNA damages *(58)* and nick supercoiled DNA *(59)*. Some NPs indirectly damage DNA because of ROS production, which can lead to DNA strand breaks, cross-linking, and adducts of the bases or sugars *(60)*. TiO_2 and CeO_2 NPs generate oxygen radicals that can nick supercoiled DNA *(61, 62)*. AgNPs were found to permeate into bacteria and cause DNA damage by releasing toxic Ag^+ *(63)*. Despite a wealth of studies on the genotoxicity of NPs *(64-70)*, little is known about the potential mutagenic and teratogenic effect of nanomaterials *(71, 72)*.

1.2.1.4. Cell damage via reactive oxygen species

As mentioned previously, due to the ultrasmall sizes and high surface areas, almost all NPs can have ROS production, which is able to damage every cell component, and tends to trigger further radical formation *(44)*. For example, Fenton chemistry occurs during the oxidation of proteins containing iron-sulfur groups, and harmful aldehydes are released during lipid peroxidation.

1.2.1.5. Interruption of energy transduction

Electron transport phosphorylation and energy transduction processes on cell membranes, and membrane damages may disrupt these processes. Fullerene derivatives have been reported to inhibit *E. coli* respiration of glucose *(73)*. CeO_2 NPs may oxidize membrane components by interfering the electron transport chain, and cause cytotoxicity *(74)*.

1.2.1.6. Release of toxic components

Certain NPs cause toxicity to bacterial cells by releasing harmful components, such as heavy metals or ions. QDs contain noble or transition metals, such as CdSe, CdTe, CdSeTe, ZnSe, InAs, or PbSe, in their core; CdS or ZnS in their shell; and an organic coating. The photodegradation of QDs will lead to release and exposure of potentially toxic metals to the cells. Release of Ag^+ has been considered the key to the cytotoxicity of AgNPs *(63)*. Ag^+ interacts with thiol groups of proteins, resulting in inactivation of vital enzymes. Ag^+ was also shown to prevent DNA replication and affect the structure and permeability of the cell membrane *(75)*.

1.3. Understanding the particle properties with toxicity relevance

To elucidate the modes of action of toxicity of different nanomaterials, to underpin the processes of their environmental fate and behavior, and to be able to manufacture environmentally benign nanomaterials, much work is still needed to advance knowledge in the area of physicochemical characterization of nanomaterials, and how characteristics and properties of these nanomaterials influence their fate and behavior in the environment. This type of knowledge will largely allow us to understand and predict potential toxicity in different environmental receptors *(23, 76, 77)*.

Much of the recent literature provides us substantial information regarding the nanotoxicity and its relationship with potential relevant properties of NPs such as size, shape, surface area, surface functionalization, morphology, crystallinity, and composition *(31, 78-82)*, as illustrated by Figure 1.1. Although a number of reviews stressed the importance of characterizing physicochemical properties when assessing potential human and environmental hazards of nanomateirals *(23, 83, 84)*, extensive characterization often requires specialist technical expertise, time consuming and expensive approaches. Thus, some important properties may be poorly characterized, especially in the environmentally relevant aqueous conditions. It is also worth mentioning that most properties of NPs in

aqueous media are dynamic rather than static, meaning that the properties such as particle size distribution and surface charge may change over time as a function of ionic strength or pH. Furthermore, some of the particle properties are interrelated with each other. For example, particle size determines the surface area (small sizes yield high surface areas). Particle shape may not only change the transport behavior (e.g., diffusion rates) and collision efficiency due to steric hindrance, but also alter surface crystallinity, surface energy, and surface reactivity *(85-87)*. Thus, it is quite risky to draw correlations between a single factor and its observable biological effects. At last, the origin of the experimental condition effects on nanotoxicity should better be related to the particle property changes rather than the experimental condition effect alone.

1.3.1. Interconnections between particle properties

As shown in Table 1.1, particle properties are often found interrelated to each other, as indicated by the black dots, while the cross symbols indicate no obvious relations. For instance, primary particle sizes of nanomaterials often influence the particle size distribution in aqueous phase due to the aggregation. NPs often do not appear as individual particles. One reason for this is their marked propensity to agglomerate because agglomeration reduces the enormous surface area (or surface energy), which is energetically favorable. As a result of aggregation, surface area and surface energy are different between pristine NPs and aggregated NPs. As mentioned above, particle shape determines what crystallographic surfaces of NPs are exposed to the bulk liquid or cells, resulting in crystallinity effects on biological systems. Moreover, shape also influences the particle size distribution *(88)*, which indirectly changes the bioavailability of nanomaterials *(83)*. On the other hand, Table 1.2 shows that various environmental factors (e.g., pH and ionic strength) often vary the particle properties and results in "Ripple effect" that induces the changes of lots of other properties. For example, the presence of electrolytes in the aqueous media will change the particle distribution as well

as the surface area and surface charge. Thus, when studying one single factor (either environmental factors or particle properties) in the biological impacts, one may need to consider the interconnections and dynamics in order to obtain a comprehensive understanding of experimental observations.

1.3.2. Dynamic features of environmental behavior

Many nanotoxicological experiments ended up with a non-nano format (dissolved or macroparticulates) of NPs *(89-91)*. The observed toxic mechanisms are most likely to be associated with the chemical destabilization processes of NPs, which might include the generation of reactive oxygen species (ROS) and associated oxidative stress, aggregation, release of metal ions, metal ion speciation, and particle adsorption onto the cell surfaces.

The unique properties of NPs arise from the miniaturization of the bulk phases of the same materials *(1)*. Unfortunately, even apparently stable dispersions will gradually aggregate out of the aqueous phase over time (e.g., several days) *(92)*. The rate of aggregation of particles in an aqueous medium will partly depend on particle–particle collision frequency (e.g., Brownian motion and particle number concentration in the medium), the energy of the collision, and the attractive-repulsive properties of the particles involved (e.g., repelling surface charges on two positively charged particles); as well as similar interactions with other colloid materials such as natural organic matter present in the medium. As part of the induced issues from aggregation, the exposure surface areas of NPs will be changed, which may influence the ROS production that significantly depends on available surface areas with high surface reactivity *(93)*. Accordingly, the cytotoxicity of aggregated NPs should be different from monodispersed NPs of the same materials.

Toxic heavy metals can be released from most metallic or metal oxide NPs *(94)*. Ion release kinetics is found to be size-dependent *(95-98)* and have cytoxic effects on cells *(82, 99, 100)*. The same scenario is found for bio-adsorption (adsorption of NPs onto the cell surfaces) processes *(31, 101)*. Other factors, such as surface roughness, surface adhesiveness, surface hydrophobicity/hydrophilicity, or heterogeneity, may also have dynamic evolution process as the NP surfaces are functionalized by being adsorbed with naturally occurring colloids or organic matters *(102, 103)*.

1.3.3. Kinetics of environmental behavior and its influence on toxicokinetics

As a result of the dynamic environmental behavior, it is reasonable to observe the correlations between kinetic behavior of NPs and their toxicokinetics such as membrane disruption, cell penetration, and cellular death. As shown in Table 1.3, all the individual particle properties have impacts on the kinetic behavior of NPs in the environment and consequently the toxicokinetics of NPs is varied by both the particle properties as well as the associated dynamic or kinetics environmental processes.

Table 1.1. The mutual effects between particle properties.

Particle properties	Particle size	Particle size distribution	Shape	Surface area	Surface charge	Surface functionalization	Surface energy	Crystallinity
Particle size	×	● *(104)*	×	●	●	N.A.	● *(105)*	● *(87, 106)*
Particle size distribution	●	×	×	●	●	N.A.	●	●
Shape	●	●	×	●	●	N.A.	●	● *(87, 106)*
Surface area	●	●	●	×	●	N.A.	●	●
Surface charge	●	● *(107)*	●	●	×	×	●	●
Surface functionalization	● *(87)*	●	● *(87, 106)*	●	●	×	●	N.A.
Surface energy	●	●	●	●	●	●	×	●
Crystallinity	●	●	●	●	●	●	●	×

● indicates that the particle property specified on the row influences the corresponding particle property specified in the column, × indicates no obvious influences, N.A. indicates no study were found to address, and the number in the quote lists the reference(s) that indicates the influences.

Table 1.2. The influences of environmental conditions on particle properties.

Environmental factors	Particle size	Particle size distribution	Shape	Surface area	Surface charge	Surface functionalization	Surface energy	Crystallinity
pH	×	● *(108)*	●	●	● *(109)*	×	●	●
Ionic strength	●	● *(109-111)*	●	●	● *(109)*	×	●	●
Electrolyte type (mono-and di-valent cations)	●	● *(107, 109-111)*	×	●	● *(107, 109)*	×	●	●
Temperature	●	● *(112)*	●	×	●	●	●	●
Natural occurring colloids	●	●	●	●	×	●	●	●
Dissolved organic matter (DOM)	×	● *(108)*	●	●	●	● *(103)*	●	×
Dissolved oxygen	●	●	●	●	●	●	×	●
Ultraviolet (UV)	×	×	×	×	●	×	●	×
Carbon dioxide	●	●	●	●	●	●	●	×

Table 1.3. Particle properties and their influences on kinetics behavior of NPs as well as the biological effects.

Particle properties	**Kinetic behavior**			**Toxicokinetics**		
	Aggregation kinetics	Ion release kinetics	Bio-adsorption kinetics	Membrane disruption	Internalization or penetration	Viability or mortality
Particle size	● *(104)*	● *(94, 95, 97, 98)*	● *(31, 101)*	● *(31)*	● *(81)*	● *(82, 113)*
Particle size distribution	● *(83, 104)*	●	●	● *(114)*	*(83)*	● *(83, 114)*
Shape	● *(88)*	●	●	●	● *(115)*	● *(80, 116)*
Surface area	●	●	●	●	●	*(93)*
Surface charge	●	●	● *(117)*	● *(117)*	● *(117)*	● *(118)*
Surface functionalization	●	●	● *(78, 79, 119, 120)*	●	●	● *(78, 79)*
Surface energy	●	●	● *(78, 119)*	●	●	●
Crystallinity	●	●	●	●	●	●
Concentration	● *(108)*	●	●	●	●	●

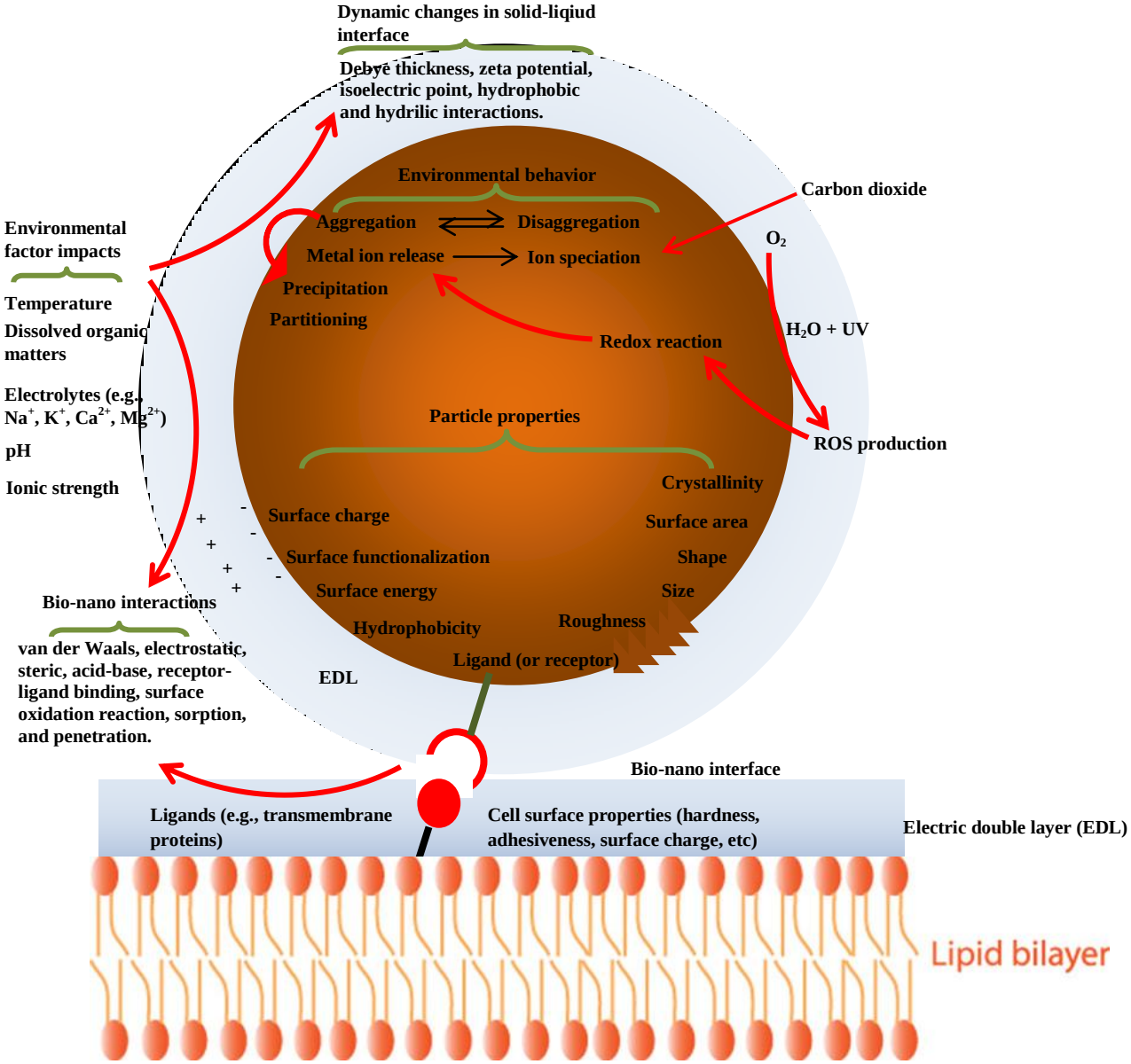

Figure 1.1. Representation of the interface between a nanoparticle and an intact lipid bilayer representative of a cell surface. Various environmental factors, particle properties, and their interrelationships are depicted.

1.4. Fundamental mechanisms of the interactions between NPs and biological interface in aquatic systems

It is generally accepted that all nanotoxicity events arise from surface interactions between NPs and biological interface, such as adsorption *(1, 20)*, which has been demonstrated on bacteria *(101, 103, 121)* and the intestinal epithelium *(31)*. Such surface interactions appear to be logically described by "first principle" theories in colloidal stability, such as DLVO theory. Table 1.4 lists all the major interfacial forces and the relevant contributing factors that needs to specify for calculation. Despite considerable applications, sizable discrepancies were found between DLVO predications and experimental observations in colloidal behavior *(122-125)*, especially at the nanoscale. For instance, the DLVO theory treats interacting surfaces as infinite smooth and flat ones, which in reality does not exist *(126-129)*. Surface heterogeneity still poses a huge challenge for users of the DLVO theory, even though some pioneers incorporated the extended DLVO to account for the non-DLVO effects, including hydration force *(130, 131)*, surface roughness *(132, 133)*, hydrophobic *(134)*, oscillatory *(133)*, osmotic (depletion attraction) *(135, 136)*, and steric, or Helfrich repulsion (affected by entropy effect) *(137)*.

This challenge increases greatly when it comes to the bio-nano interface. First, cells have non-rigid compliant membrane that deforms as a result of the physical confinement or attachment, which leads to a complicated scenario when NPs approach cells. A further complexity arises from non-uniformity and heterogeneous surface characteristics of cells that dramatically alter the interactions with NPs. For example, the presence of surface proteins or other biomolecular structures make the cell surface to have generally 10-50 nm variations in surface roughness. For a micrometer-sized particles interacting with such patchy cell surface, the interactions should more be controlled by the average interfacial energy. However, NPs with 10-50 nm sizes may

vary greatly depending on its interacting locations of the cell surfaces. The third complexity is that the living cells may secret proteins and release other metabolic materials that transform the original surfaces of NPs to totally different ones. This influence is time-dependent or dynamic, which yields the similar situations as we discussed above about the dynamic features of the environmental behavior of NPs. At last, random biophysicochemical process for the living cells may increase the difficulty in predicting bio-nano interactions theoretically. For example, cells may incorporate NPs by active endocytosis.

The above analysis is based on the features of cell surfaces, and more complex factors may also arise from the infinite and interconnected particle properties of the engineered NPs as we extensively discussed previously. Now this study raises the following two questions: to determine and describe the biological consequences of nanomaterial exposure, such as diffusing through cell membranes *(27)*, endocytosis *(138-140)* and cell adhesion *(27)*, what theories or governing functions are we going to develop and use? How can we improve the first-principle theories like DLVO to aid the understanding of the bio-nano interactions? The chapter 2 outlines the main objectives and scope in current study to address and answer these two questions.

Table 1.4. Typical interfacial forces between NPs and biological surfaces *(141-143)*.

Force	Origin	Contributing factors
van der Waals interaction	Electrical and magnetic polarizations.	Interacting surface energy, interaction distance, and particle size.
Electrostatic interaction	Charged interfaces attract counter-ions and repel co-ions through Coulombic forces, giving rise to the formation of an electrostatic double layer	Surface charge, ionic strength, pH, and particle size.
Acid-base interaction	Interactions between hydrogen-donors and hydrogen-acceptors.	Surface hydrophobicity, surface tension, and particle size.
Steric interaction	Polymeric species or biopolymers give rise to spring-like repulsive interactions.	Surface coating coverage, charge density of the polymers and the distribution of polymer configuration.
Polymer bridging interaction	Polymeric species or biopolymers containing charged functional groups can be attracted by oppositely charged moieties on a substrate surface.	Electrolyte, ionic strength, and pH.
Solvent interaction	Lyophilic materials interact favorably with solvent molecules; Lyophobic materials interact unfavorably with solvent molecules.	Hydrophobicity and hydrophilicity of interaction surfaces.
Hydrodynamic interaction	Convective drag, shear, lift and Brownian diffusion.	Hydrodynamic conditions (e.g., Reynolds number), temperature, viscosity, and etc.

1.5. Reference

(1) Nel, A.; Xia, T.; Madler, L.; Li, N. Toxic potential of materials at the nanolevel. *Science* **2006,** *311* (5761), 622-627.

(2) Alivisatos, A. P. Semiconductor nanocrystals: New materials through control of size. *Abstracts of Papers of the American Chemical Society* **1996,** *212*, 30-Inor.

(3) Bailey, R. E.; Nie, S. M. Alloyed semiconductor quantum dots: Tuning the optical properties without changing the particle size. *J. Am. Chem. Soc.* **2003,** *125* (23), 7100-7106.

(4) Zheng, J.; Zhang, C. W.; Dickson, R. M. Highly fluorescent, water-soluble, size-tunable gold quantum dots. *Phys. Rev. Lett.* **2004,** *93* (7), -.

(5) Chang, S.; Zhou, M.; Grover, C. P. Information coding and retrieving using fluorescent semiconductor nanocrystals for object identification. *Opt. Express* **2004,** *12* (1), 143-148.

(6) Barve, A. V.; Lee, S. J.; Noh, S. K.; Krishna, S. Review of current progress in quantum dot infrared photodetectors. *Laser & Photonics Reviews* **2010,** *4* (6), 738-750.

(7) Chan, W. C. W.; Nie, S. M. Quantum dot bioconjugates for ultrasensitive nonisotopic detection. *Science* **1998,** *281* (5385), 2016-2018.

(8) Nagatani, H.; Sakamoto, T.; Torikai, T.; Sagara, T. Encapsulation of Anilinonaphthalenesulfonates in Carboxylate-Terminated PAMAM Dendrimer at the Polarized Water vertical bar 1,2-Dichloroethane Interface. *langmuir* **2010,** *26* (22), 17686-17694.

(9) Boisselier, E.; Diallo, A. K.; Salmon, L.; Ornelas, C.; Ruiz, J.; Astruc, D. Encapsulation and Stabilization of Gold Nanoparticles with "Click" Polyethyleneglycol Dendrimers. *J. Am. Chem. Soc.* **2010,** *132* (8), 2729-2742.

(10) Dutta, T.; Jain, N. K.; McMillan, N. A. J.; Parekh, H. S. Dendrimer nanocarriers as versatile vectors in gene delivery. *Nanomedicine-Nanotechnology Biology and Medicine* **2010,** *6* (1), 25-34.

(11) Corma, A.; Chane-Ching, J. Y.; Airiau, M.; MartInez, C. Synthesis and catalytic properties of thermally and hydrothermally stable, high-surface-area SiO_2-CeO_2 mesostructured composite materials and their application for the removal of sulfur compounds from gasoline. *J. Catal.* **2004,** *224* (2), 441-448.

(12) Lu, X. H.; Zheng, D. Z.; Zhang, P.; Liang, C. L.; Liu, P.; Tong, Y. X. Facile synthesis of free-standing CeO_2 nanorods for photoelectrochemical applications. *Chem. Commun.* **2010,** *46* (41), 7721-7723.

(13) Kang, Y. M.; Kwon, S. H.; Song, P. K. Study on mechanical and electro-optical properties of ITO/CeO_2 films deposited on PI substrate for flexible organic solar cells. *Curr. Appl. Phys.* **2010,** *10* (3), S491-S494.

(14) Xu, L.; Song, H. W.; Dong, B. A.; Wang, Y.; Chen, J. S.; Bai, X. Preparation and Bifunctional Gas Sensing Properties of Porous In_2O_3-CeO_2 Binary Oxide Nanotubes. *Inorg. Chem.* **2010,** *49* (22), 10590-10597.

(15) Anandan, S.; Ashokkumar, M. Sonochemical synthesis of Au-TiO_2 nanoparticles for the sonophotocatalytic degradation of organic pollutants in aqueous environment. *Ultrason. Sonochem.* **2009,** *16* (3), 316-320.

(16) Macyk, W.; Szacilowski, K.; Stochel, G.; Buchalska, M.; Kuncewicz, J.; Labuz, P. Titanium(IV) complexes as direct TiO_2 photosensitizers. *Coord. Chem. Rev.* **2010,** *254* (21-22), 2687-2701.
(17) Lee, J.; Mahendra, S.; Alvarez, P. J. J. Nanomaterials in the Construction Industry: A Review of Their Applications and Environmental Health and Safety Considerations. *ACS Nano* **2010,** *4* (7), 3580-3590.
(18) Nel, A. Air pollution-related illness: Effects of particles. *Science* **2005,** *308* (5723), 804-806.
(19) Society, R. ''Nanoscience and nanotechnologies:Opportunities and uncertainties'. available online at www.nanotec.org.uk/finalReport.htm.
(20) Oberdörster, G.; Oberdörster, E.; Oberdörster, J. Nanotoxicology: an emerging discipline evolving from studies of ultrafine particles. *Environ. Health. Perspect.* **2005,** *113* (7), 823-839.
(21) GAO *Report to the Chairman, Committee on Environment and Public Works, U.S. Senate* 2010.
(22) Mueller, N. C.; Nowack, B. Exposure modeling of engineered nanoparticles in the environment. *Environ. Sci. Technol.* **2008,** *42* (12), 4447-4453.
(23) Klaine, S. J.; Alvarez, P. J. J.; Batley, G. E.; Fernandes, T. F.; Handy, R. D.; Lyon, D. Y.; Mahendra, S.; McLaughlin, M. J.; Lead, J. R. Nanomaterials in the environment: behavior, fate, bioavailability, and effects. *Environ. Toxicol. Chem.* **2008,** *27* (9), 1825–1851
(24) Stone, V.; Nowack, B.; Baun, A.; van den Brink, N.; von der Kammer, F.; Dusinska, M.; Handy, R.; Hankin, S.; Hassellov, M.; Joner, E.; Fernandes, T. F. Nanomaterials for environmental studies: Classification, reference material issues, and strategies for physico-chemical characterisation. *Science of the Total Environment* **2010,** *408* (7), 1745-1754.
(25) Kloepfer, J. A.; Mielke, R. E.; Nadeau, J. L. Uptake of CdSe and CdSe/ZnS quantum dots into bacteria via purine-dependent mechanisms. *Appl. Environ. Microbiol.* **2005,** *71* (5), 2548-2557.
(26) Zhang, W.; Yao, Y.; Chen, Y. Imaging and Quantifying the Morphology and Nanoelectrical Properties of Quantum Dot Nanoparticles Interacting with DNA. *J. Phys. Chem. C* **2011,** *115* (3), 599–606.
(27) Geiser, M.; Rothen-Rutishauser, B.; Kapp, N.; Schurch, S.; Kreyling, W.; Schulz, H.; Semmler, M.; Hof, V. I.; Heyder, J.; Gehr, P. Ultrafine particles cross cellular membranes by nonphagocytic mechanisms in lungs and in cultured cells. *Environ. Health Perspect.* **2005,** *113* (11), 1555-1560.
(28) Jia, X.; Chen, X.; Xu, Y.; Han, X.; Xu, Z. Tracing transport of chitosan nanoparticles and molecules in Caco-2 cells by fluorescent labeling. *Carbohydrate Polymers* **2009,** *78* (2), 323-329.
(29) Koeneman, B. A.; Zhang, Y.; Westerhoff, P.; Chen, Y.; Crittenden, J. C.; Capco, D. G. Toxicity and cellular responses of intestinal cells exposed to titanium dioxide *Cell Biol. Toxicol.* **2009,** *26* (3), 225-238.
(30) Koeneman, B. A.; Zhang, Y.; Hristovski, K.; Westerhoff, P.; Chen, Y.; Crittenden, J. C.; Capco, D. G. Experimental approach for an in vitro toxicity assay with non-aggregated quantum dots. *Toxicology in Vitro* **2009,** *23* (5), 955–962.

(31) Zhang, W.; Kalive, M.; Capco, D. G.; Chen, Y. Adsorption of hematite nanoparticles onto Caco-2 cells and the cellular impairments: effect of particle size *Nanotechnology* **2010,** *21* (35), 355103.
(32) Cousins, B. G.; Allison, H. E.; Doherty, P. J.; Edwards, C.; Garvey, M. J.; Martin, D. S.; Williams, R. L. Effects of a nanoparticulate silica substrate on cell attachment of Candida albicans. *J Appl Microbiol* **2007,** *102* (3), 757-65.
(33) Tsao, N.; Kanakamma, P. P.; Luh, T. Y.; Chou, C. K.; Lei, H. Y. Inhibition of *Escherichia* coli-induced meningitis by carboxyfullerence. *Antimicrob. Agents Chemother.* **1999,** *43* (9), 2273-2277.
(34) Morones, J. R.; Elechiguerra, J. L.; Camacho, A.; Holt, K.; Kouri, J. B.; Ramirez, J. T.; Yacaman, M. J. The bactericidal effect of silver nanoparticles. *Nanotechnology* **2005,** *16* (10), 2346-2353.
(35) Li, M.; Zhu, L.; Lin, D. Toxicity of ZnO Nanoparticles to *Escherichia* coli: Mechanism and the Influence of Medium Components. *Environ. Sci. Technol.* **2011,** *45* (5), 1977-1983.
(36) Brayner, R.; Ferrari-Iliou, R.; Brivois, N.; Djediat, S.; Benedetti, M. F.; Fievet, F. Toxicological impact studies based on *Escherichia* coli bacteria in ultrafine ZnO nanoparticles colloidal medium. *Nano Lett.* **2006,** *6* (4), 866-870.
(37) Huang, Z.; Zheng, X.; Yan, D.; Yin, G.; Liao, X.; Kang, Y.; Yao, Y.; Huang, D.; Hao, B. Toxicological effect of ZnO nanoparticles based on bacteria. *Langmuir* **2008,** *24* (8), 4140-4144.
(38) Vileno, B.; Jeney, S.; Sienkiewicz, A.; Marcoux, P. R.; Miller, L. M.; Forro, L. Evidence of lipid peroxidation and protein phosphorylation in cells upon oxidative stress photo-generated by fullerols. *Biophys. Chem.* **2010,** *152* (1-3), 164-169.
(39) Huang, C. C.; Aronstam, R. S.; Chen, D. R.; Huang, Y. W. Oxidative stress, calcium homeostasis, and altered gene expression in human lung epithelial cells exposed to ZnO nanoparticles. *Toxicology in Vitro* **2010,** *24* (1), 45-55.
(40) Lin, W. S.; Huang, Y. W.; Zhou, X. D.; Ma, Y. F. Toxicity of cerium oxide nanoparticles in human lung cancer cells. *International Journal of Toxicology* **2006,** *25* (6), 451-457.
(41) Byers, R. J.; Hitchman, E. R. Quantum Dots Brighten Biological Imaging. *Progress in Histochemistry and Cytochemistry* **2011,** *45* (4), 201-237.
(42) Chen, X. Y.; Li, J. R.; Li, X. C.; Jiang, L. A new step to the mechanism of the enhancement effect of gold nanoparticles on glucose oxidase. *Biochem Biophys Res Commun* **1998,** *245* (2), 352-5.
(43) Park, H.; Choi, B. G.; Park, T. J.; Yang, M. H.; Kim, J. S.; Jang, S. Y.; Heo, N. S.; Lee, S. Y.; Kong, J.; Hong, W. H. Solution Chemistry of Self-Assembled Graphene Nanohybrids for High-Performance Flexible Biosensors. *ACS Nano* **2010,** *4* (5), 2910-2918.
(44) Imlay, J. A. Pathways of oxidative damage. *Annual Review of Microbiology* **2003,** *57*, 395-418.
(45) Teichroeb, J. H.; Forrest, J. A.; Jones, L. W. Size-dependent denaturing kinetics of bovine serum albumin adsorbed onto gold nanospheres. *Eur Phys J E Soft Matter* **2008,** *26* (4), 411-415.

(46) Lee, C. A.; Tsai, Y. C. Preparation of multiwalled carbon nanotube-chitosan-alcohol dehydrogenase nanobiocomposite for amperometric detection of ethanol. *Sensors and Actuators B-Chemical* **2009,** *138* (2), 518-523.
(47) Wang, Z. Y.; Zhao, J.; Li, F. M.; Gao, D. M.; Xing, B. S. Adsorption and inhibition of acetylcholinesterase by different nanoparticles. *Chemosphere* **2009,** *77* (1), 67-73.
(48) Zhang, C. Y.; Hu, J. Single Quantum Dot-Based Nanosensor for Multiple DNA Detection. *Anal. Chem.* **2010,** *82* (5), 1921-1927.
(49) Zhang, C. Y.; Yeh, H. C.; Kuroki, M. T.; Wang, T. H. Single-quantum-dot-based DNA nanosensor. *Nat. Mater.* **2005,** *4* (11), 826-831.
(50) Obonyo, O.; Fisher, E.; Edwards, M.; Douroumis, D. Quantum dots synthesis and biological applications as imaging and drug delivery systems. *Crit. Rev. Biotechnol.* **2010,** *30* (4), 283-301.
(51) Qi, Z. D.; Li, D. W.; Jiang, P.; Jiang, F. L.; Li, Y. S.; Liu, Y.; Wong, W. K.; Cheah, K. W. Biocompatible CdSe quantum dot-based photosensitizer under two-photon excitation for photodynamic therapy. *J. Mater. Chem.* **2011,** *21* (8), 2455-2458.
(52) Rakovich, A.; Savateeva, D.; Rakovich, T.; Donegan, J. F.; Rakovich, Y. P.; Kelly, V.; Lesnyak, V.; Eychmuller, A. ot/Dye Hybrid System as Photosensitizer for Photodynamic Th. *Nanoscale Research Letters* **2010,** *5* (4), 753-760.
(53) Otake, E.; Sakuma, S.; Torii, K.; Maeda, A.; Ohi, H.; Yano, S.; Morita, A. Effect and Mechanism of a New Photodynamic Therapy with Glycoconjugated Fullerene. *Photochem. Photobiol.* **2010,** *86* (6), 1356-1363.
(54) Zhao, X. C.; Striolo, A.; Cummings, P. T. C-60 binds to and deforms nucleotides. *Biophys. J* . **2005,** *89* (6), 3856-3862.
(55) Chen, G. J.; Qiao, X.; Qiao, P. Q.; Xu, G. J.; Xu, J. Y.; Tian, J. L.; Gu, W.; Liu, X.; Yan, S. P. Synthesis, DNA binding, photo-induced DNA cleavage, cytotoxicity and apoptosis studies of copper(II) complexes. *J. Inorg. Biochem.* **2011,** *105* (2), 119-126.
(56) Chakravarty, A. R. Photocleavage of DNA by copper(II) complexes. *J. Chem. Sci.* **2006,** *118* (6), 443-453.
(57) Takenaka, S.; Yamashita, K.; Takagi, M.; Hatta, T.; Tsuge, O. Photo-induced DNA cleavage by water-soluble cationic fullerene derivatives. *Chem. Lett.* **1999,** (4), 321-322.
(58) Gagn, F.; Auclair, J.; Turcotte, P.; Fournier, M.; Gagnon, C.; Sauv, S.; Blaise, C. Ecotoxicity of CdTe quantum dots to freshwater mussels: Impacts on immune system, oxidative stress and genotoxicity. *Aquat. Toxicol.* **2008,** *86* (3), 333-340.
(59) Green, M.; Howman, E. Semiconductor quantum dots and free radical induced DNA nicking. *Chem. Commun* **2005**, 121-123.
(60) Touati, D. Iron and oxidative stress in bacteria. *Arch. Biochem. Biophys.* **2000,** *373* (1), 1-6.
(61) Trouiller, B.; Reliene, R.; Westbrook, A.; Solaimani, P.; Schiestl, R. H. Titanium Dioxide Nanoparticles Induce DNA Damage and Genetic Instability In vivo in Mice. *Cancer Res.* **2009,** *69* (22), 8784-8789.
(62) Auffan, M.; Rose, J.; Orsiere, T.; De Meo, M.; Thill, A.; Zeyons, O.; Proux, O.; Masion, A.; Chaurand, P.; Spalla, O.; Botta, A.; Wiesner, M. R.; Bottero, J. Y. CeO2 nanoparticles induce DNA damage towards human dermal fibroblasts in vitro. *Nanotoxicology* **2009,** *3* (2), 161-U115.

(63) Park, E. J.; Yi, J.; Kim, Y.; Choi, K.; Park, K. Silver nanoparticles induce cytotoxicity by a Trojan-horse type mechanism. *Toxicology in Vitro* **2010,** *24* (3), 872-878.
(64) Ahamed, M.; Siddiqui, M. A.; Akhtar, M. J.; Ahmad, I.; Pant, A. B.; Alhadlaq, H. A. Genotoxic potential of copper oxide nanoparticles in human lung epithelial cells. *Biochem. Biophys. Res. Commun.* **2010,** *396* (2), 578-583.
(65) Osman, I. F.; Baumgartner, A.; Cemeli, E.; Fletcher, J. N.; Anderson, D. Genotoxicity and cytotoxicity of zinc oxide and titanium dioxide in HEp-2 cells. *Nanomedicine* **2010,** *5* (8), 1193-1203.
(66) Warheit, D. B.; Donner, E. M. Rationale of genotoxicity testing of nanomaterials: Regulatory requirements and appropriateness of available OECD test guidelines. *Nanotoxicology* **2010,** *4* (4), 409-413.
(67) Singh, S.; D'Britto, V.; Prabhune, A. A.; Ramana, C. V.; Dhawan, A.; Prasad, B. L. V. Cytotoxic and genotoxic assessment of glycolipid-reduced and -capped gold and silver nanoparticles. *New J. Chem.* **2010,** *34* (2), 294-301.
(68) Shinohara, N.; Matsumoto, K.; Endoh, S.; Maru, J.; Nakanishi, J. In vitro and in vivo genotoxicity tests on fullerene C-60 nanoparticles. *Toxicol. Lett.* **2009,** *191* (2-3), 289-296.
(69) Pierscionek, B. K.; Li, Y. B.; Yasseen, A. A.; Colhoun, L. M.; Schachar, R. A.; Chen, W. Nanoceria have no genotoxic effect on human lens epithelial cells. *Nanotechnology* **2010,** *21* (3), -.
(70) Falck, G. C. M.; Lindberg, H. K.; Suhonen, S.; Vippola, M.; Vanhala, E.; Catalan, J.; Savolainen, K.; Norppa, H. Genotoxic effects of nanosized and fine TiO_2. *Human & Experimental Toxicology* **2009,** *28* (6-7), 339-352.
(71) Yu, C. C.; Wang, J. J.; Lee, C. L.; Lee, S. H.; Pan, T. M. Safety and Mutagenicity Evaluation of Nanoparticulate Red Mold Rice. *J. Agric. Food. Chem.* **2008,** *56* (22), 11038-11048.
(72) Nelson, S. M.; Mahmoud, T.; Beaux, M.; Shapiro, P.; McIlroy, D. N.; Stenkamp, D. L. Toxic and teratogenic silica nanowires in developing vertebrate embryos. *Nanomedicine-Nanotechnology Biology and Medicine* **2010,** *6* (1), 93-102.
(73) Mashino, T.; Okuda, K.; Hirota, T.; Hirobe, M.; Nagano, T.; Mochizuki, M. Inhibition of *E. coli* growth by fullerene derivatives and inhibition mechanism. *Bioorganic & Medicinal Chemistry Letters* **1999,** *9* (20), 2959-2962.
(74) Thill, A.; Zeyons, O.; Spalla, O.; Chauvat, F.; Rose, J.; Auffan, M.; Flank, A. M. Cytotoxicity of CeO_2 Nanoparticles for *Escherichia coli*. Physico-Chemical Insight of the Cytotoxicity Mechanism. *Environ. Sci. Technol.* **2006,** *40* (19), 6151-6156.
(75) Feng, Q. L.; Wu, J.; Chen, G. Q.; Cui, F. Z.; Kim, T. N.; Kim, J. O. A mechanistic study of the antibacterial effect of silver ions on Escherichia coli and Staphylococcus aureus. *J. Biomed. Mater. Res.* **2000,** *52* (4), 662-668.
(76) Colvin, V. L. The potential environmental impact of engineered nanomaterials. *Nat. Biotechnol.* **2003,** *21* (10), 1166-1170.
(77) Stone, V.; Nowack, B.; Baun, A.; van den Brink, N.; von der Kammer, F.; Dusinska, M.; Handy, R.; Hankin, S.; Hassellov, M.; Joner, E.; Fernandes, T. F. Nanomaterials for environmental studies: Classification, reference material issues, and strategies for physico-chemical characterisation. *Sci. Total Environ.* **2010,** *408* (7), 1745-1754.

(78) Horie, M.; Nishio, K.; Fujita, K.; Endoh, S.; Miyauchi, A.; Saito, Y.; Iwahashi, H.; Yamamoto, K.; Murayama, H.; Nakano, H.; Nanashima, N.; Niki, E.; Yoshida, Y. Protein adsorption of ultrafine metal oxide and its influence on cytotoxicity toward cultured cells. *Chem. Res. Toxicol.* **2009,** *22* (3), 543-553.
(79) Deguchi, S.; Yamazaki, T.; Mukai, S. A.; Usami, R.; Horikoshi, K. Stabilization of C60 nanoparticles by protein adsorption and its implications for toxicity studies. *Chem Res Toxicol* **2007,** *20* (6), 854-8.
(80) Pal, S.; Tak, Y. K.; Song, J. M. Does the antibacterial activity of silver nanoparticles depend on the shape of the nanoparticle? A study of the gram-negative bacterium Escherichia coli. *Appl. Environ. Microbiol.* **2007,** *73* (6), 1712-1720.
(81) Lu, F.; Wu, S. H.; Hung, Y.; Mou, C. Y. Size effect on cell uptake in well-suspended, uniform mesoporous silica nanoparticles. *Small* **2009,** *5* (12), 1408-1413.
(82) Watari, F.; Takashi, N.; Yokoyama, A.; Uo, M.; Akasaka, T.; Sato, Y.; Abe, S.; Totsuka, Y.; Tohji, K. Material nanosizing effect on living organisms: non-specific, biointeractive, physical size effects. *J. R. Soc. Interface* **2009,** *6*, 371-388.
(83) Auffan, M.; Rose, J.; Wiesner, M. R.; Bottero, J.-Y. Chemical stability of metallic nanoparticles: A parameter controlling their potential cellular toxicity in vitro. *Environ. Pollut.* **2009,** *157* (4), 1127-1133.
(84) Tiede, K.; Boxall, A. B. A.; Tear, S. P.; Lewis, J.; David, H.; Hassellov, M. Detection and characterization of engineered nanoparticles in food and the environment. *Food Addit. Contam.* **2008,** *25* (7), 795-821.
(85) Kan, C. X.; Zhu, J. J.; Zhu, X. G. Silver nanostructures with well-controlled shapes: synthesis, characterization and growth mechanisms. *J. Phys. D: Appl. Phys.* **2008,** *41* (15), -.
(86) Si, R.; Flytzani-Stephanopoulos, M. Shape and crystal-plane effects of nanoscale ceria on the activity of Au-CeO_2 catalysts for the water-gas shift reaction. *Angewandte Chemie-International Edition* **2008,** *47* (15), 2884-2887.
(87) Wiley, B.; Sun, Y. G.; Mayers, B.; Xia, Y. N. Shape-controlled synthesis of metal nanostructures: The case of silver. *Chem. Eur. J.* **2005,** *11* (2), 454-463.
(88) Zhou, D. X.; Keller, A. A. Role of morphology in the aggregation kinetics of ZnO nanoparticles. *Water Res.* **2010,** *44* (9), 2948-2956.
(89) Zhu, X.; Zhu, L.; Li, Y.; Duan, Z.; Chen, W.; Alvarez, P. J. J. Developmental toxicity in zebrafish (Danio rerio) embryos after exposure to manufactured nanomaterials: Buckminsterfullerene aggregates (nC60) and fullerol. *Environ. Toxicol. Chem.* **2007,** *26* (5), 976-979.
(90) Zhu, X.; Chang, Y.; Chen, Y. Toxicity and bioaccumulation of TiO_2 nanoparticle aggregates in Daphnia magna. *Chemosphere* **2009,** *78* (3), 209-215.
(91) Zhu, X.; Wang, J.; Zhang, X.; Chang, Y.; Chen, Y. The impact of ZnO nanoparticle aggregates on the embryonic development of zebrafish (Danio rerio). *Nanotechnology* **2009,** *20*, 9.
(92) Zhang, Y.; Chen, Y.; Westerhoff, P.; Hristovski, K.; Crittenden, J. C. Stability of commercial metal oxide nanoparticles in water. *Water Res.* **2008,** *42* (8-9), 2204-2212.
(93) Van Hoecke, K.; De Schamphelaere, K. A.; Van der Meeren, P.; Lucas, S.; Janssen, C. R. Ecotoxicity of silica nanoparticles to the green alga Pseudokirchneriella subcapitata: importance of surface area. *Environ. Toxicol. Chem.* **2008,** *27* (9), 1948-1957.

(94) Meulenkamp, E. A. Size Dependence of the Dissolution of ZnO Nanoparticles. *J. Phys. Chem. B* **1998,** *102* (40), 7764-7769.
(95) Liu, J.; Aruguete, D. M.; Murayama, M.; Hochella, M. F. Influence of Size and Aggregation on the Reactivity of an Environmentally and Industrially Relevant Manomaterial (PbS). *Environ. Sci. Technol.* **2009,** *43* (21), 8178-8183.
(96) Ho, C.-M.; Yau, S. K.-W.; Lok, C.-N.; So, M.-H.; Che, C.-M. Oxidative Dissolution of Silver Nanoparticles by Biologically Relevant Oxidants: A Kinetic and Mechanistic Study. *Chemistry – An Asian Journal* **2010,** *5* (2), 285-293.
(97) Elzey, S.; Grassian, V. H. Nanoparticle Dissolution from the Particle Perspective: Insights from Particle Sizing Measurements. *langmuir* **2010,** *26* (15), 12505-12508.
(98) Schmidt, J.; Vogelsberger, W. Dissolution kinetics of titanium dioxide nanoparticles: the observation of an unusual kinetic size effect. *J Phys Chem B* **2006,** *110* (9), 3955-63.
(99) Fabrega, J.; Fawcett, S. R.; Renshaw, J. C.; Lead, J. R. Silver Nanoparticle Impact on Bacterial Growth: Effect of pH, Concentration, and Organic Matter. *Environ. Sci. Technol.* **2009,** *43* (19), 7285-7290.
(100) Kittler, S.; Greulich, C.; Diendorf, J.; Koller, M.; Epple, M. Toxicity of Silver Nanoparticles Increases during Storage Because of Slow Dissolution under Release of Silver Ions. *Chem. Mater.* **2010,** *22* (16), 4548-4554.
(101) Zhang, W.; Rittmann, B.; Chen, Y. Size Effects on Adsorption of Hematite Nanoparticles on *E. coli* cells. *Environ. Sci. Technol.* **2011,** *45* (6), 2172-2178.
(102) Spalla, O.; eacute; kicheff, P. Adhesion between Oxide Nanoparticles: Influence of Surface Complexation. *J Colloid Interface Sci* **1997,** *192* (1), 43-65.
(103) Li, Z. Q.; Greden, K.; Alvarez, P. J. J.; Gregory, K. B.; Lowry, G. V. Adsorbed Polymer and NOM Limits Adhesion and Toxicity of Nano Scale Zerovalent Iron to *E. coli*. *Environ. Sci. Tech.* **2010,** *44* (9), 3462-3467.
(104) He, Y. T.; Wan, J. M.; Tokunaga, T. Kinetic stability of hematite nanoparticles: the effect of particle sizes. *J. Nanopart. Res.* **2008,** *10* (2), 321-332.
(105) Nanda, K. K.; Maisels, A.; Kruis, F. E.; Fissan, H.; Stappert, S. Higher surface energy of free nanoparticles. *Phys Rev Lett* **2003,** *91* (10), 106102.
(106) Wiley, B.; Sun, Y. G.; Xia, Y. Synthesis of silver nanostructures with controlled shapes and properties. *Acc. Chem. Res.* **2007,** *40* (10), 1067-1076.
(107) Chen, K. L.; Mylon, S. E.; Elimelech, M. Aggregation kinetics of alginate-coated hematite nanoparticles in monovalent and divalent electrolytes. *Environ. Sci. Tech.* **2006,** *40* (5), 1516-1523.
(108) Baalousha, M. Aggregation and disaggregation of iron oxide nanoparticles: Influence of particle concentration, pH and natural organic matter. *Sci. Total Environ.* **2009,** *407* (6), 2093-2101.
(109) El Badawy, A. M.; Luxton, T. P.; Silva, R. G.; Scheckel, K. G.; Suidan, M. T.; Tolaymat, T. M. Impact of Environmental Conditions (pH, Ionic Strength, and Electrolyte Type) on the Surface Charge and Aggregation of Silver Nanoparticles Suspensions. *Environ. Sci. Technol.* **2010,** *44* (4), 1260-1266.
(110) Kallay, N.; Zalac, S. Stability of nanodispersions: a model for kinetics of aggregation of nanoparticles. *J. Colloid Interface Sci.* **2002,** *253* (1), 70-76.

(111) French, R. A.; Jacobson, A. R.; Kim, B.; Isley, S. L.; Penn, R. L.; Baveye, P. C. Influence of Ionic Strength, pH, and Cation Valence on Aggregation Kinetics of Titanium Dioxide Nanoparticles. *Environ. Sci. Technol.* **2009,** *43* (5), 1354-1359.
(112) Garcia-Garcia, S.; Jonsson, M.; Wold, S. Temperature effect on the stability of bentonite colloids in water. *J. Colloid Interface Sci.* **2006,** *298* (2), 694-705.
(113) Pan, Y.; Neuss, S.; Leifert, A.; Fischler, M.; Wen, F.; Simon, U.; Schmid, G.; Brandau, W.; Jahnen-Dechent, W. Size-dependent cytotoxicity of gold nanoparticles. *Small* **2007,** *3*, 1941-1949.
(114) Sharma, V. K. Aggregation and toxicity of titanium dioxide nanoparticles in aquatic environment-A Review. *J. Environ. Sci. Health, Part A: Environ. Sci. Eng.* **2009,** *44* (14), 1485-1495.
(115) Zhang, K.; Fang, H.; Chen, Z.; Taylor, J. S.; Wooley, K. L. Shape effects of nanoparticles conjugated with cell-penetrating peptides (HIV Tat PTD) on CHO cell uptake. *Bioconjug Chem* **2008,** *19*, 1880-1887.
(116) Kittler, S.; Greulich, C.; Koller, M.; Epple, M. Synthesis of PVP-coated silver nanoparticles and their biological activity towards human mesenchymal stem cells. *Materialwiss. Werkst.* **2009,** *40* (4), 258-264.
(117) Cho, E. C.; Xie, J.; Wurm, P. A.; Xia, Y. Understanding the role of surface charges in cellular adsorption versus internalization by selectively removing gold nanoparticles on the cell surface with a I2/KI etchant. *Nano Lett.* **2009,** *9* (3), 1080-1084.
(118) El Badawy, A. M.; Silva, R. G.; Morris, B.; Scheckel, K. G.; Suidan, M. T.; Tolaymat, T. M. Surface Charge-Dependent Toxicity of Silver Nanoparticles. *Environ. Sci. Technol.* **2011,** *45* (1), 283-287.
(119) Dutta, D.; Sundaram, S. K.; Teeguarden, J. G.; Riley, B. J.; Fifield, L. S.; Jacobs, J. M.; Addleman, S. R.; Kaysen, G. A.; Moudgil, B. M.; Weber, T. J. Adsorbed proteins influence the biological activity and molecular targeting of nanomaterials. *Toxicol. Sci.* **2007,** *100* (1), 303-315.
(120) Behrens, I.; Pena, A. I.; Alonso, M. J.; Kissel, T. Comparative uptake studies of bioadhesive and non-bioadhesive nanoparticles in human intestinal cell lines and rats: the effect of mucus on particle adsorption and transport. *Pharm Res* **2002,** *19* (8), 1185-93.
(121) Schwegmann, H.; Feitz, A. J.; Frimmel, F. H. Influence of the zeta potential on the sorption and toxicity of iron oxide nanoparticles on *S. cerevisiae* and *E. coli*. *J. Colloid Interface Sci.* **2010,** *347* (1), 43-48.
(122) Hoek, E. M. V.; Bhattacharjee, S.; Elimelech, M. Effect of Membrane Surface Roughness on Colloid membrane DLVO Interactions. *langmuir* **2003,** *19* (11), 4836-4847.
(123) Richard Bowen, W.; Doneva, T. A. Atomic force microscopy studies of nanofiltration membranes: surface morphology, pore size distribution and adhesion. *Desalination* **2000,** *129* (2), 163-172.
(124) Elimelech, M.; O'Melia, C. R. Kinetics of deposition of colloidal particles in porous media. *Environ. Sci. Tech.* **2002,** *24* (10), 1528-1536.
(125) Elimelech, M.; Xiaohua, Z.; Childress, A. E.; Seungkwan, H. Role of membrane surface morphology in colloidal fouling of cellulose acetate and composite aromatic polyamide reverse osmosis membranes. *J. Membr. Sci.* **1997,** *127* (1), 101-109.
(126) Hermansson, M. The DLVO theory in microbial adhesion. *Colloids Surf., B* **1999,** *14* (1-4), 105-119.

(127) Sun, N.; Walz, J. Y. A model for calculating electrostatic interactions between colloidal particles of arbitrary surface topology. *Journal of Colloid and Interface Science* **2001,** *234* (1), 90-105.
(128) Bacchin, P.; Aimar, P.; Sanchez, V. Influence of surface interaction on transfer during colloid ultrafiltration. *J. Membr. Sci.* **1996,** *115* (1), 49-63.
(129) Pujar, N. S.; Zydney, A. L. Electrostatic effects on protein partitioning in size-exclusion chromatography and membrane ultrafiltration. *J. Chromatogr. A* **1998,** *796* (2), 229-238.
(130) Butt, H.-J. Measuring electrostatic, van der Waals, and hydration forces in electrolyte solutions with an atomic force microscope. *Biophys. J.* **1991,** *60* (6), 1438-1444.
(131) Chang, Y.-I.; Chang, P.-K. The role of hydration force on the stability of the suspension of Saccharomyces cerevisiae-application of the extended DLVO theory. *Colloids Surf., A* **2002,** *211* (1), 67-77.
(132) Hoek, E. M. V.; Agarwal, G. K. Extended DLVO interactions between spherical particles and rough surfaces. *J. Colloid Interface Sci.* **2006,** *298* (1), 50-58.
(133) Bostrom, M.; Williams, D. R. M.; Ninham, B. W. Specific ion effects: Why DLVO theory fails for biology and colloid systems. *Physical Review Letters* **2001,** *8716* (16), -.
(134) Ong, Y. L.; Razatos, A.; Georgiou, G.; Sharma, M. M. Adhesion Forces between E. coli Bacteria and Biomaterial Surfaces. *langmuir* **1999,** *15* (8), 2719-2725.
(135) Marenduzzo, D.; Finan, K.; Cook, P. R. The depletion attraction: an underappreciated force driving cellular organization. *J. Cell Biol.* **2006,** *175* (5), 681-686.
(136) YODH, A. G.; LIN, K.; CROCKER, J. C.; DINSMORE, A. D.; VERMA, R.; KAPLAN, P. D. Entropically driven self-assembly and interaction in suspension. *Philos. Trans. R. Soc. London, Ser. A* **2001,** *359* (1782), 921-937.
(137) Rijnaarts, H. H. M.; Norde, W.; Lyklema, J.; Zehnder, A. J. B. DLVO and steric contributions to bacterial deposition in media of different ionic strengths. *Colloids Surf., B* **1999,** *14* (1-4), 179-195.
(138) Wilhelm, C.; Gazeau, F.; Roger, J.; Pons, J. N.; Bacri, J. C. Interaction of anionic superparamagnetic nanoparticles with cells: kinetic analyses of membrane adsorption and subsequent internalization. *langmuir* **2002,** *18* (21), 8148-8155.
(139) Duan, H.; Nie, S. Cell-penetrating quantum dots based on multivalent and endosome-disrupting surface coatings. *J. Am. Chem. Soc.* **2007,** *129* (11), 3333-3338.
(140) Rothen-Rutishauser, B. M.; Schurch, S.; Haenni, B.; Kapp, N.; Gehr, P. Interaction of fine particles and nanoparticles with red blood cells visualized with advanced microscopic techniques. *Environ. Sci. Technol.* **2006,** *40* (14), 4353-4359.
(141) Petosa, A. R.; Jaisi, D. P.; Quevedo, I. R.; Elimelech, M.; Tufenkji, N. Aggregation and Deposition of Engineered Nanomaterials in Aquatic Environments: Role of Physicochemical Interactions. *Environ. Sci. Technol.* **2010,** *44* (17), 6532-6549.
(142) Nel, A. E.; Madler, L.; Velegol, D.; Xia, T.; Hoek, E. M. V.; Somasundaran, P.; Klaessig, F.; Castranova, V.; Thompson, M. Understanding biophysicochemical interactions at the nano-bio interface. *Nat. Mater.* **2009,** *8* (7), 543-557.
(143) Oss, C. J. v. *Interfacial Forces in Aquaeous Media*. Second Edition ed.; Taylor & Francis Group: Boca Raton, Florida, 2006; p 81-83.

CHAPTER 2

RESEARCH OBJECTIVES

2.1. Research objectives

Today, the complexity of bio-nano interactions as well as the potential adverse effects associated with nanomaterial exposure still remain largely elusive, which motivates us to carry out extensive research to harness the inadequate knowledge in this regard. The overall goal of this study is to gain better understandings about the nanoscale processes, between NPs and between NPs and biological surfaces. The specific scopes of this study are to investigate the size-dependence of NPs in kinetics of aggregation, ion release, and adsorption onto cell surfaces, as well as the interfacial characteristics including interfacial forces, hydrophobicity, and surface electronic potential. The study was carried out by experimental approach and by formulating mathematical models to evaluate the above-mentioned kinetics processes and interfacial properties.

2.2. Organization of this thesis

Chapter 1 briefly outlines the current understandings about nanotoxicity and its potential or widely accepted mechanisms. Then I critically reviewed the particle properties with toxicity relevance and discussed the interconnections between different NP properties, dynamic evolution of these properties for NPs in aqueous phase, and the complex influences of the interconnections and dynamic features of the particle properties on toxicokinetics that were experimentally recognized from previous research.

Chapter 2 introduces the research goal, thesis structure, and important contributions to the area of nanotechnology implication research.

Chapter 3 delineates the aggregation kinetics of three typical metal oxide NPs (CeO_2, α-Fe_2O_3, and CuO) in aqueous media. The Extended Derjaguin-Landau-Verwey-Overbeek (EDLVO) theory, which considers the acid-base interaction energy, was employed to calculate the interaction potential, and moreover, the aggregation kinetics model was established for the first time by combining the Arrhenius equation and the EDLVO theory. This combined model not only can interpret the dynamic feature of aggregation kinetics, particle size effect, ionic strength effect, and temperature effect, but also potentially can be used for predicting the aggregation kinetics of all kinds of NPs in aqueous phases. Furthermore, attempts were also made to derive the aggregation kinetics based on the "first-principles" theories such as flocculation theory and Smoluchowski equation.

Chapter 4 studied rather complicated aqueous behavior of AgNPs representative of reactive metallic NPs. Ion release and aggregation are simultaneously occurring to AgNPs in aqueous media. I specifically investigated the effects of particle size, particle concentration, and dissolved oxygen on these two processes. In addition, the mutual effects on the two process kinetics are discussed as well. Ag^+ release rates and aggregation rates were found to be dependent on primary particle size, concentration, and other environmental factors such as dissolved oxygen (DO) and pH. This study outlines the importance of accounting DO as one of the important factors for the stability of chemically reactive NPs besides ionic strength, pH, and temperature that are extensively studied in most literature.

After characterizing the two typical environmental behavior (aggregation and ion release) of NPs, Chapter 5 and Chapter 6 investigated bio-nano interactions which started with the adsorption kinetics of hematite NPs (as a typical metal oxide NPs) onto human epithelial cells (Caco-2) and bacterial cells (*E. coli*) respectively. The size effects on the adsorption kinetics were primarily discussed and analyzed. In addition to adsorption

kinetics, the cell surface damages, cell penetration, surface potential variations, and interfacial forces after adsorption of NPs were systematically investigated. These findings will lead to a more thorough knowledge of bio-nano interfacial interaction mechanisms and allow us to establish criteria for designing environmentally benign nanomaterials.

Chapters 7 and 8 are developing new experimental approach for resolving two important surface properties: the nanoscale hydrophobicity and surface potential, which are highly decisive in the fate and transport of nanomaterials in the environment. As previously recognized, conventional characterization methods for environmental pollutants are often applicable to nanomaterials due to the inhomogeneous properties (e.g., solubility and aggregation) in aqueous media. For example, the critical drawback of both the contact angles and zeta potential measurements is that they reflect macroscopic or overall characteristics of a surface. Nevertheless, nanomaterial surfaces are structurally complex (e.g., different shapes and asperities) and chemically heterogeneous and cannot be considered as a smooth surface of a sphere. Therefore, innovative approach is needed to be developed and address these two properties at nanoscale. My research is to derive a theoretical framework that correlates the adhesion force between the AFM cantilever tip and any surfaces of nanomaterials to the surface energy that are conventionally obtained by measuring the contact angle. This innovative approach allows us to evaluate the surface hydrophobicity at nanoscale with the resolution of the contact area between the tip and any substrate surfaces. In other words, to assess the nanoscale hydrophobicity, we can use adhesion force as surrogate to quantify the surface hydrophobicity instead of contact angle measurement, which gives macroscopic surface characteristics.

Chapter 9 briefly recommends future research addressing the key factors associated with bio-nano interactions.

2.3. Originality and merit of research

The findings of this study are original and aimed at achieving better understandings of nanoscale processes, between NPs and between NPs and biointerfaces, as mentioned previously in the research goal. The most important message to deliver from this study is to refresh people about the interconnected and dynamic particle properties of NPs in aqueous media and unique nanoscale interfacial characteristics in bio-nano interactions. Specifically, the knowledge gained from this study is dedicated to the development of nanotechnology implication research from the following six major aspects:

(1) Aggregation kinetics of metal or metal oxide NPs in aqueous media;

(2) Ion release kinetics of AgNPs;

(3) Adsorption kinetics of NPs onto cell surfaces;

(4) Interfacial force between NPs and bacterial cell surfaces;

(5) Development of electric mode of AFM or KFM in probing the nanoelectric properties of NPs and bio-nano interfaces;

(6) Method developments for measuring the nanoscale hydrophobicity of nanomaterials.

CHAPTER 3

AGGREGATION KINETICS OF METAL OXIDE NANOPARTICLES AND KINETICS MODELING

Work of this chapter is related to the publications or manuscripts:
Wen Zhang, Kungang Li, John Crittenden, and Yongsheng Chen. Aggregation kinetics of metal oxide NPs and kinetics modeling. In preparation.

3.1. Abstract

The stability and particle interactions of nanoparticles (NPs) play significant roles in their environmental fate and transport. This chapter investigated aggregation kinetics of three typical metal oxide NPs (CeO_2, α-Fe_2O_3, and CuO) in aqueous media. The aggregation data of CeO_2 NPs was primarily used for establishing the kinetics model for interpreting and predicting the hydrodynamic size evolution during particle aggregation, while the data for α-Fe_2O_3, and CuO were further used to validate the model. Our results showed that the classic Derjaguin−Landau−Verwey−Overbeek (DLVO) theory prediction was found to deviate from the time-resolved dynamic light scattering (TR-DLS) experimental data. Thus, the Extended DLVO (EDLVO) theory, which considers the acid-base interaction energy, was employed to successfully overcome such discrepancies. Moreover, the aggregation kinetics model was established for the first time by combining the Arrhenius equation and the EDLVO theory and was further validated with the experimental data. This model equation not only interprets the dynamic changes of aggregation kinetics over time, particle size effect, ionic strength effect, and temperature effect, but also potentially is useful in predicting the aggregation kinetics of all kinds of NPs in aqueous phases. Finally, this work laid groundwork for the theoretical modeling of NP aggregation and provided insight into nanoscale processes.

3.2. Introduction

Due to the rapid expansion of nanotechnology and the increasing applications of nanomaterials, it is widely accepted and reasonably needed to further advance knowledge in the area of environmental fate and transport of nanomaterials *(1-3)*. Upon release, nanoparticles (NPs) are likely to interact with their surrounding environment as well as to aggregate, depending on the balance between interparticle forces, namely van der Waals and electrostatic interactions *(1, 2)*. Aggregation will strongly impact their mobility, and reactivity of NPs, as well as biological interactions (e.g., bioavailability) *(1-3)*. Some metallic, metal oxide and carbon-based nanomaterials exhibit in vitro toxicity that has been linked with the colloidal stability in aqueous media *(4-6)*. Thus, studying the stability and aggregation behavior of NPs is of great importance for understanding and predicting the fate, transport, and biological impacts *(7-9)*.

The NP aggregation has been studied by several investigators over the past few years *(10, 11)*. The solution chemistries (e.g., pH, ionic strength and valence, the content of natural organic matters or NOM) as well as particle size and concentration were systematically examined previously *(12-17)*. There has been few studies that touched aggregation kinetics modeling *(18)*, which is essentially important for fundamentally understanding and predicting such nanoscale processes. Recently, the early stage aggregation kinetics (the time in which the aggregate's hydrodynamic diameter grows by 25%) is widely described by attachment efficiency (α), also known as the inverse stability ratio ($1/W$) *(12, 15, 19)*. Depending on the rate of aggregation, the NP aggregation can be divided into the diffusion-limited (DLCA) and reaction-limited (RLCA) clustering aggregation regimes. In the RLCA regime, an increase in the electrolyte concentration screens the surface charge and reduces the energy barrier to aggregation, thus leading to faster aggregation. However, at electrolyte concentrations above the critical coagulation concentration (CCC), the energy barrier is eliminated, leading to the DLCA (i.e., $\alpha = 1/W = 1$). This method has been proven useful in studying the kinetics in the initial

aggregation stages for many particle systems *(12, 15, 19, 20)*. However, the theoretical calculation of the stability ratio (*1/W*) based on the classic DLVO theory often finds inconsistency with experimental observations *(19, 21)*. Moreover, attachment efficiency is unable to interpret the post-aggregation kinetics (e.g., hydrodynamic sizes of aggregates become greater than 25% of the origin sizes). Thus, the fundamental mechanisms of nanoscale aggregation kinetics still remain elusive.

Despite wide application, there appears to be a sizable discrepancy between the classic DLVO predictions and experimental observations as mentioned above and in many other colloidal systems *(22, 23)*. To increase the accuracy of the classical DLVO prediction, the extended DLVO (EDLVO) theory has been developed *(24-26)*. Usually, hydration force *(27, 28)*, hydrophobic *(29)*, osmotic (depletion attraction) *(30, 31)*, and steric or Helfrich repulsion (an entropy effect) *(32)* are considered in additional to DLVO forces. Model predictions made with EDLVO correspond better to measured results *(33, 34)*. However, the EDLVO theory alone is limited to the quantitative description of the aggregation relying on thermodynamics (i.e., the energy barrier for interparticle interactions) and could hardly be used in the kinetics aspect *(35)*. As investigated previously *(15, 19, 36)*, the particle aggregation can be treated as a second-order reaction under low concentrations of NPs, and the rate constant for the aggregation kinetics has an Arrhenius form, which is widely used to interpret the temperature dependence of reaction rate constants *(37)*. The activation energy in the Arrhenius equation has the similar meaning with the energy barrier in the EDLVO theories, which both tend to prevent the reaction to happen *(38)*. Therefore, it would be interesting to explore the combination of the Arrhenius equation and the EDLVO theory in the analysis of aggregation kinetics.

In line with this rationale (more details are provided in next section), this study investigated the aggregation kinetics of three typical metal oxide (namely, CeO_2, α-Fe_2O_3, and CuO) NPs using TR-DLS. These metal NPs were selected because they are

commonly used in commercial applications or relevant studies and were reported to have toxicological significance *(12, 14, 35, 39-42)*. Primary discussions of the aggregation kinetics model employed the aggregation data of CeO_2 NPs, whereas the aggregation of hematite and CuO NPs were also investigated and particularly used for validating the model prediction on temperature effects. The aggregation kinetics model was established with the Arrhenius equation, which was modified by substituting the activation energy with the energy barrier calculated from the EDLVO theory. The model was further examined in regard to the effects of particle size, ionic strength and temperature of the aqueous media. Furthermore, a theoretical kinetic model for particle aggregation was derived on the basis of flocculation theory that considers attachment efficiency and frequency. As a comparison, this theoretical equation also provides meaningful insight into the nanoscale aggregation kinetics.

3.3. Theory

The theory of Colloid Stability considers collision frequency and efficiency *(43)*. Collision frequency was theoretically solved by Smoluchowski *(44, 45)*, while the basis for evaluation of the collision efficiency was given by Fuchs *(46)*. To use the Fuchs theory, the interaction energy as a function of the distance between interacting particles must be resolved by the classic DLVO theory. As mentioned above, recently, the kinetics of NP aggregation has been investigated extensively and one of the most mature theories about aggregation kinetics is elaborated by attachment efficiency *(10, 11)*, which well describes the early-stage aggregation of primary NPs.

$$\left[\frac{dr_H(t)}{dt}\right]_{t\to 0} \propto \left(k_{11}\right) N_0 \qquad (1)$$

where $r_H(t)$ is the hydrodynamic radius of aggregates as a function of time t, N_0 is the initial number concentration of the primary particles, and k_{11} is the aggregation rate

constant. In fact, this quantitative interpretation of aggregation kinetics of NPs is on the basis of the Brønsted concept and the Ficker's Law *(18)*, treating NPs as homogeneous reactants like molecules or ions. This treatment is reasonable because when NPs are small compared to the extent of the electric double layer (EDL), the NPs surrounded by the EDL is similar to an ion situated in the center of an ionic cloud. In the course of collision two NPs in contact have a common diffuse layer or "ionic cloud". Thus, the interparticle interactions may be considered in the same way as for two interacting ions or as a homogeneous reaction and consequently described by the Brønsted theory, which considers the "transition state" in the dynamic reactions, leading to oriented or random configuration of aggregates *(47-49)*.

However, despite the wide applications, attachment efficiency also finds its limitations or insufficiency in predicting the particle aggregation kinetics. As noted above, the post-aggregation kinetics that evolves large particle interactions or aggregation in DLCA regime cannot be described, partially because of the loss of potency of the Brønsted theory. Particle transport characteristics (e.g., mobility or diffusivity) began to influence the aggregation kinetics more significantly, switching the mode of aggregation from a pseudo-chemical reaction to a particle collision process *(50)*. This switch can also lead to a change in the evolution of fractal dimension of aggregates. Many aggregation processes are fractal in nature *(51)*, i.e., the mass of a fractal aggregate, *m(R)*, is related to the hydrodynamic radius, r_H, to a power of the fractal dimension, d_F,: $m(R) \propto r_H^{d_F}$. For the slow aggregation, particles have more time to configure themselves into a more ordered and oriented structure, thus, the fractal dimension is high. Typical DLCA and RLCA aggregates possess a d_F of 1.7~1.8 and approximately 2.1 respectively *(52)*.

Previously, we introduced an adsorption kinetic model for NPs onto the bio-interface based on the interfacial force boundary layer (IFBL) theory that indicates when the particle transport governs aggregation kinetics, the Ficker's Law may become

insufficient in describing the transport phenomena of NPs; whereas the roles of interfacial forces or DLVO interactions may arise and begin to influence the particle mobility, exhibiting a certain extent of size effects *(35)*. In respect to balancing the roles of interfacial forces and conventional transport mechanisms (e.g., advection and dispersion), Nikolakis et al. proposed a transport growth model to account for the presence of the energy barrier to the particle coagulation in addition to the dispersion term *(50)*:

$$\frac{\partial c}{\partial t} = \frac{1}{r^2}\frac{\partial}{\partial r}\left[Dr^2 \frac{\partial c}{\partial r} + r^2 c \frac{D}{k_B T}\frac{\partial U}{\partial r} \right] \tag{2}$$

where c is the NP concentration, D is the diffusion coefficient of the NPs, k_B is Boltzmann constant (1.38×10^{-23} J/K), T is absolute temperature, r is the transport distance, and U is the interaction energy between particles. Eq. (2) gives a better qualitative understanding about the inter-exchanging roles of dispersion and interfacial energy on the transport behavior of NPs. The first term ($Dr^2 \frac{\partial c}{\partial r}$) accounts for the effect of dispersion, which tends to play a more significant role in the initial stage of aggregation due to the high number concentrations of primary NPs and the high diffusion coefficient (D) for small NPs and gradually diminish its role as the primary particle concentration decreases and the aggregate's size increases. In contrast, the interaction energy between small NPs is low at the early stage of aggregation and thus the second term ($r^2 c \frac{D}{k_B T}\frac{\partial U}{\partial r}$) that represents the interaction energy effect does not substantially impact the transport. Nevertheless, for big NPs or aggregated sizes, the energy barrier that has to be overcome between two NPs come in contact significantly increases and moreover, the diffusion coefficient for large NPs is low. Therefore, the role of the interaction energy on particle transport mechanisms begins to increase.

To use Eq. (2), appropriate boundary conditions and assumptions must be made and the most important derivation from Eq. (2) is the kinetics of aggregation as shown in Eq. (3):

$$\frac{dr_H}{dt} = \frac{2}{9}\frac{k_B T c_0 r_s^2 (r_H + r_s)}{r_H^2\left[2\int_0^\infty \frac{e^{U/k_B T}}{(u+2)^2}du\right]} \tag{3}$$

where $u=2d/(r_H+r_s)$ and d is the interacting distance between two NPs, and other symbols are defined previously. As mentioned above, the interaction energy (U) is a function of the interacting distance (d) and is comprised of the attractive van der Waals interaction energy (vdW) and the repulsive electrostatic double layer interaction energy (EL) in the classic DLVO theory, as well as the Lewis acid-base interaction energy (AB), which is considered in the calculation of this study, as an addition in the EDLVO theory. Eq. (3) indicates that the hydrodynamic radius growth rate is dependent on initial particle size (r_s), concentration (c_0), temperature (T), hydrodynamic size (r_H), and the interaction energy (U).

Although Eq. (3) yielded an excellent agreement with experimental observations in nanocrystal growth kinetics, it requires a sophisticated mathematical approach to solve Eq. (3) by numerical integration with appropriate boundary conditions. In engineering applications, this mathematical approach is intricate and is not easy to use. Most importantly, this equation that is used to describe nanocrystal growth kinetics has not been validated for use in describing the aggregation kinetics of NPs. Thus, there is a need to seek a simplified form of kinetics equation with the consideration of the role of interaction energy in particle transport mechanisms. In fact, Eq. (3) is in a form of the Arrhenius equation and the activation energy term (E_a) is replaced by the interaction energy (U). The Arrhenius equation has well been employed to describe the reaction kinetics in engineering applications due to its simplicity and ease of use. In this study,

we attempted to modify the Arrhenius equation by replacing the activation energy with the interaction energy calculated from the EDLVO theory, shown in Figure 3.1, and more details are provided below in sections 3.3.7. This combination of the Arrhenius equation and the EDLVO theory may well reflect the influences of both diffusion and interaction energy on the aggregation kinetics and gives us a unique angle of exploring the kinetics behavior of environmental transport at nanoscale.

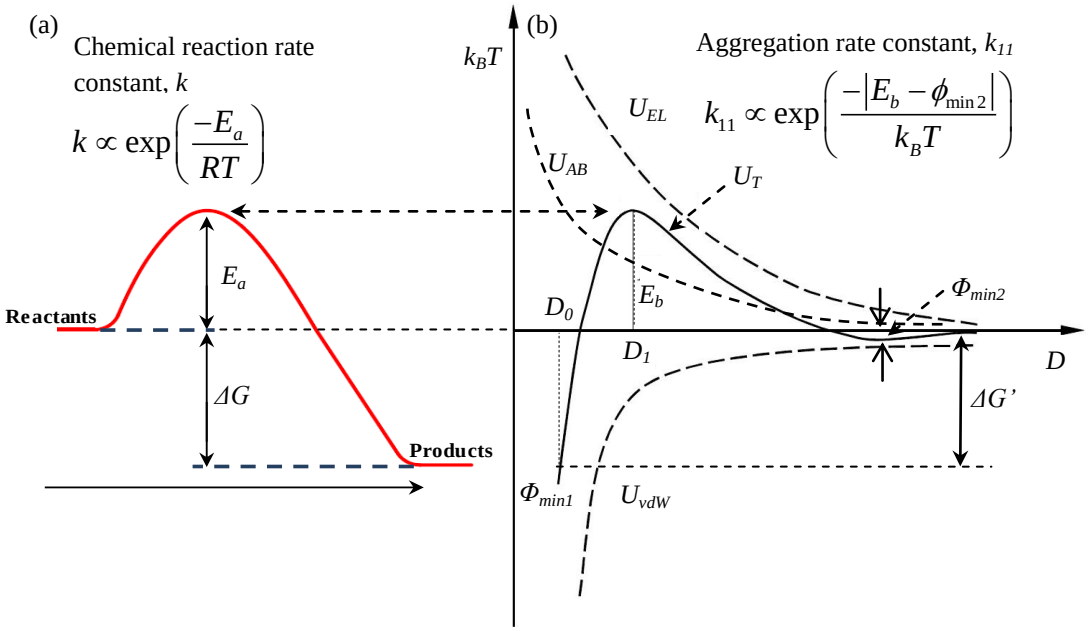

Figure 3.1. (a) A typical reaction thermodynamics curve, which shows the activation energy (E_a) required for the reaction to proceed. (b) Net interaction energy (U_T) between two approaching particles in solution obtained by the EDLVO theory. Typical interaction energy curves have a primary energy minimum ($\phi_{\min 1}$), an energy barrier (E_b), and a secondary energy minimum ($\phi_{\min 2}$).

3.4. Materials and Methods

3.4.1. NPs

Water suspension of CeO_2 NPs was purchased from Sigma Aldrich with the manufacturer's reported size of 70~100 nm. CuO NPs was purchased in powder form from Sigma Aldrich with the manufacturer's reported size of 20~50 nm. After dispersal in deionized (DI) water, CuO NP suspension was sonicated for 35-45 min (Misonix sonicator S-4000, Qsonica, LLC). Hematite (α-Fe_2O_3) NPs were synthesized with the mean diameter of 53 nm according to the method of Penners and Koopal *(53)* with the minor modifications as we reported previously *(41, 54)*. Unless indicated, the mass concentrations of 20 mg/L in [M^{n+}] for the three types of NPs was used in zeta potential measurement and aggregation kinetics experiments.

3.4.2. NPs characterization

The morphology and sizes of NPs were studied by a transmission electron microscopy (TEM) and atomic force microscopy (AFM). TEM was operated on a Philips EM420 at 47 kV. TEM samples were prepared by placing 5 µL of the water suspension on copper grids with a continuous carbon film coating, followed by solvent evaporation at room temperature. AFM was operated on an Agilent 5500 Molecular Imaging AFM in tapping mode with a scanning speed of 2000~5000 nm/s and a drive amplitude of 2 V *(55)*. 2.5 µl of the water suspension was deposited on a clean silicon wafer and dried at room temperature for 15 min.

The crystallography was analyzed using X-Ray Diffraction (XRD) pattern using X-ray powder diffractometer (Philips PW 1800, PANalytical Almelo, The Netherlands) with a Cu Kα radiation (λ = 1.54 Å). XRD analysis were recorded at a scanning rate of 0.02^o s^{-1} in the 2θ range of 30~10^o.

3.4.3. Particle size distribution

The particle size distribution (PSD) and the hydrodynamic radius (r_H) were determined on a Zetasizer Nano ZS instrument (Malvern Instruments). 1.5 ml of the water suspensions of NPs was placed into a standard macro-cuvette (10 mm path length). The measurement temperature was maintained at 25^{o}C, and the scattering angle was 173^{o}. For each sample, the instrument reported a PSD diagram with a polydispersivity index (PDI) value indicative of the dispersion quality.

3.4.4. Zeta potential

The same Zetasizer Nano ZS instrument was also used to measure electrophoretic mobility which was subsequently transformed to ζ potential using the Smoluchowski's approximation. ζ potentials of NPs at different pHs were measured in water suspensions using the folded capillary cell (DTS1060, Malvern Instruments). The pH value of the NP suspension was adjusted by 0.1 M NaOH or 0.1 M HCl and the total ionic strength of the suspension after the adjustment was controlled less than 10 mM to reduce aggregation of NPs. The pH covered a range of 2 to 10 with measurements made at increments of approximately 0.8 pH units. At each pH, the reported zeta potentials and associated uncertainty were determined from three independent measurements. A refractive index (RI) of 2.15, 2.94 and 2.55 were used respectively for CeO_2 *(56)*, hematite *(12)*, and CuO NPs. Five measurements (15~30 cycles per measurement) were made for each suspension at different pHs.

3.4.5. Surface energy analysis by contact angle measurement

NPs were spin-coated on a clean silicon wafer by a spin coater device (WS-400E, Laurell Technologies Corporation). The thin layer or film of NPs were coated on clean silicon wafers by dropping a 200 µL of the water suspension of NPs with a mass concentration of approximately 100 mg/L in [M^{n+}] on the substrate and spinning at 3000

rpm for 5 min. Finally, air dry for 15~30 min before measuring the contact angle. Three kinds of probe solvents (DI water, Glycerol, and Formamide) were used and their surface tension properties were summarized in Table 3.1. The values of contact angles (θ_L) for each type of solvents were measured on a Ram é-hart Model 250 goniometer.

3.4.6. Aggregation kinetics

The aggregation experiments were performed using time resolved-dynamic light scattering (TR-DLS) on the Malvern Zetasizer instrument. All experiments used the same mass concentrations of NPs. pH of the aqueous media was maintained at approximately pH 5.7 and the ionic strength was within the range of 1 mM to 100 mM by adding KCl. The average hydrodynamic radii of NPs were monitored starting immediately after the addition of NPs into the media, with a complete autocorrelation function recorded every 6 s. The aggregation rate at the early stage of aggregation as indicated by the slope of hydrodynamic radius (dr_H/dt) was determined by fitting a linear function to the experimental data recorded during a time interval.

3.4.7. Aggregation kinetics modeling

According to hard sphere collision theory *(57)*, the reaction rate constant (k) is expressed:

$$k_{11} = f \exp(\frac{-E_a}{RT}) \tag{4}$$

$$f = \frac{1}{2}\pi\sigma_{AB}^2\left(\frac{8\pi k_B T}{\mu m_{AB}}\right)^{1/2} N_A \tag{5}$$

$$m_{AB} = \frac{m_A m_B}{m_A + m_B} \tag{6}$$

where *f* is the frequency factor for the reaction, E_a is the activation energy (J/mol), *R* is the gas constant, 8.314 J/(K mol), *T* is absolute temperature, 298 K, k_B is Boltzmann constant, 1.38×10^{-23} J/K, σ_{AB} is the collision radius, m_{AB} is the reduced mass, m_A and m_B are the molecular weights of reactants A and B, μ is the dynamic viscosity of the medium that accounts for the medium effect on diffusivity of NPs in aqueous phase, and all other parameters are specified previously. According to previous research, aggregation is predominately contributed by the collisions of small sized primary NPs largely due to their higher mobility *(18)*. Thus, with aggregated sizes increasing (e.g., $m_A \gg m_B$), m_{AB} is approximated to be the mass of the primary NPs (m_B). To relate the chemical reaction kinetics to the aggregation kinetics, aggregation is treated as a pseudo-reaction process *(12)*. The role of interaction energy (U_{iwi}^{TOT}) in colloidal interactions has an analogue with chemical reaction thermodynamics. The activation energy (E_a) for a chemical reaction and the interaction energy barrier (E_b) for particle aggregation both serve as a barrier that prevents a reaction process from occurring, and both govern the reaction rate in an Arrhenius form. In our model development, the activation energy (E_a) is replaced by the absolute value of the difference between E_b and secondary energy minimum ($\phi_{\min 2}$) because $\phi_{\min 2}$ is widely considered as the initial driving force for particle attachment *(58)*. Thus, Eq. (4) can be rewritten as:

$$k_{11} \approx \frac{1}{2}\pi\sigma_{AB}^2\left(\frac{8\pi k_B T}{\mu\rho\frac{4}{3}\pi r^3}\right)^{1/2} N_A \exp\left(\frac{-\left|E_b-\phi_{\min 2}\right|}{k_B T}\right) \quad (7)$$

Here we treated NPs as perfect spheres with the radius of *r*. Under the Rayleigh-Gans-Debye approximation *(59, 60)*, the aggregation rate be approximated by:

$$\frac{dr_H}{dt} \approx k_{11} N_0 = \frac{1}{2}\pi\sigma_{AB}^2 \left(\frac{8\pi k_B T}{\mu\rho\frac{4}{3}\pi r^3} \right)^{1/2} N_A \exp(\frac{-\left|E_b - \phi_{\min 2}\right|}{k_B T}) N_0 \quad (8)$$

where N_0 is the initial particle concentration, which is further equal to $\left[\frac{M}{\rho\frac{4}{3}\pi r^3} \right]$. M is the initial mass concentration of NPs (mg/L), and ρ is the the density of NPs (kg/m^3). Thus, Eq. (8) can be rearranged to:

$$\frac{dr_H}{dt} = \frac{3}{8}\sqrt{6} \cdot \sigma_{AB}^2 \cdot \rho^{-1.5} \cdot \mu^{-0.5} \cdot r^{-4.5} \cdot M \cdot N_A \cdot \left(k_B T\right)^{1/2} \exp(\frac{-\left|E_b - \phi_{\min 2}\right|}{k_B T}) \quad (9)$$

Except for the term $[\,(k_B T)^{1/2} \exp(\frac{-\left|E_b - \phi_{\min 2}\right|}{k_B T})\,]$, all the other parameters are constants. $\left|E_b - \phi_{\min 2}\right|$ can be obtained from the interaction energy profile at a particular hydrodynamic radius of *r(t)* according to the classic DLVO or EDLVO theory.

3.4.8. The EDLVO theory

Under the Derjaguin integration approximation, the interparticle (*i*) interaction energy (U_{iwi}) is expressed as *(61-64)*:

$$U_{iwi}^{DLVO}(D) = U_{iwi}^{vdW}(D) + U_{iwi}^{EL}(D) \quad (10)$$

$$U_{iwi}^{EDLVO}(D) = U_{iwi}^{vdW}(D) + U_{iwi}^{EL}(D) + U_{iwi}^{AB}(D) \quad (11)$$

$$U_{iwi}^{vdW}(D) = -\frac{A_H}{6}\left[\frac{8R_R^2}{D\left(8R_R + D\right)} + \frac{8R_R^2}{\left(4R_R + D\right)^2} + \ln\frac{D\left(8R_R + D\right)}{\left(4R_R + D\right)^2} \right] \quad (11a)$$

$$U_{iwi}^{EL}(D) = \frac{128\pi k_B T n \gamma_i^2}{\kappa^2} \times \frac{4R_R^2}{8R_R + D} \exp\left(-\kappa D\right) \quad (11b)$$

$$\gamma_i = \tanh\left(\frac{z_i e \psi_{Si}}{4 k_B T}\right) \tag{11c}$$

$$\kappa^{-1} = \sqrt{\frac{\varepsilon \varepsilon_0 k_B T}{2 N_A I e^2}} \tag{11d}$$

$$U_{iwi}^{AB}(D) = \pi \cdot r_H \cdot \lambda \cdot \Delta G_{iwi,D_0}^{AB} \cdot \exp\left(\frac{D_0 - D}{\lambda}\right) \tag{11e}$$

where U_{iwi} is the total interaction energy as a function of interaction distance (D). $U_{iwi}^{vdW}(D)$ is the van der Waals interaction energy; $U_{iwi}^{EL}(D)$ is the electrostatic interaction energy; $U_{iwi}^{AB}(D)$ is the acid-base interaction energy; and A_H is the particle (i) to particle (i) Hamaker constant in water (w) and is an intrinsic property of the two interacting materials, indicating the strength of the long-range mutual attraction between them *(65)*; R_R is the reduced particle radius, $R_R = R_1 R_2/(R_1+R_2)$; For the monodisperse NPs, R_R is reduced to 1/2 of R_1, which is the measured hydrodynamic radius ($r_H(t)$). D is the separation distance between the interaction surfaces; n is the number of cations or anions per volume; z_i is the valency of the ith ion; e is unit charge, 1.602×10^{-19} C; ψ_{S1} and ψ_{S2} are the intrinsic constant surface potentials (mV) for the two interacting particle surfaces in aqueous media, which was calculated from ζ potential via the nonlinear Poisson-Boltzmann equation under the Debye-Hückel approximation *(66)*; κ^{-1} is the Debye length (nm); ε_0 is the dielectric permittivity of a vacuum, 8.854×10^{-12} C/(V m); ε is the dielectric constant of water, 78.5; N_A is the Avogadro's number, 6.02×10^{23} mol^{-1}; I is the ionic strength (M), $I = 0.5\cdot\Sigma c_i Z_i^2$, where c_i is the molar concentration of one species ions (i); λ is the correlation length, or decay length, of the molecules of the liquid medium (for pure water, this was estimated to be 0.6 nm *(34)*); and $\Delta G_{iwi,D_0}^{AB}$ is the polar or acid-base free energy of interaction between particles of the same material, i, immersed in a liquid, w, at

the distance (D_0) *(67)*, which is the minimum equilibrium distance due to Born repulsion, 0.158 nm *(61)*.

3.5. Results and discussion

3.5.1. Morphology of NPs

TEM and AFM were both employed to investigate the morphology and size distribution of the NPs used in this study. The TEM images in the left column of Figure 3.2 show that the NPs were close to spherical in shape with relatively uniform size distributions, especially for hematite NPs. The mean diameters are approximately 90 (CeO_2), 55 (hematite), and 30 (CuO) nm, which are consistent with the manufacturer-reported values. The AFM images the right column of Figure 3.2 show the NPs were highly stacked together probably because of particle agglomeration on the silicon surface during the sample preparation process. However, the individual particle sizes, approximated by the AFM images, agree well with the particle sizes determined from the TEM images.

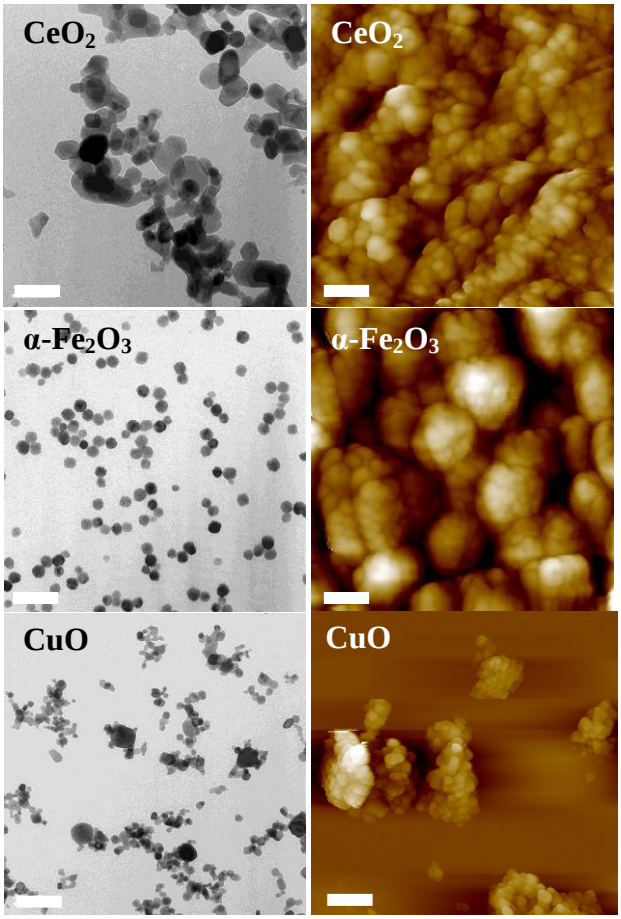

Figure 3.2. TEM images (left column) and AFM images (right column) of CeO_2, hematite, and CuO NPs. The white scale bars equal 200 nm.

3.5.2. PSD and ζ potentials of NPs

Figure 3.3a shows the particle size distribution (PSD) of CeO_2 NPs dispersed in water suspension with the mass concentration of 20 mg/L. The mean hydrodynamic diameters were approximately 120, 50, 100 nm for CeO_2, hematite, and CuO NPs, respecitvely. Except hematite, the hydrodynamic sizes of CeO_2 and CuO NPs were both greater than the vendor's reported sizes and the sizes determined from TEM images, which are consistent with previous studies *(17, 68)*. Hematite NPs possesses a hydrodynamic size that is close to the TEM measurement, which may be partially due to the excellent stability (no aggregation) of hematite NPs in aqueous media as we previously reported *(35, 41)*. In contrast, CeO_2 and CuO NPs may have a certain aggregation or surrounded by thicker water film on surfaces, which consequently led to greater hydrodynamic sizes. The extent of aggregation is also indicated by the polydispersivity indexes (PDIs), which were 0.18 (CeO_2), 0.08 (hematite), and 0.20 (CuO). According to the manufacterer's manual, the higher PDI, the greater the extent of aggregation is. The PDIs are all less than 0.25, indicating the NP suspension is still considered monodispersed and the effects of aggregation or sedimentation on the DLS measurement can be negligible.

ζ potentials play an important role in the dispersion stability of NPs in aqeuous media. The ζ potential values of the three types of NPs in their water suspensions at different pH values are presented in Figure 3.3b. ζ potentials of three particle sizes have distinct functions of pH and the isoelectric point pH_{iep} (pH of zero ζ potential) are around pH 7.1, 8.5, and 9.5 for CeO_2, hematite, and CuO NPs, respectively, which roughly agrees with previous studies on CeO_2 *(17, 69, 70)*, hematite *(14, 35, 41)*, and CuO *(68)*. Based on the ζ potentials of the three NPs, pH 5.7 was selected as an operating pH for aggregation kinetics experiments, because, at this pH, the NPs have positive surface

charge, ζ (CeO_2) $\approx$ 20 mV, ζ (hematite) $\approx$ 12 mV, and ζ (CuO) $\approx$ 35 mV, respectively and thus, the NP suspensions were initially stablized by electrostatic repulsion.

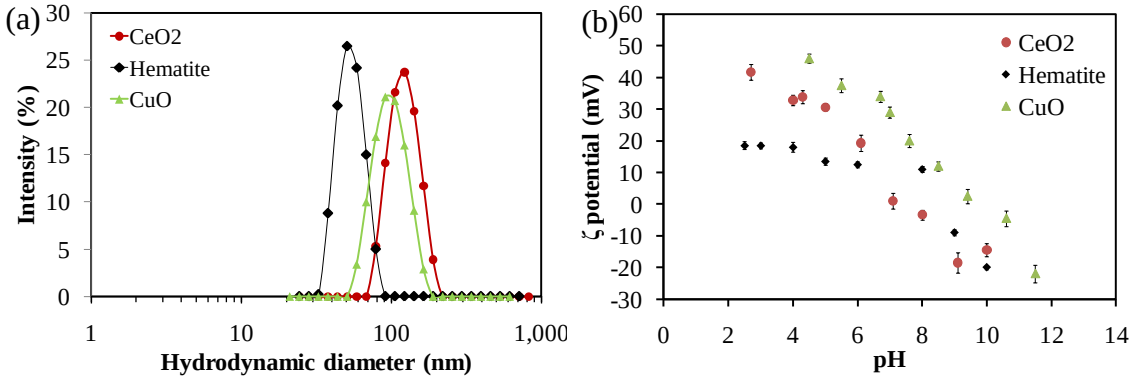

Figure 3.3. (a) PSD of CeO_2, hematite and CuO NPs in water suspensions. (b) ζ potentials of the three types of NPs at different pHs.

3.5.3. XRD analysis of NPs

Characterization of crystallinity is important because the crystallinity, structural disorder on the surface, as well as the presence of different crystallographic planes, are recently emphasized on the relevance to the surface reactivity of NPs and biological toxicity *(71, 72)*. The XRD diffractograms and the corresponding indexes for each peak for the three types of NPs are shown in Figure 3.4. CeO_2 NPs gave diffraction angles of 28.6 °, 33.1 °, 47.6 °, 56.5 °, 76.9 °, 79.2 °, and 88.3 °, all of which matched the results of previous studies *(17)*. The diffraction spectrum for CuO NPs indicates that CuO NPs is a monoclinic structure *(73, 74)*. Unfortunately, our synthesized hematite did not yield detectable signal in XRD analysis, and here I show the diffraction peaks for hematite NPs are indexed to a pure corundum structure of hematite (Space group R3c , JCPDS No. 33-0664) *(14)*.

The Scherrer equation can be used to estimate mean size of NPs based on XRD intensity:

$$d = \frac{0.9\lambda}{\beta \cos\theta} \tag{12}$$

where d corresponds to the mean diameter of the NPs, λ is the wavelength of X-ray radiation source, θ is the Bragg angle and β is the angular full width at half maximum (FWHM) of the X-ray diffraction peak at the diffraction angle (Cullity 1978). The mean sizes of CeO_2 and CuO NPs estimated based on the (220) and (111) peak were 85 and 28 nm, which compare well with the mean particle sizes measured from the TEM images.

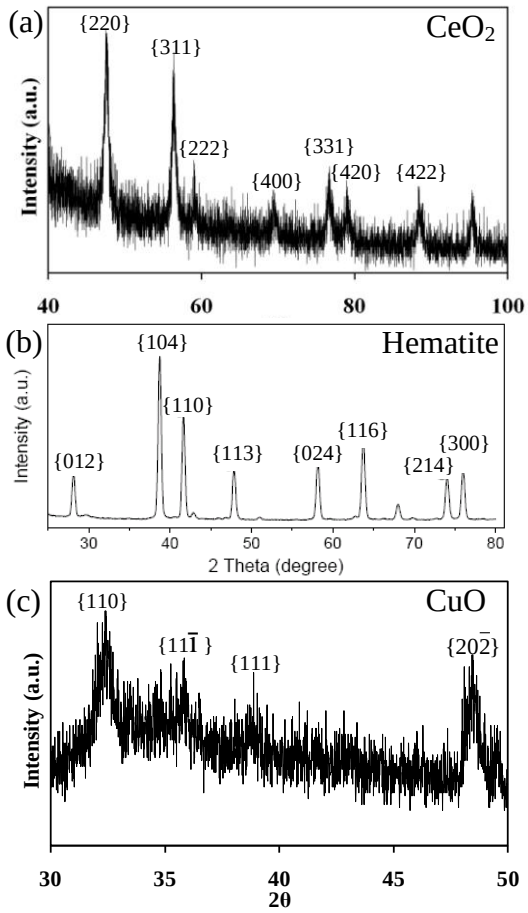

Figure 3.4. XRD spectra of CeO_2, hematite, and CuO NPs, and (b) is adapted from ref. *(14)*.

3.5.4. Surface energy analysis by contact angle measurement

The surface energy properties of NPs directly determines the interaction energy through Hamaker constant ($A_{H,iwi}$) and the standard free energy of acid-base interactions ($\Delta G^{AB}_{iwi,D_0}$). The Hamaker constant between interacting particles (*i*) in water (*w*) can be computed by the method of van Oss *(34)*:

$$A_{H,iwi} = 24\pi D_0^2 \left(\sqrt{\gamma_i^{LW}} - \sqrt{\gamma_w^{LW}} \right)^2 \tag{13}$$

where γ_i^{LW} is the Lifshitz-van der Waals apolar component of the surface energy. γ_i^{LW} can be further calculated by the Young-Dupré equation for a non-spreading liquid (*L*) on a solid surface (i) *(75, 76)*:

$$(1+\cos\theta_L)\cdot\gamma_L = 2(\sqrt{\gamma_i^{LW}\gamma_L^{LW}} + \sqrt{\gamma_i^{+}\gamma_L^{-}} + \sqrt{\gamma_i^{-}\gamma_L^{+}}) \tag{14}$$

$$\gamma_i^{AB} = 2\sqrt{\gamma_i^{+}\gamma_i^{-}} \tag{15}$$

where γ_L is the surface tension of probe liquids ($\gamma_L = \gamma_L^{LW} + \gamma_L^{AB}$). According to Eq. (14), γ_i^{LW} and the polar surface tension components: electron-acceptor (γ^+) and electron-donor (γ^-) can be solved once the surface tension properties of probe liquids (γ_L , γ_L^+ , and γ_L^-) and the contact angles (θ_L) of probe liquids on the samples surfaces are known, which are available in literature and shown in Table 3.1. The results of γ_i^{LW} , γ_i^+ and γ_i^- are summarized in Table 3.2 and the acid-base interaction surface tension (γ_i^{AB}) of NPs can be further determined by Eq. (15). Consequently, Hamaker constants ($A_{H,iwi}$) can be determined by Eq. (13), while $\Delta G^{AB}_{iwi,D_0}$ for interactions between NPs (*i*) in water (*w*) is calculated by the Dupré equation *(34)*:

$$\Delta G_{iwi,D_0}^{AB} = -4\left[\left(\sqrt{\gamma_i^+} - \sqrt{\gamma_w^+}\right)\left(\sqrt{\gamma_i^-} - \sqrt{\gamma_w^-}\right)\right] \quad (16)$$

Our results are in comparable orders of magnitude with the literature-reported values of $A_{H,iwi}$ for CeO_2 (5.57×10^{-20} J) *(69)* and hematite ($1\sim5\times10^{-20}$ J) *(14)*. For CuO, the surface tension components are different from the results from Ogwu et al. *(77)* probably because the surface hydrophobicity of our CuO NPs is quite different from that of Ogwu et al. and this is supported by the significant difference in contact angles of water. Another important indication from water contact angle (θ_L) is that when θ_L is less than 15^o, the hydration force becomes significant which may greatly stabilizes the colloidal suspension *(78)*, while the hydrophobic force becomes appreciable when θ_L >64^o which provides main driving force for particle coagulation *(79)*. Thus, based on the water contact angles, it is apparent that the suspension of CeO_2, hematite, and CuO NPs should be stabilized by hydration force or the acid-base interaction.

Table 3.1 Surface tension properties (mJ/m^2) of probe liquids at 20^{o}C *(34)* and contact angles (θ_L) on different sample surfaces.

	γ_L	γ_i^{LW}	γ_L^+	γ_L^-	γ_i^{AB}	θ_L (^{o})		
						CeO_2	hematite	CuO
DI water	72.8	21.8	25.5	25.5	51.0	49.5 ± 0.2	16.5 ± 0.6	41.0 ± 0.6
Glycerol	64.0	34.0	3.9	57.4	30.0	10.2 ± 5.5	45.9 ± 0.3	36.6 ± 5.2
Formamide	58.0	39.0	2.3	39.6	19.0	28.2 ± 4.7	10.2 ± 0.2	25.6 ± 0.9

Table 3.2 Surface energy components (mJ/m^2), the calculated Hamaker constants, and the standard acid-base interaction energy of three types of NPs.

NPs	γ_i^{LW}	Surface energy components			$A_{H,iwi}$ (J)	$\Delta G_{iwi,D_0}^{AB}$ (mJ/m^2)
		γ_i^+	γ_i^-	γ_i^{AB}		
CeO_2	1.0	0	57.7	0	5.1×10^{-20}	1.9
Hematite	45.8	0	57.0	0	8.5×10^{-20}	4.9
CuO	7.5	9.1	0	0	1.4×10^{-20}	-41

3.5.5. Particle number distribution evolution during aggregation

During the aggregation, particle size distribution (PSD) is dynamically changing over time, which has important influences on particle mobility and transport. The size distribution obtained from the DLS technique has three different definitions on basis of particle number, scattered intensity, and particle volume. In natural waters the number of particles increases with decreasing particle diameter and the frequency distribution typically follows a power law distribution of the form, $\frac{dN}{d(d_p)} = A(d_p)^{-\beta} \simeq \frac{\Delta N}{\Delta(d_p)}$, where A is power law density coefficient, d_p is particle diameter, and β is power law slope coefficient. Take the log of both sides of this equation results in the following expression, which can be plotted to determine the coefficients A and β: $\log\left[\frac{\Delta N}{\Delta(d_p)}\right] = \log A - \beta \log(d_p)$. Figure 3.5 shows a typical plot of PSD changes at different aggregation stages indicated by the Z-average. The coefficient A can be determined when d_p=1. It is observed that as particle aggregated, logA increased indicating that the total number of particles in each size range increased. The slope of β is a measure of the relative number of particles in each size range *(80)*. If β <1, the PSD is dominated by large particles, if β =1, all particles sizes are represented equally, and if >1, the PSD is dominated by small particles. Typical values of β for most natural waters varies between 2 and 5 *(81)*. Linear curving fitting for the data of the plot in Figure 3.5 could reveal that the β values for CeO_2 NPs during aggregation is within 2.2 and 2.3. Thus, aggregation may significantly change the logA while have minor effect on the value of β. Also, since β >1, the PSD is dominated by small CeO_2 NPs. Other NPs we tested (i.e., hematite and CuO) yielded similar observations in the evolution of PSDs (results are not shown here).

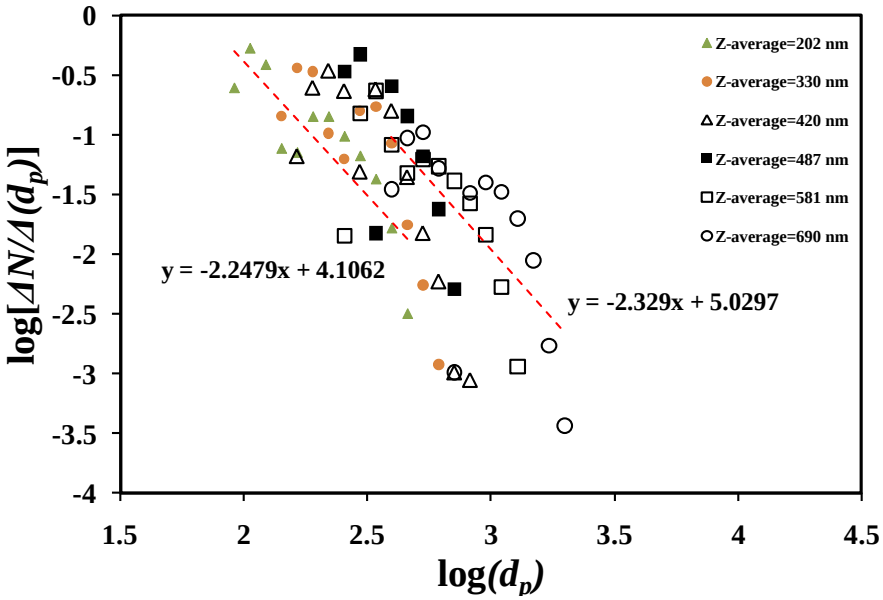

Figure 3.5. Evolution of particle size distribution on basis of particle number during aggregation of CeO_2 NPs. Two linear regression curves and the fitting equations for the date corresponding to the Z-averages of 202 and 690 nm are shown in this graph.

3.5.6. The discrepancy between the classic DLVO prediction and experimental observations of the aggregation kinetics: the case of CeO_2 NPs

As indicated above, the acid-base interaction can not be negligible in the aspect of the suspension stability of NPs. In the classic DLVO theory, this interaction is not considered, which may contribute to the prediction discrepency from the experimental observations. Figure 3.6a shows that the hydrodynamic sizes of CeO_2 NPs increased faster at the higher ionic strength (0.025 ~ 0.1 M). Clearly, at low ionic strength (0.002 ~ 0.01 M), electrostatic repulsion dominated, and thus almost no aggregation was observed during the experimental period. The increased particle aggregation rate at high ionic strength is largely ascribed to the compression of the EDL and the reduction of the electrostatic repulsion. This is easily verified by the calculation of the interaction energy profiles with the DLVO theory as shown in Figure 3.6b. For the ionic strength below 0.005 M, the interaction energy barrier is present and thus prevents aggregation and consistently the data in Figure 3.6a also shows no aggregation occurred to CeO_2 NPs. However, with an ionic strength above 0.005 M, the energy barrier diminished or became negative, but some anticipated aggregation was not observed (e.g., under the ionic strength beteween 0.005 and 0.01 M), which highlighted the discrepancy in the DLVO prediction. Similar findings on this discrepancy were found for hematite, CuO NPs (results are not shown) and other colloidal systems *(22, 23, 82, 83)*. As mentioned above, this discrepancy is probably caused by the lack of consideration of non-DLVO forces *(84-86)*. Also, the DLVO theory treats the interacting surface as an infinitely smooth surface (i.e., molecularly smooth) and in reality surface heterogeneity effects cannot be ignored *(65, 87, 88)*, which may also lead to the prediction deviations. In contrast, the EDLVO theory that considers the acid-base interaction energy predicts that the energy barrier was present under all ionic strength conditions, indicating that the repulsion from the acid-base interactions should be one of the rate-limit factors for aggregation kinetics.

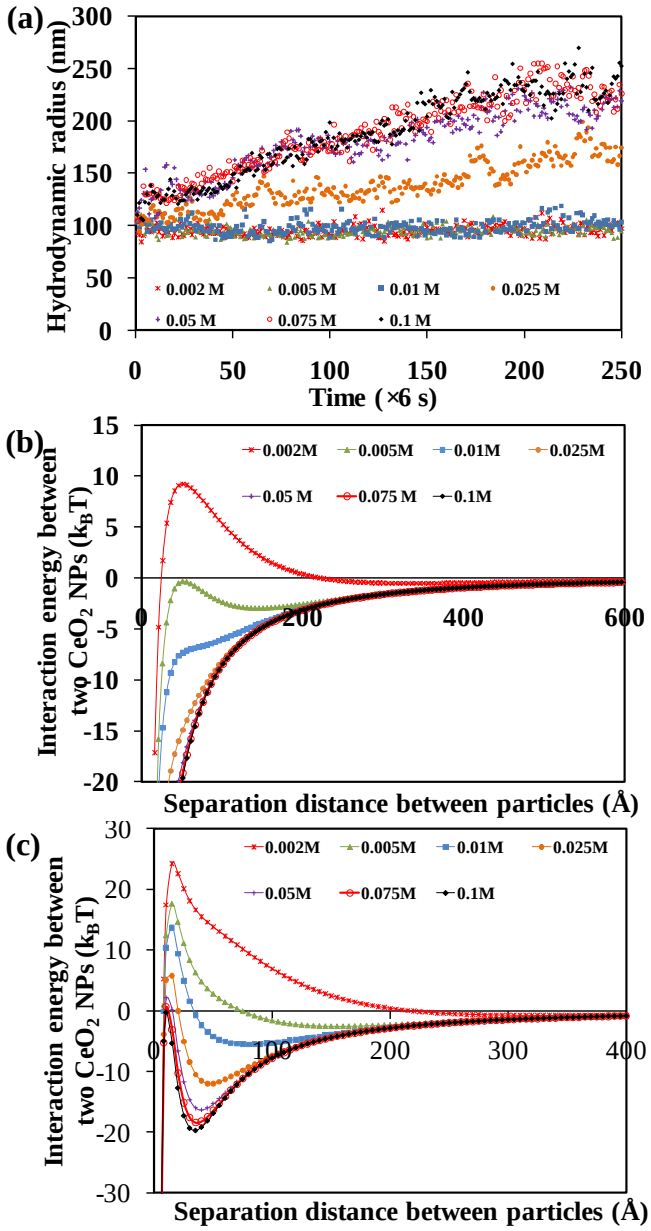

Figure 3.6. (a) Aggregation kinetics of CeO_2 NPs under different ionic strengths. (b) Interaction energy between CeO_2 NPs (120 nm in radius) under different ionic strengths calculated from the classic DLVO theory. (c) Interaction energy calculated from the EDLVO theory.

3.5.7. Modeling the size effect on the aggregation kinetics

The aggregation kinetic model or Eq. (9) is evaluated by the TR-DLS data of CeO_2 NPs under the ionic strength of 0.02 M, as shown in Figure 3.7a. The aggregation shows the common feature of hydrodynamic radius growth for NP aggregation: stage 1 (linear growth stage), stage 2 (deceleration growth stage), and stage 3 (stationary growth stage). To use the model prediction, a number of aggregated sizes (r_H) were randomly chosen from each stage to calculate the aggregation rate with Eq. (9). This calculation evloved the interaction energy calculation with Eqs. (13), from which the values of $\left|E_b - \phi_{\min 2}\right|$ for each aggregated size was determined and substituted into Eq. (9). The slopes were used to indicate the experimental results of aggregation rates at different aggregation stages and were directly measured from the aggregation kinetics curve. The model calculation of aggregation rates versus the slopes is plotted in Figure 3.7b. Higher aggregation rates corresponded to larger slopes, which indicates that our model prediction is well correlated with the experimental data. Although the model prediction should yield a linear relationship with the slopes according to Eq. (9), the curve fitting indicated that the model predicted aggregation rates best fitted the slopes ($y=10^{-9}e^{9.3862x}$) in an exponential function with the correlation coefficient (R^2) of 0.97.

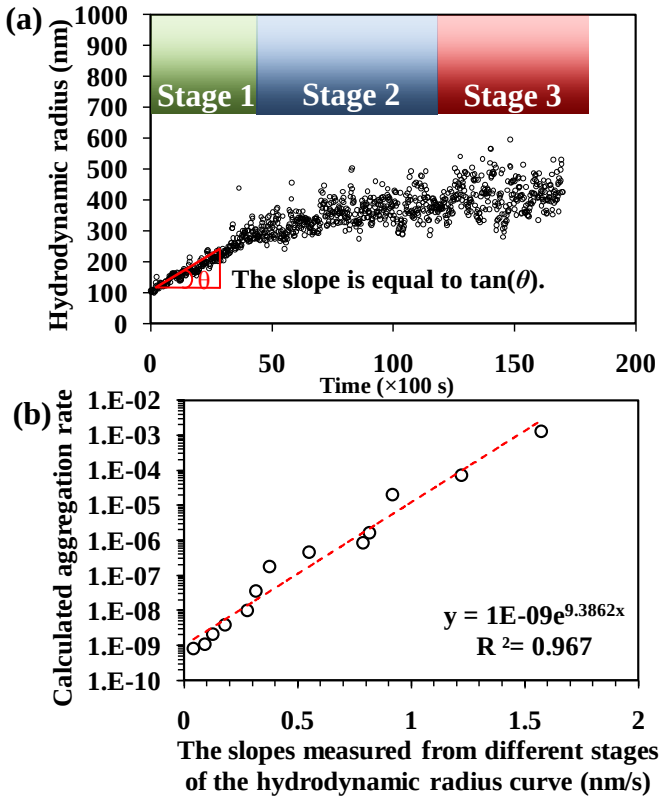

Figure 3.7. (a) Aggregation kinetics curve of CeO_2 NPs at an ionic strength of 0.02 M. (b) Aggregation rates calcuated from Eq. (9) on Y-axis versus the slopes measured from the aggregation kinetics curve on X-axis. The particle radii used in the model calculation and slope measurement include 120, 150, 200, 250, 280, 290, 300, 330, 360, and 390, 400, 410, and 420 nm. The calculated aggregation rate has a unit of $\frac{3}{8}\sqrt{6}\cdot\sigma_{AB}^{2}\cdot\mu^{-0.5}\cdot\rho^{-1.5}\cdot r^{-4.5}\cdot M\cdot N_A\cdot\left(k_BT\right)^{1/2}$, which is constant for the same experimental settings.

3.5.8. Modeling the ionic strength effect on the aggregation kinetics

To evaluated the model prediction on the ionic strength effect, the aggregation kinetics data in Figure 3.6a was used and three aggregated sizes in radius (125, 160, and 200 nm) under the ionic strengths of 0.01, 0.025, 0.05, 0.075, and 0.1 M were chosen to calculate and measure the aggregation rates. For example, the interaction energy profiles for the 160-nm aggregated size under different ionic strengths are calculated and shown in Figure 3.8a, from which the changes of the interaction energy barriers and the values of $\left|E_b - \phi_{\min 2}\right|$ are clearly visualized. Similar to section 3.5.5, the calculated aggregation rates are plotted versus the slopes as shown in Figure 3.8b. As indicated by the inset, the data points are aligned from low to high ionic strengths in the direction of the red arrow. Clearly, increasing the ionic strength led to higher aggregation rates, which is consistent with the model and expeirmental observations. Figure 3.8b also shows that small aggregated sizes (125 nm) had greater aggregation rates than large ones (200 nm), which matched the results discussed above. Finally, the curve fitting revealed again that the calculated aggregation rates best by the model has an exponential functions with the slopes with the correlation coefficients (R^2) of 0.88~0.97.

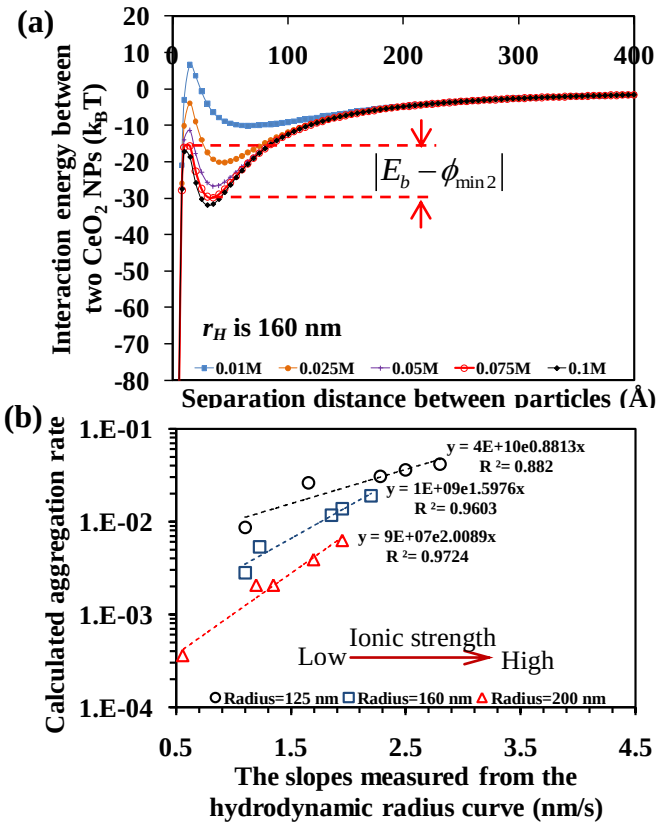

Figure 3.8. (a) The interaction energy profiles under different ionic strengths for aggregated particles of 160 nm in radius. (b) Aggregation rates calculated from Eq. (9) versus the slopes measured from the aggregation kinetics curves. The calculated aggregation rate has a unit of $\frac{3}{8}\sqrt{6}\cdot\sigma_{AB}^2\cdot\mu^{-0.5}\cdot\rho^{-1.5}\cdot r^{-4.5}\cdot M\cdot N_A\cdot(k_BT)^{1/2}$, which is constant for the same experimental settings.

3.5.9. Modeling the temperature effect on aggregation kinetics

To study the effect of temperature on the aggregation kinetics, the TR-DSL experiments were conducted at 10 ℃, 25 ℃, and 45 ℃ respectively for the suspensions of three types of NPs. Figure 3.9a~c shows the aggregation curves of three types of NPs at different temperatures. Increasing the temperature substantially increased the aggregation rates, and by means of our model, we may further explore the fundamental mechanisms of temperature effects. As shown in Figure 3.9d~f, the interaction energy profiles for the three types of NPs are also influenced by temperature variations. Increasing temperature decreased the energy barrier for each type of NPs, which would increase the aggregation rate according to Eq. (9). The model calculated aggregation rates for different NPs are again plotted versus the slopes measured from the aggregation curves, which are shown Figure 3.9g~i. Clearly, the model prediction on aggregation rates is well correlated with the experimental measurements. From these results, we can see different NPs have different responses in aggregation kinetics over the temperature variations, and the high temperature increases the collision frequency between particles by increasing random kinetic energy of NPs *(89, 90)*. Moreover, the results suggest that our model incorporate the temperature effect on aggregation kinetics and is widely applicable to multiple types of NPs.

There are certainly lots of relevant discussions on other factors on aggregation kinetics such as the particle concentration effect (M) and the particle radius (r) effect that were not included in this chapter, which are directly related to the aggregation rate acording to our model in Eq. (9). High particle concentrations increase the collision frequency and thus increase the aggregation rate, which is previously elaborated *(14, 91)*. Small particle sizes leads to higher aggregation rates largely because of their higher particle density and mobility *(4, 14, 35)*. Also, it is worth mentioning that the development and modeling discussion are primarily conducted with the results of CeO_2

NPs, whereas hematite and CuO NPs yielded similar findings in terms of size and ionic strenth effects, and thus the results were not shown here. To extend the applicability of the kinetics model, we further evaluated the model with the kinetics data of a few other NPs that were studied in other published literature as to be discussed in the next section.

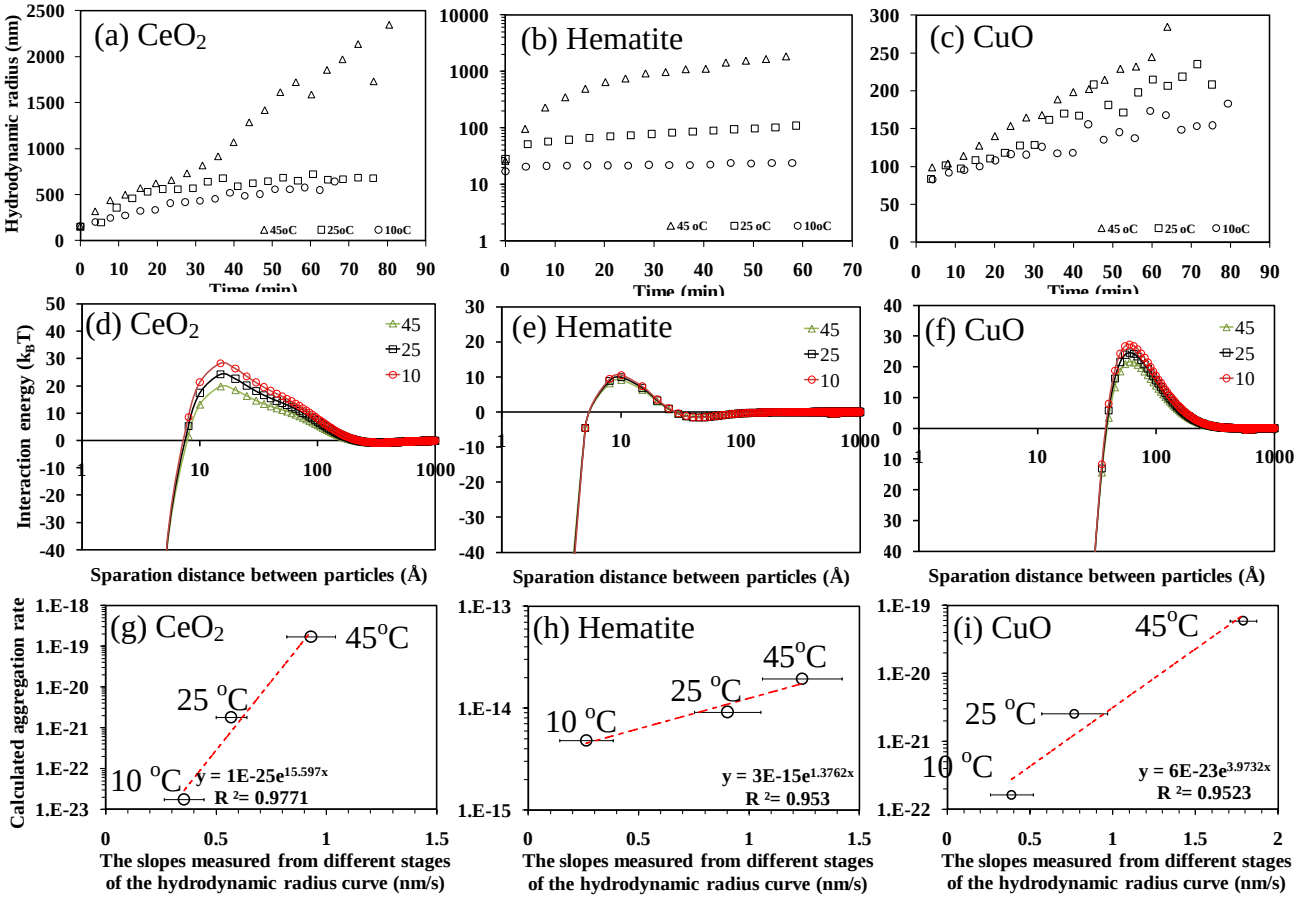

Figure 3.9. (a)~(c) Aggregation kinetics of CeO_2, hematite, and CuO NPs at different temperatures. (d)~(f) The interaction energy profiles of these NPs . Model parameters: r_H (CeO_2)=120 nm, r_H (hematite)=25 nm, and r_H (CuO)=50 nm. ζ potential (CeO_2) =21.5 mV, ζ potential (hematite)=10 mV, and ζ potential (CuO)=37 mV. Ionic strength is 0.002 M, pH=6, temperatures include 10, 25, and 45 °C. (g)~(i) Aggregation rates calculated from Eq. (9) versus the slopes (when t→0) measured from the aggregation kinetics curves. The calculated aggregation rate has a unit of $\frac{3}{8}\sqrt{6}\cdot\sigma_{AB}^2\cdot\mu^{-0.5}\cdot\rho^{-1.5}\cdot r^{-4.5}\cdot M\cdot N_A$, which is constant for the same experimental settings.

3.5.10. Comparison of the aggregation kinetics model fittings

The goal of this study is not to find the good correlation but to develop a rapid and simple tool that can be used to predict the evolution of hydrodynamic sizes of any type of NPs in the aggregation process, which is relevant and needed for assessing the environmental fate and toxicity of NPs *(6)*. Unfortunately, our kinetics model in Eq. (9) has no analytical solutions as well similar to the model in Eq. (3) proposed by Nikolakis et al. Thus, a precise solution of the aggregation rate is not easily achievable. The aggregation of NPs is obviously a complicated process, which may not be described by a simple model. Nevertheless, based on previous literature *(9, 10, 12, 14-20, 91-94)*, all aggregation curves of various types of NPs have a deceleratory shape that led to a final equilibrated hydrdynamic size at longer time. Thus, aggregation kinetics can be tentatively described by a pseudo-first-order reaction kinetic rate equation, which is mentioned in section 3.3.7:

$$r_H(t) = r_{H,final}(1-\exp(-kt)) + r_H(0) \tag{17}$$

where $r_{H,final}$ is the final value of the hydrodynamic radius when $t\rightarrow\infty$, k is the rate coefficient, and $r_H(0)$ is the initial hydrdodynamic radius. Taking the derivative of Eq. (17) yields the aggregation rate:

$$\frac{dr_H}{dt} = k \cdot r_{H,final} \cdot \exp(-kt) \tag{18}$$

Clearly, Eq. (18) has the same exponential form with our proposed kinetics model in Eq. (9), and in fact the product of the rate coefficient (k) and time (t) yields the function of $\left|E_b - \phi_{\min 2}\right|$ versus the aggregation time. Using Eq. (17), we fitted the aggregation curves of multiple types of NPs and nanomaterials from the published literature and summerized the fitting resutls in Table 3.3. Comparing the fitted values of the rate coefficients (k) for different NPs, we can see that the ionic strenght and temperature both have consistent and

strong influences on the rate coefficients. High ionic strenght and high temeperature tend to increase the rate coefficients to some extent, which are shown in the data of other literature and our study. However, the concentration effect is not obvious or not consistent. For instance, the rate coefficients of hemaite (65 nm) NPs with 44, 132, and 440 mg/L under 40 mM ionic strength did not show significant dependence on the particle concentration.

Moreover, it is clear that although the rate coeffients (k) vary with the particle type, ionic strength, and temperature based on the resutls in Table 3.3, all the values of k for different types of NPs are in comparable orders of magnitude. Thus, the model in Eq. (17) may potentially be useful for describing and predicting the evolution of hydrodynamic radius growth during aggregation, which, as mentioned above, is important for understanding the environmental fate and toxicity of NPs.

Table 3.3. Comparisons of the curve fit with Eq. (17) for other published data of aggregation kinetics.

NPs	Diameter (nm)	Concentration (mg/L)	pH	Ionic strength (mM)*	Temperature (^oC)	Rate coefficient k (s^{-1})	Reference
Hematite	65 nm	44	5.7	40	23	$(4.0\pm0.2)\times10^{-3}$	Figures 7 and 10 in *(14)*
		44	5.7	50	23	$(4.1\pm0.2)\times10^{-3}$	
		44	5.7	70	23	$(1.0\pm0.1)\times10^{-2}$	
		132	5.7	50	23	$(4.1\pm0.1)\times10^{-3}$	
		440	5.7	50	23	$(3.6\pm0.3)\times10^{-3}$	
Alginate-Coated Hematite	40	1.5×10^{8} particle/mL	12.2	15.9	23	$(1.0\pm0.2)\times10^{-4}$	Figures 7 in *(12)*
			12.2	39.2	23	$(1.7\pm0.3)\times10^{-4}$	
ZnO	20	100	8.1	10	N.A.	$(7.4\pm0.3)\times10^{-5}$	Figures 2 and 10 in *(95)*
		100	8.1	100	N.A.	$(3.9\pm0.1)\times10^{-4}$	
		10	8.1	10	N.A.	$(2.2\pm0.1)\times10^{-4}$	
Citrate-coated silver NPs	54	9.0×10^{10} particle/mL	N.A.	50	0	$(6.5\pm0.2)\times10^{-5}$	Figure 3 in *(94)*
			N.A.	200	0	$(1.1\pm0.2)\times10^{-4}$	
			N.A.	500	0	$(1.2\pm0.1)\times10^{-4}$	
SWCNT	78.1	N.A.	6.0	2 $CaCl_2$	23	$(1.4\pm0.2)\times10^{-4}$	Figure 5 in *(20)*
		N.A.	6.0	20 $CaCl_2$	23	$(1.4\pm0.3)\times10^{-4}$	
MWCNT	135	N.A.	6.0	10	23	$(6.1\pm0.3)\times10^{-4}$	Figure S6 in *(15)*
		N.A.	6.0	2 $CaCl_2$	23	$(5.5\pm0.3)\times10^{-4}$	
CeO_2	70~100	20	5.7	25	25	$(1.2\pm0.3)\times10^{-3}$	Figure 3.6 and Figure 3.9 of this study
		20	5.7	100	25	$(2.6\pm0.2)\times10^{-3}$	
		20	5.7	2	10	$(7.1\pm0.2)\times10^{-4}$	
		20	5.7	2	25	$(9.5\pm0.2)\times10^{-4}$	
		20	5.7	2	45	$(9.3\pm0.3)\times10^{-4}$	
Hematite	55	20	5.7	2	10	$(6.7\pm0.3)\times10^{-4}$	
		20	5.7	2	25	$(7.5\pm0.1)\times10^{-3}$	
		20	5.7	2	45	$(1.0\pm0.1)\times10^{-2}$	
CuO	30	20	5.7	2	10	$(1.9\pm0.3)\times10^{-3}$	
		20	5.7	2	25	$(3.1\pm0.2)\times10^{-3}$	
		20	5.7	2	45	$(5.1\pm0.1)\times10^{-3}$	

*Unless specified, monovelant electrolytes (e.g., NaCl) were used to produce the ionic strength.

3.5.12. Deviation of aggregation kinetics based on "first-principle" theories

In contrast to the empirical modeling that has been discussed above, aggregation kinetic model may be derived from the "first-principles" from the well-established flocculation and collision theories in colloidal science. This section introduces a derivation based on the microscale flocculation of monodisperse particles, and the flocculation rate can be represented by the loss rate of singlets *(81)*:

$$r_i = \frac{dn_i}{dt} = -\frac{4}{3}\alpha\beta n_i^2 \tag{19}$$

where n_i is the number concentration of aggregates which are comprised of i primary particles (also called i-class or i-fold particles or aggregates), α is the collision efficiency, β is collision frequency function, μ is the dynamic viscosity of the, T is absolute temperature (K), and k_B is Boltzmann constant (1.38×10^{-23} J/K). The collision efficiency α is defined as *(19, 96)*:

$$\alpha = \frac{\left[\int_0^\infty \lambda(u)\frac{\exp\left(U_{iwi}^{vdw}(h)/k_BT\right)}{(2+u)^2}du\right]}{\left[\int_0^\infty \lambda(u)\frac{\exp\left(U_{iwi}^{DLVO}(h)/k_BT\right)}{(2+u)^2}du\right]} \tag{20}$$

Taking into account the van der Waals forces and hydrodynamic interactions, the collision frequency rate is expressed as *(97)*:

$$\beta(i,i) = \frac{8kT}{3\mu}\left[2\int_0^\infty \lambda(u)\frac{\exp\left(U_{iwi}^{vdw}(h)/k_BT\right)}{(2+u)^2}du\right]^{-1} \tag{21}$$

where h is the surface to surface separation distance between two particles (nm); r is the particle radius (nm); $u=h/r$; U_{iwi}^{DLVO} is the total interaction energy between particles separated with a distance h. In classical DLVO theory, U_{iwi}^{DLVO} is the sum of the van der

Waals attraction energy U_{iwi}^{vdw} and the electrical repulsion energy U_{iwi}^{EL}. $\lambda(h)$ is the correcting factor for the diffusion coefficient, which is related to the separation distance by this equation *(98)*:

$$\lambda(u)=\frac{6(u)^2+13(u)+2}{6(u)^2+4(u)} \tag{22}$$

Now Eq. (1) can be transformed to:

$$n_i=\frac{n_0}{1+\frac{4kT}{3\mu}\left[2\int_0^{\infty}\lambda(u)\frac{\exp\left(U_{iwi}^{DLVO}(h)/k_BT\right)}{(2+u)^2}du\right]n_0t} \tag{23}$$

where n_0 is the initial particle number concentration. Many aggregation processes are fractal in nature *(51, 99)*, i.e., the length of a fractal aggregate is related to the hydrodynamic radius (r) to a power of the fractal dimension (d_F): $n_i=r_i^{-d_F}$. Thus, Eq. (23) can be rewritten as:

$$\begin{aligned} r(t)&=\left\{\frac{n_0}{1+\frac{4kT}{3\mu}\left[2\int_0^{\infty}\lambda(u)\frac{\exp\left(U_{iwi}^{DLVO}(h)/kT\right)}{(2+u)^2}du\right]n_0t}\right\}^{-\frac{1}{d_F}} \\ &=r_0\left\{1+\frac{4kT}{3\mu}\left[2\int_0^{\infty}\lambda(u)\frac{\exp\left(U_{iwi}^{DLVO}(h)/kT\right)}{(2+u)^2}du\right]n_0t\right\}^{\frac{1}{d_F}} \end{aligned} \tag{24}$$

The equation (24) gives a theoretical derivation for aggregated particle's size *r(t)* as function of time, interaction energy, temperature, and initial particle concentration. Visual inspection on the boundary conditions such as time t=0 or t→∞, the results of *r(t)* seems to be reasonable. Particularly, the previously studies indicated that the DLCA kinetics are power-law, $r \propto t^{1/dF}$, which supports the form of Eq. (24).

The key to derive Eq. (24) is to relate the particle number rate of aggregation to the aggregation rate of particle size changes via the fractal relationship, which is a major leap and assumption. Other than that, there seem no inherent limitations in this kinetics model. This equation clearly allows us to conduct future work in describing various aggregation kinetics of NPs, and we may vary the "adjustable parameters" such as d_F, because it is clear that DLCA and RLCA aggregation kinetics possess a d_F of 1.7~1.8 and approximately 2.1, respectively *(52)*. Moreover, the interaction energy term in Eq. (24) may potentially interpret the effects of particle size, temperature, and ionic strength on aggregation kinetics.

3.6. Research significance

In summary, the rapid and simple prediction tools for aggregation kinetics are needed to assess the environmental and biological impacts of engineered NPs and are also beneficial for better understanding the relationship between the aggregation kinetics and toxicokinetics of NPs. The empirical kinetic model we proposed in Eq. (9) or Eq. (17) and theoretical model in Eq. (24) can potentially be used to predict and analyze the aggregation kinetics of all types of engineered NPs in aqueous media. The kinetics modeling provides insight into the nanoscale processes of aggregation that allow us to better understand the fundamental mechanisms of environmental fate and transformations of NPs.

3.7. Reference

(1) Zhu, X.; Wang, J.; Zhang, X.; Chang, Y.; Chen, Y. The impact of ZnO nanoparticle aggregates on the embryonic development of zebrafish (Danio rerio). *Nanotechnology* **2009,** *20*, 9.

(2) Baun, A.; Hartmann, N. B.; Grieger, K.; Kusk, K. O. Ecotoxicity of engineered nanoparticles to aquatic invertebrates: a brief review and recommendations for future toxicity testing. *Ecotoxicology* **2008,** *17* (5), 387-395.

(3) Persson, B. N. J. On the mechanism of adhesion in biological systems. *J. Chem. Phys.* **2003,** *118* (16), 7614-7621.

(4) Limbach, L. K.; Li, Y.; Grass, R. N.; Brunner, T. J.; Hintermann, M. A.; Muller, M.; Gunther, D.; Stark, W. J. Oxide Nanoparticle Uptake in Human Lung Fibroblasts: Effects of Particle Size, Agglomeration, and Diffusion at Low Concentrations. *Environ. Sci. Technol.* **2005,** *39* (23), 9370-9376.

(5) Mutlu, G. M.; Budinger, G. R. S.; Green, A. A.; Urich, D.; Soberanes, S.; Chiarella, S. E.; Alheid, G. F.; McCrimmon, D. R.; Szleifer, I.; Hersam, M. C. Biocompatible Nanoscale Dispersion of Single-Walled Carbon Nanotubes Minimizes in vivo Pulmonary Toxicity. *Nano Letters* **2010,** *10* (5), 1664-1670.

(6) Auffan, M.; Rose, J.; Wiesner, M. R.; Bottero, J.-Y. Chemical stability of metallic nanoparticles: A parameter controlling their potential cellular toxicity in vitro. *Environ. Pollut.* **2009,** *157* (4), 1127-1133.

(7) Darlington, T. K.; Neigh, A. M.; Spencer, M. T.; Nguyen, O. T.; Oldenburg, S. J. Nanoparticle characteristics affecting environmental fate and transport through soil. *Environ Toxicol Chem* **2009,** *28* (6), 1191-1199.

(8) Klaine, S. J.; Alvarez, P. J. J.; Batley, G. E.; Fernandes, T. F.; Handy, R. D.; Lyon, D. Y.; Mahendra, S.; McLaughlin, M. J.; Lead, J. R. Nanomaterials in the environment: behavior, fate, bioavailability, and effects. *Environ. Toxicol. Chem.* **2008,** *27* (9), 1825–1851

(9) Sharma, V. K. Aggregation and toxicity of titanium dioxide nanoparticles in aquatic environment-A Review. *J. Environ. Sci. Health, Part A: Environ. Sci. Eng.* **2009,** *44* (14), 1485-1495.
(10) Keller, A. A.; Wang, H.; Zhou, D.; Lenihan, H. S.; Cherr, G.; Cardinale, B. J.; Miller, R.; Ji, Z. Stability and Aggregation of Metal Oxide Nanoparticles in Natural Aqueous Matrices. *Environ. Sci. Technol.* **2010,** *44* (6), 1962-1967.
(11) Petosa, A. R.; Jaisi, D. P.; Quevedo, I. R.; Elimelech, M.; Tufenkji, N. Aggregation and Deposition of Engineered Nanomaterials in Aquatic Environments: Role of Physicochemical Interactions. *Environ. Sci. Technol.* **2010,** *44* (17), 6532-6549.
(12) Chen, K. L.; Mylon, S. E.; Elimelech, M. Aggregation kinetics of alginate-coated hematite nanoparticles in monovalent and divalent electrolytes. *Environ. Sci. Tech.* **2006,** *40* (5), 1516-1523.
(13) Chen, K. L.; Elimelech, M. Influence of humic acid on the aggregation kinetics of fullerene (C-60) nanoparticles in monovalent and divalent electrolyte solutions. *J. Colloid Interface Sci.* **2007,** *309* (1), 126-134.
(14) He, Y. T.; Wan, J. M.; Tokunaga, T. Kinetic stability of hematite nanoparticles: the effect of particle sizes. *J. Nanopart. Res.* **2008,** *10* (2), 321-332.
(15) Saleh, N. B.; Pfefferle, L. D.; Elimelech, M. Aggregation Kinetics of Multiwalled Carbon Nanotubes in Aquatic Systems: Measurements and Environmental Implications. *Environ. Sci. Technol.* **2008,** *42* (21), 7963-7969.
(16) French, R. A.; Jacobson, A. R.; Kim, B.; Isley, S. L.; Penn, R. L.; Baveye, P. C. Influence of Ionic Strength, pH, and Cation Valence on Aggregation Kinetics of Titanium Dioxide Nanoparticles. *Environ. Sci. Technol.* **2009,** *43* (5), 1354-1359.
(17) Buettner, K. M.; Rinciog, C. I.; E.Mylon, S. Aggregation Kinetics of Cerium Oxide Nanoparticles in Monovalent and Divalent Electrolytes. *Colloids Surf., A* **2010,** *366* (1-3), 74-79.
(18) Kallay, N.; Zalac, S. Stability of nanodispersions: a model for kinetics of aggregation of nanoparticles. *J. Colloid Interface Sci.* **2002,** *253* (1), 70-76.
(19) Chen, K. L.; Elimelech, M. Aggregation and deposition kinetics of fullerene (C-60) nanoparticles. *Langmuir* **2006,** *22* (26), 10994-11001.
(20) Saleh, N. B.; Pfefferle, L. D.; Elimelech, M. Influence of Biomacromolecules and Humic Acid on the Aggregation Kinetics of Single-Walled Carbon Nanotubes. *Environ. Sci. Tech.* **2010,** *44* (7), 2412-2418.
(21) Behrens, S. H.; Christl, D. I.; Emmerzael, R.; Schurtenberger, P.; Borkovec, M. Charging and Aggregation Properties of Carboxyl Latex Particles:Experiments versus DLVO Theory. *langmuir* **2000,** *16* (6), 2566-2575.
(22) Hoek, E. M. V.; Bhattacharjee, S.; Elimelech, M. Effect of Membrane Surface Roughness on Colloid membrane DLVO Interactions. *langmuir* **2003,** *19* (11), 4836-4847.
(23) Richard Bowen, W.; Doneva, T. A. Atomic force microscopy studies of nanofiltration membranes: surface morphology, pore size distribution and adhesion. *Desalination* **2000,** *129* (2), 163-172.
(24) Elimelech, M.; O'Melia, C. R. Effect of particle size on collision efficiency in the deposition of Brownian particles with electrostatic energy barriers. *Langmuir* **1990,** *6* (6), 1153-1163.

(25) Bhattacharjee, S.; Ko, C.-H.; Elimelech, M. DLVO Interaction between Rough Surfaces. *langmuir* **1998,** *14* (12), 3365-3375.
(26) Walz, J. Y. The effect of surface heterogeneities on colloidal forces. *Adv. Colloid Interface Sci.* **1998,** *74*, 119-168.
(27) Butt, H.-J. Measuring electrostatic, van der Waals, and hydration forces in electrolyte solutions with an atomic force microscope. *Biophys. J.* **1991,** *60* (6), 1438-1444.
(28) Chang, Y.-I.; Chang, P.-K. The role of hydration force on the stability of the suspension of Saccharomyces cerevisiae-application of the extended DLVO theory. *Colloids Surf., A* **2002,** *211* (1), 67-77.
(29) Ong, Y. L.; Razatos, A.; Georgiou, G.; Sharma, M. M. Adhesion Forces between E. coli Bacteria and Biomaterial Surfaces. *langmuir* **1999,** *15* (8), 2719-2725.
(30) Marenduzzo, D.; Finan, K.; Cook, P. R. The depletion attraction: an underappreciated force driving cellular organization. *J. Cell Biol.* **2006,** *175* (5), 681-686.
(31) YODH, A. G.; LIN, K.; CROCKER, J. C.; DINSMORE, A. D.; VERMA, R.; KAPLAN, P. D. Entropically driven self-assembly and interaction in suspension. *Philos. Trans. R. Soc. London, Ser. A* **2001,** *359* (1782), 921-937.
(32) Rijnaarts, H. H. M.; Norde, W.; Lyklema, J.; Zehnder, A. J. B. DLVO and steric contributions to bacterial deposition in media of different ionic strengths. *Colloids Surf., B* **1999,** *14* (1-4), 179-195.
(33) Sposito, G.; Grasso, D. *Electrical double layer structure, forces, and fields at the clay-water interface*. Hsu JP ed.; Marcel Dekker: New York, 1998.
(34) Oss, C. J. v. *Interfacial Forces in Aquaeous Media*. Second Edition ed.; Taylor & Francis Group: Boca Raton, Florida, 2006; p 81-83.
(35) Zhang, W.; Rittmann, B.; Chen, Y. Size Effects on Adsorption of Hematite Nanoparticles on *E. coli* cells. *Environ. Sci. Technol.* **2011,** *45* (6), 2172-2178.
(36) Ryan, J. N.; Elimelech, M. Colloid mobilization and transport in groundwater. *Colloids Surf., A* **1996,** *107*, 1-56.
(37) Flynn, J. H. Temperature-Dependence of the Rate of Reaction in Thermal-Analysis - the Arrhenius Equation in Condensed Phase Kinetics. *J. Therm. Anal.* **1990,** *36* (4), 1579-1593.
(38) Yang, J.; Hand, D. W.; Hokanson, D. R.; Crittenden, J. C. Application of an isothermal, three-phase catalytic reactor model to predict unsteady-state fixed-bed performance. *Environ. Sci. Tech.* **2003,** *37* (2), 428-436.
(39) Kim, I. S.; Baek, M.; Choi, S. J. Comparative Cytotoxicity of Al_2O_3, CeO_2, TiO_2 and ZnO Nanoparticles to Human Lung Cells. *J. Nanosci.Nanotech.* **2010,** *10* (5), 3453-3458.
(40) Van Hoecke, K.; Quik, J. T. K.; Mankiewicz-Boczek, J.; De Schamphelaere, K. A. C.; Elsaesser, A.; Van der Meeren, P.; Barnes, C.; McKerr, G.; Howard, C. V.; Van De Meent, D.; Rydzynski, K.; Dawson, K. A.; Salvati, A.; Lesniak, A.; Lynch, I.; Silversmit, G.; De Samber, B.; Vincze, L.; Janssen, C. R. Fate and Effects of CeO_2 Nanoparticles in Aquatic Ecotoxicity Tests. *Environ. Sci. Tech.* **2009,** *43* (12), 4537-4546.
(41) Zhang, W.; Kalive, M.; Capco, D. G.; Chen, Y. Adsorption of hematite nanoparticles onto Caco-2 cells and the cellular impairments: effect of particle size *Nanotechnology* **2010,** *21* (35), 355103.

(42) Development, O. f. E. C. a. List of Manufactured Nanomaterials and List of Endpoints for Phase One of the OECD Testing Programme. Series on the Safety of Manufactured Nanomaterials No. 6. http://www.olis.oecd.org/olis/2008doc.nsf/LinkTo/NT000034C6/$FILE/JT03248749.PDF.
(43) Verwey, E. J. W. Theory of the Stability of Lyophobic Colloids. *Journal of Physical and Colloid Chemistry* **1947,** *51* (3), 631-636.
(44) von Smoluchowski, M. Three lectures on diffusion, Brown's molecular movements and the coagulation of colloid parts. *Physikalische Zeitschrift* **1916,** *17*, 585-599.
(45) von Smoluchowski, M. Three presentations on diffusion, molecular movement according to Brown and coagulation of colloid particles. *Physikalische Zeitschrift* **1916,** *17*, 557-571.
(46) Fuchs, N. Theory of coagulation. *Zeitschrift Fur Physikalische Chemie-Abteilung a-Chemische Thermodynamik Kinetik Elektrochemie Eigenschaftslehre* **1934,** *171* (3/4), 199-208.
(47) Ribeiro, C.; Lee, E. J. H.; Longo, E.; Leite, E. R. A Kinetic Model to Describe Nanocrystal Growth by the Oriented Attachment Mechanism. *Chemphyschem* **2005,** *6* (4), 690-696.
(48) Penn, R. L. Kinetics of oriented aggregation. *J. Phys. Chem. B* **2004,** *108* (34), 12707-12712.
(49) Ribeiro, C.; Lee, E. J. H.; Longo, E.; Leite, E. R. Oriented Attachment Mechanism in Anisotropic Nanocrystals: A "Polymerization" Approach. *Chemphyschem* **2006,** *7* (3), 664-670.
(50) Nikolakis, V.; Kokkoli, E.; Tirrell, M.; Tsapatsis, M.; Vlachos, D. G. Zeolite growth by addition of subcolloidal particles: Modeling and experimental validation. *Chem. Mater.* **2000,** *12* (3), 845-853.
(51) Lin, M. Y.; Lindsay, H. M.; Weitz, D. A.; Ball, R. C.; Klein, R.; Meakin, P. Universality in Colloid Aggregation. *Nature* **1989,** *339* (6223), 360-362.
(52) Burns, J. L.; Yan, Y. D.; Jameson, G. J.; Biggs, S. A light scattering study of the fractal aggregation behavior of a model colloidal system. *langmuir* **1997,** *13* (24), 6413-6420.
(53) Penners, N. H. G.; Koopal, L. K. Preparation and optical properties of homodisperse hematite hydrosols. *Colloids Surf.* **1986,** *19* (2-3), 337-349.
(54) Zhang, W.; Stack, A. G.; Chen, Y. Interaction Force Measurement between *E. coli* Cells and Nanoparticles Immobilized Surfaces by Using AFM. *Colloids Surf., B* **2010,** *82* (2), 316-324
(55) Balnois, E.; Wilkinson, K. J.; Lead, J. R.; Buffle, J. Atomic force microscopy of humic substances: effects of pH and ionic strength. *Environ. Sci. Technol.* **1999,** *33* (21), 3911-3917.
(56) Fauchadour, D.; Jeanson, T.; Bousseau, J.-N.; Echalier/, B., Nanoparticles of Cerium Oxide - Application to Coatings Technologies In *Nano and Hybrid Coatings conference*, The Paint Research Association: Manchester, UK., 2005.
(57) Law and Stoichiometry. http://www.engin.umich.edu/~cre/03chap/html/collision/

(58) Franchi, A.; O'Melia, C. R. Effects of Natural Organic Matter and Solution Chemistry on the Deposition and Reentrainment of Colloids in Porous Media. *Environ. Sci. Tech.* **2003,** *37* (6), 1122-1129.
(59) Holthoff, H.; Borkovec, M.; Schurtenberger, P. Determination of light-scattering form factors of latex particle dimers with simultaneous static and dynamic light scattering in an aggregating suspension. *Phys. Rev. E: Stat. Phys., Plasmas, Fluids,* **1997,** *56* (6), 6945-6953.
(60) Holthoff, H.; Schmitt, A.; FernandezBarbero, A.; Borkovec, M.; CabrerizoVilchez, M. A.; Schurtenberger, P.; HidalgoAlvarez, R. Measurement of absolute coagulation rate constants for colloidal particles: Comparison of single and multiparticle light scattering techniques. *J. Colloid Interface Sci.* **1997,** *192* (2), 463-470.
(61) Hoek, E. M. V.; Agarwal, G. K. Extended DLVO interactions between spherical particles and rough surfaces. *J. Colloid Interface Sci.* **2006,** *298* (1), 50-58.
(62) Garc á-Garc á, S.; Wold, S.; Jonsson, M. Effects of temperature on the stability of colloidal montmorillonite particles at different pH and ionic strength. *Applied Clay Science* **2009,** *43* (1), 21-26.
(63) Garcia-Garcia, S.; Jonsson, M.; Wold, S. Temperature effect on the stability of bentonite colloids in water. *J. Colloid Interface Sci.* **2006,** *298* (2), 694-705.
(64) Gregory, J. Interaction of Unequal Double-Layers at Constant Charge. *J. Colloid Interface Sci.* **1975,** *51* (1), 44-51.
(65) Hermansson, M. The DLVO theory in microbial adhesion. *Colloids Surf., B* **1999,** *14* (1-4), 105-119.
(66) Stumm, W.; Morgan, J. J. *Aquatic chemistry*. 3rd ed.; John Wiley & Sons, Inc.: New York, 1996.
(67) Grasso, D.; Subramaniam, K.; Butkus, M.; Strevett, K.; Bergendahl, J. A review of non-DLVO interactions in environmental colloidal systems. *Rev. Environ. Sci. Biotechnol.* **2002,** *1*, 17-38.
(68) Karlsson, H. L.; Cronholm, P.; Gustafsson, J.; Moller, L. Copper oxide nanoparticles are highly toxic: A comparison between metal oxide nanoparticles and carbon nanotubes. *Chem. Res. Toxicol.* **2008,** *21* (9), 1726-1732.
(69) Karimian, H.; Babaluo, A. A. Halos mechanism in stabilizing of colloidal suspensions: Nanoparticle weight fraction and pH effects. *J. Eur. Ceram. Soc.* **2007,** *27* (1), 19-25.
(70) Pelletier, D. A.; Suresh, A. K.; Holton, G. A.; McKeown, C. K.; Wang, W.; Gu, B. H.; Mortensen, N. P.; Allison, D. P.; Joy, D. C.; Allison, M. R.; Brown, S. D.; Phelps, T. J.; Doktycz, M. J. Effects of Engineered Cerium Oxide Nanoparticles on Bacterial Growth and Viability. *Appl. Environ. Microbiol.* **2010,** *76* (24), 7981-7989.
(71) Gilbert, B.; Huang, F.; Zhang, H.; Waychunas, G. A.; Banfield, J. F. Nanoparticles: Strained and Stiff. *Science* **2004,** *305* (5684), 651-654.
(72) Kittler, S.; Greulich, C.; Koller, M.; Epple, M. Synthesis of PVP-coated silver nanoparticles and their biological activity towards human mesenchymal stem cells. *Materialwiss. Werkst.* **2009,** *40* (4), 258-264.
(73) Shrestha, K. M.; Sorensen, C. M.; Klabunde, K. J. Synthesis of CuO Nanorods, Reduction of CuO into Cu Nanorods, and Diffuse Reflectance Measurements of CuO and Cu Nanomaterials in the Near Infrared Region. *J. Phys. Chem. C* **2010,** *114* (34), 14368-14376.

(74) Zhou, K. B.; Wang, R. P.; Xu, B. Q.; Li, Y. D. Synthesis, characterization and catalytic properties of CuO nanocrystals with various shapes. *Nanotechnology* **2006,** *17* (15), 3939-3943.
(75) Wang, J. L.; Yoon, R. H. AFM forces measured between gold surfaces coated with self-assembled monolayers of 1-hexadecanethiol. *langmuir* **2008,** *24* (15), 7889-7896.
(76) Yoon, R.; Pazhianur, R. Direct force measurement between hydrophobic glass sphere and covellite electrode in potassium ethyl xanthate solutions at pH 9.2. *Colloids Surf., A* **1998,** *144* (1-3), 59-69.
(77) Ogwu, A.; Placido, F.; Ademosu, O.; Moh, S.; Crossan, E.; Bouquerel, E. An extended Derjaguin-Landau-Verwey-Overbeek theory approach to determining the surface energy of copper oxide thin films prepared by reactive magnetron sputtering. *Metall. Mater. Trans. A* **2005,** *36* (9), 2435-2439.
(78) Derjaguin, B. V.; Churaev, N. V. Structural component of disjoining pressure. *J. Colloid Interface Sci.* **1974,** *49* (2), 249-255.
(79) Ducker, W. A.; Grant, L. M. Effect of Substrate Hydrophobicity on Surfactant Surface aggregate Geometry. *J. Phys. Chem.* **1996,** *100* (28), 11507-11511.
(80) Trussell, R. R.; Tate, C. H. In *Measurement of particle size distribution in water treatment, Advances in laboratory techniques for water quality control,* Philadelphia, PA, 1979; American water works association.
(81) Crittenden, J. *Water Treatment: Principles and Design* Wiley; 2 edition: 2005.
(82) Elimelech, M.; O'Melia, C. R. Kinetics of deposition of colloidal particles in porous media. *Environ. Sci. Tech.* **2002,** *24* (10), 1528-1536.
(83) Elimelech, M.; Xiaohua, Z.; Childress, A. E.; Seungkwan, H. Role of membrane surface morphology in colloidal fouling of cellulose acetate and composite aromatic polyamide reverse osmosis membranes. *J. Membr. Sci.* **1997,** *127* (1), 101-109.
(84) Sun, N.; Walz, J. Y. A model for calculating electrostatic interactions between colloidal particles of arbitrary surface topology. *J. Colloid Interface Sci.* **2001,** *234* (1), 90-105.
(85) Hirose, M.; Ito, H.; Kamiyama, Y. Effect of skin layer surface structures on the flux behaviour of RO membranes. *J. Membr. Sci.* **1996,** *121* (2), 209-215.
(86) Bhattacharjee, S.; Kim, A. S.; Elimelech, M. Concentration Polarization of Interacting Solute Particles in Cross-Flow Membrane Filtration. *J. Colloid Interface Sci.* **1999,** *212* (1), 81-99.
(87) Bacchin, P.; Aimar, P.; Sanchez, V. Influence of surface interaction on transfer during colloid ultrafiltration. *J. Membr. Sci.* **1996,** *115* (1), 49-63.
(88) Pujar, N. S.; Zydney, A. L. Electrostatic effects on protein partitioning in size-exclusion chromatography and membrane ultrafiltration. *J. Chromatogr. A* **1998,** *796* (2), 229-238.
(89) Prasher, R.; Bhattacharya, P.; Phelan, P. E. Brownian-motion-based convective-conductive model for the effective thermal conductivity of nanofluids. *J. Heat Transf.* **2006,** *128* (6), 588-595.
(90) Ding, G.; Peng, H.; Jiang, W.; Gao, Y. The migration characteristics of nanoparticles in the pool boiling process of nanorefrigerant and nanorefrigerant-oil mixture. *Int. J. Refrig* **2009,** *32* (1), 114-123.

(91) Baalousha, M. Aggregation and disaggregation of iron oxide nanoparticles: Influence of particle concentration, pH and natural organic matter. *Sci. Total Environ.* **2009,** *407* (6), 2093-2101.
(92) Heidmann, I.; Christl, I.; Kretzschmar, R. Aggregation kinetics of kaolinite-fulvic acid colloids as affected by the sorption of Cu and Pb. *Environ. Sci. Tech.* **2005,** *39* (3), 807-813.
(93) Phenrat, T.; Saleh, N.; Sirk, K.; Tilton, R. D.; Lowry, G. V. Aggregation and sedimentation of aqueous nanoscale zerovalent iron dispersions. *Environ. Sci. Technol.* **2007,** *41* (1), 284-290.
(94) Trinh, L. T. T.; Kjoniksen, A. L.; Zhu, K. Z.; Knudsen, K. D.; Volden, S.; Glomm, W. R.; Nystrom, B. Slow salt-induced aggregation of citrate-covered silver particles in aqueous solutions of cellulose derivatives. *Colloid. Polym. Sci.* **2009,** *287* (12), 1391-1404.
(95) Zhou, D. X.; Keller, A. A. Role of morphology in the aggregation kinetics of ZnO nanoparticles. *Water Res.* **2010,** *44* (9), 2948-2956.
(96) Mcgown, D. N. L.; Parfitt, G. D. Improved Theoretical Calculation of Stability Ratio for Colloidal Systems. *Journal of Physical Chemistry* **1967,** *71* (2), 449-&.
(97) Elimelech, M. *Particle deposition and aggregation: measurement, modelling, and simulation*. Butterworth-Heinemann;: Oxford, England; Boston, 1995; p xv., 441 p.
(98) Honig, E. P.; Roeberse.Gj; Wiersema, P. H. Effect of Hydrodynamic Interaction on Coagulation Rate of Hydrophobic Colloids. *Journal of Colloid and Interface Science* **1971,** *36* (1), 97-109.
(99) Lin, M. Y.; Lindsay, H. M.; Weitz, D. A.; Klein, R.; Ball, R. C.; Meakin, P. Universal Diffusion-Limited Colloid Aggregation. *Journal of Physics-Condensed Matter* **1990,** *2* (13), 3093-3113.

CHAPTER 4

AGGREGATION AND ION RELEASE KINETICS OF CITRATE-COATED SILVER NANOPARTICLES AND KINETICS MODELING

Work of this chapter is related to the publications or manuscripts:
(1) Wen Zhang, Ying Yao, Nicole Sullivan, Yongsheng Chen. Modeling the primary size effects of citrate-coated silver nanoparticles on their ion release kinetics. ***Environmental Science and Technology***, DOI: 10.1021/es104205a.
(2) Wen Zhang, Ying Yao, Kungang Li, Ying Huang, Yongsheng Chen. Influence of Dissolved Oxygen on Aggregation Kinetics of Citrate-coated Silver Nanoparticles. ***Environmental pollution***. Under review.

4.1. Abstract

Aggregation and ion release are two important environmental behavior of silver nanoparticles (AgNPs) in the environments. These behavior are linked to their fate, transport, and biological impacts. This study investigated the aggregation kinetics of citrate-coated AgNPs in open and closed systems under environmentally relevant solution chemistries. The time-resolved dynamic light scattering (TR-DLS) experiments indicated that in both open and closed systems, the hydrodynamic radii of different sizes of AgNPs grew linearly at the initial 6 h. However, the linear radius growth rates in open system were approximately 2~3 times higher than those in closed system. After 6 h, the hydrodynamic radii became trendless in open system, but still gradually increased in closed system. AgNPs tend to aggregate slowly under anaerobic conditions and potentially appear as AgNPs (instead of aggregates) for a long residence time, which may results in a different fate and transport of silver NPs. This difference in aggregation kinetics between open and closed systems may be caused by silver ion release and subsequent ion speciation. The ion release kinetics of AgNPs was found to depend on particle size and concentration, whereas the concentrations of dissolved oxygen and protons were not rate-limiting factors for ion release. A theoretical model based on the hard sphere theory using the Arrhenius equation was developed, and the model fitted the experimental data quite well, and reached excellent agreement on the particle size and

concentration dependency. This model provides fundamental insight into the kinetic behavior of AgNPs in the environment, which deepens our understanding of the potential persistence and environmental impacts of AgNPs.

4.2. Introduction

The widespread use of silver nanoparticles (AgNPs) in food packaging, clothing and other household products inevitably leads to AgNP release into the environment *(1-3)*. Much evidence has shown that AgNPs are toxic to bacteria *(1)* and some aquatic organisms *(2, 3)* and accumulate in phytoplankton and marine invertebrates *(4-6)*. After entry into the aquatic environment, AgNPs likely will release silver ions (or Ag^+) and coexist with their ionic species *(7, 8)*. AgNPs and Ag^+ exhibit different physicochemical properties and subsequent biological potency *(9-11)*. For example, AgNPs cause cell death by pitting bacterial cell membranes and increasing permeability *(12)*; they also exhibit size- and shape-dependent toxicity *(1, 13)*. In contrast, Ag^+ interacts with the thiol groups of proteins *(14)*, resulting in inactivation of vital enzymes; disrupt bacterial membrane integrity and permeability *(15)*; and likely affect DNA replication *(16)*. When compared on the basis of total mass added, the antibacterial activity of AgNPs was found to be lower than that of Ag^+ *(17, 18)*. However, AgNPs are reported to exhibit the "Trojan-horse mechanism," potentially disrupting cellular functions inside the cells *(19)*. Thus, the ratio of AgNPs to Ag^+ is a critical factor in understanding and assessing the toxicity of AgNPs *(2, 3, 9, 20)*.

Characterizations of AgNPs (e.g, stability, potential ion release and aggregation) are essential for understanding the environmental and biological impacts *(8, 21-23)* and are also the basis for validating and normalizing the results of different toxicity experiments *(24-26)*. Aggregation of AgNPs changes particle properties (i.e.,size, and morphology) as well as particle transport (i.e., diffusivity), which eventually alter bioavailability and cellular toxicity *(13, 19, 27-30)*. In the presence of dissolved oxygen

(DO) in the aqueous environments, AgNPs not only aggregate but also release Ag^+ due to oxidation *(9, 17, 31)*, which induces rather complex physicochemical processes (i.e., aggregation, oxidation of AgNPs, Ag^+ release, complexation and speciation of Ag^+ with natural organic matter (NOM) and electrolytes, and equilibrium between precipitation and dissolution of different silver species). In contrast, anoxic and anaerobic conditions exert low redox potentials, which may inhibit Ag^+ release and other process kinetics. Since AgNPs likely enter rivers, deep soils, sediments, and underground water, where redox conditions may vary the ion release and aggregation of AgNPs, the bioavailabity and toxicity of AgNPs can be dependent on the redox conditions *(11)*. Thus, to fully understand such dependency, it is necessary to characterize the physicochemical processes of AgNPs under relevant environmental conditions.

AgNP stability with respect to aggregation is governed by environmental conditions and particle characteristics. Numerous studies have demonstrated the effects of capping ligand, pH, ionic strength, electrolyte valence, and NOM content of an aquatic system on the aggregation state of NPs *(18, 32-36)*. The effects of mono- and divalent ions and pH on the stability of NPs can be well interpreted by the classic Derjaguin-Landau-Verwey-Overbeek (DLVO) theory. In the presence of NOM and polymeric chemicals (e.g., capping agents), non-DLVO forces, particularly steric force, can also play an important role in the aggregation *(37)*. Aggregation reduces surface area available for oxidation and thus potentially decreases ion release kinetics, ROS production, and toxicity *(9, 38)*. Aggregation can be enhanced by high concentrations of NOM *(39)*, ionic strength *(33)*, and addition of Ca^{2+} *(18, 34)*. In addition, Badawy et al. demonstrate that AgNPs with positive and negative capping agents exhibited surface charge-dependent toxicity on the *bacillus* species probably due to the different aggregation states *(40)*. In spite of the plethora of previous studies of AgNPs *(18, 33, 34)*,

there is still a lack of information on DO effects on the suspension stability (or toxicity) of AgNPs.

Previous studies on ion release kinetics of AgNPs primarily focused on environmental factors, such as dissolved oxygen (DO), pH, temperature, salinity (or ionic strength), and the presence of natural organic matter (NOM) *(9, 31)*. Kittler et al. also studied surface coating effects on the kinetics of Ag^+ release *(31)*. Unfortunately, the effects of intrinsic particle properties (e.g., size) on ion release kinetics have not been fully investigated even though this may provide direct evidence correlating the particle properties with toxicity *(11, 26, 28)*. This information is also essential for manufacturers who wish to produce environmentally benign nanomaterials. More importantly, the solution chemistries (e.g., deionized (DI) water with oxygenation) used in some studies are not environmentally relevant. Lastly, the comprehensive modeling description for ion release kinetics, which is pivotal for establishing correlations between ion release kinetics of AgNPs and their toxicokinetics, is still inadequate *(41, 42)*. Although Kittler et al. developed an empirical model using first-order reaction kinetics, the model parameters neither carry mechanistic meanings nor explain the size dependence of ion release. Thus, the need to advance ion release kinetics modeling of AgNPs is evident and is also essential for decision-makers when establishing regulations regarding nanosilver manufacturing and disposal *(21)*.

Citrate-coated AgNPs are used in this study because they are the most popular silver colloids that are lab-synthesized for general and specific applications *(43, 44)*; the citrate coating serves as both the reducing agent and a stabilizer by decorating the particles with negative charges *(41, 42)*. Citrate-coated AgNPs are the most widely used in commercial products and are recommended by the Organization for Economic Co-operation and Development (OECD) for standard use in toxicology *(9, 20)*.

The main objective of this study was to investigate stability of AgNP suspensions by evaluating the effect of DO on aggregation kinetics of AgNPs dispersed in Hoagland medium, a common hydroponic nutrient medium for growing plants *(45)*. The electrolytic nutrients of this medium simulate relevant ionic conditions in soils *(46)*, sediments *(47)*, and ground water systems *(48, 49)*, environmental matrices that AgNPs are likely to enter. Finally, efforts were made to analyze the effects of AgNP size, concentration, and silver ion release on the aggregation kinetics. The other part of this study aims to elucidate the fundamental mechanisms of Ag^+ release kinetics through experimental and modeling approaches. The ion release experiments were conducted in glass media bottles filled with quarter-strength Hoagland medium. I specifically focused on the effects of primary particle size and concentration on ion release kinetics, because previous research has indicated that factors such as DO, pH, salinity, and temperature likely affect ion release from AgNPs *(9, 31)*. To quantitatively describe the ion release kinetics, I derived a kinetic model, which may provide insight into the mechanisms of ion release kinetics of AgNPs in aqueous environments. The knowledge of these results will contribute to a thorough understanding of environmental behavior and implications of AgNPs.

4.3. Materials and Methods

4.3.1. AgNPs

Water suspensions of citrate-coated AgNPs (20, 40, and 80 nm) without dissolved citrate were purchased from Ted Pella, Inc. (Redding, CA, USA). According to the vendor, the AgNPs will remain monodispersed in the stock suspension without aggregation for a minimum of one year when stored in a sealed bottle at 4 ^{o}C. The total AgNP concentrations of 20-, 40-, and 80-nm AgNPs in the stock suspensions were 6.47 ± 0.02, 6.56 ± 0.10, and 6.21 ± 0.29 mg/L, respectively, and the stock suspensions contained no Ag^{+} as measured by inductively coupled plasma-mass spectrometry (ICP-MS, Elan DRC II, PerkinElmer, USA), which is described below.

4.3.2. Characterization of AgNPs

The morphology and sizes of AgNPs were determined by transmission electron microscopy (TEM) on a Philips EM420 at 120 kV. TEM samples were prepared by placing 5 μL of the aqueous AgNP water suspension on copper grids with a continuous carbon film coating, followed by solvent evaporation at room temperature. The mean particle diameters and size distribution were computed with at least 30 particles from each TEM micrograph.

The crystallography of AgNPs was analyzed with X-ray diffraction (XRD) using an X-ray powder diffractometer (Philips PW 1800, PANalytical Almelo, The Netherlands) with a Cu Kα radiation (λ = 1.54 Å). XRD analysis was recorded at a scanning rate of 0.02^{o}/s in the 2θ range of 35~45^{o}.

The particle size distribution (PSD) and hydrodynamic radius were determined by dynamic light scattering (DLS) on a Zetasizer Nano ZS instrument (Malvern Instruments, UK) using 1.5 mL of 600 μg/L AgNP suspension diluted with DI water in a standard macro-cuvette (pass length: 10 mm). The temperature was maintained at 25 ^{o}C, and the

scattering angle was 173°. A refractive index (RI) of 1.07 and an absorption value of 0.01 were used for the AgNPs *(50)*.

Prior to ICP-MS analysis, all glassware and digestion vessels were carefully cleaned and soaked in 10% (v/v) HNO_3 for 24 h, and finally rinsed five times with 18 MΩ DI water. AgNP suspensions were digested as follows: 1 mL of sample suspension was mixed with 2 mL of trace-metal grade HNO_3 (67~70%, w/w, Fisher Scientific) and heated on a hotplate at 120 °C for 20 min. Then, the digested solutions were diluted and analyzed by ICP-MS.

4.3.3. Electrolyte suspension for aggregation experiments

The electrolyte medium contains the following salts with concentrations (mg/L) shown in parentheses: KH_2PO_4 (52), $Ca(NO_3)_2$ (40.25), $CaSO_4$ (72.25), KNO_3 (34.25), $MgSO_4$ (117.25), and K_2SO_4 (40.25). The medium, as introduced above, is a modified quarter-strength Hoagland medium that simulates environmentally relevant ionic strength. Aliquots of the stock suspension of AgNPs were added to the medium and diluted into the desired mass concentrations (i.e., 300 and 600 μg/L). While the two concentrations may not be environmentally relevant, they were used in the experiments to obtain an evident concentration effect on aggregation kinetics and to observe detectable released Ag^+ concentrations from AgNPs in the medium.

To obtain a constant DO, the medium was aerated with air to achieve an equilibrated DO of 7.8 mg/L. The medium was placed in the cuvettes sealed with a cap with a tiny puncture to permit air exposure and to avoid water evaporation. To further increase DO or redox levels in the medium, the medium was added with H_2O_2. To achieve a zero or low DO (measured DO was less than 0.1 mg/L), the medium was purged with high-purity (99.999%) nitrogen for 30 min and transferred into the cuvette quickly. The head space of the cuvette was purged with nitrogen while the stock AgNP

suspensions were added into the medium. The cuvette was then capped and further sealed tightly with parafilm. pH of the medium with addition of AgNP suspension was maintained at 5.6 ± 0.2 and the only varied factor in this study was DO or the redox level.

4.3.4. Aggregation kinetics under different redox conditions

Aggregation kinetics of AgNPs was investigated using time-resolved dynamic light scattering (TR-DLS) on the Malvern instrument with similar configurations as described above. Aggregation experiments immediately began after the mixture suspension was prepared and the hydrodynamic diameters of AgNPs were monitored. The monitoring lasted more than 300 h, and for each size and concentration the hydrodynamic radius measurement was repeated 3~5 times to confirm the aggregation observations.

4.3.5. Ag^+ Release Experiment

The ion release experiments were conducted in 125-mL glass media bottles containing 100 mL of modified quarter-strength Hoagland medium. Before AgNPs were dispersed into the medium, it was equilibrated with the air; the equilibrated DO and pH of the medium were approximately 7.8 ± 0.2 mg/L and 5.6 ± 0.1, respectively. Two concentrations (300 and 600 μg/L) of AgNPs were added to the medium, and then the glass media bottles were placed in the dark with no stirring (and thus no hydrodynamic effects on ion release kinetics). Every 12 or 24 h, 4 mL of the medium was sampled from the bottle, and the released Ag^+ was separated from the AgNPs using Amicon Ultra-4 centrifugal filter units with pore diameters of 1~2 nm (Amicon Ultracel 3K, Millipore, USA). After centrifugation for 40 min at 5000 × g (5430R, Eppendorf, German), 3 mL of the filtrate was collected and mixed with 2 mL of 67% nitric acid for ICP-MS analysis (Figure S2 shows the potential adsorption of Ag^+ onto the filter). Monitoring of Ag^+ concentrations in the medium lasted approximately 350 h with pseudo-equilibrium observed. The Ag^+ release experiments were repeated three times.

4.4. Results and discussion

4.4.1. Characterization of AgNPs

Figure 4.1a~c shows TEM micrographs of the morphology of the AgNPs used in this study. The AgNPs are close to spherical, and the three different primary diameters were 19.9 ± 0.5, 40 ± 0.6, and 80 ± 0.7 nm, which were consistent with the manufacturer-reported values.

The X-ray diffraction patterns in Figure 4.1d~f indicate that the AgNPs have a typical face-centered cubic (FCC) structure, and a lattice parameter of 0.407 nm, which is the same as the reference data (0.4085 nm) *(41)*. Moreover, the multi-ringed electron diffraction patterns in Figure 4.1g~i further confirm that the AgNPs are FCC polycrystalline. The electron diffraction patterns for the three sizes of AgNPs are the same, and the indexes for these rings indicate that the AgNPs used have the typical face-centered cubic (FCC) structure, which is consistent with crystalline silver. Although HRTEM (high-resolution TEM) may be required to provide accurate information about the crystallinity (e.g., polyscrystalline, monocrystalline, or fused monocrystalline), the multi-ringed electron diffraction pattern suggests that the AgNPs may be polycrystalline. Also, the particle sizes of silver nanocrystals can be calculated from XRD spectra based on the Scherrer equation *(51)*, $t = \frac{0.9\lambda}{B\cos\theta}$, where t corresponds to the particle size, λ is the x-ray wavelength, θ is the Bragg angle, and B corresponds to the full width at half-maximum (FWHM). The particle sizes were calculated to be 12 nm, 22 nm, and 36 nm based on the (111) peak. These calculated values are smaller than the TEM measurement results, probably because the AgNPs contain the defects such as a fused structure (fused small single crystals), or polycrystallinity that yielded an intensity measure of the crystal size within the AgNPs *(52)*. Differently sizes of NPs can yield different rates of ion release due to the difference in crystallinity *(53)*. The crystallinity of nanocrystals and

structural disorder on their surfaces, as well as the presence of different crystallographic planes, are thought to change the surface reactivity of NPs *(54)*.

Figure 1j~l shows PSD diagrams of AgNPs dispersed in DI water, which indicate that the three sizes of AgNPs had distinct hydrodynamic diameters. Polydispersivity index (PDI) is a dimensionless measure of the broadness of the size distribution reported from the Zetasizer Nano ZS instrument. The PDI values are 0.038, 0.184, and 0.166 for 20, 40, and 80-nm AgNPs, respectively. As all of these are less than 0.25, the AgNPs are considered well dispersed in the suspension without aggregation.

The surface charges, as indicated by ζ potentials, were measured under different pH values and are shown in Figure 4.2. The AgNPs were negatively charged at pH >2, which is consistent with previous studies *(9, 34)*.

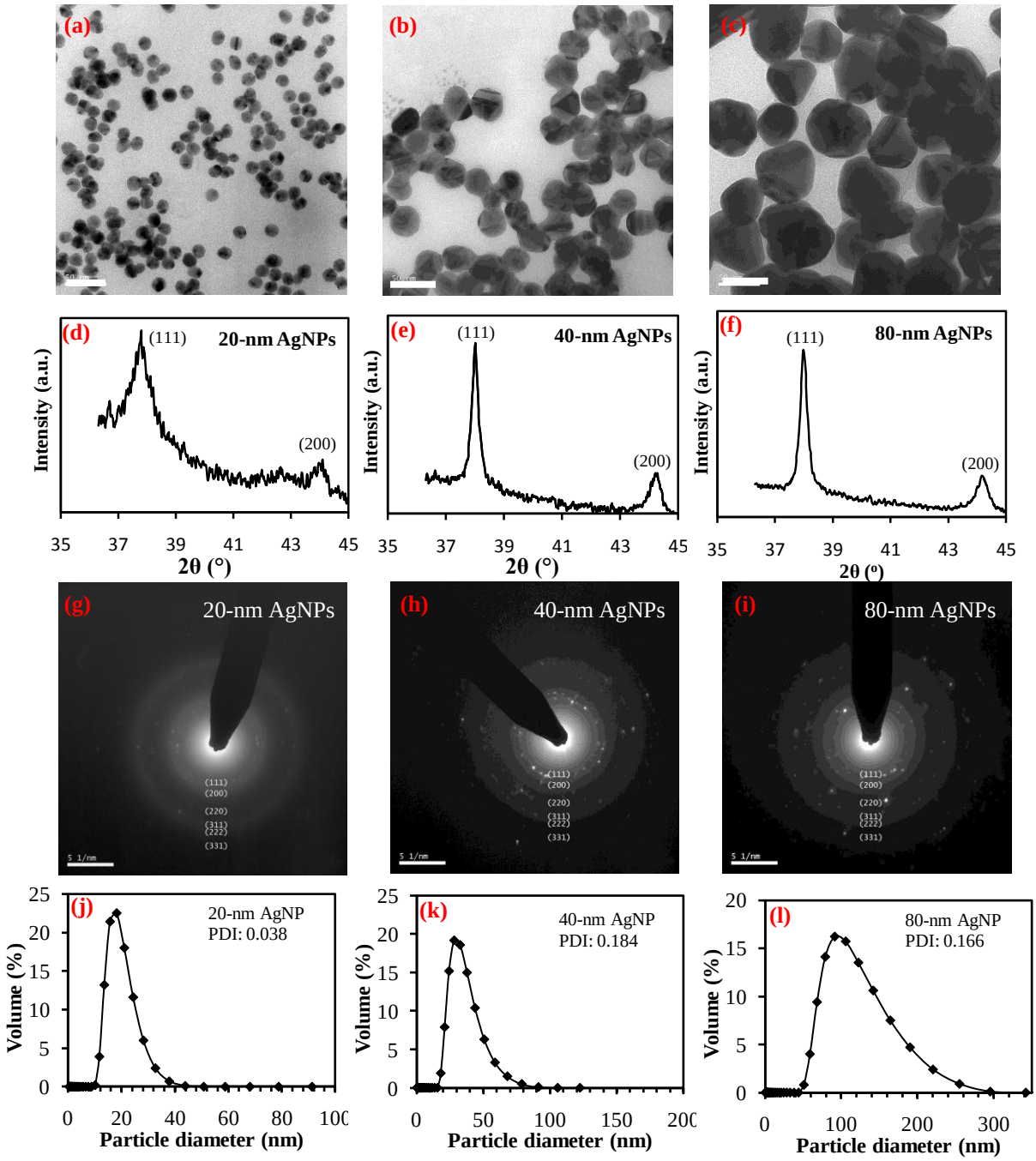

Figure 4.1. (a~c) TEM images of 20, 40, and 80-nm AgNPs on a carbon-coated grid. The white bar on the bottom left equals 100 nm. (d~f) X-ray diffraction patterns. (g~i) Electron diffraction rings for AgNPs of 20 nm, 40 nm, and 80 nm. (j~l) PSD diagrams in terms of volume percentage of AgNPs dispersed in DI water.

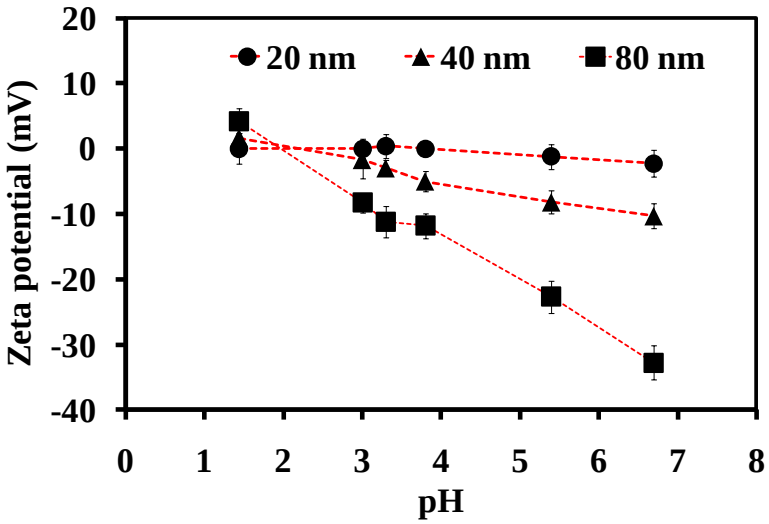

Figure 4.2. ζ potentials of AgNPs in water suspension as a function of pH (the addition of acid and base to adjust the pH negligibly alters the ionic strength).

4.4.2. Aggregation kinetics of AgNPs: roles of DO, particle size, and concentration

Formation of aggregates of AgNPs in electrolyte solutions has been observed previously *(18, 33, 34)*, and my results reached similar findings, as shown in Fig. 2 and Fig. 3 with and without DO present in the medium. High ion content compresses the electric double layer (EDL) and thus reduces the electrostatic repulsion, which leads to aggregation. At the same time, surface charage of AgNPs could be altered by ionic species, as confirmed by the measurement of ζ potentials of AgNPs under different ionic strengths in Figure 8.2b. I further compared aggregation kinetics of AgNPs in the medium with and without DO as shown in Figure 4.3 and Figure 4.4. The hydrodynamic diameters increased almost linearly within the initial 4~6 h for all cases, while the impact of DO became significant after the linear aggregation stage. With exposure to DO, there appeared to be some periodic fluctuations and random distribution in hydrodynamic diameter (Figure 4.3), whereas the hydrodynamic diameters increased stably without DO (Figure 4.4). The DO effect on the aggregation rate during the linear aggregation stage seems substantial as well. The slopes (dD_H/dt) of the hydrodynamic diameter curves, as obtained by the curve fits in the right columns of Figure 4.3 and Figure 4.4, can be used to indicate the aggregation rate. Apparently, AgNPs, in the presence of DO, aggregated 3~8 times faster than those did without DO present, depending on the primary particle size. A possible explanation is that AgNPs with exposure to DO released Ag^+, which was reported previously *(9, 54)* and was further confirmed in the following analysis of ion release kinetics. The released Ag^+ increased ionic strength and thus may enhance aggregation. One may argue that compared to the concentrations (~mg/L) of different divalent and monovalent cations, such as Ca^{2+} and Mg^{2+} in the medium, the released Ag^+ concentrations (~μg/L) were relatively low. Considering that the total initial silver concentrations were only 300 and 600 μg/L, electrostatic repulsion may not be significantly affected by the released Ag^+ (more discussion in the next section). Thus, other unknown mechanisms in addition to Ag^+ release may possibly influence

aggregation kinetics, such as surface energy changes due to the adsorption of Ag^+ or surface oxidation *(55, 56)*, which require future studies to explore.

Another noticeable feature in aggregation kinetics of AgNPs with DO is that after 50 to 150 h, the hydrodynamic diameters of AgNPs began to decline, whereas without DO the aggregated diameters eventually reached pseudo-equilibrated diameters of 400~500 nm within the experimental period. The decline in hydrodynamic sizes with DO could be attributed to dissolution of AgNPs and sedimentation of large aggregates. We compared sedimentation speed and the random movement speed due to Brownian motion for AgNPs, and as shown in Figure 4.5, the sedimentation speed of AgNP aggregates was found to be at least one order of magnitude lower than the random kinetic motion speed. Thus, sedimentation should not substantially cause AgNPs to precipitate, and the dominant cause of the decline in hydrodynamic diameters was the oxidative dissolution of AgNPs.

The effects of particle size and concentration on aggregation kinetics were both evident. 20-nm AgNPs had much steeper slopes than did 40- and 80-nm AgNPs as shown in Figure 4.3 and Figure 4.4, and this finding is consistent with previous results for other NPs *(57, 58)*. The small AgNPs had much higher local particle density with the same initial mass concentrations, and particle aggregation has pseudo-second-order kinetics under low concentrations *(59, 60)*. Thus, small NPs aggregated faster than large NPs. For the same reason, increasing the initial concentrations from 300 to 600 μg/L for AgNPs, we observed a significant increase in the aggregation rates for all three sizes of AgNPs, approximately 21%~49% with DO present and 28%~93% without DO.

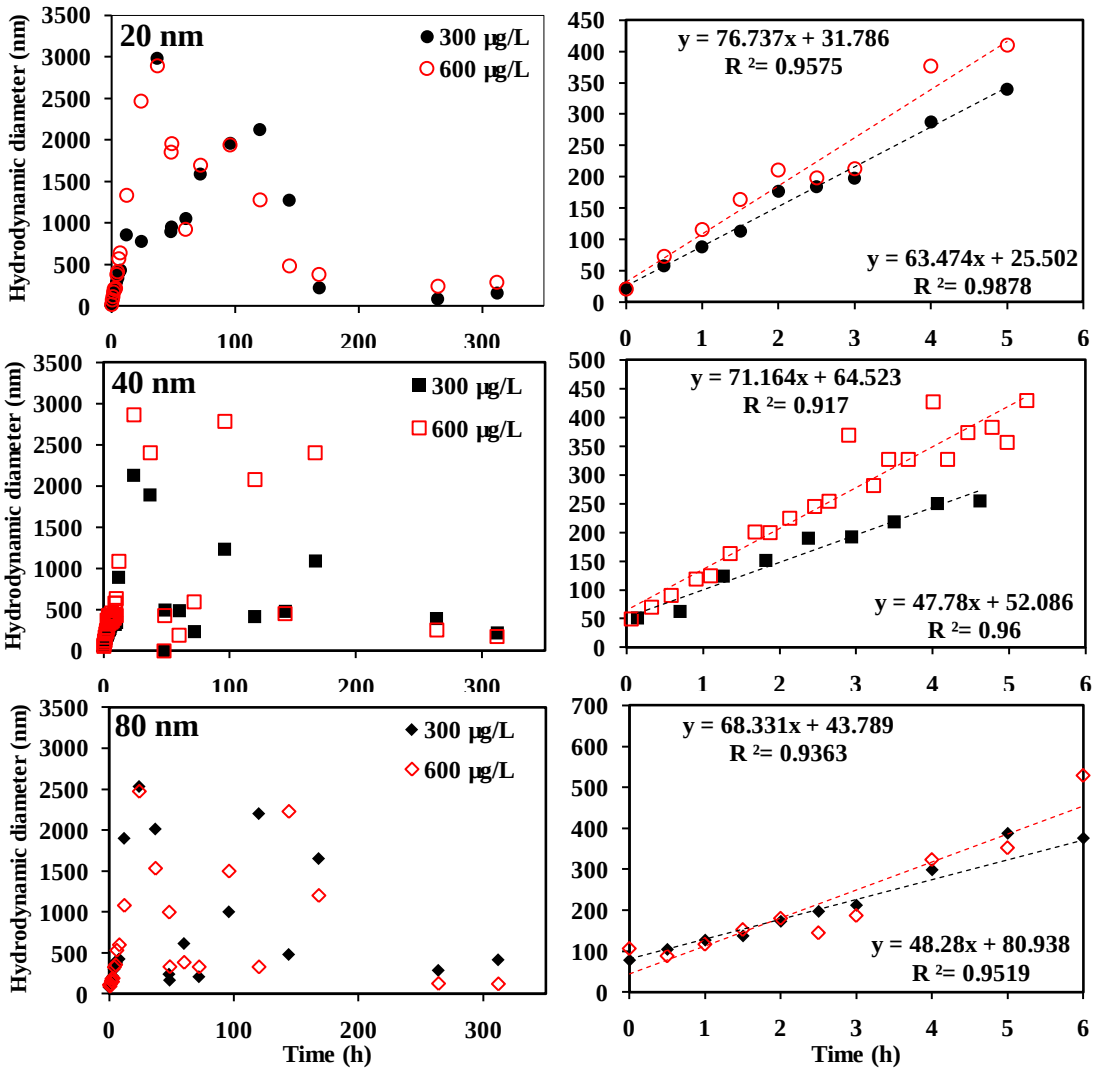

Figure 4.3. Aggregation kinetics of AgNPs in the aqueous medium with 7.8 mg/L of DO. The right column shows the linear growth stage of the hydrodynamic diameters.

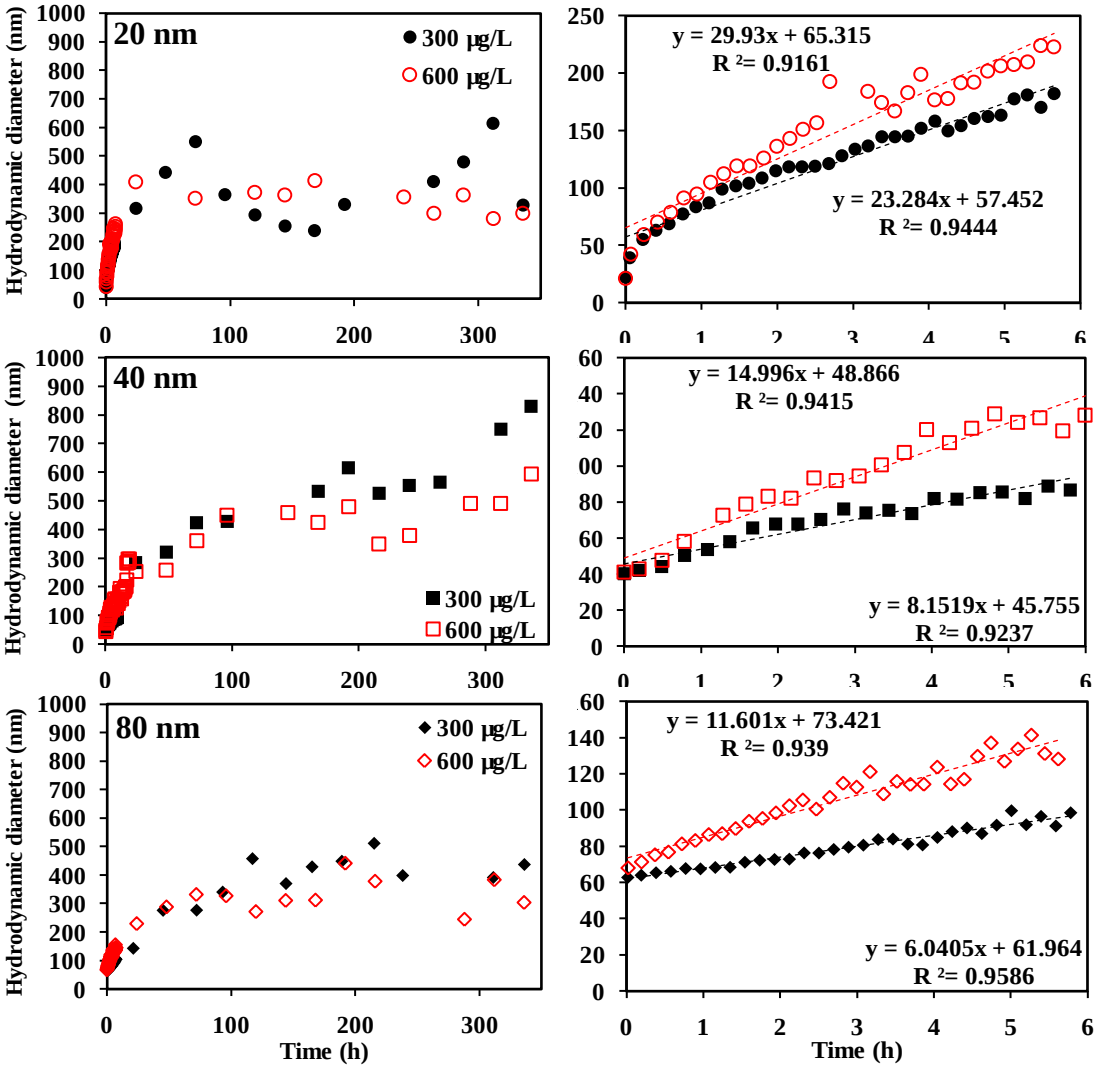

Figure 4.4. Aggregation kinetics of AgNPs in the aqueous medium without exposure to air. The right column shows the linear growth stage of the hydrodynamic diameters.

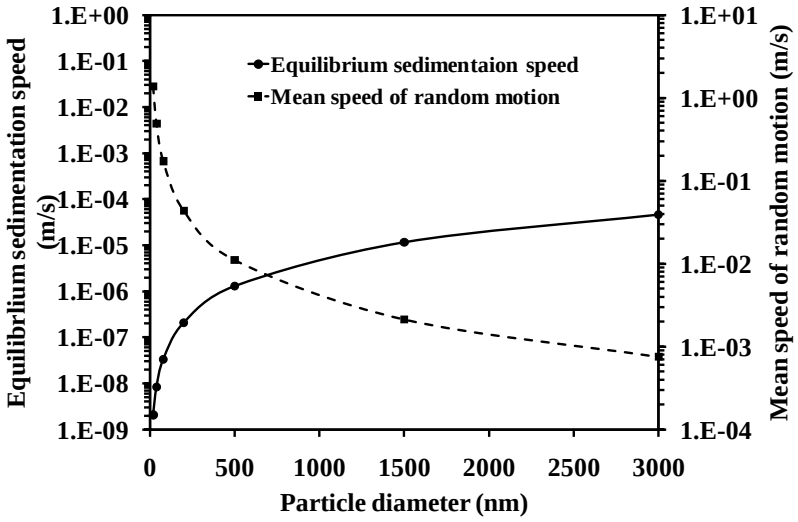

Figure 4.5. Equilibrium speeds of sedimentation calculated by the Stokes' equation (ignoring friction) *(61)* and the mean speed of random kinetic energy for different sizes of AgNPs in water calculated by the Maxwell velocity distribution *(62, 63)*. The input parameters for the Stokes' equation: ρ_g is the density of AgNP aggregates (≈10.5 g/cm^3), ρ_y is the medium density (≈1 g/cm^3 at 25 ^{o}C); μ is the medium dynamic viscosity (1.0×10^{-3} Pa s); d is the particle diameter, and g is the gravity acceleration (9.8 N/kg). where k_B is Boltzmann constant (1.38×10^{-23} J/K), T is the absolute temperature, and m is the mass weight of a single AgNP.

4.4.3. Model Development with the Arrhenius Equation

We derived the Ag^+ release rate (γ_{Ag^+}) on basis of the hard sphere collision theory that has been used previously for modeling the nanoparticle dissolution kinetics *(64, 65)*. The proposed oxidation reaction stoichiometry of AgNPs is *(9, 26)*:

$$Ag_{(s)} + \frac{1}{2}O_{2(aq)} + 2H^{+}_{(aq)} \leftrightarrow 2Ag^{+}_{(aq)} + H_2O_{(l)}$$

Due to their small size, AgNPs may act as soluble reactants and the oxidation reaction can be described by first-order reaction kinetics. Accordingly, γ_{Ag^+} can be expressed by the Arrhenius equation:

$$\gamma_{Ag^+} = kC_{AgNPs}[O_2]^{0.5}\cdot[H^+]^2 = f\cdot\exp(\frac{-E_a}{k_BT})\cdot[AgNPs]\cdot[O_2]^{0.5}\cdot[H^+]^2 \quad (1)$$

$$f = \pi\sigma_{AB}^2\left(\frac{8\pi k_BT}{\mu_{AB}}\right)^{1/2} N_A \quad (1\text{-}1)$$

$$\sigma_{AB} = \sigma_A + \sigma_B \quad (1\text{-}2)$$

$$\mu_{AB} = \frac{m_Am_B}{m_A + m_B} \quad (1\text{-}3)$$

where γ_{Ag^+} is the Ag^+ release rate (mol/(L h)); k is the reaction rate constant (mol/h); [AgNPs], [O_2], and [H^+] are the molar concentrations (mol/L) of AgNPs, DO, and proton, respectively; f is the frequency factor for the reaction; E_a is the activation energy (J); T is temperature (298 K); k_B is the Boltzmann constant (1.38×10^{-23} J/K); N_A is Avogadro's number (6.02×10^{23}/mol); σ_{AB} is the collision radius (nm); σ_A and σ_B are the molecular radii of the reactants A and B (nm); μ_{AB} is the reduced mass (g/mol); and m_A and m_B are the molecular weights of reactants A and B (g/mol). For the silver oxidation reaction,

reactant A is AgNPs and reactant B is either oxygen or protons. The radius of oxygen or protons is much smaller than that of an AgNP (r). Likewise, the molecular weights of oxygen and proton are much lower than that of AgNP. Therefore, Eq. (1-2) and (1-3) can be simplified to $\sigma_{AB} = r$ and $\mu_{AB} = m_B$. Rearranging Eq. (1-1) yields $f = \pi r^2 \left(\frac{8\pi k_B T}{m_B} \right)^{1/2} N_A$, and thus γ_{Ag^+} can be written as:

$$\gamma_{Ag^+} = \pi r^2 \left(\frac{8\pi k_B T}{m_B} \right)^{1/2} N_A \exp\left(\frac{-E_a}{k_B T}\right)[AgNPs] \cdot [O_2]^{0.5} \cdot [H^+]^2 \quad (2)$$

The molar concentration ([*AgNPs*]) of AgNPs can be replaced by the mass-based concentration ([*Ag*]):

$$[AgNPs] = \frac{[Ag]}{N_A \rho \frac{4}{3}\pi r^3} \quad (3)$$

where the initial [*Ag*] values were 300 and 600 μg/L, r is the AgNP radius (nm), and ρ is the the density of AgNPs (≈10.5 g/cm^3). Combining Eqs. (2) and (3) yields:

$$\gamma_{Ag^+} = \frac{3}{4} \left(\frac{8\pi k_B T}{m_B} \right)^{1/2} \cdot \rho^{-1} \cdot \exp\left(\frac{-E_a}{k_B T}\right) \cdot [Ag] \cdot r^{-1} \cdot [O_2]^{0.5} \cdot [H^+]^2 \quad (4)$$

Eq. (4) reveals that γ_{Ag^+} could increase monotonically with increasing [*Ag*], [O_2], or [H^+] and is inversely proportional to r. Furthermore, increasing the temperature could significantly increase γ_{Ag^+}. All these predictions agree with previous findings *(9, 17, 31)*. To describe the experimental results with the model, we derived the released Ag^+ concentration ($[Ag^+]_{released}$) as a function of time (t) with Eq. (4). Since

$\gamma_{Ag^+} = \frac{d[Ag^+]_{released}}{dt}$ and $[Ag^+]_{released} = [Ag]_{initial} - [Ag]$, $[Ag^+]_{released}$ can be solved by integrating Eq.(4):

$$[Ag^+]_{released} = [Ag]_{initial} - \exp(b - a \cdot t) \tag{5}$$

In Eq. (5), *a* and *b* are the fitting parameters, and $a = \frac{3}{4}\left(\frac{8k_BT}{m_B}\right)^{1/2} \cdot \rho^{-1} \cdot \exp(\frac{-E_a}{k_BT}) \cdot r^{-1} \cdot [O_2]^{0.5} \cdot [H^+]^2$. When *t* is zero, $[Ag^+]_{released}$ is zero, thus $b = \ln([Ag]_{initial})$. $[O_2]$ and $[H^+]$ are treated as constants over time, an assumption that is verified in the following sections. Thus, Eq. (5) can be rewritten as:

$$[Ag^+]_{released} = [Ag]_{initial}[1 - \exp(-a \cdot t)] \tag{6}$$

Eq. (6) is used to fit the experimental results with a and b or $[Ag]_{initial}$ as fitting parameters using the nonlinear least-squares curve fitting technique.

4.4.4. Ion Release Kinetics and Model Fitting

Figure 4.6 shows the concentrations of the released Ag^+ over time in the medium. For all sizes of AgNPs, the released Ag^+ concentrations increased almost linearly within the first 8~12 h, and some slight fluctuation in Ag^+ concentrations was observed for 40- and 80-nm NPs after the equilibrium was reached. The initial Ag^+ concentrations were nonzero and slightly different for each size, which indicates that oxidation may have occurred for each size at time=0, probably due to unintended exposure to oxygen during the experimental setup. Increasing the initial AgNP concentration from 300 to 600 μg/L significantly increased the ion release rates for each size of AgNPs, which agrees with my model prediction. Small AgNPs (e.g., 20 nm) took longer (approximately 300 h) to reach reaction equilibrium, whereas large NPs (e.g., 80 nm) reached equilibrium after 100 h. In all cases (three sizes of AgNPs at two initial concentrations), AgNPs did not completely dissolve as a result of oxidation through the entire experimental period, which was also found by Kettler et al. and Liu et al. *(9, 31)*. Thermodynamic analysis predicts that only in the long term should AgNPs be completely dissolved in aqueous environments containing sufficient DO *(9)*. Thus, the observed "equilibrated" state of the Ag^+ release kinetics within 350 h does not correspond to the physicochemical "equilibrium" in which the released silver concentrations should be independent of the amount of AgNPs present. Obviously, Figure 4.6 reveals that the "equilibrated" concentrations of Ag^+ depend on the primary particle size and the initial AgNP concentration. This can be explained by the different thermodynamic properties of AgNPs as compared with their bulk phase *(53, 66)*. Small AgNPs have higher specific surface areas and higher enthalpies of formation compared to the same amount of bulk silver *(26)*. In addition, the faster ion release rate for smaller AgNPs agrees with previous studies on minerals that are well interpreted with the Kelvin equation *(55, 67)*, which indicated that small particles had higher solubility than their larger counterparts.

Sotiriou et al. also observed high ion release rates for small AgNPs, which may contribute to greater antibacterial activity *(17)*.

Speciation of Ag^+ was proven not to influence the ion release kinetics significantly, because thermodynamic calculations using MINEQL 4.5 estimated that more than 99% of the silver is present as soluble Ag^+ at equilibrium *(9)*.

The black dashed lines in Figure 2 show the model fit using Eq. (6). The goodness of the fit between the model and the experimental data was evaluated by the objective function (*O.F.*) defined below, in addition to the squared correlation coefficients (R^2), both of which are summarized in Table 4.1, $OF = \sqrt{\frac{1}{N-1}\sum_{i=1}^{N}\left(\frac{K_{\exp,i} - K_{cal,i}}{K_{\exp,i}}\right)^2}$, where $K_{exp,i}$ and $K_{cal,i}$ are the experimental and model-calculated released Ag^+ concentrations, respectively, for a particular particle size (i) and concentration at a certain reaction time, and N is the number of data points. For my fit, *O.F.* was minimized by adjusting the parameters of a and b for each size/concentration and for different reaction times. Thus, a lower *O.F.* value indicates a better model fit to the experimental data. The data for 40-nm NPs yielded the lowest *O.F.* value (0.09); the other NPs had values around 0.3. The values of R^2 are within 0.90 to 0.99, indicating that the model could explain at least 90% of the variance of the experimental data. Visual inspection of how the model fit matches the experimental data (see Figure 4.6) and shows no systematic errors.

Table 4.1 also summarizes the fitting parameters, a and b. If the activation energy (E_a) is assumed to be the same for different sizes of AgNPs, the values of a should be in the order 20 nm > 40 nm > 80 nm, as a is inversely proportional to r. However, the values of a for 20-nm AgNPs are neither twice those for 40-nm AgNPs, nor four times those for 80-nm AgNPs, which suggests that E_a may vary with particle size. Considering the size dependence of surface energy, crystallinity, and crystallographic plane

distribution *(42, 54)* for AgNPs of different sizes, surface reactivity and E_a can be size-dependent too. Moreover, even with the same total surface area, small NPs have a greater fraction of atoms at edges and corners than large particles, which makes the surface more reactive *(55)*.

The fitted values of *b* for 20- and 40-nm AgNPs are similar each other, whereas the values for 80-nm AgNPs are slightly lower but still in a comparable order of magnitude. The fitted values of $[Ag]_{initial}$ are much lower than the actual applied concentrations of AgNPs (300 and 600 μg/L) as shown in Table S3. As mentioned above, this is because the model is fitted with the data on Ag^+ release, which did not correspond to a complete dissolution of AgNPs.

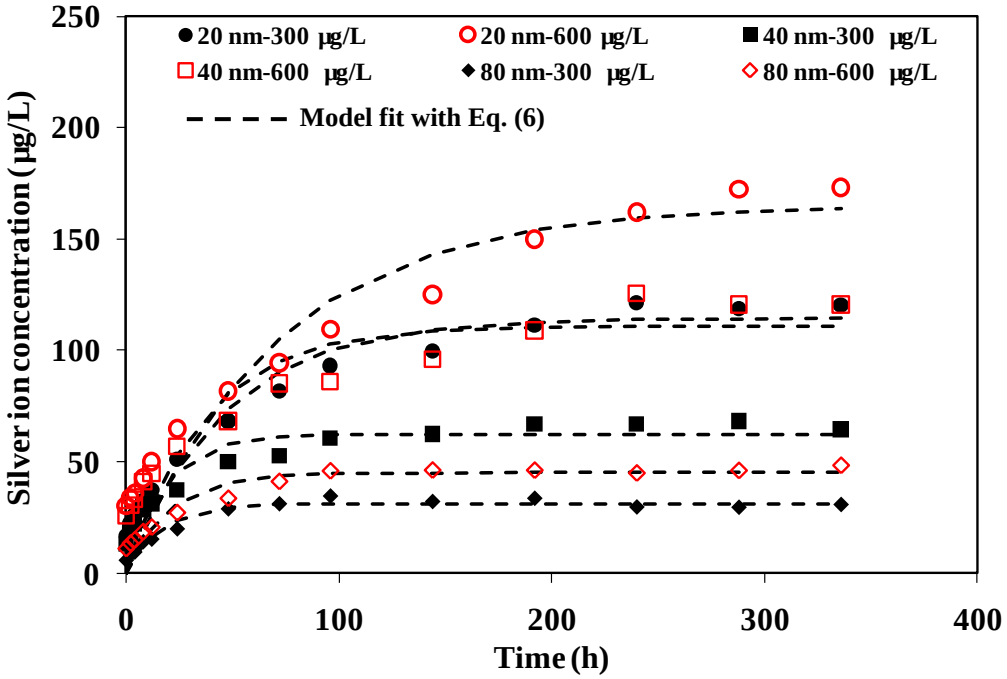

Figure 4.6. Ag^{+} release kinetics in quarter-strength Hoagland medium; the model fits are shown by the black dashed lines.

Table 4.1. Fit equations, correlation coefficients, and fitting parameters.

Size and concentration	*O.F.*	Correlation coefficient (R^2)	*a* (s^{-1})	*b* (dimensionless)	$[Ag]_{initial}$ (µg/L)
20 nm-300 µg/L	0.40	0.97	0.0217	-4.7397	114.4
20 nm-600 µg/L	0.45	0.96	0.0141	-5.10552	164.93
40 nm-300 µg/L	0.35	0.93	0.0542	-4.13376	62.4122
40 nm-600 µg/L	0.41	0.92	0.027	-4.70925	110.9684
80 nm-300 µg/L	0.32	0.96	0.0597	-3.44257	31.2672
80 nm-600 µg/L	0.35	0.95	0.0487	-3.80751	45.038

4.4.5. Environmental factors for Ag^+ release kinetics

As mentioned previously, $[O_2]$ and $[H^+]$ are assumed to be constant over time during the experimental period, which allows us to derive $[Ag^+]_{released}$ as a function of time. These assumptions are verified by comparison between the consumption and mass transfer rates of DO and protons in the oxidation reaction.

When the medium was exposed to the air, the transfer of oxygen from air to the aqueous phase ($O_{2(g)} \rightleftharpoons O_{2(aq)}$) continuously sustained DO. Likewise, the transfer of carbon dioxide ($CO_{2(g)} \rightleftharpoons CO_{2(aq)} + H_2O \rightleftharpoons H_2CO_{3(aq)} \rightleftharpoons H^+_{(aq)} + HCO_3^-$) and its speciation provide protons and a buffer capacity for pH. To calculate the consumption rates of DO and protons, the ion release rates are first calculated using Eq. (5); these are shown in Table 4.2:

$$\gamma_{Ag^+} = \frac{d[Ag^+]}{dt} = \frac{[Ag^+]_{t+\Delta t} - [Ag^+]_t}{\Delta t} \quad (7)$$

where $[Ag^+]_{t+\Delta t}$ and $[Ag^+]_t$ are the concentrations of released Ag^+ at time t and $t+\Delta t$, which are obtained from Figure 4.6. Then, the consumption rates of DO and protons at different reaction times also can be determined based on the reaction stoichiometry. Table 4.2 shows that the Ag^+ release rates were highest at the beginning of the reaction and gradually decreased. Interestingly, high initial AgNP concentration (600 μg/L) did not significantly increase the ion release rates for any of the three sizes; instead, the ion release seemed to be slightly inhibited within the initial 4 h, after which the rates began to increase and eventually exceeded those for 300 μg/L. This probably occurred for two reasons. First, the increasing concentration of AgNPs may temporarily limit the diffusivity of oxygen and protons to reaction sites on silver particle surfaces according to the Stokes-Einstein equation *(68, 69)* and thus slow the oxidation process. Second, AgNPs aggregated rapidly during the oxidation at the larger concentration of AgNPs, as

shown later, because aggregation is reported to have pseudo-second-order kinetics *(70)*. Thus, AgNPs at the initial concentration of 600 μg/L may aggregate faster and thus have less surface area available for oxidation reactions in comparison to samples containing 300 μg/L.

To compare the reaction consumption rates with the mass transfer rate of oxygen, we determined the overall mass transfer coefficient ($K_L a$) for oxygen in quarter-strength Hoagland medium using the standard clean water test method *(71)*. The DO measurement and the detailed calculation of $K_L a$ is provided in appendix A. Based on $K_L a$, the oxygen mass transfer rate was 6.01 μmol/(L h), which is much higher than the oxygen consumption rates in Table 4.2, indicating that DO was not a rate-limiting factor in this study.

Similarly, the pH was monitored during different experimental stages and Figure 4.8 shows that the medium's pH was stable at approximately 5.6. Minor changes in pH occurred after nitrogen purging, exposure to the air, or the addition of AgNPs, probably because the mass transfer of carbon dioxide and speciation provided sufficient protons and buffer capacity for the oxidation of AgNPs. Therefore, the assumptions in my model derivations are justified.

Table 4.2. Average ion release rates and consumption rates of DO and protons*.

	Particle size and concentration	Reaction period (h)				
		0-2	2-4	4-8	8-12	12-48
Ag^+ release rate ($\mu mol\ L^{-1}\ h^{-1}$)	20 nm-300 µg/L	0.026	0.018	0.015	0.011	0.010
	20 nm-600 µg/L	0.018	0.009	0.016	0.017	0.011
	40 nm-300 µg/L	0.023	0.019	0.014	0.006	0.005
	40 nm-600 µg/L	0.021	0.014	0.018	0.009	0.009
	80 nm-300 µg/L	0.011	0.006	0.011	0.003	0.004
	80 nm-600 µg/L	0.011	0.007	0.009	0.005	0.005
DO consumption rate ($\mu mol\ L^{-1}\ h^{-1}$)	20 nm-300 µg/L	0.007	0.005	0.004	0.003	0.003
	20 nm-600 µg/L	0.004	0.002	0.004	0.004	0.003
	40 nm-300 µg/L	0.006	0.005	0.003	0.002	0.001
	40 nm-600 µg/L	0.005	0.003	0.004	0.002	0.002
	80 nm-300 µg/L	0.003	0.001	0.003	0.001	0.001
	80 nm-600 µg/L	0.003	0.002	0.002	0.001	0.001

* Proton consumption rates equal the Ag^+ release rates (see reaction stoichiometry) and thus are not shown here.

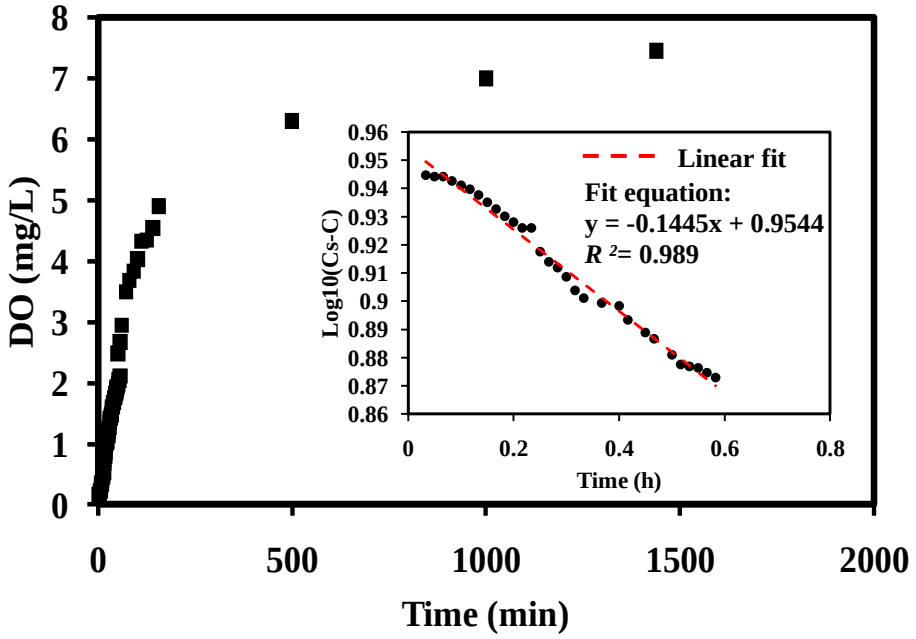

Figure 4.7. DO curve for Hoagland medium after nitrogen purging. The inset shows the plot of $\log_{10}(C_S - C_{DO,t})$ versus *t*.

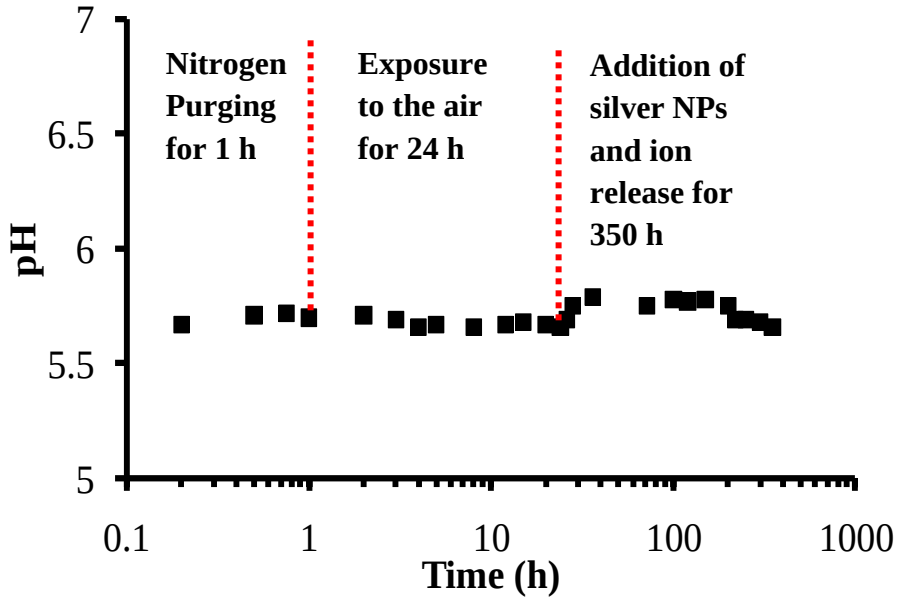

Figure 4.8. pH measurement of Hoagland medium under different treatment conditions.

4.4.6. Interrelationship between the two processes of AgNPs in aqueous environments

As indicated above, an increase in ionic strength due to the release of Ag^+ was thought to cause an increased aggregation of AgNPs, because the high ionic strength should compress the EDL associated with the particles, decrease their ζ potential, diminish interparticle repulsion, and therefore promote aggregation *(72)*. If this assumption holds, higher DO concentrations (or higher redox potentials) should increase the aggregation rates of AgNPs to some extent. To verify this hypothesis, we investigated the aggregation kinetics of 20-nm AgNPs in the medium spiked with different concentrations of H_2O_2. The standard redox potential (E^0=0.98 V) of the oxidation reaction between Ag^0 and H_2O_2 is twice higher that potential between Ag^0 and O_2 (E^0=0.47 V) at 25 ^oC. Compared to the reaction with O_2, the reaction with H_2O_2 is more thermodynamically favorable for AgNPs. From the reaction kinetics aspect, increasing H_2O_2 concentration as a reactant will increase the reaction rate and thus increase the release rate of Ag^+ from AgNPs, as observed previously *(9)*. In spite of the favorable oxidation with H_2O_2, Figure 4.9 shows that aggregation kinetics of AgNPs seems to be barely affected by the increased release rates of Ag^+ in the presence of H_2O_2 in comparison to the presence of 7.8 mg/L of DO. As we mentioned earlier, the released Ag^+ may not reach a significant concentration that dramatically impacts the stability of AgNPs. Two other possible reasons are that Ag^+ may rapidly form other complexes that reduce the real concentrations of Ag^+ and the number of AgNPs decreased as a result of oxidation, which could reduce the aggregation rate of AgNPs. Apparently, attribution to the increased ionic strength may not sufficiently interpret the enhanced aggregation kinetics of AgNPs.

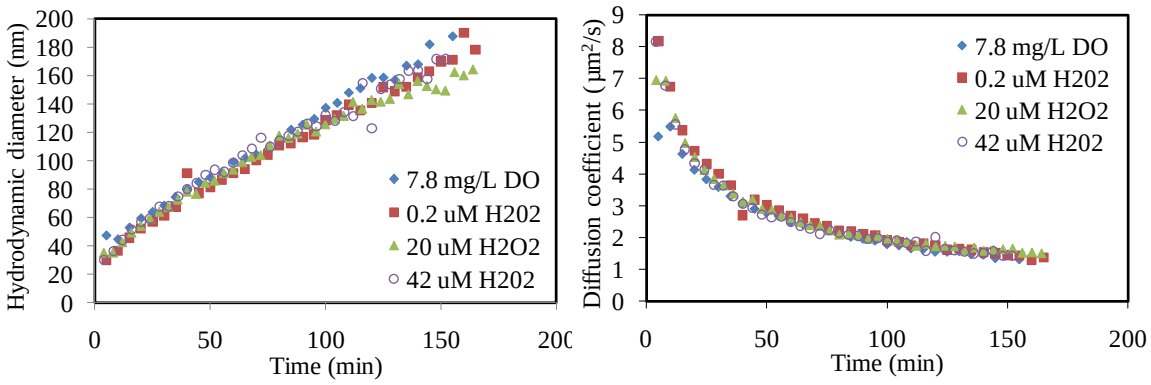

Figure 4.9. Variations of hydrodynamic diameter and diffusion coefficient of 20-nm AgNPs in the medium with addition of different concentrations of H_2O_2.

In addition to the effect of released Ag^+, other physicochemical processes, as outlined in Figure 4.10, may occur simultaneously to AgNP aggregation and influence the stability of AgNPs *(9, 20, 73, 74)*, such as oxidation of AgNPs, Ag^+ release, Ag^+ speciation, Ag^+ complexation, and precipitation and dissolution of silver complexes. In the presence of oxygen, AgNPs were oxidized, which is confirmed by measuring the released Ag^+. Ag^+ can rapidly form other species with anions (e.g., OH^- and CO_3^{2-}). Due to the low solubility, some silver species, such as Ag_2O and Ag_2SO_4, may have precipitation and dissolution equilibriums. The oxidation and potential adsorption of oxidized forms of silver (e.g., Ag_2O) will likely change surface energy, which is dependent on crystallinity and the crystallographic plane of nanocrystals *(42, 54)*. According to DLVO theory, the changes of surface energy will vary the interparticle interactions (e.g., van der Waals interactions may be changed) *(75)*.

The influences of the above complex physicochemical processes as well as the interparticle interactions are reflected by the multimodal particle size distribution (PSD) as measured by DLS. As expected, the data in Figure 4.11 shows a shift in peak maximum of the PSDs for the 20-nm AgNP suspension to larger sizes and then smaller sizes with time, due to the influences of dynamic oxidation, aggregation, and other physicochemical processes. Furthermore, the PSDs became more polydispersed. An initially monomodal PSD (time = 0) became bimodal and multimodal over time, whereas the PSD for 20-nm AgNPs without exposure to DO maintained a monomodal size distribution. The shift in the peak maximum to smaller sizes was mainly due to the oxidative dissolution of AgNPs and their aggregates rather than sedimentation as discussed in previous section. A longer experimental period (i.e., 120 d) was once reported to oxidize all AgNPs into Ag^+ *(9)*. In my cases, AgNPs did not completely dissolve under natural conditions (DO is supplied via air-water transfer) through the entire experimental period, which was also found by *(31)*.

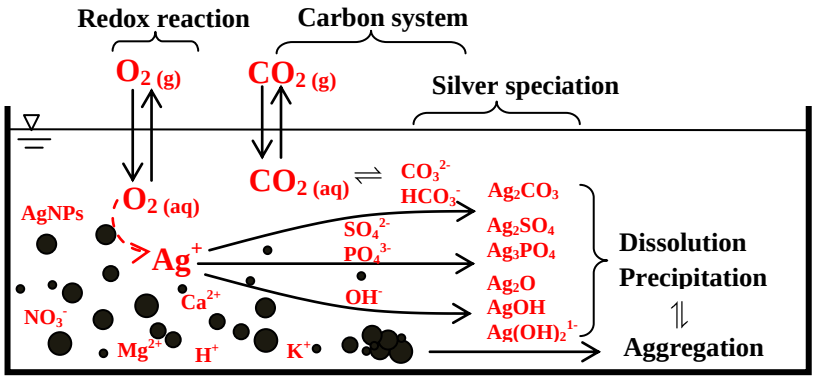

Figure 4.10. physicochemical processes that potentially occur to AgNPs in the quarter-strength Hoagland medium. The black dots represent AgNPs. Not all silver species are included in this graph (e.g., $AgCl_2^-$, $AgCl_3^{2-}$, and $AgCl_4^{3-}$).

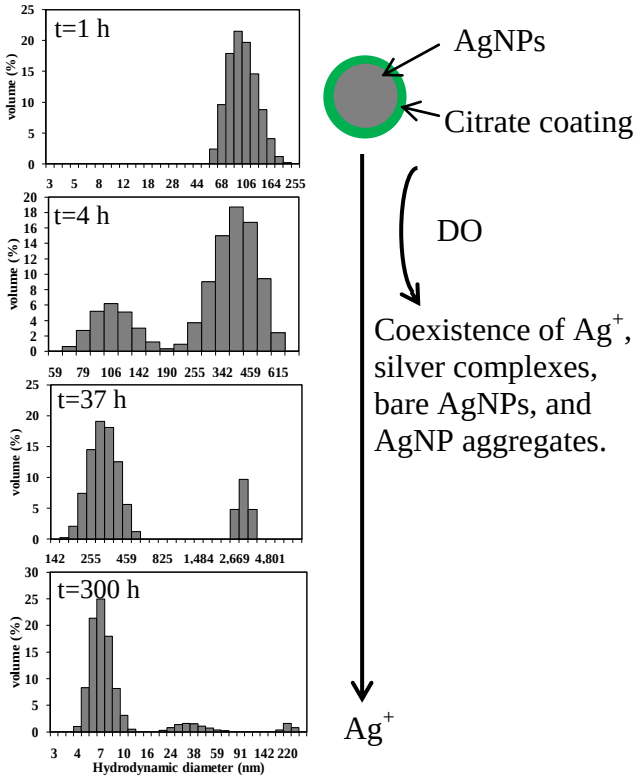

Figure 4.11. PSD with time during 20-nm AgNP aggregation in the medium with DO present (left) and possible fate and transformations of AgNPs in typical aqueous environments (right).

4.5. Research significance

Previous studies have extensively studied the influences of solution properties such as monovalent and divalent salts, pH, temperature, as well as natural organic matters (NOM) on the aggregation kinetics, fate, and transport of nanomaterials *(35, 72, 76-80)*. Clearly, in the natural environment, AgNPs, probably including other reactive NPs (e.g., zero-valent iron), rather than those chemically inert NPs (e.g., most metal oxide NPs), will also be greatly influenced by oxygen content or DO. My results indicate that the aggregation behavior of AgNPs with or without DO present in the medium were different, and silver oxidation could lead to a much greater extent of aggregation than that without DO, as confirmed by different primary sizes and concentrations. To my knowledge, this is the first study to report the DO effect of AgNP aggregation, which lay out the ground work for accounting the importance of DO into environmental transport assessment of AgNPs. These findings are important for understanding the environmental behavior of AgNPs in the typical solution chemistries of aquatic environments and also beneficial for interpreting the antibacterial effects, which are usually associated with Ag^+ release. For example, oxidative stress from reactive oxidative species (ROS) generation on AgNP surfaces *(28)*, and the binding of thiol groups (–SH) with Ag^+ that leads to malfunction of proteins *(26)* are two widely accepted antibacterial mechanism of AgNPs. Clearly, these antibiotic mechanisms of AgNPs only function in the presence of DO, and whether AgNPs without DO present are toxic still remains largely elusive. Thus, distinguishing the roles of different factors (e.g., aggregation state, DO, and adsorbed NOM) in the evaluation of AgNP toxicity in aqueous media will be the objects of future studies.

The ion release behavior of NPs may be linked to their fate, transport, and even biological impacts. Better predictive models are clearly needed to understand their environmental behavior and biological impacts. Although my current study is oriented toward a quantitative understanding of particle size and concentration effects on ion

release kinetics, additional model simulations on the effects of temperature, DO, and pH appeared to be consistent with previous studies. The kinetic model is capable of interpreting the ion release kinetics as a function of reaction time, primary particle size, particle concentration, DO, pH, and temperature. These model equations potentially can predict the metal ion release kinetics of any type of metal-containing NPs as a result of chemical reactions (e.g., oxidation). The present results, both modeling and experimental, suggest that the primary particle size of citrate-coated AgNPs, rather than the aggregated sizes, will dramatically govern the Ag^+ release kinetics. The ion release kinetics modeling may lay the groundwork for developing appropriate models to describe the kinetic behavior of NPs in environmentally relevant solution chemistries.

4.6. Reference

(1) Morones, J. R.; Elechiguerra, J. L.; Camacho, A.; Holt, K.; Kouri, J. B.; Ramirez, J. T.; Yacaman, M. J. The bactericidal effect of silver nanoparticles. *Nanotechnology* **2005,** *16* (10), 2346-2353.

(2) Navarro, E.; Piccapietra, F.; Wagner, B.; Marconi, F.; Kaegi, R.; Odzak, N.; Sigg, L.; Behra, R. Toxicity of Silver Nanoparticles to *Chlamydomonas reinhardtii*. *Environ. Sci. Technol.* **2008,** *42* (23), 8959-8964.

(3) Asharani, P. V.; Wu, Y. L.; Gong, Z. Y.; Valiyaveettil, S. Toxicity of silver nanoparticles in zebrafish models. *Nanotechnology* **2008,** *19* (25), 8.

(4) Fisher, N. S.; Wang, W.-X. Trophic transfer of silver to marine herbivores: A review of recent studies. *Environ. Toxicol. Chem.* **1998,** *17* (4), 562-571.

(5) Dhawan, A.; Sharma, V. Toxicity assessment of nanomaterials: methods and challenges. *Anal. Bioanal. Chem.* **2010,** *398* (2), 589-605.

(6) Shaw, J. R.; Wood, C. M.; Birge, W. J.; Hogstrand, C. Toxicity of silver to the marine teleost (Oligocottus maculosus): Effects of salinity and ammonia. *Environ. Toxicol. Chem.* **1998,** *17* (4), 594-600.

(7) Farré, M.; Gajda-Schrantz, K.; Kantiani, L.; Barceló, D. Ecotoxicity and analysis of nanomaterials in the aquatic environment. *Anal. Bioanal. Chem.* **2009,** *393* (1), 81-95.

(8) Klaine, S. J.; Alvarez, P. J. J.; Batley, G. E.; Fernandes, T. F.; Handy, R. D.; Lyon, D. Y.; Mahendra, S.; McLaughlin, M. J.; Lead, J. R. Nanomaterials in the environment: behavior, fate, bioavailability, and effects. *Environ. Toxicol. Chem.* **2008,** *27* (9), 1825–1851

(9) Liu, J. Y.; Hurt, R. H. Ion Release Kinetics and Particle Persistence in Aqueous Nano-Silver Colloids. *Environ. Sci. Technol.* **2010,** *44* (6), 2169-2175.

(10) Panyala, N. R.; Pena-Mendez, E. M.; Havel, J. Silver or silver nanoparticles: a hazardous threat to the environment and human health? *J. Appl. Biomed.* **2008,** *6* (3), 117-129.

(11) Fabrega, J.; Fawcett, S. R.; Renshaw, J. C.; Lead, J. R. Silver Nanoparticle Impact on Bacterial Growth: Effect of pH, Concentration, and Organic Matter. *Environ. Sci. Technol.* **2009,** *43* (19), 7285-7290.
(12) Shahverdi, A. R.; Fakhimi, A.; Shahverdi, H. R.; Minaian, S. Synthesis and effect of silver nanoparticles on the antibacterial activity of different antibiotics against *Staphylococcus aureus* and *Escherichia coli*. *Nanomedicine: NBM* **2007,** *3* (2), 168-171.
(13) Pal, S.; Tak, Y. K.; Song, J. M. Does the antibacterial activity of silver nanoparticles depend on the shape of the nanoparticle? A study of the gram-negative bacterium Escherichia coli. *Appl. Environ. Microbiol.* **2007,** *73* (6), 1712-1720.
(14) Matsumura, Y.; Yoshikata, K.; Kunisaki, S.; Tsuchido, T. Mode of bactericidal action of silver zeolite and its comparison with that of silver nitrate. *Appl. Environ. Microbiol.* **2003,** *69* (7), 4278-4281.
(15) Feng, Q. L.; Wu, J.; Chen, G. Q.; Cui, F. Z.; Kim, T. N.; Kim, J. O. A mechanistic study of the antibacterial effect of silver ions on Escherichia coli and Staphylococcus aureus. *J. Biomed. Mater. Res.* **2000,** *52* (4), 662-668.
(16) Neal, A. L. What can be inferred from bacterium-nanoparticle interactions about the potential consequences of environmental exposure to nanoparticles? *Ecotoxicology* **2008,** *17* (5), 362-371.
(17) Sotiriou, G. A.; Pratsinis, S. E. Antibacterial Activity of Nanosilver Ions and Particles. *Environ. Sci. Technol.* **2010,** *44* (14), 5649-5654.
(18) Jin, X.; Li, M.; Wang, J.; Marambio-Jones, C.; Peng, F.; Huang, X.; Damoiseaux, R.; Hoek, E. M. V. High-Throughput Screening of Silver Nanoparticle Stability and Bacterial Inactivation in Aquatic Media: Influence of Specific Ions. *Environ. Sci. Technol.* **2010**.
(19) Park, E. J.; Yi, J.; Kim, Y.; Choi, K.; Park, K. Silver nanoparticles induce cytotoxicity by a Trojan-horse type mechanism. *Toxicology in Vitro* **2010,** *24* (3), 872-878.
(20) Damm, C.; Munstedt, H. Kinetic aspects of the silver ion release from antimicrobial polyamide/silver nanocomposites. *Appl. Phys. A* **2008,** *91* (3), 479-486.
(21) Hassellov, M.; Readman, J. W.; Ranville, J. F.; Tiede, K. Nanoparticle analysis and characterization methodologies in environmental risk assessment of engineered nanoparticles. *Ecotoxicology* **2008,** *17* (5), 344-61.
(22) Darlington, T. K.; Neigh, A. M.; Spencer, M. T.; Nguyen, O. T.; Oldenburg, S. J. Nanoparticle characteristics affecting environmental fate and transport through soil. *Environ Toxicol Chem* **2009,** *28* (6), 1191-1199.
(23) Zhang, Y.; Chen, Y. S.; Westerhoff, P.; Crittenden, J. Impact of natural organic matter and divalent cations on the stability of aqueous nanoparticles. *Water Res.* **2009,** *43* (17), 4249-4257.
(24) Nurmi, J. T.; Tratnyek, P. G.; Sarathy, V.; Baer, D. R.; Amonette, J. E.; Pecher, K.; Wang, C.; Linehan, J. C.; Matson, D. W.; Penn, R. L.; Driessen, M. D. Characterization and properties of metallic iron nanoparticles: spectroscopy, electrochemistry, and kinetics. *Environ. Sci. Technol.* **2005,** *39* (5), 1221-1230.
(25) Murdock, R. C.; Braydich-Stolle, L.; Schrand, A. M.; Schlager, J. J.; Hussain, S. M. Characterization of nanomaterial dispersion in solution prior to in vitro exposure using dynamic light scattering technique. *Toxicol. Sci.* **2008,** *101* (2), 239-253.

(26) Marambio-Jones, C.; Hoek, E. M. V. A review of the antibacterial effects of silver nanomaterials and potential implications for human health and the environment. *J. Nanopart. Res.* **2010,** *12* (5), 1531-1551.
(27) Auffan, M.; Rose, J.; Wiesner, M. R.; Bottero, J.-Y. Chemical stability of metallic nanoparticles: A parameter controlling their potential cellular toxicity in vitro. *Environ. Pollut.* **2009,** *157* (4), 1127-1133.
(28) Choi, O.; Hu, Z. Q. Size dependent and reactive oxygen species related nanosilver toxicity to nitrifying bacteria. *Environ. Sci. Technol.* **2008,** *42* (12), 4583-4588.
(29) Liu, W.; Wu, Y. A.; Wang, C.; Li, H. C.; Wang, T.; Liao, C. Y.; Cui, L.; Zhou, Q. F.; Yan, B.; Jiang, G. B. Impact of silver nanoparticles on human cells: Effect of particle size. *Nanotoxicology* **2010,** *4* (3), 319-330.
(30) Jiang, J.; Oberdörster, G.; Biswas, P. Characterization of size, surface charge, and agglomeration state of nanoparticle dispersions for toxicological studies. *Journal of Nanoparticle Research* **2009,** *11* (1), 77-89.
(31) Kittler, S.; Greulich, C.; Diendorf, J.; Koller, M.; Epple, M. Toxicity of Silver Nanoparticles Increases during Storage Because of Slow Dissolution under Release of Silver Ions. *Chem. Mater.* **2010,** *22* (16), 4548-4554.
(32) Keller, A. A.; Wang, H.; Zhou, D.; Lenihan, H. S.; Cherr, G.; Cardinale, B. J.; Miller, R.; Ji, Z. Stability and Aggregation of Metal Oxide Nanoparticles in Natural Aqueous Matrices. *Environ. Sci. Technol.* **2010,** *44* (6), 1962-1967.
(33) Trinh, L. T. T.; Kjoniksen, A. L.; Zhu, K. Z.; Knudsen, K. D.; Volden, S.; Glomm, W. R.; Nystrom, B. Slow salt-induced aggregation of citrate-covered silver particles in aqueous solutions of cellulose derivatives. *Colloid. Polym. Sci.* **2009,** *287* (12), 1391-1404.
(34) El Badawy, A. M.; Luxton, T. P.; Silva, R. G.; Scheckel, K. G.; Suidan, M. T.; Tolaymat, T. M. Impact of Environmental Conditions (pH, Ionic Strength, and Electrolyte Type) on the Surface Charge and Aggregation of Silver Nanoparticles Suspensions. *Environ. Sci. Technol.* **2010,** *44* (4), 1260-1266.
(35) Petosa, A. R.; Jaisi, D. P.; Quevedo, I. R.; Elimelech, M.; Tufenkji, N. Aggregation and Deposition of Engineered Nanomaterials in Aquatic Environments: Role of Physicochemical Interactions. *Environ. Sci. Technol.* **2010,** *44* (17), 6532-6549.
(36) Zhang, Y.; Chen, Y.; Westerhoff, P.; Hristovski, K.; Crittenden, J. C. Stability of commercial metal oxide nanoparticles in water. *Water Res.* **2008,** *42* (8-9), 2204-2212.
(37) Alexander, S. Adsorption of Chain Molecules with a Polar Head a-Scaling Description. *Journal De Physique* **1977,** *38* (8), 983-987.
(38) Dorjnamjin, D.; Ariunaa, M.; Shim, Y. K. Synthesis of silver nanoparticles using hydroxyl functionalized ionic liquids and their antimicrobial activity. *International Journal of Molecular Sciences* **2008,** *9* (5), 807-819.
(39) Gao, J.; Youn, S.; Hovsepyan, A.; Llaneza, V. L.; Wang, Y.; Bitton, G.; Bonzongo, J. C. J. Dispersion and Toxicity of Selected Manufactured Nanomaterials in Natural River Water Samples: Effects of Water Chemical Composition. *Environ. Sci. Technol.* **2009,** *43* (9), 3322-3328.
(40) El Badawy, A. M.; Silva, R. G.; Morris, B.; Scheckel, K. G.; Suidan, M. T.; Tolaymat, T. M. Surface Charge-Dependent Toxicity of Silver Nanoparticles. *Environ. Sci. Technol.* **2011,** *45* (1), 283-287.

(41) Wiley, B.; Sun, Y. G.; Xia, Y. Synthesis of silver nanostructures with controlled shapes and properties. *Acc. Chem. Res.* **2007,** *40* (10), 1067-1076.
(42) Wiley, B.; Sun, Y. G.; Mayers, B.; Xia, Y. N. Shape-controlled synthesis of metal nanostructures: The case of silver. *Chem. Eur. J.* **2005,** *11* (2), 454-463.
(43) Tolaymat, T. M.; El Badawy, A. M.; Genaidy, A.; Scheckel, K. G.; Luxton, T. P.; Suidan, M. An evidence-based environmental perspective of manufactured silver nanoparticle in syntheses and applications: A systematic review and critical appraisal of peer-reviewed scientific papers. *Sci. Total Environ.* **2010,** *408* (5), 999-1006.
(44) Pillai, Z. S.; Kamat, P. V. What Factors Control the Size and Shape of Silver Nanoparticles in the Citrate Ion Reduction Method? *J. Phys. Chem. B* **2003,** *108* (3), 945-951.
(45) Griffin, G. J.; Hale, M. G.; Shay, F. J. Nature and quantity of sloughed organic matter produced by roots of axenic peanut plants. *Soil Biol. Biochem.* **1976,** *8* (1), 29-32.
(46) Gibeaut, D. M.; Hulett, J.; Cramer, G. R.; Seemann, J. R. Maximal biomass of Arabidopsis thaliana using a simple, low-maintenance hydroponic method and favorable environmental conditions. *Plant Physiol.* **1997,** *115* (2), 317-319.
(47) Reddy, K. R.; Tucker, J. C. Growth and nutrient uptake of Pennywort (Hydrcotyle umbellata L.), as Influenced by the nitrogen concentration of the water. *J. Aquat. Plant Manage* **1985,** *23*, 35-40.
(48) Corseuil, H. X.; Moreno, F. N. Phytoremediation potential of willow trees for aquifers contaminated with ethanol-blended gasoline. *Water Res.* **2001,** *35* (12), 3013-3017.
(49) Annandale, J. G.; Jovanovic, N. Z.; Tanner, P. D.; Benadé, N.; Du Plessis, H. M. The Sustainability of Irrigation with Gypsiferous Mine Water and Implications for the Mining Industry in South Africa. *Mine Water Environ.* **2002,** *21* (2), 81-90.
(50) Velikov, K. P.; Zegers, G. E.; van Blaaderen, A. Synthesis and characterization of large colloidal silver particles. *langmuir* **2003,** *19* (4), 1384-1389.
(51) Kwi Jong, L.; et al. Environmentally friendly synthesis of organic-soluble silver nanoparticles for printed electronics. *Nanotechnology* **2007,** *18* (33), 335601.
(52) Klug, H. P.; Alexander, L. E. *X-Ray Diffraction Procedures*. John Wiley and Sons: New York, NY, 1978.
(53) Gilbert, B.; Huang, F.; Zhang, H.; Waychunas, G. A.; Banfield, J. F. Nanoparticles: Strained and Stiff. *Science* **2004,** *305* (5684), 651-654.
(54) Kittler, S.; Greulich, C.; Koller, M.; Epple, M. Synthesis of PVP-coated silver nanoparticles and their biological activity towards human mesenchymal stem cells. *Materialwiss. Werkst.* **2009,** *40* (4), 258-264.
(55) Liu, J.; Aruguete, D. M.; Murayama, M.; Hochella, M. F. Influence of Size and Aggregation on the Reactivity of an Environmentally and Industrially Relevant Manomaterial (PbS). *Environ. Sci. Technol.* **2009,** *43* (21), 8178-8183.
(56) Elzey, S.; Grassian, V. H. Nanoparticle Dissolution from the Particle Perspective: Insights from Particle Sizing Measurements. *langmuir* **2010,** *26* (15), 12505-12508.
(57) He, Y. T.; Wan, J. M.; Tokunaga, T. Kinetic stability of hematite nanoparticles: the effect of particle sizes. *J. Nanopart. Res.* **2008,** *10* (2), 321-332.
(58) Phenrat, T.; Saleh, N.; Sirk, K.; Tilton, R. D.; Lowry, G. V. Aggregation and sedimentation of aqueous nanoscale zerovalent iron dispersions. *Environ. Sci. Technol.* **2007,** *41* (1), 284-290.

(59) Saleh, N. B.; Pfefferle, L. D.; Elimelech, M. Aggregation Kinetics of Multiwalled Carbon Nanotubes in Aquatic Systems: Measurements and Environmental Implications. *Environ. Sci. Technol.* **2008,** *42* (21), 7963-7969.
(60) Chen, K. L.; Elimelech, M. Aggregation and deposition kinetics of fullerene (C-60) nanoparticles. *langmuir* **2006,** *22* (26), 10994-11001.
(61) Limbach, L. K.; Li, Y.; Grass, R. N.; Brunner, T. J.; Hintermann, M. A.; Muller, M.; Gunther, D.; Stark, W. J. Oxide Nanoparticle Uptake in Human Lung Fibroblasts: Effects of Particle Size, Agglomeration, and Diffusion at Low Concentrations. *Environ. Sci. Technol.* **2005,** *39* (23), 9370-9376.
(62) Rudyak, V. Y.; Kharlamov, G. V.; Belkin, A. A. Molecular dynamics simulation of nanoparticles diffusion in dense gases and liquids. *Journal of Aerosol Science* **2000,** *31* (Supplement 1), 432-433.
(63) Rudyak, V. Y.; Kharlamov, G. V.; Belkin, A. A. Diffusion of nanoparticles and macromolecules in dense gases and liquids. *High Temp.* **2001,** *39* (2), 264-271.
(64) Ho, C.-M.; Yau, S. K.-W.; Lok, C.-N.; So, M.-H.; Che, C.-M. Oxidative Dissolution of Silver Nanoparticles by Biologically Relevant Oxidants: A Kinetic and Mechanistic Study. *Chemistry – An Asian Journal* **2010,** *5* (2), 285-293.
(65) Meulenkamp, E. A. Size Dependence of the Dissolution of ZnO Nanoparticles. *J. Phys. Chem. B* **1998,** *102* (40), 7764-7769.
(66) Luo, W. H.; Hu, W. Y.; Xiao, S. F. Size effect on the thermodynamic properties of silver nanoparticles. *J. Phys. Chem. C* **2008,** *112* (7), 2359-2369.
(67) Stumm, W.; Morgan, J. J. *Aquatic chemistry*. 3rd ed.; John Wiley & Sons, Inc.: New York, 1996.
(68) Mackay, M. E.; Dao, T. T.; Tuteja, A.; Ho, D. L.; Van Horn, B.; Kim, H.-C.; Hawker, C. J. Nanoscale effects leading to non-Einstein-like decrease in viscosity. *Nat Mater* **2003,** *2* (11), 762-766.
(69) Tarasenko, A.; Jastrabik, L. Influence of cytoskeleton on nanoparticle migration in biological cells. *Appl. Phys. Lett.* **2009,** *95* (17), 173705.
(70) Chen, K. L.; Mylon, S. E.; Elimelech, M. Aggregation kinetics of alginate-coated hematite nanoparticles in monovalent and divalent electrolytes. *Environ. Sci. Tech.* **2006,** *40* (5), 1516-1523.
(71) Tchobanoglous, G.; Burton, F. *Wastewater engineering treatment, disposal, and reuse*. Third edition ed.; Metcalf & Eddy: 1991.
(72) French, R. A.; Jacobson, A. R.; Kim, B.; Isley, S. L.; Penn, R. L.; Baveye, P. C. Influence of Ionic Strength, pH, and Cation Valence on Aggregation Kinetics of Titanium Dioxide Nanoparticles. *Environ. Sci. Technol.* **2009,** *43* (5), 1354-1359.
(73) Fortin, C.; Campbell, P. G. C. Thiosulfate enhances silver uptake by a green alga: Role of anion transporters in metal uptake. *Environ. Sci. Technol* **2001,** *35* (11), 2214-2218.
(74) Bell, R. A.; Kramer, J. R. Structural chemistry and geochemistry of silver-sulfur compounds: Critical review. *Environ. Toxicol. Chem.* **1999,** *18* (1), 9-22.
(75) Oss, C. J. v. *Interfacial Forces in Aquaeous Media*. Second Edition ed.; Taylor & Francis Group: Boca Raton, Florida, 2006; p 81-83.
(76) Van Hoecke, K.; Quik, J. T. K.; Mankiewicz-Boczek, J.; De Schamphelaere, K. A. C.; Elsaesser, A.; Van der Meeren, P.; Barnes, C.; McKerr, G.; Howard, C. V.; Van De Meent, D.; Rydzynski, K.; Dawson, K. A.; Salvati, A.; Lesniak, A.; Lynch, I.; Silversmit,

G.; De Samber, B.; Vincze, L.; Janssen, C. R. Fate and Effects of CeO_2 Nanoparticles in Aquatic Ecotoxicity Tests. *Environ. Sci. Tech.* **2009,** *43* (12), 4537-4546.
(77) Saleh, N. B.; Pfefferle, L. D.; Elimelech, M. Influence of Biomacromolecules and Humic Acid on the Aggregation Kinetics of Single-Walled Carbon Nanotubes. *Environ. Sci. Tech.* **2010,** *44* (7), 2412-2418.
(78) Li, Z. Q.; Greden, K.; Alvarez, P. J. J.; Gregory, K. B.; Lowry, G. V. Adsorbed Polymer and NOM Limits Adhesion and Toxicity of Nano Scale Zerovalent Iron to *E. coli*. *Environ. Sci. Tech.* **2010,** *44* (9), 3462-3467.
(79) Jin, X.; Li, M.; Wang, J.; Marambio-Jones, C.; Peng, F.; Huang, X.; Damoiseaux, R.; Hoek, E. M. V. High-Throughput Screening of Silver Nanoparticle Stability and Bacterial Inactivation in Aquatic Media: Influence of Specific Ions. *Environ. Sci. Technol.* **2010,** *44* (19), 7321-7328.
(80) Domingos, R. F.; Tufenkji, N.; Wilkinson, K. J. Aggregation of Titanium Dioxide Nanoparticles: Role of a Fulvic Acid. *Environ. Sci. Technol.* **2009,** *43* (5), 1282-1286.

CHAPTER 5

ADSORPTION OF HEMATITE NANOPARTICLES ON CACO-2 CELLS AND THE CELLULAR IMPAIRMENTS: EFFECT OF PARTICLE SIZE

Work of this chapter is related to the publications or manuscripts:
Wen Zhang, Madhavi Kalive, David G Capco, and Yongsheng Chen, Adsorption of hematite nanoparticles onto Caco-2 cells and the cellular impairments: effect of particle size. ***Nanotechnology*** **21 355103.**

5.1. Abstract

The increasing applications of engineered nanomaterials nowadays have elevated the potential of human exposure through various routes including inhalation, skin penetration, and digestion. To date there is scarce information of quantitative description of the interactions between nanoparticles (NPs) and cell surfaces and the detrimental effect from the exposure. The work of this chapter is to study *in vitro* exposure of Caco-2 cells to hematite (α-Fe_2O_3) NPs and to determine the particle size effects on the adsorption behavior. Cellular impairment were also investigated and compared. Caco-2 cells were cultured as a model epithelium to mirror human intestinal cells and used to evaluate the impacts of the exposure to NPs by measuring transepithelial electrical resistance (TEER). Cell surface disruption, localization, and translocation of NPs through the cells were analyzed with immunocytochemical staining and Confocal microscopy. Results showed that hematite NPs had mean diameters of 26, 53, 76, and 98 nm and were positively charged with minor aggregation in the buffer solution. Adsorption of the four sizes of NPs on cells reached equilibrium within approximately 5 min but adsorption kinetics were found to be size dependent. The adsorption rates expressed as mg m^{-2} min^{-1} were greater for large NPs (76 and 98 nm) than those for small NPs (26 and 53 nm). However, adsorption rates expressed as number m^{-2} min^{-1} were

much greater for small NPs than large ones. After the adsorption equilibrium was reached, the adsorbed mass of NPs on unit area of cells was calculated and showed no significant size dependence. Longer exposure time (>3 h) induced adverse cellular effects as indicated by the drop of TEER compared to the control cells without the exposure to NPs. NPs initially triggered a dynamic reorganization and detachment of microvilli structures on Caco-2 cell surfaces. Following this impact, the drop of TEER occurred more significantly, particularly for the exposure to 26 nm, which was consistent with the observations with the confocal microscopy that the junctions were more severely disrupted by 26 nm NPs than other sizes. In conclusion, this chapter demonstrates the interactions at the ultrastructural level from initial surface adsorption of NPs upon cells, to the subsequent microvilli reorganization, membrane penetration, and the disruption of adherens junction and provides the fundamental information of size effects on NP behavior which is often poorly addressed for *in vitro* cytotoxicity studies of NPs.

5.2. Introduction

Increasing production and applications of manufactured nanomaterials will inevitably cause contact of nanoparticles (NPs) with humans and the environment *(1)*. The unique properties of NPs raise concerns about adverse effects on biological systems, which, at the cellular level, include structural arrangements and disruption *(2-5)*. A number of different NPs have been studied in search of the evidence of cytotoxicity *(6-8)*.

In the route of the introduction of NPs to biological systems, surface interactions of NPs with cells determine where the NPs localize, whether they remain attached, or penetrate the cell membrane and enter the cell *(9)*. Adsorption, a common phenomenon and the first step after NPs in contact with cells, may critically influence the fate of NPs in cells. Particularly, it may determine whether they can be accumulated on the cell surfaces or induce cytotoxicity, or cause anti-inflammatory effects in cells *(10-14)*. Previous studies have shown that translocation is largely dependent on particle size:

smaller particles are more readily absorbed *(15-19)*. However, conventional *in vitro* experiments serving as an evaluation method for surface interactions and the affinity between NPs and cells have been challenged by the inhomogeneous properties of NPs in different ways *(20)*. One of the main limitations for such experiments is that the actual size and morphology of NPs in aqueous environments are complex and subject to change in different environmental conditions (pH, ionic strength, and etc) *(21)*. Another limitation is available detection instruments which can precisely detect single NPs and therefore the changes of NPs in sizes were rarely addressed *(22, 23)*. For example, changes in the surface charge as particle size decreases will alter the adsorption affinity of NPs toward cells. Such changes may induce significant impacts on *in vitro* experimental results but have rarely been investigated because in part the existing instruments are unable to track the dynamical changes of these properties (size and surface charge) of NPs *(24)*. Quantitative research on the impacts of NP exposure on whole organisms is scarce but initial work has demonstrated the potential of NPs to enter and migrate within the living organisms *(25, 26)*. NPs may pass through cells by diffusing across cell membranes *(27)*, endocytosis *(28)*, and/or non-phagocytic mechanisms *(29)*. To the best of my knowledge, no data is currently available on particle size effects on adsorption behavior of NPs and the associated exposure effects on cells.

The purpose of this study is to elucidate the adsorption behavior of different sizes of hematite (α-Fe_2O_3) NPs and to investigate their impacts on Caco-2 cell and the cellular structures. Hematite NPs are the most stable form of iron oxide commonly used in semiconductor industries and found in sediments *(30)*. More importantly, hematite NPs were chosen as a common model of metal oxide NPs due to their discrete size distribution with very low aggregation in solutions *(31)*. The Caco-2 cell line used in this study represents human intestinal epithelial cells with properties similar to *in vivo* human intestinal cells which are most likely to be exposed to NPs through ingestion *(8)*.

Moreover, the International Life Sciences Institute Research Foundation/Risk Science Institute (ILSI RF/RSI) Nanomaterial Toxicity Screening Working Group recommends Caco-2 human cell lines for this type of research *(9)*.

The adsorption was assessed by comparing the adsorbed mass of different sizes of hematite NPs on the Caco-2 cell surfaces, while the cellular effects were assessed by Transepithelial Electrical Resistance (TEER) measured across the cells to monitor the integrity of the epithelium. The migrations of NPs through cells were further visualized by immunocytochemical staining and confocal microscopy. Our findings would provide insight information about the fate, transport and effects of NPs on the human gastrointestinal tract or digestive system.

5.3. Materials and Methods

5.3.1. Hematite NPs

The hematite NPs were synthesized in our laboratory using the method reported by Penners and Koopal *(32)*. Briefly, 20 mM FeCl3 in 4 mM HCl solution was incubated for 24 h at 100 ± 0.1 oC in a forced convection flask and the sediments were collected by centrifugal separation. Sizes of NPs were controlled by incubation time. Prior to each use, originally synthesized hematite NPs with four different sizes (26, 53, 76, and 98 nm) were concentrated by high speed centrifuge to make stock suspensions. The hydrodynamic size and zeta potential of NPs dispersed in the liquid were both characterized by DLS performed on a Malvern Instruments Zetasizer Nano ZS instrument. NPs were examined after suspension in DI water (pH ≈ 6.0) and phosphate buffer saline (PBS, 200 mM, pH ≈ 7.2). 1 ml liquid sample was transferred to a Malvern square cuvette for DLS measurements and average size was calculated by the software from the intensity, volume, and number distributions. The precise measurement of particle size in solid state was further comfirmed by a TEM of a TOPCON 002 B model at an accelerating voltage of 160 kV. Over 30 particles randomly chosen from the images were counted and used to determine the mean diameter of each size reported.

5.3.2. Cell culture

The Caco-2 human intestinal cell line, which is brush border expressing, was maintained as previously described *(33-35)*. Briefly, cells were kept at 37^{o}C in a humidified 10% CO_2 incubator in DMEM (from Mediatech, 10-013: 200 mg/L $CaCl_2$, 97.7 mg/L $MgSO_4$, with a pH of 7.0 ~ 7.4) supplemented with 10% fetal bovine serum (Invitrogen), 10 μg/mL transferrin (Roche), and 1% penicillin-streptomycin-amphotericin B (Cambrex). The cells were purchased from the American Type Culture Collection (ATCC) at passage number 48. The cells were passaged once a week and fed twice a week; experiments were conducted on cells between passage numbers 50~65. Caco-2

was further cultured in the Petri dish of 35 mm in diameter and the mature Caco-2 cells had a diameter of 20 μm ~ 30 μm. A hemocytometer (VWR Levy double counting chamber, cat. number 15170-208) was used to determine the number of cells per plate. Densities of approximately 25,000 cells per plate were used in adsorption experiments. For all experiments, Caco-2 cells were grown for 3 weeks prior to use to permit formation of a differentiated epithelial sheet with a well-developed brush border *(36, 37)*. Zeta potential of Caco-2 cells dispersed in PBS (200 mM, pH ≈ 7.2) was also determined by the DLS (Malvern Instruments Zetasizer).

5.3.3. Adsorption experiments and exposure of hematite NPs to Caco-2 cells

Adsorption kinetics of hematite NPs on Caco-2 cells was explored for different particle sizes under different initially applied concentrations. First, Caco-2 cells were transferred to and grown attached to the bottom surface of a small Petri dish (3 cm in diameter) and before the adsorption experiment the serum medium was decanted and replaced with 1.5 ml PBS (200 mM, pH 7.2). Correspondingly, 0.5 ml of freshly concentrated NP suspensions were carefully transferred to the buffer medium without disturbing the cell lines. Control groups were made with NPs and the buffer to test the possible adsorption of NPs upon the surface of Petri dish. After the addition of NPs into the medium, the Petri dish was sealed up carefully with parafilm and placed onto the mixer platform with upside down for shaking as shown in Figure 5.1. For each size of NPs three initially applied concentrations (100, 200, and 300 mg/L) were used and at different adsorption times (5, 15, 25, and 45 min) the Petri dishes were taken off from the platform and the supernatant was carefully sampled for quantification of NPs.

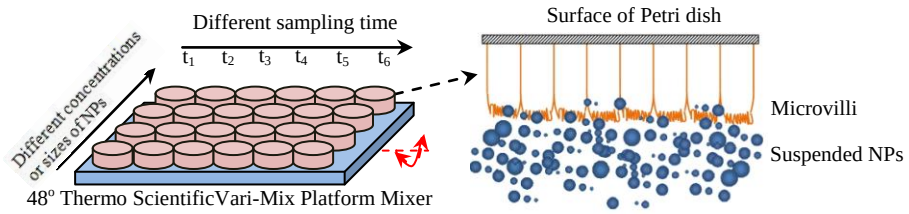

Figure 5.1. Simplified representation of the adsorption experiments. The Petri dish was placed upside down so that NPs adsorbed instead of deposited on the cells. The mixer was set with a rotating speed of 20 rpm and a 48^{o} rotating angle. t_1, t_2, and t_3 etc indicate the different sampling time (different adsorption time). When cells were exposed to NPs, initially NPs mainly adsorbed onto the surface and eventually uptaken through diffusion or other mechanisms into cell body which will be shown in the section 5.3.3.

5.3.4. Quantification of hematite NPs

All liquid samples taken from the supernatant of each Petri dishes were digested based on our previous developed methods *(31)*. Briefly, Liquid samples were fully digested and ionized using HNO_3 (*Trace*SELECT®, for trace analysis, 69.0%, Sigma-Aldrich, Inc., St Louis, MO, USA) under the heat on 150 ^{o}C hotplate. The digested samples were diluted and injected into the induced coupled plasma-optical emission spectrometry (ICP-OES, Thermo iCAP 6300, USA) for quantification of iron species (the emission wave lengths monitored were 238.2 nm and 239.5 nm). The hematite concentration was then indicated by the concentration of iron concentration determined by ICP-OES.

5.3.5. Adsorption kinetics calculation

To describe the adsorption kinetics of NPs on cells, we used the following model equation suggested by Wihelm *et al*.*(20)*:

$$\frac{dM(t)}{dt} = k_a C[M_0 - M(t)] - k_d M(t) \quad (1)$$

where *M(t)* is the total mass of NPs adsorbed per unit area of cell surfaces, mg m^{-2}; *t* is the adsorption time, h; *ka* is the overall association constant, (mg L^{-1})$^{-1}$ h^{-1}; *kd* is the overall dissociation constant, h^{-1}; *C* is the initially applied concentration of NPs in the buffer, mg L^{-1}; and M_0 is the maximum adsorbed mass of NPs that on the cell surface, mg m^{-2}. Currently no data are available for this value, so we assume M_0 = 20000 mg m^{-2} and the choice of this value did not affect the size dependence of the above fit parameters (K_a and K_d) *(38)*. Solving this differential equation yields

$$M(t) = \frac{k_a C M_0}{k_a C + k_d}(1 - \exp[-(k_a C + k_d)t]) \quad (2)$$

where $1/(k_a C + k_d)$ is defined as the characteristic time (τ),h, which gives the overall rate of the adsorption process (namely, adsorption and internalization *(38)*); and k_a / k_d is defined as the affinity constant (K), $(\text{mg L}^{-1})^{-1}$, which indicates the extent to which the adsorption of NPs is likely to occur on cells. A larger K indicates a higher affinity between NPs and cells.

The adsorption rate of NPs on Caco-2 cells was estimated by the equation (3). Clearly, the adsorption rate is time-dependent and thus equation (3) was only used to estimate the mean rate during the initial 5 min of adsorption experiment.

$$\frac{dN}{dt} = \frac{(C_i - C_t)}{X \cdot \alpha \cdot \rho \cdot \left(\frac{4\pi}{3} r^3 \right) \cdot t} V \tag{3}$$

where dN/dt is the number of NPs adsorbed on the unit area of cells per time of adsorption, $\text{m}^{-2}\ \text{min}^{-1}$; C_i is the initially applied concentrations of hematite NPs, mg/L; C_t is the NP concentration in the bulk liquid after adsorption time (t), mg/L, and C_t is the same with $M(t)$ in equation (2); V is the total volume of the mixed suspension, 2 ml; and X is the exposure area of cell surfaces, m^2; I estimated X in the following way: since the most probable number of Caco-2 cells ≈ 25,000 as stated above in the section 2.2 and the mean diameter of single Caco-2 cell was assumed 30 μm as observed from phase contrast images, the exposure area of the Caco-2 cells is $25000 \times 3.14 \times (30 \times 10^{-6})^2/4 = 1.77 \times 10^{-5}\ \text{m}^2$; ρ is the density of hematite NPs, 5.3 g/cm^3; α is the mass ratio of iron in the chemical formula $[Fe_2O_3]_n$, which is equal to is $(2 \times 56)/(2 \times 56 + 3 \times 16) = 0.7$; and r is the mean radius of the NPs, nm.

5.3.6. Scanning Electron Microscopic study of cell membranes of Caco-2

To investigate the structural disruption of Caco-2 cells after a 5-day acute exposure to 98 nm sized nanohematite at 300 mg/L, Caco-2 cells were examined by scanning

electron microscopy (SEM, FEI XL30 EFSEM). All chemicals were bought from EM Sciences for this study (Electron Microscopy Sciences, Pa). Briefly, the NP exposed cells were fixed for one hour in a mix of 8% formaldehyde, 8% glutaraldehyde and 0.2M sodium phosphate (pH 7.0) at room temperature. The cells were then washed quickly in 0.2 M sodium phosphate (pH 7.0) three times. A 1% osmium tetroxide solution made in 0.2 M sodium phosphate (pH 7.0) and deionized water was used to postfixed the cells for 45 min at room temperature. The cells were then briefly rinsed with deionized water. The cells were then dehydrated as a serial dehydration in 20 %, 40 %, 60 %, 80 % and 100 % acetone. The cells were then dried by "critical point drying" and sputter coated with gold particles before viewing in the scanning electron microscope.

5.3.7. Cell assay of exposure induced impairment with TEER technique

TEER was measured and provided a rapid assay at the cellular level to report whether the epithelial integrity has been breached as a result of exposure to hematite NPs. Details about TEER operation can be found in our previous paper *(33)*. Briefly, an EVOM (World Precision Instruments, Inc.) and "chopstick" electrodes (World Precision Instruments, Inc.) were utilized to obtain resistance readings from the epithelial tissue. Caco-2 cells were seeded on collagen coated, 0.4 μm pore, 6.5 mm diameter Transwell membrane inserts (Corning, Inc.) and grown for at least 21 days to form an intact and well differentiated monolayer *(39, 40)*. The chopstick electrode was then used to measure the resistance after calibrating with a CalliCell (World Precision Instruments, Inc.). The 'blank' was measured by having an insert with no cells, only media. This gives a good measure of the background resistance. TEER was calculated by the equation:

$$R_{TEER} = [R_C - R_B] \times A \quad (4)$$

where R_{TEER} is transepithelial electrical resistance (Ω cm^2); R_C is resistance from the cells (Ω); R_B is the background resistance (Ω); and A is the surface area of the filter insert

(cm^2). Once the cells show a transepithelial resistance, the NPs were applied at various concentrations to the filter insert on the cells. The cells were incubated with the NPs for various time periods. The TEER was then checked following the procedure above to indicate the exposure effect of NPs to the cells. Assays were performed in triplicate. Data were expressed as means ± standard deviations. Statistical analysis was performed by the one tail *t*-test with $p<0.05$ considered to be a statistically significant difference.

5.3.8. Immunocytochemistry and Confocal microscopy

To analyze the cells by Z-series scans using confocal microscopy, immunocytochemistry was performed to stain the cells. The Caco-2 cells were grown on the Transwell membrane inserts to an optimal TEER measurement of at least 600 Ωcm^2. They were then fixed for 30 min in 2% formaldehyde in ICB (ICB: 100 mM KCl, 5 mM $MgCl_2$, 3 mM EGTA and 20 mM HEPES (pH 6.8), in H_2O) and permeabilized for 1 hr in ICB with 2% paraformaldehyde and 1% Tween-20. The samples were then washed 3 times for 15 min each wash with ICB-BSA buffer (1% BSA in ICB). A primary antibody was then added to the cells in the antibody dilution buffer (1% non-fat milk, 0.5% Tween-20 in ICB) at a 1:100 dilution overnight at 4^oC. The primary antibody used was γ-catenin which is used to detect the cell junctions. The following day, the cells were washed with ICB-BSA buffer 3 times 15 min each wash. The appropriate fluophor conjugated secondary antibodies were added to the cells overnight at 4^oC. The secondary antibodies were made in the antibody dilution buffer at a 1:500 antibody concentration. The following day, cells were washed with the ICB-BSA buffer 3 times 15 min each wash, then placed in DRAQ5 (2.4 μg/mL in ICB [AXXORA, LLC San Diego, CA]) for a 15 min incubation. This was done to visualize the nucleus of the cells microscopically. The membrane inserts with the cells were mounted on cover slips to be viewed through a confocal microscope. Scanning was done at 0.3 μm sections through a membrane insert.

The software from Leica confocal microscope was used to overlay the Z-series sections and visualize them as 3D images.

5.4. Results and discussion

5.4.1. Dispersion and size distribution of hematite NPs in PBS

TEM images were taken to measure the mean particle size and morphologies of the original synthesized NPs as shown in Figure 5.2A~D. Hematite NPs were spherical in shape and the scale could be readily measured from the images. Four different sizes (26, 53, 76, and 98 nm) of hematite NPs were synthesized and were examined by DLS as shown in Figure 5.3. As observed in many studies *(21, 41, 42)*, most NPs tend to aggregate rapidly when exposed to cell culture media. Maintaining a uniform size distribution of NPs in an aqueous environment is important for the success and validity of such experiments, especially for comparison studies on size effects. In my preliminary studies, particle size distribution (PSD) of a number of commercially available NPs (TiO_2 and α-Al_2O_3 etc) were assessed to determine if they had consistent sizes as reported from manufacturers. The most suitable NPs for adsorption experiments without significant changes in PSD were hematite (α-Fe_2O_3) NPs. One of the possible reasons is that hematite NPs of each size were hydrophilic and positive charged that strongly prevent hematite NPs from aggregation. The zeta potential was 9.5 ± 0.5 mV in PBS ($pH \approx 7.2$) and not found to be significantly size-dependent *(31)*. Thus the electrostatic repulsion kept hematite NPs stably dispersed in a cell culture medium and PBS. The PSD results for NPs suspended in the stock solution in Figure 5.3A were compared to that in the buffer solution in Figure 5.3B. The mean diameters for the four sizes of NPs were not changed significantly in the buffer solution. Compared to TEM images in Figure 5.2,

these NPs also had approximately the same or slightly larger diameters in DI water or the buffer solution. This provides the most unique and compelling support for my study of size effects on adsorption kinetics.

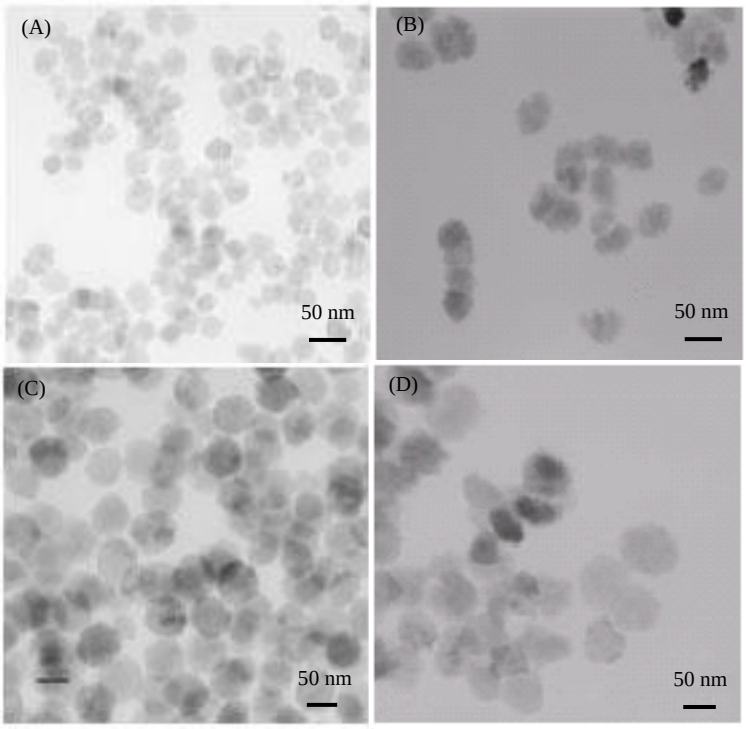

Figure 5.2. Transmission electron microscopy (TEM) of hematite NPs for size comparison. Freshly made NPs dispersed in solution were directly deposited onto the TEM grid. (A) 26 ± 3 nm, (B) 53 ± 6 nm, (C) 76 ± 3 nm, and (D) 98 ± 8 nm; Size values are the mean diameter plus standard deviation based on the measurement of over 30 particles randomly selected.

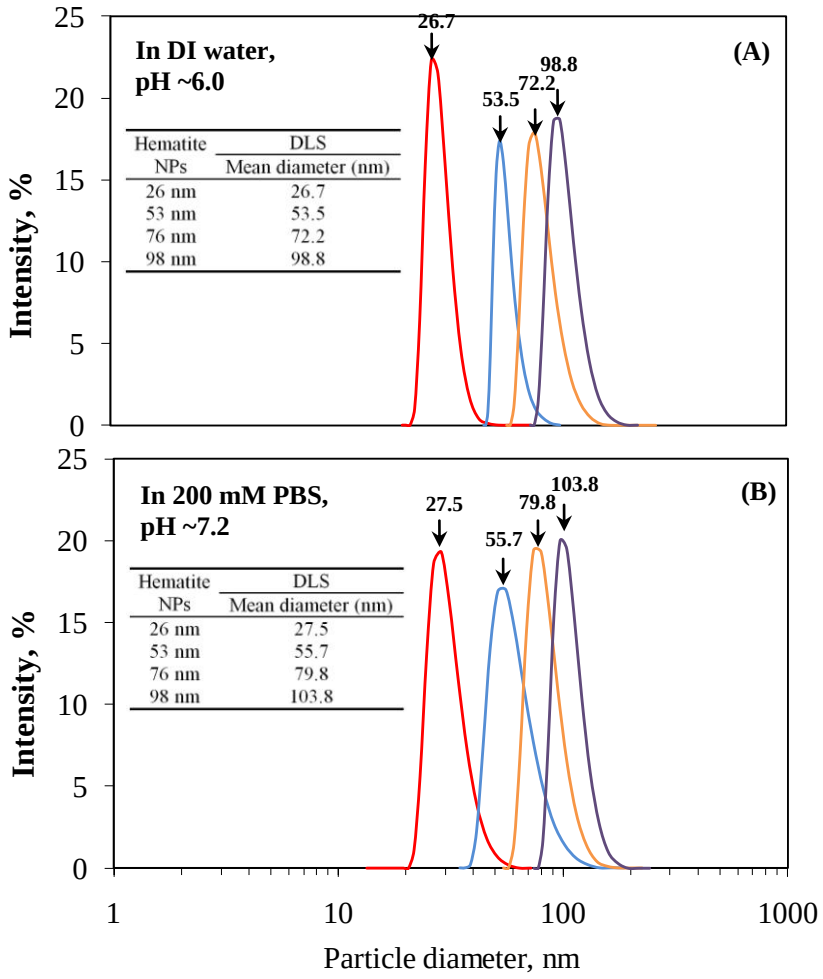

Figure 5.3. Particle size distribution (PSD) diagrams for different sizes of hematite NPs in DI water (A) and in PBS (B) for adsorption experiment. The tables next to the distribution curves show the mean hydrodynamic diameters measured by DLS instrument.

5.4.2. Adsorption kinetics of different sizes of NPs on Caco-2 cells

The hematite NPs were treated as soluble substances and their adsorption behavior were studied following the similar way as the soluble matters. This is probably reasonable since soluble substances are traditionally defined as those that can pass through 0.45 μm filters *(43)*, hematite NPs were clearly much smaller in size than 0.45 μm as supported by the DLS measurement.

In the adsorption kinetics experiment, three different concentrations of NPs were applied to the buffer and exposed to cells. The concentrations of hematite NPs in the control groups were monitored and almost constant during the adsorption experiments under three initially applied concentrations of 100, 200, and 300 mg/L. This indicates that the background adsorption (on the Petri dish) of hematite NPs in the control group can be negligible. Figure 5.4 shows the concentration changes of NPs in the buffer with adsorption time. The adsorption occurred in a relatively faster fashion with an average equilibrium time of around 5 min. The strong attraction between NPs and Caco-cells may be mediated by electrostatic and van der Waals forces *(44, 45)*. This can be supported by the zeta potential measurement, which showed that Caco-2 cells carried negative charges (-7.3 ±0.6 mV) in PBS.

The size effect on the adsorption kinetics can be examined from the mass concentrations of large NPs in the buffer, which were found to drop much faster for large NPs than that of small NPs in Figure 5.4. The four sizes of hematite NPs reached the adsorption equilibrium almost at the same time (approximately 5 min). Their concentrations in the bulk liquid dropped significantly after 5 min and some had an obvious desorption at 10 min. The residual concentrations after the adsorption equilibrium varied for different sizes and the initial concentrations of NPs. For example, for 100 and 200 mg/L initial concentrations, 53 nm NPs had the highest residual concentrations, followed by 26 nm and other large NPs (76 and 98 nm). When 300 mg/L

was applied, 26 nm NPs had the highest residual concentrations, which indicated that 26 nm NPs may have the lowest adsorbed mass on the cell surfaces.

Adsorption kinetics in Figure 5.4 was calculated with the Wihelm equation (equation (2)). Here the best fit results for the data with the initial concentration of 100 mg/L are shown in Table 5.1. 200 and 300 mg/L initial concentrations yielded similar trends for the fit parameters over different sizes of NPs and thus are not shown here. Apparently, large NPs have a smaller characteristics time τ and higher affinity K than small NPs. Obviously, adsorption affinity in the Wihelm equation relied on the comparison of the adsorbed mass of hematite NPs on cells for each size of NPs during the adsorption.

For particle adsorption, it is also worth exploring the adsorption kinetics in adsorbed particle number per time. The NP-cell interactions and the interparticle interactions may both influence the adsorption kinetics and the amount of adsorbed NPs on cell surfaces *(46)*. For example, due to the high diffusivity, small NPs tend to accumulate fast on the cell surfaces but with less mass weight while large NPs may accumulate slower with higher mass weight *(21)*. The adsorption rates were calculated as number of NPs per unit cell surface area and unit time with equation (3) for the initial 5 min of adsorption experiments. Figure 5.5A shows an interesting relation between particle size and adsorption rate, which was an opposite trend of size dependence compared to the adsorption rate expressed by the change in mass concentration.

Figure 5.5B shows the results of the adsorbed mass of different sizes of hematite NPs under different initially applied concentrations. There was no significant difference in the adsorbed mass between different sizes of hematite NPs under the same initially applied concentrations. One exception is that for 300 mg/L 26 nm NPs had the similar adsorbed mass as they did for 200 mg/L. Increasing the initially applied concentrations of NPs could significantly increase the adsorbed mass almost linearly. Overall, this study

provided evidence that the size of hematite NPs exerts a significant effect on adsorption rate (*dN/dt*) rather than the adsorbed mass, which might also depend on the interparticle interactions in multiple-layer adsorptions as discussed above.

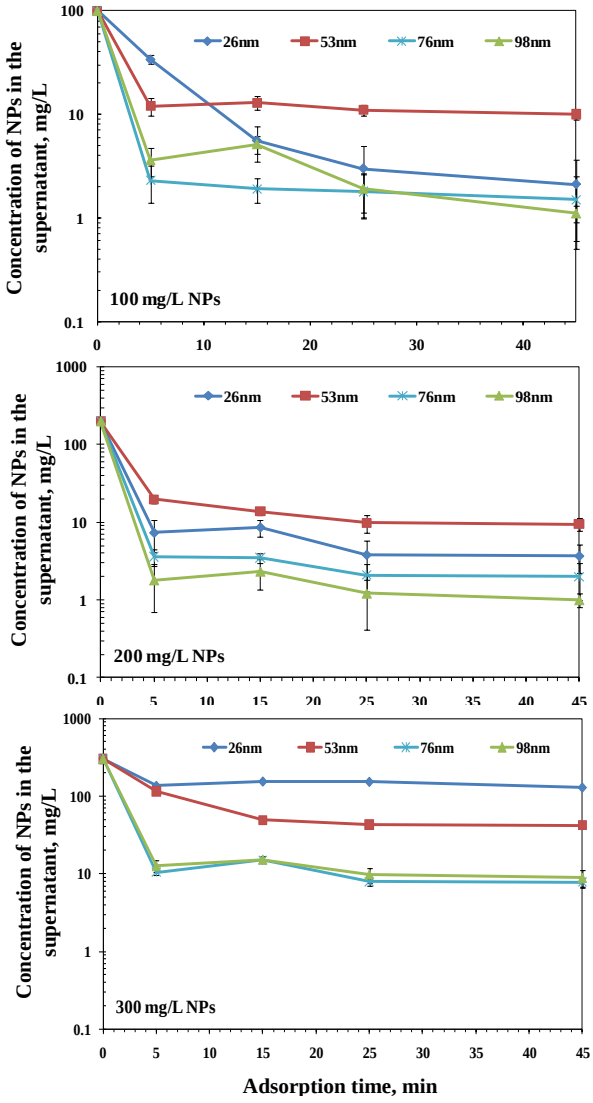

Figure 5.4. Adsorption kinetics of different sizes of NPs on Caco-2 cells with different initial concentrations as indicated in the bottom left corner of each graph. All data points are averages from triplicate data, and error bars represent one standard deviation. When error bars are not visible, they are small and therefore hidden behind the data symbols.

Table 5.1. Kinetic parameters obtained by fitting the data of 100 mg/L as the initially applied concentration with equation (2).

Particle diameter (nm)	$\tau \times 10^{-3}$ (h)	$k_a \times 10^{-2}$ $((mg\ L^{-1})^{-1}\ h^{-1})$	k_d (h^{-1})	$K \times 10^{-5}$ $((mg\ L^{-1})^{-1})$	R^2
26	6.02	1.13	152.04	7.40	0.90
53	5.36	1.23	140.40	8.75	1.00
76	4.18	1.35	126.02	10.7	1.00
98	4.28	1.35	127.12	10.6	1.00

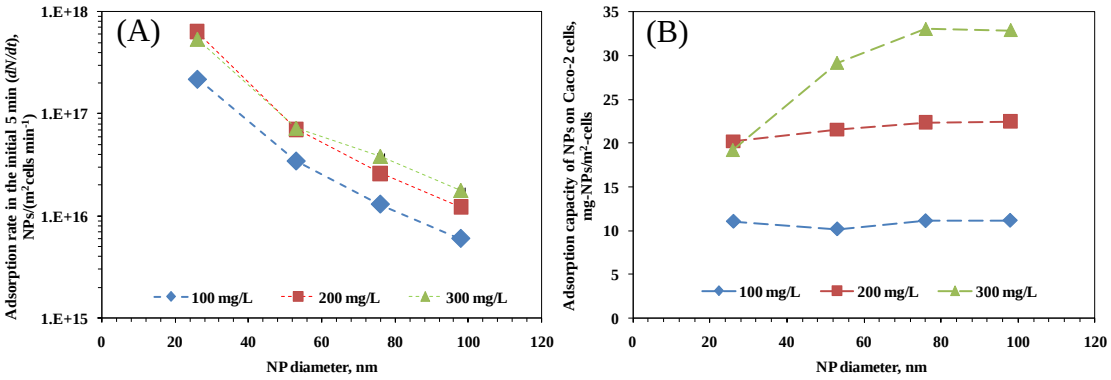

Figure 5.5. (A): Adsorption rate (expressed as number of hematite NPs adsorbed on cells per unit cell surface and per unit time) and its dependence on particle size; (B): The adsorbed mass of different sizes of hematite NPs under different initially applied concentrations.

5.4.3. Structural disruption of microvilli on the cell surface

Following the adsorption, the cellular effects of exposure to hematite NPs was minimal over the first hour *(8)*. However, at longer times of exposure, the microvilli (the external structures on the surface of the epithelium) showed evident disruption since they are the structures that may show initial changes in response to NP application. However, It was observed with SEM that dramatic changes in structural organization of microvilli were induced by exposure to NPs during about 5 days of the exposure. Figure 5.6 shows a typical surface disruption of microvilli after exposure to 300 mg/L of 98 nm hematite NPs for 3 days. The disruption was commonly observed in the cells after exposure to four sizes of hematite NPs and increasing the initially applied concentrations did not significantly promote the disruption. This structural reorganization may be driven by the depletion attraction mechanism as shown in Figure 5.6. Depletion attraction tends to minimize the surface exposure to the macromolecular solute (NPs) driven by entropic effects. As illustrated by Marenduzzo, et al. *(47)*, the entropic level of the whole system (as highlighted by the red box in Figure 5.6) would increase if the microvilli come into contact and the volume (the shaded area in Figure 5.6) available to NPs increased as microvilli overlapped each other. The SEM observations are well consistent with this hypothesis. The toxicity mechanisms for most manufactured NPs have not yet been elucidated clearly and usually require a case-to-case study. Based on this work, disruption of microvilli structures may be a key mechanism leading to the subsequent translocation and toxicity of hematite NPs toward the inside of Caco-2 cells.

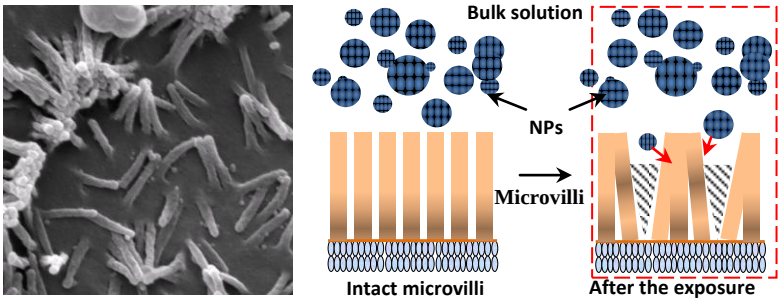

Figure 5.6. The left SEM image shows the morphological changes of microvilli on Caco-2 cell surfaces after the exposure to hematite NPs. The right animation shows the possible mechanism of depletion attraction by which the structures of microvilli were affected. When two microvilli come into contact, the relatively small NPs exert a force equivalent to their osmotic pressure on the opposite sides of the two large microvilli to keep them together (indicated by red arrows). The shaded region is the increased volume available to the NPs and this may facilitate the transport of the NPs into the deeper inside of the membrane.

5.4.4. Disruption of junctional complexes in an epithelium by the exposure to hematite NPs

As mentioned above, initial interaction between positively charged hematite NPs and the negatively charged cell surfaces is primarily mediated by electrostatic interactions *(48)*. Membrane structure and functions are possibly disturbed by of the interactions of NPs with membrane proteins and phospholipids, which constitute the major structure of cell-cell junctions *(49)*. To investigate cellular impacts from exposure of hematite NPs, the epithelial integrity was evaluated by monitoring TEER. There was no immediate change on TEER during and after the adsorption process. However, after 3 hr, the exposure to hematite NPs caused a drop in TEER of Caco-2 cell lines, especially for the sizes 26 nm. The untreated control cells maintained a higher TEER as shown in Figure 5.7. The drop in TEER showed that cells were most affected by the exposure to 26 nm NPs, followed by 53 nm and 98 nm NPs. For 76 nm, the TEER curves fluctuated seriously, and at 300 mg/L, the TEER increased even higher than the control, which was an obviously erroneous but the cause was unknown. When the concentration of each size of NPs was increased from 100 mg/L to 300 mg/L, the drop in TEER for sizes of 26 nm was much greater and faster than the rest sizes of NPs. Since the drop in TEER could be caused either by cell death or disruption of the epithelial integrity *(8)* and the TEER results might indicate that 26 nm had the greatest potential to induce cell death or disruption of epithelial organization for Caco-2 cells while the exposure to 53 nm, 76 nm and 98 nm NPs also had adverse impacts but in relatively weaker manner.

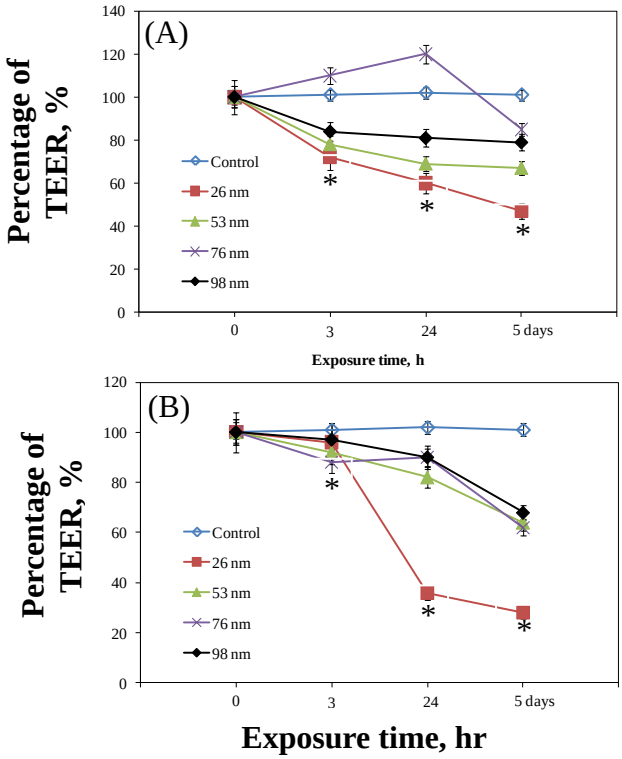

Figure 5.7. TEER of Caco-2 epithelial cells treated with 100 mg/L (A) and 300 mg/L (B) of hematite NPs. Error bars represent mean ± SD (n = 3), some of them may be obscured by the data marker; * = $p < 0.002$ when compared to Control (Caco-2 cells without being exposed to hematite NPs).

The drop of TEER indicates the disruption of epithelial integrity which is a reflection of the junctional complexes that form between cells. These junctional complexes are formed by both tight and adherens junctions. Adherens junctions give strength to the junctions and the absence of adherens junction would result in disruption of epithelial integrity. γ-catenin is a key protein in adherens junctions and in this study the integrity of the adherens junctions was assessed by monitoring the presence and organization of γ-catenin with immunocytochemical staining and confocal microscopic imaging techniques. Figure 5.8 shows a typical image that with increasing exposure time (from 3 h to 5 days) the disruption of the adherens junctions were enhanced under the exposures to 26 nm. Compared to 100 mg/L, high concentrations (300 mg/L) of NPs disrupted the adherens junctions of cell lines more rapidly (the cellular junctions became distorted) within the same exposure time for each size of hematite NPs (images were not shown here). Based on the comparisons between the junctional disruption images under the exposures to different sizes of NPs, it is found with the decreasing size of NPs, their abilities to translocation and permeation across the intestinal cells are greater which is consistent with previously reported *(50)*.

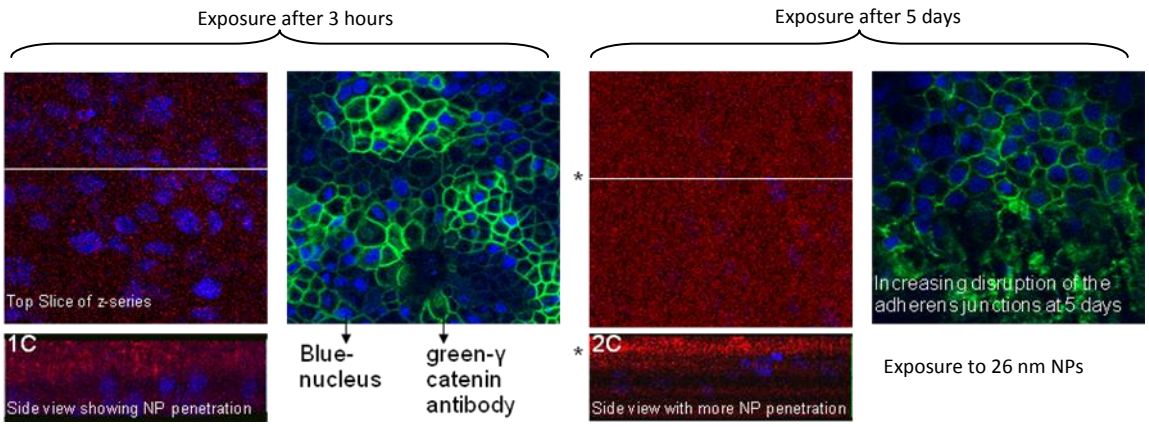

Figure 5.8. Representative confocal images of junction disruption of Caco-2 cells exposed to 26 nm hematite NPs. In these panels (1C and 2C) the red dots are the hematite NPs and the blue color represents the nucleus of a Caco-2 cell. The 3 panels show the penetration of NPs into cells at the specific time point and concentration tested. The nucleus for Caco-2 cells is toward the lower half of a cell, so NPs above the nucleus means NPs are inside the cell.

5.5. Research significance

Based on the above observations, hematite NPs showed high stability in uniform size distributions in PBS buffer which makes them ideal for use as reference nanomaterials in exposure and toxicity tests. Adsorption rates expressed as mg m^{-2} min^{-1} were greater for large NPs (76 and 98 nm) than those for small NPs (26 and 53 nm), while adsorption rates expressed as number m^{-2} min^{-1} was greater for small NPs that than for large NPs. Although different sizes of NPs had similar adsorbed mass under the same initially applied concentrations, the adsorbed mass could be increased by increasing the applied concentrations of NPs except 26 nm NPs. The exposure to NPs induced reorganization and distortion of microvilli on the outside surface of Caco-2 cells. Following that, junctional disruptions were observed as indicated by the drop of TEER. Immunocytochemical staining and confocal microscopy studies provided evidence that γ-catenin as a key protein in adherens junctions was affected by the exposure to NPs which resulted in the junctional disruption. With increasing exposure time, junctional disruption became more severe and the translocation of NPs through the cell interior was more evident. This study demonstrated that hematite NPs with different nano-scale sizes had distinct and size-dependent effects in epithelial cells. The knowledge gained from this study is an important step towards health risk assessment of NPs to the human gastrointestinal tract or digestive system.

5.6. Reference

(1) Baun, A.; Hartmann, N. B.; Grieger, K.; Kusk, K. O. Ecotoxicity of engineered nanoparticles to aquatic invertebrates: a brief review and recommendations for future toxicity testing. *Ecotoxicology* **2008,** *17* (5), 387-395.

(2) Brunner, T. J.; Wick, P.; Manser, P.; Spohn, P.; Grass, R. N.; Limbach, L. K.; Bruinink, A.; Stark, W. J. In Vitro Cytotoxicity of Oxide Nanoparticles: Comparison to Asbestos, Silica, and the Effect of Particle Solubility. *Environ. Sci. Tech.* **2006,** *40* (14), 4374-4381.

(3) Geiser, M.; Rothen-Rutishauser, B.; Kapp, N.; Schurch, S.; Kreyling, W.; Schultz, H.; Im Hof, V.; Hyder, J.; Gehr, P. Ultrafine particles can cross cellular membranes by

nonphagocytic mechanisms in lungs and cultured cell. *Environ Health Perspect* **2005,** *113* (11), 1555 - 1560.
(4) Gupta, A. K.; Gupta, M. Cytotoxicity suppression and cellular uptake enhancement of surface modified magnetic nanoparticles. *Biomaterials* **2005,** *26* (13), 1565-1573.
(5) Hussain, S. M.; Hess, K. L.; Gearhart, J. M.; Geiss, K. T.; Schlager, J. J. In vitro toxicity of nanoparticles in BRL 3A rat liver cells. *Toxicol. In Vitro* **2005,** *19* (7), 975-983.
(6) Usenko, C. Y.; Harper, S. L.; Tanguay, R. L. In vivo evaluation of carbon fullerene toxicity using embryonic zebrafish. *Carbon* **2007,** *45* (9), 1891-1898.
(7) Baun, A.; Hartmann, N.; Grieger, K.; Kusk, K. Ecotoxicity of engineered nanoparticles to aquatic invertebrates: a brief review and recommendations for future toxicity testing. *Ecotoxicology* **2008,** *17* (5), 387-395.
(8) Koeneman, B. A.; Zhang, Y.; Hristovski, K.; Westerhoff, P.; Chen, Y.; Crittenden, J. C.; Capco, D. G. Experimental approach for an in vitro toxicity assay with non-aggregated quantum dots. *Toxicology in Vitro* **2009,** *23* (5), 955–962.
(9) Oberdörster, G.; Oberdörster, E.; Oberdörster, J. Nanotoxicology: an emerging discipline evolving from studies of ultrafine particles. *Environ. Health. Perspect.* **2005,** *113* (7), 823-839.
(10) Duan, H.; Nie, S. Cell-penetrating quantum dots based on multivalent and endosome-disrupting surface coatings. *J. Am. Chem. Soc.* **2007,** *129* (11), 3333-3338.
(11) Goodman, T. T.; Olive, P. L.; Pun, S. H. Increased nanoparticle penetration in collagenase-treated multicellular spheroids. *Int. J. Nanomedicine* **2007,** *2* (2), 265-274.
(12) Mortensen, L. J.; Oberdorster, G.; Pentland, A. P.; Delouise, L. A. In vivo skin penetration of quantum dot nanoparticles in the murine model: the effect of UVR. *Nano Lett.* **2008,** *8* (9), 2779-2787.
(13) Verma, A.; Uzun, O.; Hu, Y.; Han, H. S.; Watson, N.; Chen, S.; Irvine, D. J.; Stellacci, F. Surface-structure-regulated cell-membrane penetration by monolayer-protected nanoparticles. *Nat. Mater.* **2008,** *7* (7), 588-595.
(14) Dutta, D.; Sundaram, S. K.; Teeguarden, J. G.; Riley, B. J.; Fifield, L. S.; Jacobs, J. M.; Addleman, S. R.; Kaysen, G. A.; Moudgil, B. M.; Weber, T. J. Adsorbed proteins influence the biological activity and molecular targeting of nanomaterials. *Toxicol. Sci.* **2007,** *100* (1), 303-315.
(15) Lu, F.; Wu, S. H.; Hung, Y.; Mou, C. Y. Size effect on cell uptake in well-suspended, uniform mesoporous silica nanoparticles. *Small* **2009,** *5* (12), 1408-1413.
(16) Napierska, D.; Thomassen, L. C.; Rabolli, V.; Lison, D.; Gonzalez, L.; Kirsch-Volders, M.; Martens, J. A.; Hoet, P. H. Size-dependent cytotoxicity of monodisperse silica nanoparticles in human endothelial cells. *Small* **2009,** *5*, 846-853.
(17) Shi, Z.; Huang, X.; Cai, Y.; Tang, R.; Yang, D. Size effect of hydroxyapatite nanoparticles on proliferation and apoptosis of osteoblast-like cells. *Acta. Biomater.* **2009,** *5* (1), 338-345.
(18) Watari, F.; Takashi, N.; Yokoyama, A.; Uo, M.; Akasaka, T.; Sato, Y.; Abe, S.; Totsuka, Y.; Tohji, K. Material nanosizing effect on living organisms: non-specific, biointeractive, physical size effects. *J. R. Soc. Interface* **2009,** *6*, 371-388.
(19) Hillyer, J. F.; Albrecht, R. M. Gastrointestinal persorption and tissue distribution of differently sized colloidal gold nanoparticles. *J. Pharm. Sci.* **2001,** *90* (12), 1927-1936.

(20) Wilhelm, C.; Gazeau, F.; Roger, J.; Pons, J. N.; Bacri, J. C. Interaction of anionic superparamagnetic nanoparticles with cells: kinetic analyses of membrane adsorption and subsequent internalization. *langmuir* **2002,** *18* (21), 8148-8155.
(21) Limbach, L. K.; Li, Y.; Grass, R. N.; Brunner, T. J.; Hintermann, M. A.; Muller, M.; Gunther, D.; Stark, W. J. Oxide Nanoparticle Uptake in Human Lung Fibroblasts: Effects of Particle Size, Agglomeration, and Diffusion at Low Concentrations. *Environ. Sci. Technol.* **2005,** *39* (23), 9370-9376.
(22) Navrotsky, A.; Mazeina, L.; Majzlan, J. Size-driven structural and thermodynamic complexity in iron oxides. *Science* **2008,** *319*, 1635-1638.
(23) Lu, H. M.; Han, F. Q.; Meng, X. K. Size-dependent thermodynamic properties of metallic nanowires. *J. Phys. Chem. B* **2008,** *112*, 9444-9448.
(24) Chernyshova, I. V.; Hochella, M. F., Jr.; Madden, A. S. Size-dependent structural transformations of hematite nanoparticles. 1. Phase transition. *Phys. Chem. Chem. Phys.* **2007,** *9* (14), 1736-1750.
(25) Colvin, V. L. The potential environmental impact of engineered nanomaterials. *Nat. Biotechnol.* **2003,** *21* (10), 1166-1170.
(26) Klaine, S. J.; Alvarez, P. J. J.; Batley, G. E.; Fernandes, T. F.; Handy, R. D.; Lyon, D. Y.; Mahendra, S.; McLaughlin, M. J.; Lead, J. R. Nanomaterials in the environment: behavior, fate, bioavailability, and effects. *Environ. Toxicol. Chem.* **2008,** *27* (9), 1825–1851
(27) Lin, S. J.; Keskar, G.; Wu, Y. N.; Wang, X.; Mount, A. S.; Klaine, S. J.; Moore, J. M.; Rao, A. M.; Ke, P. C. Detection of phospholipid-carbon nanotube translocation using fluorescence energy transfer. *Appl. Phys. Lett.* **2006,** *89* (14), 143118-143121.
(28) Lee, J. K. Toxicity and tissue distribution of magnetic nanoparticles in mice. *Toxicol. Sci.* **2006,** *90* (1), 267-267.
(29) Geiser, M.; Rothen-Rutishauser, B.; Kapp, N.; Schurch, S.; Kreyling, W.; Schulz, H.; Semmler, M.; Hof, V. I.; Heyder, J.; Gehr, P. Ultrafine particles cross cellular membranes by nonphagocytic mechanisms in lungs and in cultured cells. *Environ. Health Perspect.* **2005,** *113* (11), 1555-1560.
(30) Frandsen, C.; Bahl, C. R. H.; Lebech, B.; Lefmann, K.; Kuhn, L. T.; Keller, L.; Andersen, N. H.; v. Zimmermann, M.; Johnson, E.; Klausen, S. N.; Mørup, S. Oriented attachment and exchange coupling of alpha - Fe_2O_3 nanoparticles. *Phys. Rev. B: Condens. Matter* **2005,** *72* (21), 214406.
(31) Zhang, Y.; Chen, Y.; Westerhoff, P.; Hristovski, K.; Crittenden, J. C. Stability of commercial metal oxide nanoparticles in water. *Water Res.* **2008,** *42* (8-9), 2204-2212.
(32) Penners, N. H. G.; Koopal, L. K. Preparation and optical properties of homodisperse hematite hydrosols. *Colloids Surf.* **1986,** *19* (2-3), 337-349.
(33) Koeneman, B. A.; Zhang, Y.; Hristovski, K.; Westerhoff, P.; Chen, Y.; Crittenden, J. C.; Capco, D. G. Experimental approach for an in vitro toxicity assay with non-aggregated quantum dots. *Toxicology in Vitro* **2009,** *23* (5), 955-962.
(34) Koeneman, B. A.; Zhang, Y.; Westerhoff, P.; Chen, Y.; Crittenden, J. C.; Capco, D. G. Toxicity and cellular responses of intestinal cells exposed to titanium dioxide *Cell Biol. Toxicol.* **2009,** *26* (3), 225-238.
(35) Peterson, M. D.; Mooseker, M. S. Characterization of the enterocyte-like brush border cytoskeleton of the C2BBe clones of the human intestinal cell line, Caco-2. *J. Cell Sci.* **1992,** *102* (3), 581-600.

(36) Peterson, M. D.; Mooseker, M. S. An in vitro model for the analysis of intestinal brush border assembly. I. Ultrastructural analysis of cell contact-induced brush border assembly in Caco-2BBe cells. *J. Cell Sci.* **1993,** *105* (2), 445-460.
(37) Peterson, M.; Bement, W.; Mooseker, M. An in vitro model for the analysis of intestinal brush border assembly. II. Changes in expression and localization of brush border proteins during cell contact-induced brush border assembly in Caco-2BBe cells. *J. Cell Sci.* **1993,** *105* (2), 461-472.
(38) Cho, E. C.; Xie, J.; Wurm, P. A.; Xia, Y. Understanding the role of surface charges in cellular adsorption versus internalization by selectively removing gold nanoparticles on the cell surface with a I2/KI etchant. *Nano Lett.* **2009,** *9* (3), 1080-1084.
(39) MD, P.; MS., M. An in vitro model for the analysis of intestinal brush border assembly. I. Ultrastructural analysis of cell contact-induced brush border assembly in Caco-2BBe cells. *J. Cell Sci.* **1993,** *105* (Pt 2), 445-460.
(40) MD, P.; WM, B.; MS, M. An in vitro model for the analysis of intestinal brush border assembly. II.Changes in expression and localization of brush border proteins during cell contact-induced brush border assembly in Caco-2BBe cells. *J. Cell Sci.* **1993,** *105* (Pt 2), 461-472.
(41) Van Hoecke, K.; De Schamphelaere, K. A.; Van der Meeren, P.; Lucas, S.; Janssen, C. R. Ecotoxicity of silica nanoparticles to the green alga Pseudokirchneriella subcapitata: importance of surface area. *Environ. Toxicol. Chem.* **2008,** *27* (9), 1948-1957.
(42) Xie, B.; Xu, Z.; Guo, W.; Li, Q. Impact of natural organic matter on the physicochemical properties of aqueous C60 nanoparticles. *Environ Sci Technol* **2008,** *42* (8), 2853-9.
(43) Richards, G. P.; Weinheimer, D. A. Influence of adsorption time, rocking, and soluble proteins on the plaque assay of monodispersed poliovirus. *Appl. Environ. Microbiol.* **1985,** *49* (4), 744-748.
(44) Hermansson, M. The DLVO theory in microbial adhesion. *Colloids Surf., B* **1999,** *14* (1-4), 105-119.
(45) Boström, M.; Deniz, V.; Franks, G. V.; Ninham, B. W. Extended DLVO theory: Electrostatic and non-electrostatic forces in oxide suspensions. *Adv. Colloid Interface Sci.* **2006,** *123-126*, 5-15.
(46) Strauss, J.; Liu, Y. T.; Camesano, T. A. Bacterial adhesion to protein-coated surfaces: An AFM and QCM-D study. *JOM* **2009,** *61* (9), 71-74.
(47) Marenduzzo, D.; Finan, K.; Cook, P. R. The depletion attraction: an underappreciated force driving cellular organization. *J. Cell Biol.* **2006,** *175* (5), 681-686.
(48) Fischer, D.; Li, Y. X.; Ahlemeyer, B.; Krieglstein, J.; Kissel, T. In vitro cytotoxicity testing of polycations: influence of polymer structure on cell viability and hemolysis. *Biomaterials* **2003,** *24* (7), 1121-1131.
(49) Martien, R.; Loretz, B.; Sandbichler, A. M.; Schnurch, A. B. Thiolated chitosan nanoparticles: transfection study in the Caco-2 differentiated cell culture. *Nanotechnology* **2008,** *19* (4), 045101.
(50) Seaton, A.; Tran, L.; Aitken, R.; Donaldson, K. Nanoparticles, human health hazard and regulation. *Journal of The Royal Society Interface* **2010,** *7* (Suppl 1), S119-S129.

CHAPTER 6

ADSORPTION KINETICS OF HEMATITE NPS ON E. COLI CELLS: SURFACE INTERACTION FORCES, EXPOSURE IMPACTS ON STRUCTURAL INTEGRITY AND SURFACE POTENTIAL

Work of this chapter is related to the publications or manuscripts:

(1) Wen Zhang and Yongsheng Chen, Interaction force measurement between *E. coli* cells and nanoparticles immobilized surfaces by using AFM. ***Colloids and Surfaces B: Biointerfaces,*** 2011, 316-324

(2) Wen Zhang, Ying Yao, and Yongsheng Chen Quantifying and Imaging the Morphology and Nanoelectric Properties of Soluble Quantum Dot Nanoparticles Interacting with DNA. ***Journal of Physical Chemistry C***, 2011, 115 (3), 599-606.

(3) Wen Zhang, Bruce Rittmann, and Yongsheng Chen. Size effects on adsorption kinetics of hematite NPs on *E. coli* cells. ***Environmental Science and Technology***, 2011, 45 (6), 2172-2178.

(4) Wen Zhang, Joseph B Hughes, and Yongsheng Chen. Changes of mechanical and nanoelectric properties of *E. coli* cells after exposure to hematite NPs. In preparation.

6.1. Abstract

Adsorption of engineered nanoparticles (NPs) onto bacterial cells is critical for quantifying nano-bio interactions, as well as toxicokinetic properties of NPs. The first purpose of this work was to study adsorption of hematite (α-Fe_2O_3) NPs onto *Escherichia coli* cells and to determine the particle size effects on the adsorption kinetics. Adsorption of large NPs (76 and 98 nm) on cells reached equilibrium faster (within 30-40 min) than small NPs (approximately 60-90 min). The adsorption rates in mg Fe/(L **s**) decreased in the order of 98 nm > 76 nm > 53 nm > 26 nm. However, adsorption rates expressed as the number of adsorbed hematite NPs per unit cell surface area in #/(m^2 **s**) were faster for small NPs than those for large NPs. To interpret the size effects on adsorption kinetics, the Extended Derjaguin−Landau−Verwey−Overbeek (EDLVO) theory was combined with interfacial force boundary layer (IFBL) theory. The computed adsorption rates for different sizes had excellent agreement with the experimental data, and they explained that that faster kinetics for smaller NPs could be attributed to faster particle mobility and

lower energy barriers in the total interaction energy. This study lays the groundwork for quantifying the kinetic behavior of NPs interacting with microbial cells, and the results provide insight into adsorption processes at the nanoscale.

To better understand the adsorption at the bio-nano interface, we further used the atomic force microscopy (AFM) to measure interaction forces between *E. coli* cells and NPs in an aqueous environment, which could be the driving force for the adsorption process. The results showed that adhesion force strength was significantly influenced by particle size for hematite (α-Fe_2O_3) NPs and this finding was also observed for corundum (α-Al_2O_3) NPs whereas the effect on the repulsive force was not observed. The adhesion force decreased from 6.3 ± 0.7 nN to 0.8 ± 0.4 nN as hematite NPs increased from 26 nm to 98 nm in diameter. Corundum NPs exhibited a similar dependence of adhesion force on particle size. The Johnson-Kendall-Roberts (JKR) model was employed to estimate the contact area between *E. coli* cells and NPs, and based on the JKR model a new mechanical contact model that considers local effective contact area was developed. The prediction of the new model matched the size dependence of adhesion force in experimental results. Size effects on adhesion forces may originate from the difference in local effective contact areas as supported by our model. These findings provide fundamental information on the interfacial forces of NPs toward biological interface, which barely have been addressed.

In addition to quantifying the interfacial interactions between NPs and biological matrices, imaging is critical to gain more information that will beneficial to both applications of nanotechnology and its potential environmental impact. To achieve this goal, Kelvin-probe force microscopy (KFM), an electrical mode of atomic force microscopy (AFM), was employed as novel tool to investigate the surface interactions of hematite NPs with live *E. coli* cells. Our results demonstrated for the first time KFM's superior performance in resolving the individual hematite NPs interacting with live *E.*

coli cells. Both surface potential and phase images provided a striking visualization of the adsorption of hematite NPs onto *E. coli* cells and the subsequent disruption in their extracellular appendages (flagella). The surface potential of *E. coli* cells dropped significantly and dynamically with the adsorption of hematite NPs from approximately -100 mV to -600 mV, which is consistent with the changes of zeta potential measured by electrophoresis. These findings will lead to a deeper understanding of the biological impacts from exposure to NPs and allow us to better interpret the nanotoxicity.

6.2. Introduction

The remarkable properties that distinguish nanoparticles (NPs) from their bulk counterparts have promoted the rapid development of nanotechnology *(1)*. At the same time, the same properties raise the concerns about biological, ecological, and health effects that may lead to unexpected consequences when NPs enter the environment *(2-5)*. The small size of NPs has been reported to induce various biological effects: e.g., accumulation of NPs on cell surfaces *(6, 7)*, loss of cellular mobility *(1, 8)*, membrane translocation *(9, 10)* and DNA damage *(11-13)*. Some of these biological effects were observed with microorganisms *(7, 14, 15)*, which are present in the natural environment *(14)*, wastewater treatment plants *(16, 17)*, and the human digestive system *(18)*.

Surface interactions of NPs with cells begin with adsorption, a common interfacial phenomenon *(19, 20)*, and NP adsorption has been demonstrated on bacteria *(7, 14)* and the intestinal epithelium *(21)*. Whether or not adsorption occurs spontaneously is largely determined by the total interaction energy between the two approaching surfaces *(22, 23)*, which can be described by the Extended Derjaguin−Landau−Verwey−Overbeek (EDLVO) theory for biological systems *(24, 25)*. According to this theory, repulsive (or positive) energy acts as a barrier preventing adsorption, whereas attractive (or negative) energy allows adsorption *(24, 25)*.

Once adsorption begins, its kinetics is governed by factors such as the interaction energy barrier, concentrations of adsorbent and adsorbate, diffusivity, hydraulic conditions, and temperature. Several earlier studies *(26-28)* modeled colloidal adsorption employing first-order kinetics *(28)*. The temperature dependency of the adsorption rate constant was reported to have an Arrhenius form according to the interaction force boundary layer (IFBL) theory *(27, 29)*, and the activation energy in the Arrhenius form could be replaced by the interaction energy obtained from EDLVO theory *(30)*. If this relationship holds, a connection between the thermodynamic total interaction energy and adsorption kinetic rate can be established by linking EDLVO and IFBL theories *(31, 32)*. This approach was widely used to predict adsorption rate constants of many colloidal systems *(29, 33-35)* and to obtain insight into adsorption processes.

Studies on the adsorption of engineered NPs on cell surfaces are scarce, and the quantitative investigation of particle adsorption kinetics is almost untouched. One exception is the work of Wilhelm et al. *(36)*, who established a pseudo-first order kinetic model for NP binding on cell surfaces (described as Langmuir adsorption at equilibrium). Other groups employed the same kinetic model to examine the interactions of NPs with human cells *(21, 37)*. While an important step, the pseudo-first-order model does not reveal mechanisms, and human cells are different from bacterial cells. Thus, the need to advance mechanistic modeling for NP adsorption to bacterial cells is evident. One goal of this study is to extend the EDLVO and IFBL theories to the adsorption of NPs onto bacteria, which is a pivotal first step towards knowing of the fate, transport, and biological effects of nanomaterials in the environment.

I used hematite (α-Fe_2O_3) NPs as the adsorbate in adsorption experiments onto *Escherichia coli* (*E. coli*) cells as the adsorbent. Hematite NPs are the most stable form of iron oxide and are increasingly used in bio-applications such as cell targeting bioconjugates *(38, 39)*. More importantly, hematite NPs are a reference nanomaterial for

mirroring the properties of many other metal oxides *(24, 40)*, which are the most relevant to engineered NPs and of major interest *(40-42)*. *E. coli* cells are representative microorganisms widely used in toxicological tests for nanomaterials *(7, 14, 15)*. Studying the interactions of NPs with *E. coli* cells also could lead to a means of rapid toxicity screening.

Here, as the first step of the study I investigate the adsorption of different sizes of lab-synthesized hematite NPs on *E. coli* cells to reveal the size-dependent behavior of NPs toward biological interface, which is of great interest *(43-47)*. The total interaction energy was estimated using EDLVO theory, and then was combined with the IFBL theory to calculate the adsorption rate constant, and compare it with the experimental data of adsorption kinetics. The over-arching aim is to elucidate the fundamental mechanisms controlling size effects of NPs on their adsorption thermodynamics and kinetics with microbiological systems.

Much evidence has indicated interactions (e.g., adsorption) between NPs and cell surfaces are force-driven processes *(48-50)*. In particular, adhesion of NP aggregates to the exoskeletons of the test organisms was reported to cause physical effects and loss of mobility *(1, 8)*. Lovern et al. (2007) observed significant changes in *D. magna* behavior when it was exposed to lowest observed effect concentration for 48 h ($LOEC_{48\ h}$) levels of NP suspensions (TiO_2, C_{60} and a C_{60}-derivative) *(51)*. Typically, interactions of NPs with cell surfaces are dictated by surface properties such as presence of chemical functionalities, surface roughness, and surface array alignment of the interacting components *(52)*. Clearly, there is a need to understand the impact of NP surface properties with respect to their interactions with organisms and also to harness the knowledge to create environmentally benign nanomaterials.

Atomic force microscopy (AFM) is not only a powerful tool for high resolution imaging but is also used to probe interaction forces in a mode known as force

spectroscopy *(53, 54)*. This is widely used for variety of applications of surface interaction force measurements. The high adhesion force between NPs and biological surfaces may facilitate the accumulation of NPs on the cell surface and thus expose cells to high concentrations of NPs *(55-57)*. However, to measure NP interactions with *E. coli* cells using AFM, two contact surfaces, including an immobilized *E. coli* cell-coated cantilever probe surface and a NP-coated substrate surface, need to be created *(53)*. Conventionally, fixing microorganisms on the micro-sized probes involves working with a micromanipulator. Effective immobilization techniques must position the cells stably to probe forces in liquid environments, and ideally they maintain the original structures of the cells. Common techniques include mechanical trap *(58, 59)*, direct glue method with commercial adhesive (i.e., epoxy and formaldehyde resins) *(60)*, and chemical covalent functionalization of the probe using positively charged polymer coatings such as polyethyleneimine (PEI) and poly-L-lysine (PLL) *(61-64)*. However, these chemical treatments for bacteria may lead to various defects in the soft envelopes which may cause bacteria to shrink or swell and change in the Young's modulus and other elastic properties *(65-67)*. These changes may in turn influence their interation forces with NPs.

In second step of this study, the interaction forces between *E. coli* cell surfaces and two types of NPs (hematite (α-Fe_2O_3) and corundum (α-Al_2O_3)) with different sizes are investigated. *E. coli* cells were used because they are a typical bacterium widely used in toxicological studies *(15)*, and have been extensively studied with AFM with a focus on surface properties and interaction forces *(68)*. Hematite and corundum NPs were chosen because they both have stable, distinct size distributions. Moreover, they are both widely used as reference particles in colloid studies *(40, 69-71)*. Therefore, their interactions with living organisms in aquatic systems may be a considerable and a good starting point for studying the nano-bio interactions. To better understand the size effects on their interactions with *E. coli* cells, AFM in contact mode was used to measure the interaction

forces between immobilized *E. coli* cells and immobilized NPs. Interaction forces during the cycle of approach-contact-retract from the cell surface were compared for different sizes of NPs. Finally, to interpret the size effects, particularly those on adhesion force during the retraction after the contact, a modified model was developed by considering the local effective contact area with reference to the plane contact area in the Johnson-Kendall-Roberts (JKR) model *(72)*.

Surface interactions clearly play important roles in where NPs localize as well as whether they alter cell surface structures and cause interfacial property changes *(19)*. Such changes would determine if the binding of NPs with functional groups (i.e. transmembrane proteins) on cell surfaces are reversible or irreversible, adverse or not *(73)*. Extensive *in vitro* and *in vivo* toxicological studies have been carried out on various commercial NPs *(74-78)*. However, these studies may not precisely resolve the true nanoscale interactions because uncontrolled aggregation in culture medium may shift the properties of NPs far beyond the nanometer level *(19, 79)*. New detection tools such as AFM are needed to better understand the interfacial property changes of the interacting entities at the nanoscale *(69)*.

As the third step, Kelvin-probe force microscopy (KFM), an electrical mode of AFM with the unique ability of surface potential measurement *(80)*, was used in this study to map surface heterogeneities and examine the nano-electrical properties of hematite (α-Fe_2O_3) NPs and *E. coli* cells and the changes in cell properties after exposure to hematite NPs. The surface potential provides information complementary to topographical and phase images that allow us to distinguish NPs from their interacting components. Surface potential by KFM measures the absolute or intrinsic surface potential (contributed by the permanent surface groups, i.e, ≡Fe-O) of sample surfaces under low humidity *(81)*. Thus, due to the different surface compositions, KFM can potentially distinguish the interacting entities based on their unique surface potentials *(82,*

83). Moreover, surface potential is an important parameter in Poisson-Boltzmann equation for the calculation of electrostatic interaction *(84-87)*. An accurate measurement of surface potential enables us to precisely determine the electrostatic interactions between NPs and cells, which is one of the governing forces for interparticle and particle-cell interactions in aqueous environments. Thus, KFM may provide us a unique tool for studying the nano-bio interactions as well as the interfacial phenomenon in the environment.

Details about the operation principle of KFM are introduced in section 8.3.2 of chapter 8. Briefly, the electrostatic forces between the probe and various regions of the sample are detected to reveal the local mechanical and electromagnetic properties *(88)*, such as surface charges, doping levels, or dielectric constants *(89, 90)*. Recent work demonstrated that KFM has the capability to measure the surface potential of organic molecules, including organosilane self-assembled monolayers (SAMs) terminated with different functional groups *(91)*, conjugated polymer thin films *(92)*, and other organic materials (e.g., perfluoroalkyl alkanes) *(88)*. However, few KFM studies examine the interactions of NPs with biological systems. Thus, we explored the applicability of KFM in studying nano-electrical properties via surface potential measurements at the nanoscale and cellular levels. The dynamic adsorption of hematite NPs onto *E. coli* cells in an aqueous environment was visualized by KFM. Topographical, surface potential, and phase images were acquired simultaneously and used to investigate the impact of exposure on cellular morphology and surface potential. A correlation between surface accumulation of hematite NPs and surface potential changes is demonstrated. To our knowledge, this is the first use of KFM as an imaging and quantification tool for studying surface interactions between NPs and live cells.

6.3. Materials and Methods

6.3.1. Hematite and corundum NPs

The same water suspension of hematite NPs were used in this study and the detailed information about synthesis were previously introduced in chapter 6. Corundum NPs (Nanostructured & Amorphous Materials Inc., Houston, TX, USA) were dispersed in DI water (to a concentration of approximately 100 g/L) and sonicated for 20 min at 45 W. Before immobilization, the glass cover slips (2-cm×2-cm) were soaked in $H_2O/CrO_3/H_2SO_4$ (42:29:29 wt %) for 24 h and then rinsed with DI water.

Hydrodynamic diameters of dispersed NPs in DI water and in phosphate-buffered saline (PBS, 200 mM, pH 7.2) were determined by a dynamic light scattering (DLS) instrument (Malvern Instruments Zetasizer Nano ZS instrument). The concentration of hematite NPs in suspension was determined by an Induced Coupled Plasma-Optical Emission Spectrometry (ICP-OES, Thermo iCAP 6300, USA). Liquid samples were digested with trace metal grade nitric acid (Fisher Scientific, Suwanee, GA) on a 150^{o}C hot plate *(40)*. In all samples, Fe concentrations were monitored, and the concentration of hematite NPs was expressed mg/L as ferric ion.

6.3.2. Characterization of hematite NPs with TEM

Morphological characterization of hematite NPs was determined by transmission electron microscopy (TEM). 2.5 µL of the liquid suspension of hematite NPs was dropped on a copper grid (400-mesh size) coated with a carbon film (Ted Pella, Redding, CA). A TOPCON 002 B model TEM was operated at an accelerating voltage of 160 kV, and images were acquired at the same magnification of 60,000.

6.3.3. Cultivation of E. coli cells

E. coli K-12 cells (strain D21) were purchased from the *E. coli* Genetic Stock Center (Department of Biology, Yale University, New Haven, CT). The cells were

cultured in standard Luria-Bertani (LB) Medium at 37^{o}C overnight and were harvested in the stationary growth phase with the cell density of approximately 2×10^{9} cells/mL *(93)*. The harvested cells were washed three times with PBS (20 mM, pH 7.2) and finally were resuspended in 300 μL of 1 mM Tris buffer solution *(94)* with a cell concentration of approximately 1×10^{9} cells/ml.

6.3.4. Zeta potential measurement of hematite NPs and E. coli cells

Zeta potentials (ζ) of hematite NPs and *E. coli* cells dispersed in PBS also were measured by the Malvern DLS instrument. 0.8 ml of the liquid sample was injected into the folded capillary cell (DTS1060, Malvern Instruments). Refractive indices of 2.94 and 1.40 were used respectively for hematite NPs *(95)* and *E. coli* cells *(96)* for calculating the scattering wave vector.

6.3.5. Adsorption kinetics and adsorption isotherms

For adsorption kinetics and isotherm experiments, hematite NPs and *E. coli* cells were mixed in 15-ml Polystyrene centrifuge tubes. The centrifuge tubes were placed in a rotational shaker under 37^{o}C. Shaking was maintained under laminar flow conditions (200 rpm) with a Reynolds number of approximately 500 *(97)*. The total volume of the mixture suspension was 10 mL when filled with suspensions of *E. coli* cells, hematite NPs, and PBS (20 mM, pH 7.2). The concentration of *E. coli* cells in PBS was approximately 1×10^{8} cells/mL by diluting the *E. coli* cell stock suspension. The final concentrations of hematite NPs for different sizes were 100 mg/L in [Fe^{3+}]. pH (7.2 ± 0.2) was achieved in all the suspensions. Control experiments to examine the effect of centrifugal separation on hematite concentrations in the bulk liquid were conducted by dispersing hematite NPs in PBS without adding *E. coli* cells.

Adsorption kinetics was studied by monitoring the decrease in the concentration of the suspended hematite NPs in the bulk liquid. To distinguish the suspended hematite

NPs from the adsorbed portion on *E. coli* cells, *E. coli* cells (with or without adsorbed NPs) were separated from the suspended hematite NPs in the supernatant through centrifugation for 10 min at 1000 × g. The optimization of this centrifugation method was based on a previous study *(98)*.

To determine adsorbed mass of hematite NPs, 0.5 mL of liquid sample suspension was collected from the supernatant of each tube after the centrifugation and analyzed with ICP-OES. The changes in [Fe^{3+}] in the liquid samples were used to indicate the adsorption of hematite NPs on *E. coli* cells. All experiments were repeated three times, and the standard deviations were calculated based on the data from these triplicate experiments.

6.3.6. Adsorption rate calculation with the combination of EDLVO and IFBL theories

According to IFBL theory, the particle adsorption rate can be as approximated by *(27, 97, 99)*:

$$\frac{d\Gamma}{dt} = k_a C_w \tag{1}$$

where Γ is the adsorbed number of NPs per unit cell surface (#/m^2), $\frac{d\Gamma}{dt}$ is the adsorption rate in the adsorbed number per unit surface area per time (#/(m^2 s)), t is the adsorption time (s), C_w is the effective wall concentration (in units of #/L) that is describe below, and k_a is the adsorption rate constant (m/s), which can be expressed as *(100)*:

$$k_a = \frac{ID_\infty}{\int_{D=D_0}^{D=\delta_{IFBL}} [(1+\frac{R_H}{D})\exp(U_{HwE}^{TOT-EDLVO}(D)/k_BT)-1]dD} \tag{2}$$

where ID_∞ is the diffusion coefficient of NPs in the bulk (m^2/s), δ_{IFBL} is the thickness of the interfacial force boundary layer (nm) and 100 nm was used in this study *(97)*, R_H is

the hydrodynamic radius of NPs (nm), D is the interation distance (nm), k_B is Boltzmann constant (1.38×10^{-23} J/K), T is the absolute temperature (298 K), and U_{HwE}^{TOT} is the total interaction energy determined from EDLVO theory. The detailed equations are previously shown in chapter 3.

The diffusion coefficient (ID_∞) of hematite NPs, not *E. coli* cells, was incorporated into Eq. (2), because when the small-sized NPs are transported towards the cell surfaces, the diffusion of hematite NPs is the limiting factor the adsorption kinetics *(7, 14)*. Particle diffusion coefficient can be calculated using the Stokes-Einstein equation:

$$ID_\infty = \frac{k_B T}{6\pi\mu R_H} \tag{3}$$

where μ is the dynamic viscosity of the medium and 1.0×10^{-3} Pa s was used for PBS at 25 ^{o}C.

C_w, the effective wall concentration, is an average local particle concentration within the IFBL, as shown in Figure 6.1. According to IFBL approximation, particles are irreversibly bound to the surface so that the particle concentration at the surface wall can be treated as being zero. Thus, the rate of adsorption is proportional to C_w only. Clearly, it is difficult to determine C_w experimentally; therefore, we treated C_w as a fitting parameter in the modeling analysis.

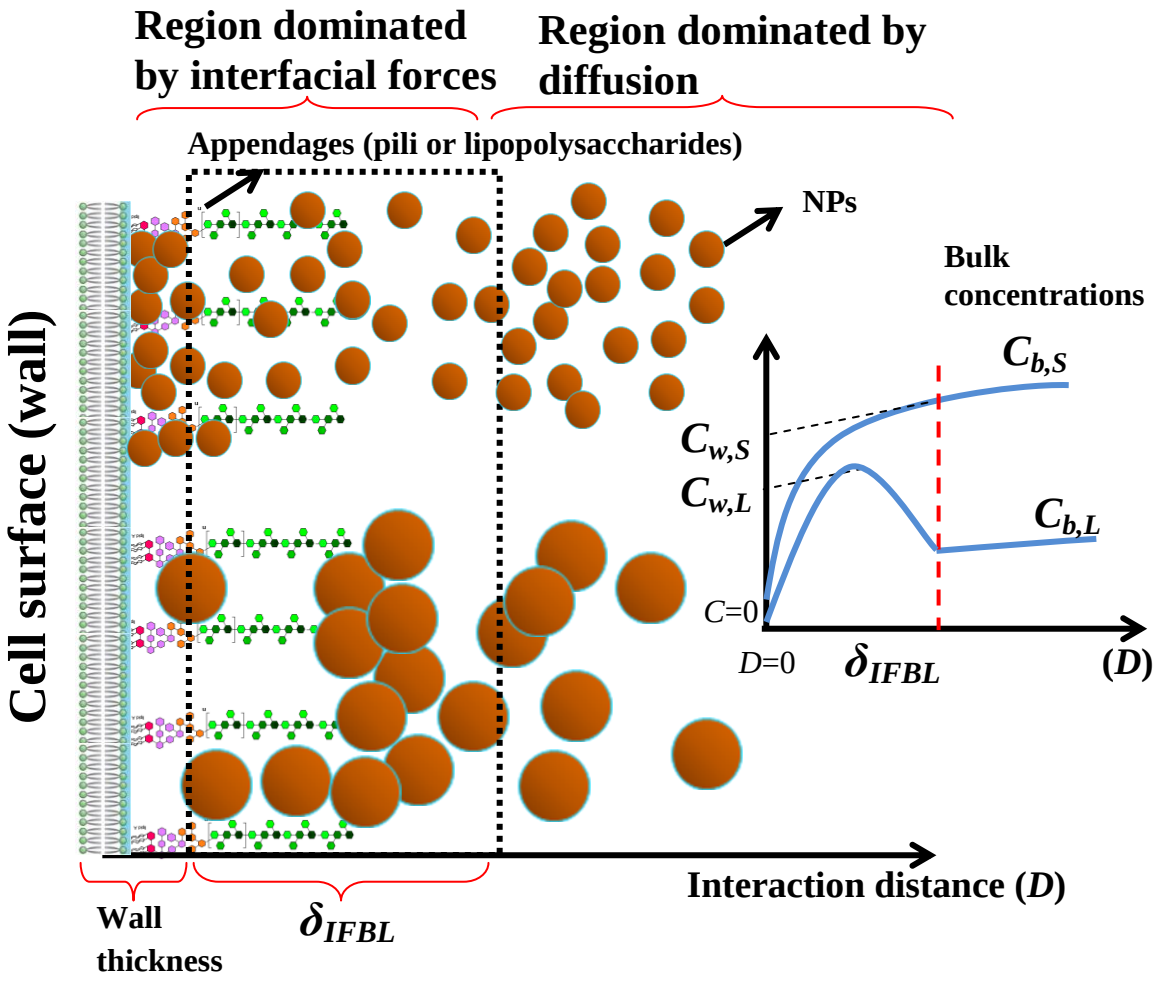

Figure 6.1. Conceptual model of particle adsorption based on IFBL theory. The inset shows two possible transient concentration profiles (the blue dashed curves) of small-sized (*S*) and large sized (*L*) NPs as a function of the separation distance (*D*) from the cell surface and the effective wall concentrations (C_w), which are illustrated as the local particle concentrations within the black dotted box of the IFBL.

6.3.7. Immobilizing E. coli cells on the probe

A common protocol was employed for *E. coli* cell immobilization on gelatin-treated cantilever probes *(64)*. Gelatin solution was prepared by dissolving 0.5 g of gelatin (Sigma, G6144) and 10 mg of chromium ammonium sulfate (Alfa Aesar, CAS# 10022-47-6) in 100 ml DI water at 60^{o}C. After cooling to 40 ^{o}C, the cantilever probes were immersed into the gelatin solution (2.5 µL) for 2 min and allowed to air dry. To obtain better immobilization, silicon nitride V-shaped cantilever probes were first examined for any defects under an optical microscope and then were rinsed with nanopure deionized (DI) water and ethanol (70%). The probes were then soaked for 5 min in acetone and irradiated for 15 min under a 254 nm UV light (UVP, UK). Finally, probes were rinsed with DI water again and stored at 4 ^{o}C.

A pellet of concentrated cells (approximately 10^{-5}~10^{-6} µl cell suspension) was manually transferred using a Si-Al filamentous tube to the side of the gelatin-treated cantilever probe with a micromanipulator (Eppendorf Transjector 5246). Treated probes were allowed to stand for 2 min and then gently rinsed with DI water to remove any loosely attached cells. The probes were used for force measurement in a liquid cell immediately after the immobilization process. The immobilization of *E. coli* cells was examined by scanning electron microscopy (SEM, FEI XL30 EFSEM) with an acceleration voltage of 25 kV.

6.3.8. Immobilizing NPs on the glass cover slip surface

One drop of the suspension of NPs at the mass concentration of approxiamtely 1 g/L was placed on the center of the cover slip, which was then placed in a vacuum dryer at room temperature for 24 h; this slow drying allowed tightly packed layers of NPs to form. The NPs immobilized on the cover slip surface were examined by AFM.

6.3.9. Imaging and interaction force measurement with AFM

An Agilent 5500 AFM (Molecular Imaging, Phoenix, Arizona, USA) was used for imaging the surfaces immobilized with NPs in acoustic alternating current (AAC) mode and the interaction forces were measured in contact mode. Alumina reflex coated silicon probes (Tap300Al, Budgetsensors. USA) were used for imaging the topography of the NPs immobilized on the cover slip in DI water (pH = 6.0 ± 0.3) with a scanning speed of 2000~5000 nm/s, a drive frequency of 8 kHz, and a drive amplitude of 0.1 V *(101).* Silicon nitride (Si_3N_4) V-shaped tipless cantilever probes with gold reflex coating (Model NP-0, Veeco Instruments Inc. USA) were used to measure the force between immobilized-*E. coli* probes and NP array surfaces in phosphate buffer solution (PBS, 200 mM, pH = 7.2 ± 0.2). At least three cantilever probes were used for each sample with 10 to 15 force measurements at two or three contact locations per cantilever probe. The initial deflection was set -1.2 ± 0.1 V with setpoint of 0 V. A force-distance curve (translated from a deflection (V) versus piezo position (nm) curve) was generated for each cycle, which included approaching the NP surface with the cantilever probe, contacting the surface, and retracting from the contact. Deflection (V) was converted to force (nN or pN) according to Hooke's law: $F = K_{sp}d$, where d is the cantilever deflection displacement (nm) and K_{sp} is the cantilever spring constant (0.06 ± 0.02 nN/nm, determined by the Agilent Thermal K tuning modulus; see Agilent 5500 User's Guide for details) *(102).*

6.3.10. KFM study on the surface properties of hematite NPs and E. coli cells

The mode of KFM was operated on an Agilent 5500 AFM (Molecular Imaging) equipped with a MAC III unit, which has three lock-in amplifiers (LIA) enabling multi-frequency measurements. LIA 1 was used for topography imaging during intermittent contact, which was performed at the first flexural resonance of the probes ω_{mech}, and LIA 2 was used for KFM, providing AC and DC voltages to the probe and detecting the

electrostatic response either directly from the photodetector (AM-AM) or from LIA 1 (AM-FM). Pt-coated silicon cantilever probes (Olympus AC240TM, Japan) with a force constant of approximately 2-5 N/m and a nominal resonance frequency of 70 kHz were used. An AC bias voltage of 2 V at a frequency of 70 kHz was applied between the probe and sample, and the DC bias was set at a frequency of 5 kHz. During KFM, the microscope is fully contained in an environmental chamber that is used to control ambient pressure, temperature (25 ± 2 ^{o}C), and humidity (approximately 10%) as measured by a VWR® humidity/temperature thermometer).

For KFM analysis, 0.5 µl of hematite NP stock suspension was deposited on a clean, undoped (N-type) silicon wafer (Sigma-Aldrich) with surface orientation (100) that was cleaved to small pieces of approximately 3 mm × 8 mm. After air drying for approximately 1 min, the silicon chip was then ready to be placed on the AFM. However, the concentration of *E. coli* cells deposited and the sample drying time dramatically influence the image quality and how much cell ultrastructure can be observed. Thus, these two factors were investigated to determine optimal conditions that yield good image quality as well as maintain the original morphology of *E. coli* cells. Briefly, the optimized operation is as follows: after exposing *E. coli* cells to hematite NPs for various periods, a 100-µl liquid sample was taken from the center of the test tube and diluted in 1 ml PBS to make the concentration of *E. coli* cells approximately 10^9 CFU/ml. Then 0.5 µl of the diluted suspension was deposited on a clean silicon wafer and placed on a 37 ^{o}C hotplate to dry for approximately 15 min. The silicon wafer was finally fixed on a small piece (1 cm × 1 cm) of conductive double sided tape (Ted Pella, USA), which was placed on a grounded microscope stage for KFM study. Topography, phase, and surface potential images were obtained simultaneously.

6.4. Results and discussion

6.4.1. Characterizations of hematite NPs

Figure 6.2a~d show the particle size distribution (PSD) diagrams of hematite NPs with four different sizes (26, 53, 76, and 98 nm) dispersed in DI water and PBS. The peak intensities in the PSD diagrams corresond to the mean hydrodynamic diameters. With polydispersivity indexes (PDIs) less than 0.25, hematite NPs were monodispersed without significant aggregation or sedimentation *(103)*. The PSD diagrams also show the dynamic changes in size distribution over time (from 30-90 min) for hematite NPs in PBS, which were minor for each size. Most commercial metal-oxide NPs tend to aggregate in the liquid *(40)*, whereas our hematite NPs exhibited stable PSDs in PBS, making them ideal nanomaterials for this study.

Figure 6.21e~h shows the TEM micrographs for hematite NPs. The NPs of each size were close to spherical in shape and had a relatively uniform size distribution. The sizes measured from the TEM images are consistent with the measurements from DLS, but slightly smaller because DLS measured the hydrodynamic sizes, which include the bound water layer thickness *(40, 70, 95, 104)*.

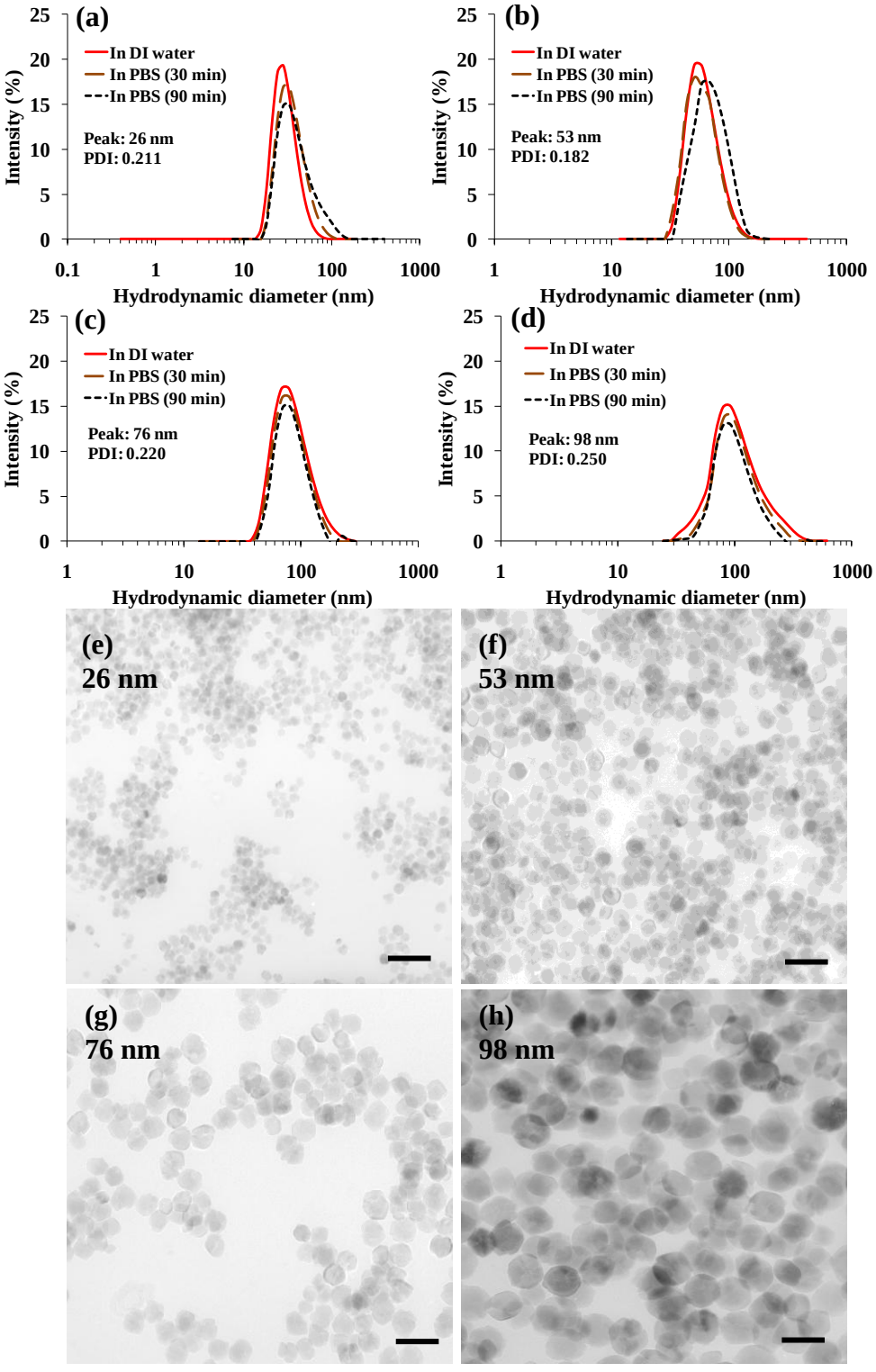

Figure 6.2. (a)-(d) PSD diagrams of hemaite NPs in DI water and PBS with a concentration of 100 mg/L. (e)-(h) TEM micrographs of hematite NPs with four different sizes. The black scale bars at the bottom right are equal to 100 nm.

6.4.2. Adsorption kinetics of hematite NPs on E. coli cells

Figure 6.3 shows the adsorption kinetics for each size of hematite NP. The rate of concentration drop for the NPs (as $[Fe^{3+}]$) was in the order 98 nm > 76 nm > 53 nm > 26 nm. Thus, large NPs (98 and 76 nm) reached pseudo-adsorption equilibrium faster (approximately 30~40 min) than small NPs (approximately 60-90 min) and without obvious desorption afterwards. Figure 6.3 shows that the NP concentrations in the control groups were almost constant over the 90-min adsorption experiments. This indicates that centrifugation did not significantly remove suspended hematite NPs from the supernatant.

Figure 6.3b shows the adsorbed number of hematite NPs per unit surface area of *E. coli* cells at different adsorption time; it was calculated based on Eq. (4):

$$\left(\frac{\Delta N}{S}\right)_t = \frac{(C_i - C_t) - (C_i - C_{C,t})}{S \cdot 0.7 \cdot \rho \cdot \left(\frac{4\pi}{3} R_H^3\right)} V \qquad (4)$$

where $\left(\frac{\Delta N}{S}\right)_t$ is the number of adsorbed hematite NPs per unit area of cells (m^{-2}) at adsorption time *t*, $(C_i - C_t)$ is the overall concentration changes of hematite NPs during adsorption, $(C_i - C_{C,t})$ accounts for the small concentration decrease due to the centrifugal separation, *V* is the suspension volume (10 mL), and *S* is the available surface area of *E. coli* cells (0.024 m^2), ρ is the density of hematite NPs (5.3 g/cm^3), and 0.7 is the mass ratio of Fe in the chemical formula $[Fe_2O_3]_n$ ($(2\times56)/(2\times56+3\times16)= 0.7$). Figure 6.3b shows that small NPs had faster adsorption kinetics than large NPs when expressed as the number of NPs adsorbed onto a unit cell surface. This number-based trend is the opposite the mass-based trend in Figure 2a, which is consistent with our previous finding with hematite NPs and a human intestinal cell line (Caco-2) *(21)*.

The faster number-based adsorption rates for small NPs are consistent with the adsorption isotherms, which are shown in Figure 6.4. The product of the adsorption affinity (α) and the maximum adsorption (C_{max}) was much higher for small NPs than for larger NPs based on the fit results using the Langmuir isotherm. Thus, α, C_{max}, or both were higher for small hematite NPs when adsorbing to *E. coli* cells as shown in Table 6.1. Small NPs were previously found to pierce and penetrate cell membrane faster than did large NPs *(21, 44, 105)*. Faster number-based adsorption rates of small NPs may be a factor in their faster toxicokinetics.

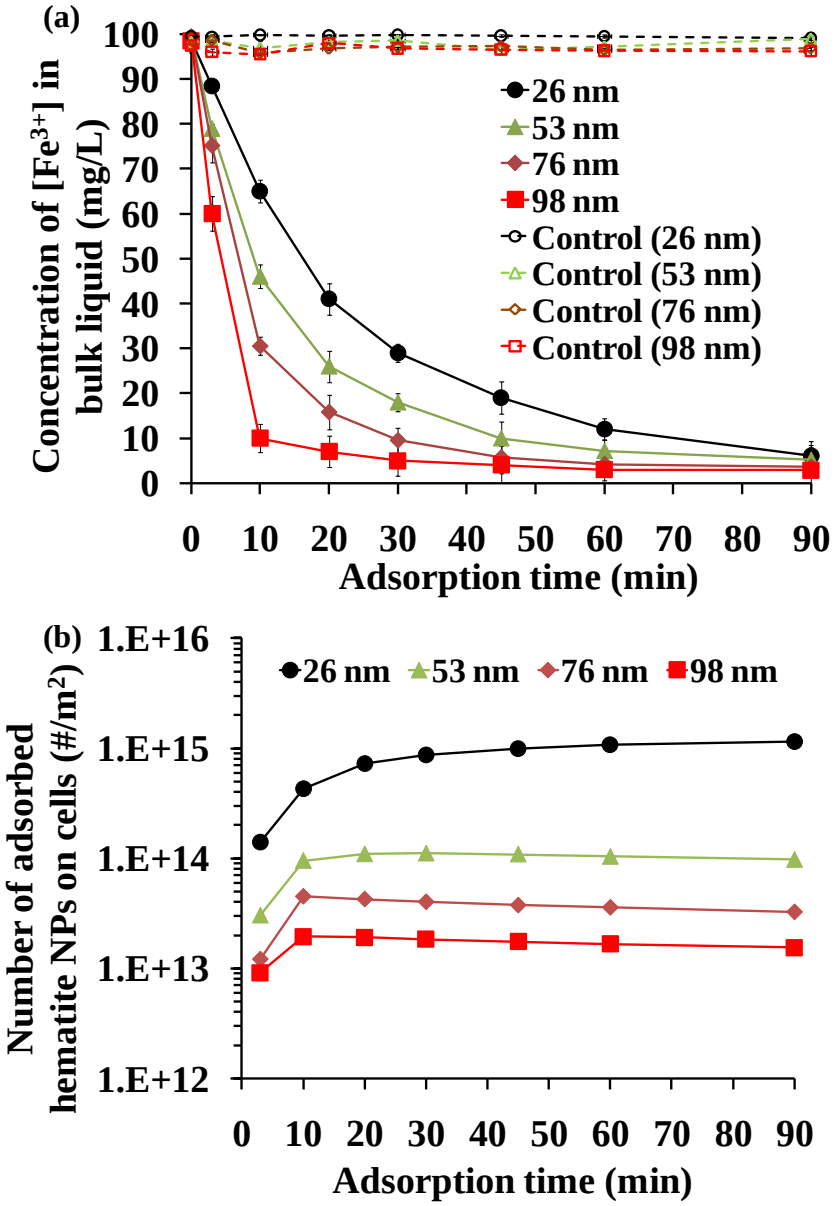

Figure 6.3. (a) The mass concentrations in [Fe^{3+}] of different sizes of hematite NPs in the bulk liquid. All data points are averages from triplicate data, and error bars represent one standard deviation. When error bars are not visible, they are small and hidden behind the data symbols. (b) The number of adsorbed hematite NPs on unit surface area of *E. coli* cells.

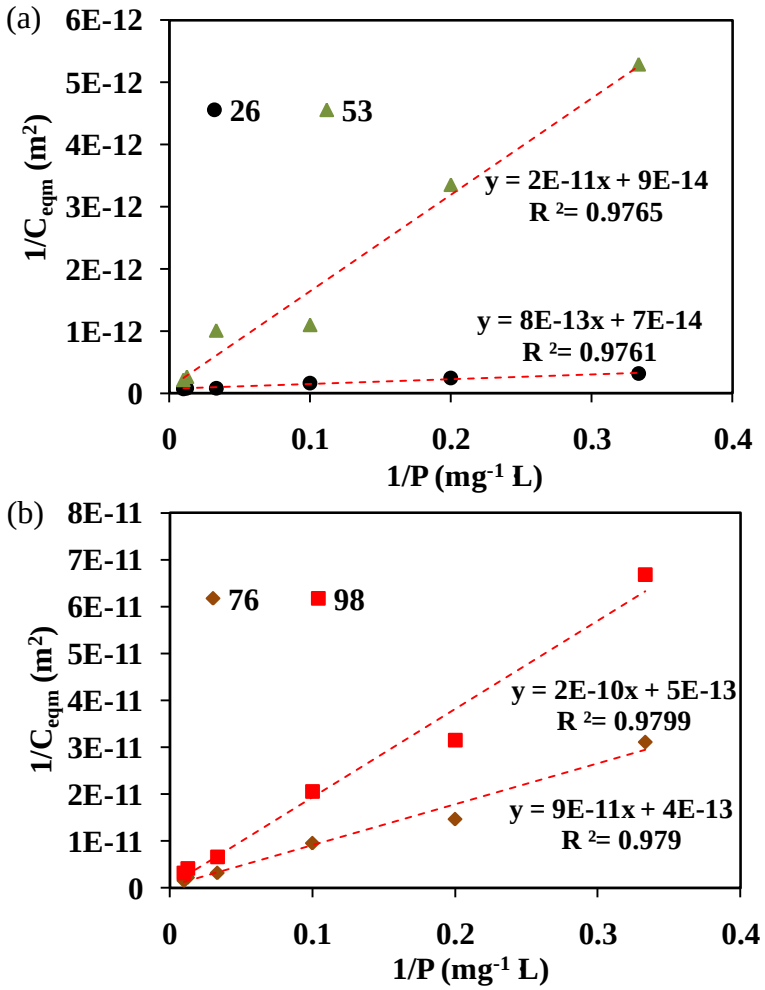

Figure 6.4. Adsorption isotherms fit with the linearized Langmuir isotherm equation for hematite NP sizes of (a) 26 and 53 nm, and (b) 76 and 98 nm. The red dashed lines are Langmuir fit curves, and the fit equations are shown as inset to the right of each curve.

Table 6.1. Langmuir constants associated with Figure 6.4.

Diameter (nm)	$1/(\alpha \cdot C_{max})$ (mg L^{-1} m^{2})	C_{max} (m^{-2})	α (mg^{-1} L)
26	8×10^{-13}	1.4×10^{13}	0.088
53	2×10^{-11}	1.1×10^{13}	0.005
76	9×10^{-11}	2.5×10^{12}	0.004
98	2×10^{-10}	2.0×10^{12}	0.003

6.4.3. Interaction energy between hematite NPs and E. coli cells

Adsorption is an interfacial interaction that is mediated by the balance between interparticle forces arising from a combination of van der Waals, electrostatic, and acid-base forces *(24, 25)*. Thus, this section compares the thermodynamics for particle adsorption based on EDLVO theory. van der Waals and acid-base components are readily calculated, where surface hydrophobicity of hematite NPs and *E. coli* cells was considered for calculating the Hamaker constant and standard acid-base interaction energy. For calculating electrostatic force, zeta potentials of different sizes of hematite NPs and *E. coli* cells were measured and are shown in Table 6.2, which are comparable to the values from previous studies *(40, 106)*. Other surface properties, such as particle roughness, surface charge heterogeneity, and polymer content, also may affect the interaction energy *(23, 107)*, but their effects have not been quantitatively represented in the EDLVO theory *(108)*. Thus, I did not include these factors.

The total interaction energies between hematite NPs and *E. coli* cells are shown in Figure 3. The total interaction energy for each size describes the variation of the interfacial energy as a function of the interacting distance when a single hematite NP approaches an *E. coli* cell. The inset in Figure 3 further displays the three components of interaction energies for 26 nm. van der Waals and electrostatic forces produce negative interaction energies and, thus, act as attractive forces *(23, 109)*. In contrast, the positive acid-base interaction energy presents repulsion due to the hydration force. Overall, each size of hematite NPs has a unique energy barrier during its approach toward *E. coli* cells, and larger NPs have higher energy barriers to overcome before they contact or adsorb onto the cells. The negative interaction energy at the secondary minimum, present at the distances of 2~4 nm for each size, may allow the adsorption of hematite NPs onto the cell surface and particle deposition at primary and secondary minimum may occur simultaneously *(33)*. However, the IFBL model considers NPs to be deposited only in the

primary minimum *(35)*, which implies that NPs predominantly adsorbed on the inner lipid membrane.

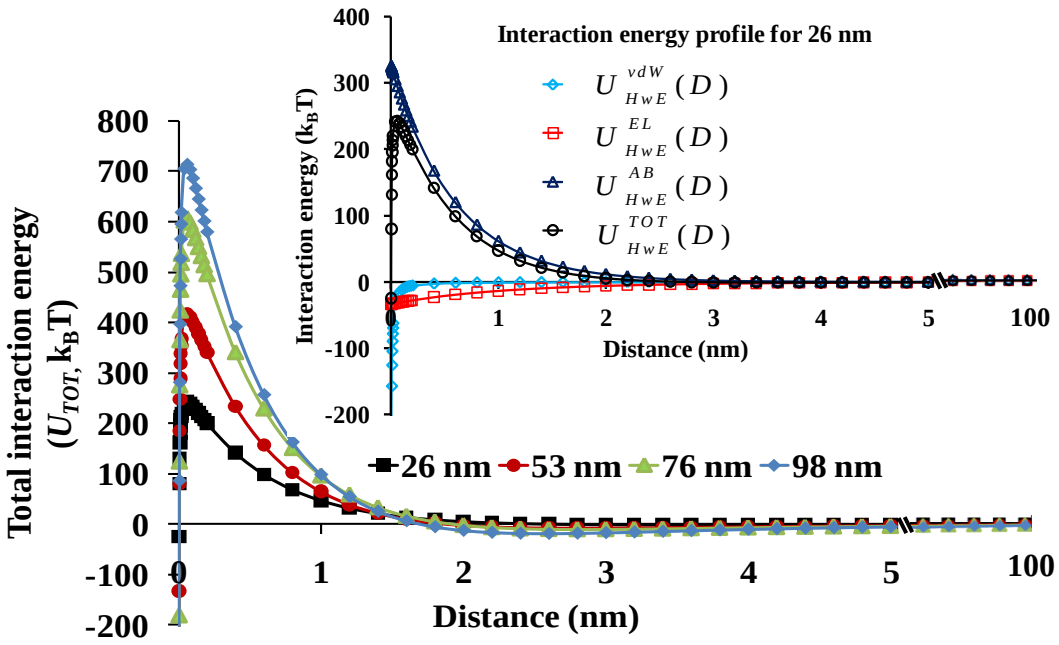

Figure 6.5. Total interaction energy between hematite NPs of four sizes and *E. coli* cells in PBS calculated from the EDLVO theory. The inset is a diagram showing the total interaction energy and the interaction energy components for 26 nm hematite NPs.

Table 6.2. ζ-potentials of hematite NPs and *E. coli* cells in PBS (20 mM, pH 7.2).

Diameter (nm)	26	53	76	98	*E. coli* cells
ζ (mV)	28.6 ±1.5	57.4 ±1.2	55.4 ±1.6	67.9 ±2.1	-29.0 ±1.3

6.4.4. Adsorption kinetics from experimental and model calculations

The experimental determination of adsorption rates was carried out by using the adsorbed number of NPs per unit cell surface $\left(\frac{\Delta N}{S \cdot \Delta t}\right)_t$, or the rate of change in adsorption density in $1/(m^2\ s)$. It was computed based on the results in Figure 6.3b by using Eq. (4) with both sides of the equation divided by time *Δt*. $\left(\frac{\Delta N}{S \cdot \Delta t}\right)_t$ values for different sizes are shown in Figure 6.6. The data points show the expected trend of declining adsorption rates with increasing adsorption time for all sizes of NPs; consistent with Figure 6.3b, the small NPs (26 and 53 nm) had up to 10 times higher adsorption rates than large NPs (76 and 98 nm). Accumulation of adsorbed hematite NPs likely increased the interaction energy barrier, which slowed the adsorption kinetics. A change in aqueous conditions (e.g., pH) also can affect the energy barrier and adsorption kinetics. However, the over-arching effect is that smaller NPs always have a lower interaction energy barrier and, thus, a higher adsorption rate than larger ones. Literature is available on how solution chemistry (e.g., salts or natural organic matter) influence the attachment efficiency of colloids *(35, 110)* on substrate surfaces. Similar trends are likely for adsorption of NPs. Therefore, this study employed PBS to avoid experimental problems while facilitating the modeling analysis of adsorption kinetics.

EDLVO and IFBL theories were joined to interpret the size dependence of adsorption rate. To use EDLVO-IFBL theories, the total interaction energies ($U_{HwE}^{TOT-EDLVO}$) for different sizes, shown in Figure 6.5, were entered in Eq. (2). Thus, adsorption rate constant (k_a) for different sizes of hematite NPs could be obtained, and the resulting k_a values are shown in Figure 6.7. As anticipated from Figure 6.3b, k_a decreased as particle size increased. The theoretical trend is a consequence of the decline of the diffusion coefficient and the increase of the energy barrier with increasing particle size according

to Eqs. (3) and (4).

Finally, we fitted the experimental data of adsorption rates with the IFBL model in Eq. (1) by using C_w as the fitting parameter. The best fit was achieved by minimizing the standard deviation of the following Objective Function (*O.F.*):

$$O.F. = \sqrt{\frac{1}{N-1}\sum_{i=1}^{N}\left(\frac{K_{\exp,i} - K_{cal,i}}{K_{\exp,i}}\right)^2} \tag{5}$$

where $K_{exp,i}$ and $K_{cal,i}$ are the experimental and calculated adsorption rates for a particular particle size (i) at a certain adsorption time, respectively, and N is the number of the data points. For our fit, *O.F.* was minimized by adjusting the value of C_w for each size and for different adsorption times. The fit values of C_w are shown in Figure 6.8a, and they are of the same order of magnitude as the number-based concentrations in the bulk liquid, shown in Figure 6.8b. Figure 6.6 shows that the model fit (the dashed lines) matched the experimental data. Model and experimental data indicate that adsorption rates exponentially declined with adsorption time and that small NPs had greater adsorption rates in units of #/(m^2 **s**) than for large NPs.

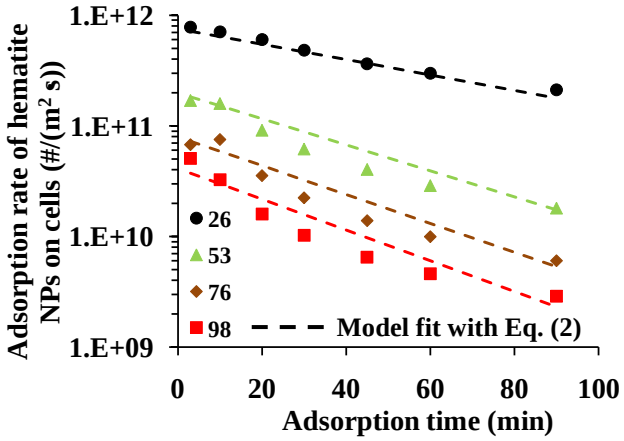

Figure 6.6. The data points with different shapes represent experimental average adsorption rates of different sizes of hematite NP. The dashed lines represent model calculations of adsorption rates.

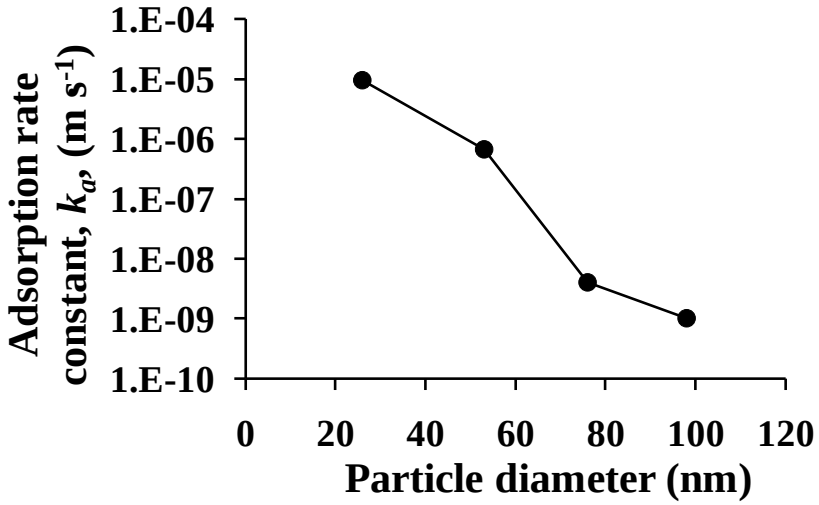

Figure 6.7. Absorption rate constants for different sizes of hematite NPs calculated with Eq. (3). The solid lines connect the points to aid visualization.

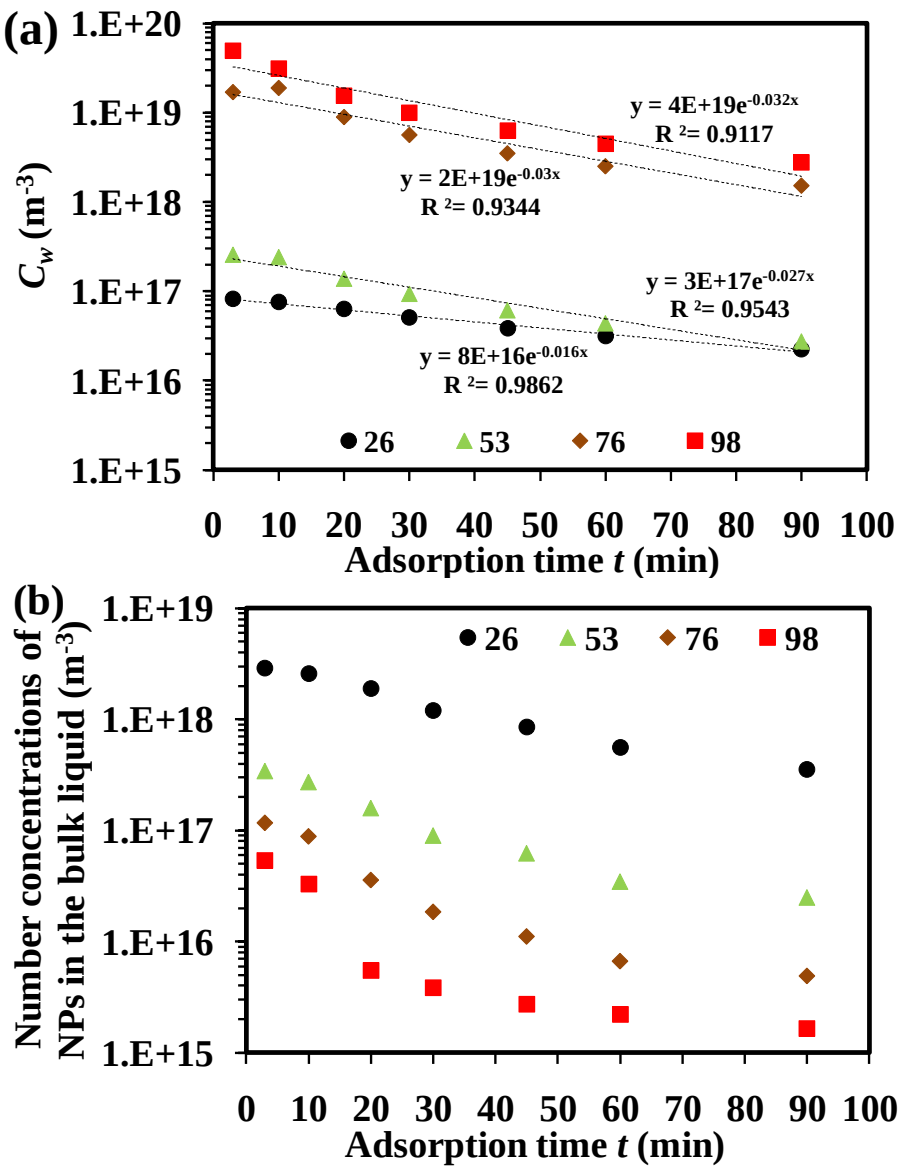

Figure 6.8. (a) The fit values of C_w for different sizes of hematite NPs over different adsorption times. (b) Number-based concentrations for different sizes of hematite NPs over different adsorption time.

6.4.5. E. coli cell-immobilized probe

Figure 6.9 shows SEM images of *E. coli* cells immobilized on the probe with a micropipette transferring a droplet of *E. coli* cell suspension on the probe end. During the AFM force measurement, precision and reproducibility were found to largely rely on two factors: a uniform layer of immobilized *E. coli* cells and consistent contact *(111)*. To make the *E. coli* cell immobilization uniform, the Si-Al filamentous tube was precisely aligned to the end of the probe and evenly spread a drop of the cell suspension on the cantilever probe, as shown in Figure 6.9.

To maintain a consistent contact with substrate surfaces, the immobilized *E. coli* cells need to fully cover all areas of the cantilever probe anywhere contact can possibly occur. However, currently measurement of the real contact areas between the probe and substrate surface is technically impossible *(53)*, as the area depends on factors such as the angle between the two contacting surfaces, the loading pressure, and the elastic properties of the cantilever. Thus, *E. coli* cells, rather than one, were immobilized on a relatively large area of the probe instead of being fixed on the very end of the probe. Measurement of the interaction force with a single cell is not suitable in this case because of potential bias and interference introduced from forces between the uncoated portion of the cantilever probe and the substrate surfaces. This effect is especially significant when measuring the adhesion force (the maximal rupture force used to separate the two contacting surfaces), which for a single cell is too small to be detectable by AFM, as observed by Kang, et al. *(67)*. Therefore, researchers tend to immobilize a bacterial layer rather than a single cell on the probe for interaction force measurement with AFM *(106, 112-114)*.

Maintaining the original structure and integrity of the bacterial surface is necessary to avoid artifacts and measure meaningful interactions *(67, 72)*. Thus, newly harvested *E. coli* cells were rapidly immobilized on a gelatin-treated probe, which was used for the

force measurements. Although the viability of the cells was not tested, our reproducible force measurements and the SEM images of the cell-coated probe after use (not shown here) indicated that the cells were in good shape in terms of surface properties and structural integrity. To reduce the surface damage to *E. coli* cells from the mechanical compression, low loading forces were applied *(111)*. By doing so, repeatable force measurements were eventually achieved.

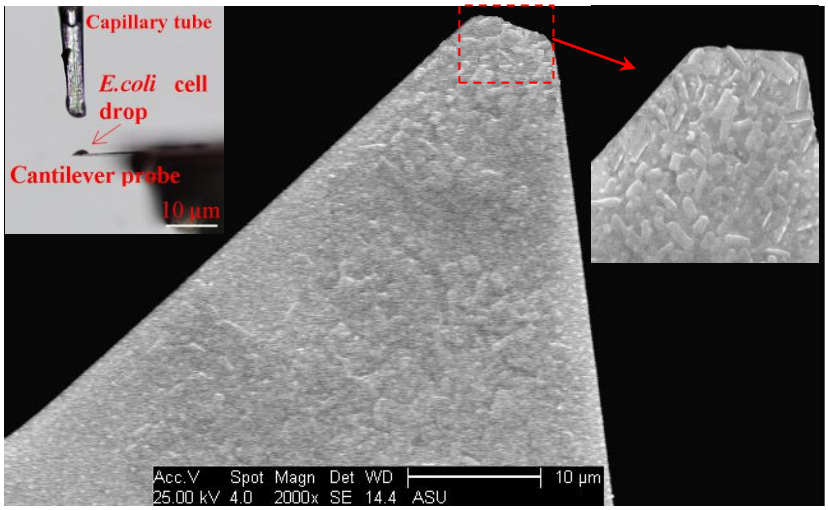

Figure 6.9. SEM image of a cantilever probe covered with immobilized *E. coli* cells.

6.4.6. Immobilized hematite NP-coated surface

The images in the left column of Figure 6.10 show that the five different sizes of hematite NPs evenly covered the glass cover slip surface. The NP layer was composed of tightly and closely packed NPs with a total thickness of 2.2 μm ~ 6.8 μm measured by AFM. Images of NPs on the glass surface were acquired by AFM before and after the force measurement. These NPs did not form aggregates, peel off, or dissolve in water during or after force measurements. To investigate the size effects on interaction forces, the built-in filter tool in the Agilent software (Picoview 5.3) was used to analyze the surface topography and roughness, which were different for different sizes of NPs (results are not shown here). These variations are roughly dependent on the sizes of the packed NPs and may contribute to differences in the interaction forces between different sizes of NPs and *E. coli* cell surfaces. The right column of Figure 6.10 presents TEM images of each size of NPs showing the morphology of our lab-synthesized hematite NPs, which were spherical in shape and had a uniform size distribution.

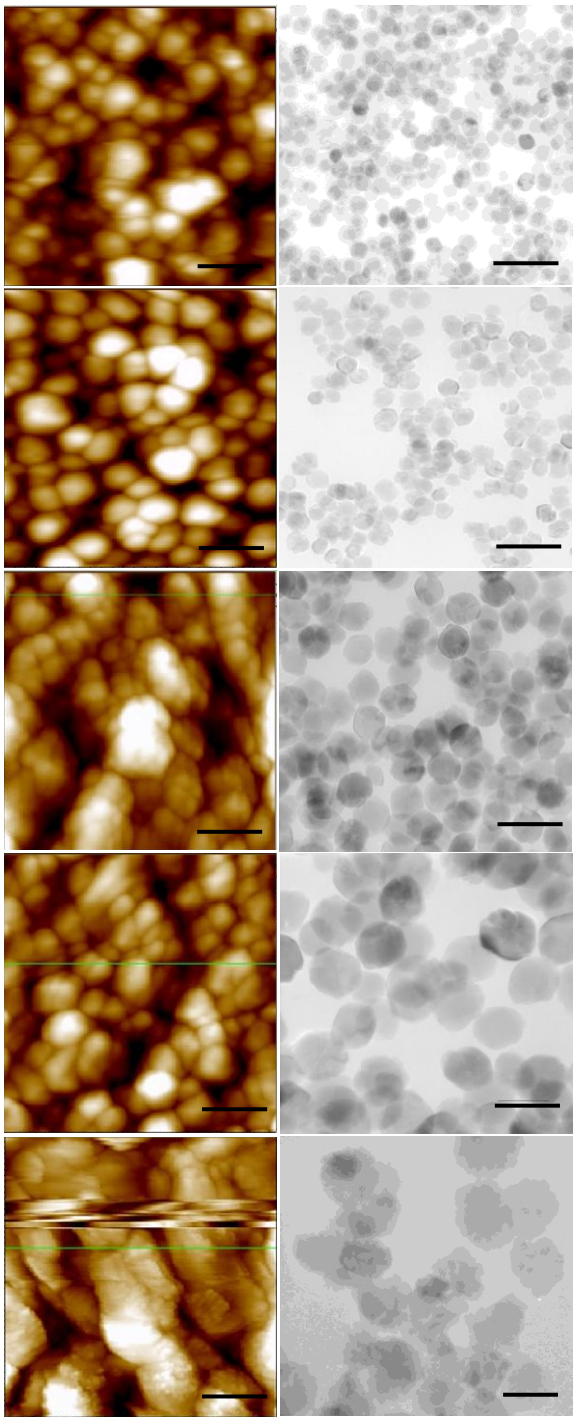

Figure 6.10. AFM images (left column) for examining the surface of hematite NP aggregates on the glass cover slip and TEM images (right column) for confirming the morphology of the synthesized hematite NPs. Mean diameters from top to bottom are 26, 44, 53, 98, and 152 nm. The black scale bar at the bottom right equals 100 nm.

6.4.7. Interaction force measurement with AFM

Figure 6.11a shows how the interaction forces were measured with AFM. The surface of the NP array (pink color) was raised by the sample stage and gradually approached the cantilever probe on which the *E. coli* cells were immobilized. The cantilever probe experienced the interaction forces, eventually bending up when it contacted the rigid NP surface, as shown in Figure 6.11a. A portion of the immobilized *E. coli* cells on the probe was in contact with NPs, as indicated by the dotted black circles. Apparently, adhesion strength is largely dependent on the contact area between the two surfaces *(115)*. This is especially true for this case, in which lipopolysaccharides (LPS), a molecule which comprises a large portion of gram negative cell outer membranes, can stretch to on the order of hundreds of nanometers, and the O-antigen on these macromolecules interacts with the metal oxide surfaces of NPs *(116)*. *E. coli* cell adhesion on the metal oxide NPs is therefore significantly mediated by the interactions of its surface groups, and the strength of adhesion could be proportional to the number of hydrogen bonds formed *(117, 118)*, which is further discussed below. The number of hydrogen bonds that can form during the adhesion is clearly related to the contact area between the two surfaces as well as their composition and reactive site densities. However, as Lantz et al. *(119)* and many other researchers *(53, 120, 121)* indicated, so far it is still impossible to determine experimentally the contact site area between the probe and a substrate surface. Fortunately, the relation between contact areas and adhesion force for a spherical tip on a planar surface can be estimated through three different models *(72)*, namely Hertz, Derjaguin-Müller-Toporov (DMT), and Johnson-Kendall-Roberts (JKR). Because contact area plays a major role in the interaction force, especially adhesion, the next section explores the estimation with the JKR model for the contact area between immobilized *E. coli* cells and NPs.

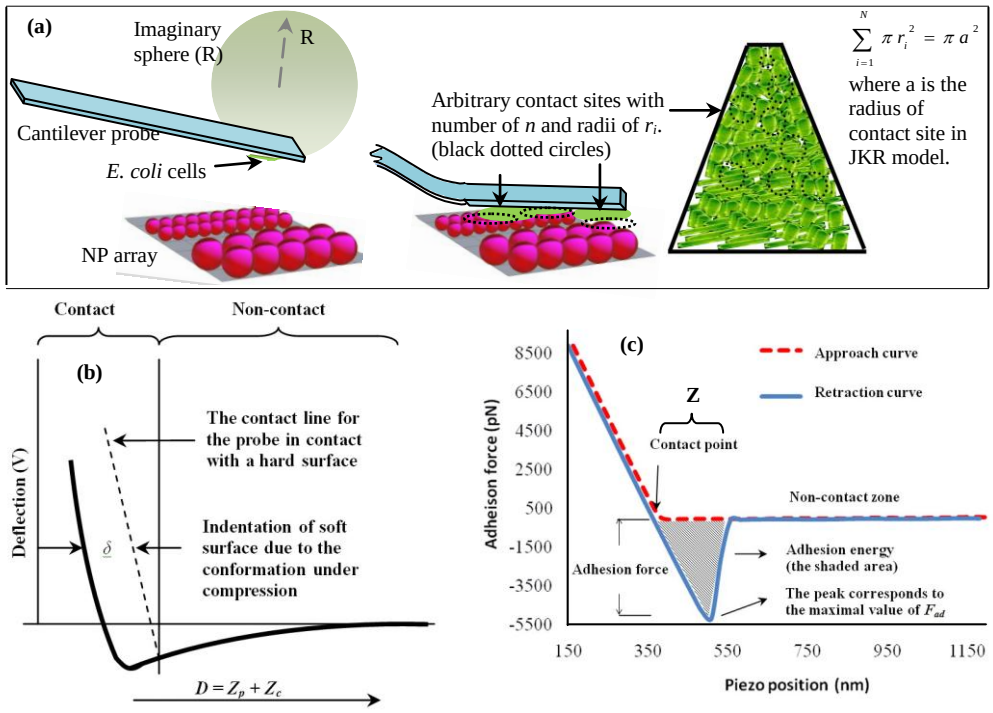

Figure 6.11. (a) Schematic of adhesion force measurement with AFM between *E. coli* cells and NPs. The cantilever probe immobilized with *E. coli* cells is approaching to the NP array and the contact surface of the probe was assumed to be a part of the surface on the imaginary sphere with radius of *R*. Multiple contact sites (indicated by the dotted black circles) between *E. coli* cells and NPs add up to a total contact area of πa^2 which is considered in the JKR model (Relative sizes of bacterial cells and NPs are not to scale). (b) Approach curves for a soft surface with indentation (δ) and a hard surface moving toward the cantilever probe. *D* is the total distance between tip and sample given by the sum of the cantilever deflection *Zc* and the piezo position Z_p. (c) Representative force-distance curve from which adhesion force (F_{ad}) and adhesion energy (W_{ad}) were calculated ($W_{ad} = \int F_{ad} dZ$, *Z* is the interaction distance of the adhesion and measured from the force-distance curves).

6.4.8. Estimation of the contact site radius with the JKR model

Among the three mechanical contact models, JKR model is most suitable for our application because it considers the adhesion inside the contact area *(122, 123)*, whereas the Hertz model neglects the adhesion and the DMT model considers the adhesion outside the contact area *(53)*. In *E. coli* cell-NP interactions, adhesion should occur in the contact area between the two surfaces, and thus JKR was used to calculate the contact site area or contact radius (*a*). However, the JKR relations have the following assumptions. First, the radius of curvature *R* of the probe tip is much larger than the contact area (a small indentation), and interaction forces outside the contact area are neglected *(85, 124)*. Second, as Figure 6.11a shows, multiple circular contact sites may exist between the rough surfaces of the immobilized *E. coli* cells and the surfaces of NPs. Consequently, we adopted the approximation made by Radmacher et al.*(125)*, who suggested that a cantilever probe coated with bacterial cells could be treated as a large sphere with a radius *R*. Therefore, the contact area between the immobilized *E. coli* cells and the substrate surface is a part of the surface area of this imaginary sphere, as shown in Figure 6.11a. This assumption may help validate the first assumption of the JKR model because the radius (*R*) of the curvature of the imaginary sphere (which can be considered a large probe tip) is much larger than the radius (*a*) of the contact area. If one of the multiple contact areas has an area of πr_i^2, the second assumption leads to $\sum_{i=1}^{N} \pi r_i^2 = \pi a^2$, where *N* is the number of contact sites; and r_i is the radius of each contact area. Other JKR relations are shown below:

$$\delta = \frac{a^2}{R} - \frac{2}{3}\sqrt{\frac{6\pi W a}{E_{TOT}}} \tag{6}$$

$$E_{TOT} = \left[\frac{3}{4}\left(\frac{1-\upsilon_s^2}{E_S} + \frac{1-\upsilon_T^2}{E_T}\right)\right]^{-1} \tag{7}$$

$$a = \sqrt[3]{\frac{R}{E_{TOT}}\left(F + 3\pi RW + \sqrt{6\pi RWF + (3\pi RW)^2}\right)} \tag{8}$$

$$F_{ad} = \frac{3\pi RW}{2} \tag{9}$$

where δ is the indentation or deformation of a samples surface under a compression (nm) and can be measured from approaching force curves according to the method shown in Figure 6.11b *(53, 72)*; a is the contact site radius (nm); R is the tip radius (the imaginary sphere radius for our case, nm); W is the adhesion energy per unit area (J/m^2); E_{TOT} is the reduced Young's modulus (MPa); υ_s, E_s, υ_T, and E_T are the Poisson's ratio and the Young's moduli of the sample (here the NP array surface) and tip (here the immobilized *E. coli* cell probe), respectively; F is the loading or compressing force (nN); F_{ad} is the adhesion force (nN); W_{ad} is the adhesion energy (J); and $w \simeq \frac{W_{ad}}{\pi a^2}$. F_{ad} and W_{ad} can be determined from the adhesion peak of the force-distance curve as illustrated in Figure 6.11c. Because adhesion force (F_{ad}), adhesion energy (W_{ad}), and indentation (δ) are readily measured from the force-distance curves, based on Eqs. (6) and (9) as well as $w \simeq \frac{W_{ad}}{\pi a^2}$, we can obtain the expression for contact area:

$$a = \frac{8}{3}\left(\frac{W_{ad}}{E_{TOT}}\right)\cdot\left(\frac{3}{2}\frac{W_{ad}}{F_{ad}} - \delta\right)^{-2} \tag{10}$$

Equation (10) was used to estimate contact radius (a). The only assumption entering in this calculation is the reduced Young's modulus (E_{TOT}), which is known to be of order several MPa. In our case, the elastic response during the interactions between the immobilized *E. coli* cells-coated probe and the NP array mainly comes from the surface properties of *E. coli* cells because the NP surface and the probe were much stiffer than the cells (e.g., for silicon nitride, E is typically 160-290 GPa *(53, 125)*). Thus, E_{TOT}

$\approx E$ for *E. coli* cells, as many other studies have assumed *(126, 127)*, and 2.5 MPa, as estimated by Perry, et al.*(126)*, entered in our calculation.

Figure 6.12a shows the experimental approach curves for immobilized *E. coli* cell-coated probes under different loading forces (F) during contact with a rigid surface (here an array of 98 nm NPs). The indentations (δ) for different loading forces were measured from these curves and are shown in Figure 6.12b. For clarity, adhesion peaks are not shown in Figure 6.12a but the adhesion force and adhesion energy were calculated based on the method introduced in Figure 6.11c. Finally, the indentation, adhesion force (F_{ad}), and adhesion energy (W_{ad}) were entered into equation (5). The contact radii (a) corresponding to different loading forces (F) were obtained and are shown in Figure 6.12b. Obviously, the contact radius is a function of loading force, which can be changed by adjusting the setpoint (V) and determined similarly to the convertion of deflection (V) to interaction force (pN), as introduced previously. Because the loading force was 1.5 ± 0.2 nN (by setting deflection to -1.2 ± 0.1 V with a setpoint of 0 V) throughout our study, the contact area radius (a) is approximately 45 ± 2 nm based on Figure 6.12b.

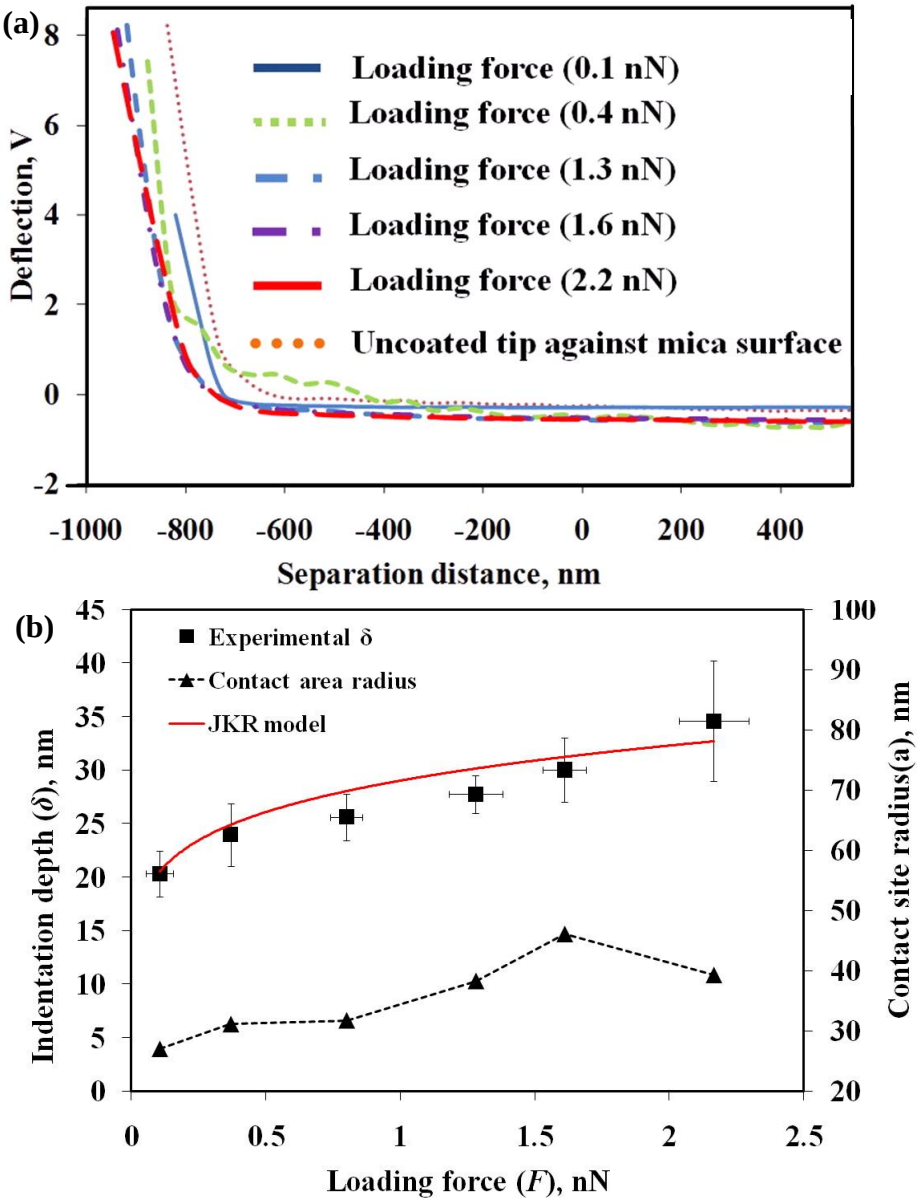

Figure 6.12. (a) Representative approach curves of the immobilized *E. coli* cell-coated probe under different loading forces (F) and the bare probe (not dependent on the loading force) against the surface coated with 98 nm hematite NPs. Indentation (δ) were estimated from the curves. (b) Experimental measurement of indentation which follows the JKR model trend.

6.4.9. Interaction forces between E. coli cells and NPs

Figure 6.13 presents representative force-distance curves for interactions between *E. coli* cell surfaces and NPs of different sizes. Figure 6.13a~e show the force-distance curves and histograms (located in the top right corner) for particle sizes from 26 nm to 152 nm. The adhesion peaks of the curves can be used to determine the maximum rupture force (or adhesion force at contact), and the histograms indicate the statistical distributions of the adhesion force measurements. However, background interactions (defined as the interaction forces between the bare cantilever probes and NPs) should be subtracted from the interaction forces shown in Figure 6.13. The silicon nitride cantilever probes (treated or untreated with gelatin) typically adhered very weakly with the surfaces of hematite NPs, and changes in NP size did not affect the repulsive forces in the approach curves or on adhesion forces in the retraction curves. Thus, the effects of background interactions on the force measurement between *E. coli* cells and the hematite NP array were negligible. As shown in Figure 6.13, NP size changes dramatically influenced the adhesion force but had no obvious effect on the repulsive force (or the size effect on the repulsive force may be too small and thus undetectable). As NP size increased from 26 nm to 98 nm, the adhesion force gradually decreased from approximately 6.3 $\pm$ 0.7 nN to 0.8 $\pm$ 0.4 nN. At 152 nm, however, adhesion force was larger, 2.6 $\pm$ 0.3 nN, as shown in Figure 6.13f.

To interpret the size effect on adhesion force, a new model was developed that considers the local effective contact areas between *E. coli* cells and the NP array. As estimated above with the JKR model, the contact area that is primarily determined by the loading or compression force exerted on the two contact surfaces in cell-nanoparticle interactions may reflect how strongly the cells and NPs can adhere to each other. More contact area likely lead to more specific and nonspecific binding interactions, which are experimentally expressed as adhesion force *(73)*. With the deformation of the soft cell

body, the effective contact area may be more complicated than the circular area with a radius (*a*) that the JKR model assumes. Our proposed model is a more realistic scenario of cell-nanoparticle contact by considering the increased contact area resulting from the contact between the deformed cell surface and the rigid particle surface. The final model equation and fitting results with the model are shown in Figure 6.13f (detailed derivations of the model equation can be found in appendix B). The experimental data for the mean adhesion forces for different sizes of NPs matched the predictions of our model. Adhesion force for the 152 nm NPs appeared to be off the size dependency trend for NPs sizes of less than 100 nm, which is probably caused by surface roughness, which affects the interfacial interactions *(128, 129)* and was examined as mentioned above. The surface height distributions (an indicator of roughness *(130)*) for 152 nm NPs were found to have a similar surface height distribution as smaller NPs (26 and 44 nm). This similarity may be reasonable based on the synthesis of hematite NPs, which is a process of crystal growth. NPs are formed by random collisions of numerous seed particles (see AFM images above). Small NPs serve as seeds for forming large NPs, and in Figure 6.10 152 nm NPs appear to have nanostructures that are similar with small NPs. Thus, when a bacterial cell surface contacts a 152 nm NP array, it is possible to generate a contact area similar to that of small NPs, which caused the adhesion force to increase abnormally.

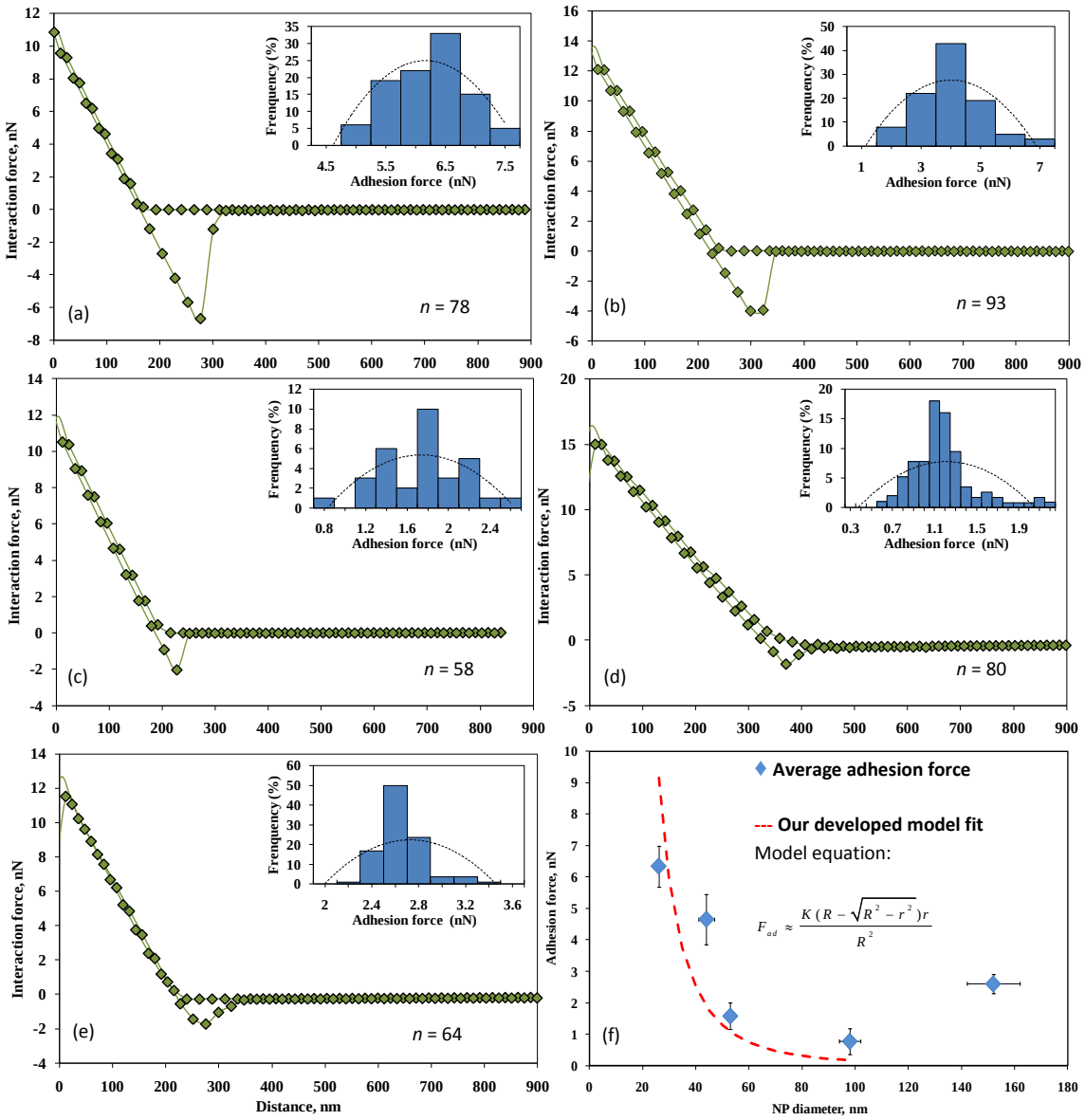

Figure 6.13. Representative force-distance curves measured between *E. coli* cells and different sizes of hematite NPs. The adhesion force distribution histogram is located in the upper right corner of each graph. (a) 26 nm. (b) 44 nm. (c) 53 nm. (d) 98 nm. (e) 152 nm. (f) Average adhesion force for different sizes of NPs and acomparison with the model trend of effective contact area (horizontal error bars indicate the standard deviation of the measured particle diameter, and vertical error bars indicate the standard deviation of average adhesion force). In each graph *n* is the number of force measurements for each size of NPs.

To corroborate the experimental observations of hematite NPs, the interaction forces between *E. coli* cells and various sizes of corundum NPs were measured. Corundum was chosen because it shares similar surface groups and other chemical properties with hematite and other metal oxide NPs *(117)*. Four different size ranges of corundum NPs were used for making NP arrays with the same protocol as hematite NPs. The nominal size ranges reported by the vendor were 25, 35, 50, and 110 nm. I observed that the surfaces of arrays composed of small NPs had relatively higher adhesion forces with *E. coli* cells than large NPs; no obvious size effect was found for repulsive forces. Figure 6.14 shows the mean adhesion forces for different sizes of corundum NPs and a comparison with the model trend. The magnitude of the adhesion force for corundum NPs was slightly higher than that of hematite NPs of the same size, which indicates that the chemical composition of the NP surface influences their adhesion force with cells.

As summarized by Butt, et al. *(53)*, many other factors affect the interaction force measurement, such as contact time, pH, and ionic strength. Logan, et al. have extensively studied the effects of these factors on interaction force measurement *(131)*. In particular, increasing the contact time between the tip and sample increases the adhesion strength *(131, 132)*. In our study, the duration of each approach-retract cycle was set 1 second and the speed of the sample stage movement was approximately 2 μm/s. The contact time was on the order of a microsecond, and thus the force measurement recorded the interaction forces occurring during a transient time, which roughly agrees with the time scale of colloidal adsorption in actual environmental systems *(133)*. Similarly, typical pH and ionic strength were used in our study.

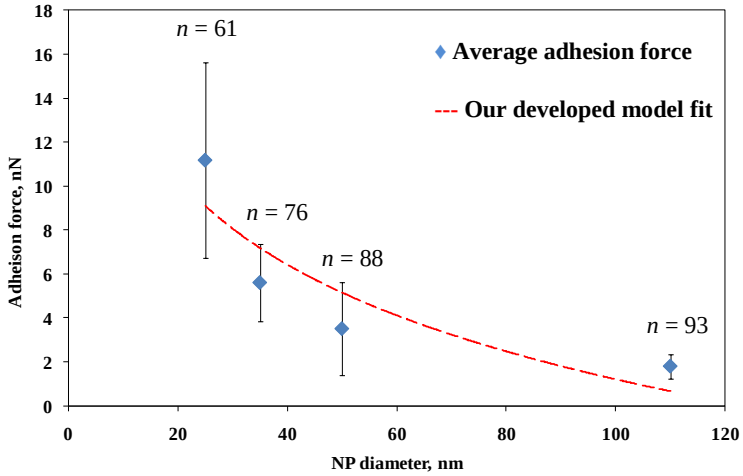

Figure 6.14. Adhesion forces between *E. coli* and NP arrays composed of various sizes of corundum NPs. All adhesion force data are averages of individual force vs. distance plots, and error bars represent one standard deviation. In each graph *n* is the number of force measurements for each size of NP array.

6.4.10. Adhesion energy calculation in support of the new model

Our proposed model assumes that local effective contact area increased as NP size decreased. To validate this assumption, the following analysis of adhesion energy (W_{ad}) and hydrogen bonding was made. As stated above, many researchers have found that chemical bonds, such as hydrogen bonds, formed between metal oxide surfaces and LPS on the *E. coli* outer cell membrane significantly contribute to the adhesion *(53, 117, 134)*, and the adhesion strength is positively proportional to the chemical bond number *(57)*. The number of hydrogen bonds was obtained by dividing the adhesion energy (W_{ad}) by the Gibbs free energy for the formation of one hydrogen bond ($\approx 10^{-20}$ J). Table 6.3 shows the adhesion energy for *E. coli* cells with different sizes of NPs and the number of hydrogen bonds. For hematite NPs, approximately 3500~88,000 hydrogen bonds were on the contact area and small NPs had more hydrogen bonds than large NPs. The same trend was observed for corundum NPs. This suggests that cell interactions with the NP arrays of small NPs have a much higher contact area. As a validation of this hydrogen bond number calculation, Jucker et al.*(117)* indicated that the surface of an *E. coli* cell contains approximately 3.5×10^{6} LPS molecules that can form hydrogen bonds with metal oxide surfaces. Given that the average cell surface area is 6×10^{-12} m^2 *(135)* and the contact area is approximately 6359 nm^2 ($= \pi \cdot 45^2$) (as estimated above with the JKR model), the average number of hydrogen bonds formed is 3709 ($= 6359 \times 10^{-18}$ $m^2 \times 3.5 \times 10^{6} / 6 \times 10^{-12}$ m^2), which is roughly consistent with the numbers on for 98 and 152 nm NPs shown in Table 6.3. However, for smaller NPs, hydrogen bond number increased with decreasing size and this may imply that the actual contact areas or effective contact areas were much larger than the one estimated by the JKR model. This is reasonable because the JKR model considers the contact area to be a plane between a rigid tip and a planar surface. However, biological surfaces such as *E. coli* cells are deformable during contact and compression, which may increase the local effective contact area and as a result the adhesion force between the NP aggregate surface and cells would be increased.

Table 6.3. Adhesion energy and hydrogen bond number.

	NP diameter (nm)	Adhesion energy ($\times 10^{-16}$ J)	Hydrogen bond number in contact site area ($\times 10^{4}$)
Hematite NPs	26	8.5 ± 1.7	8.5 ± 1.7
	44	7.7 ± 2.2	7.7 ± 2.2
	53	1.0 ± 2.6	1.0 ± 2.6
	98	0.37 ± 0.20	0.37 ± 0.20
	152	0.36 ± 0.12	0.36 ± 0.12
Corundum NPs	25	6.5 ±1.7	6.5 ± 1.7
	35	3.2 ±1.7	3.2 ± 1.7
	50	1.2 ± 1.7	1.2 ± 1.7
	110	7.3 ± 1.7	7.3 ±1.7

6.4.11. Characterization of the live E. coli cells before exposure to hematite NPs

The characterization of hematite NPs with KFM is shown in detail in Chapter 8 and here in this chapter I only show the KFM results for *E. coli* cells. Before exposure to hematite NPs, their original surface properties (morphology and surface potential) were studied with KFM. Figure 6.15a presents the morphology image of the cell in which the shape and size can be clearly observed. In addition, hair-like flagella (a common extracellular filamentous appendage firmly attached to surfaces of *E. coli* cells *(136)*) were also found adjacent to the *E. coli* cell. At a higher zoom, Figure 6.15b further shows the ultrastructure of the cell body, which was rather rough and had different heights based on the contrast. The green graph on the bottom left of Figure 6.15b is a typical topography cross-section taken along the red dashed line randomly drawn across the cell body.

Figure 6.15c presents the surface potential image of the cell. Unlike the sharp contrast observed for hematite NPs, the contrast of the surface potential image of the *E. coli* cell is not significantly sharper than the topography image. This is probably because *E. coli* extracellular materials such as transmembrane proteins, lipids, and LPS are more conductive than iron oxide *(62)*. Thus, the contrast is relatively low, but the many dark regions of the cell body reveal that the cell carried negative charge. This is consistent with the zeta potential measurement of *E. coli* cells *(7)*. In contrast to hematite NPs, the surface potential distribution across different cell regions was not homogeneous, due to the complex surface structures and compositions of *E. coli* cells. The surface potential cross-section taken along the red dashed line drawn across the cell is shown in the green graph in the bottom left of Figure 6.15c. The surface potential of the cell varied from -30 to -50 mV in the range of 300 nm to 600 nm along the red dash line.

Figure 6.15d presents the phase image of the cell. Due to the sensitivity of the phase angle to a wide spectrum of surface properties *(137)*, the phase image has better

resolution and contrast than the other images. In particular, the phase image shows that the area surrounding the cell appears to be covered by polymeric materials. *E. coli* cells secrete extracellular polymeric substances, which may remain around the cell after preparation of the cells for KFM study. The sharper contrast in the phase image may also be due to the surface properties of *E. coli* cells, which are adhesive, soft, and viscoelastic. For example, the green graph shows the cross-section of the phase angle along the same line as in the topography and surface potential images. Along the range from 300 nm to 600 nm, a negative phase shift occurred (phase angle decreased), and a dark contrast is visible in the corresponding cell region. This indicates that the cantilever tip was attracted to the cell due to adhesion force when it scanned across the cell body *(138).* This observation agrees with the common understanding of the adhesive surface property of *E. coli* cells. More complex factors may also contribute to the phase angle shift; currently the correlations between tip-sample interactions and the resulting phase images are still hard to interpret quantitatively. But as a tool for enhancing contrast, phase image appears to be powerful.

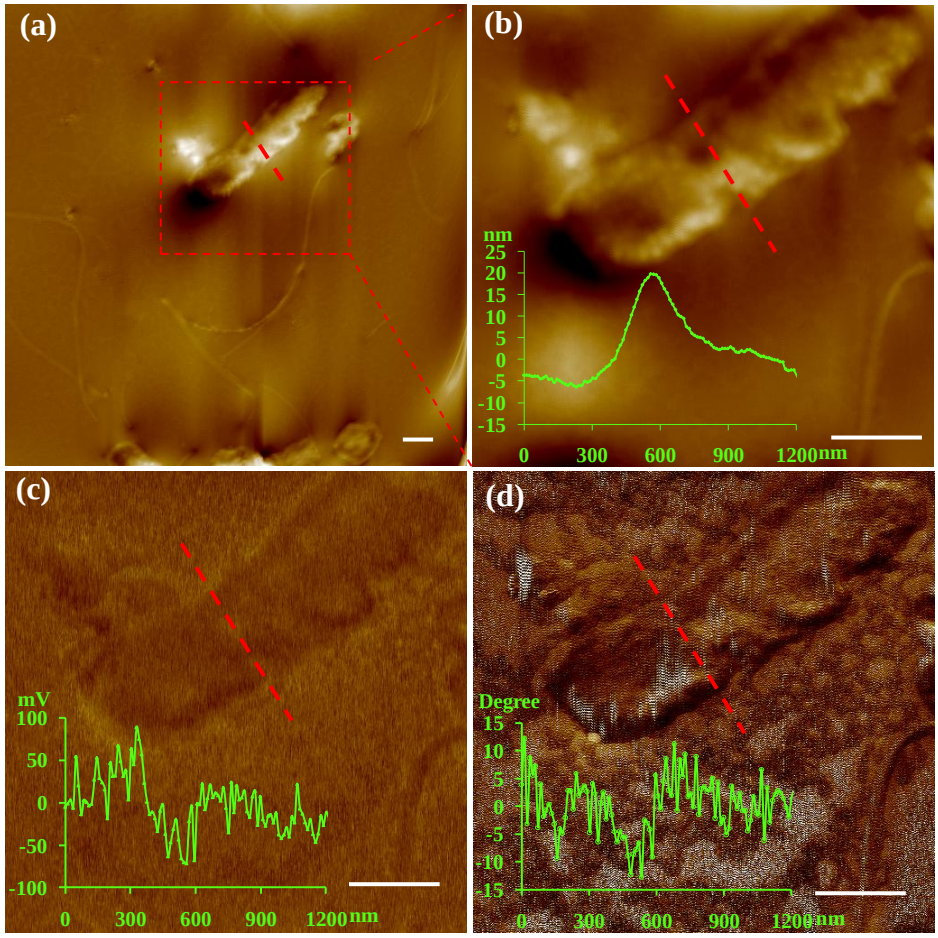

Figure 6.15. (a) and (b) show the topography of intact, live *E. coli* cells before exposure to hematite NPs; (c) and (d) show the phase and surface potential images; The cross-section profiles of the topography, surface potential, and phase images are shown in the bottom left (b), (c), and (d), respectively. These cross-sections were taken along the directions marked with the dashed red lines in the images of (b), (c), and (d). The white solid lines at the bottom right are scale bars of 300 nm.

6.4.12. Characterization of the live E. coli cells after exposure to hematite NPs

After characterizing individual hematite NPs and intact *E. coli* cells, more interests are about the exposure effects on properties of *E. coli* cells. Figure 6.16 presents the results in three columns, from left to right show topography, surface potential, and phase images. From the top to bottom, the rows present the samples obtained at exposure times of approximately 3 min, 10 min, and 20 min. The topography image in Figure 6.16a indicates that large NPs (hematite NPs and their aggregates) surrounded the cells, but cellular morphology did not change within the exposure time of 3 min. As the exposure time increased to 10 min, more hematite NPs adsorbed onto the cell surface, as marked by the red arrow in Figure 6.16d. After 20 min the cell body had shrunk significantly, and the flagella were shredded and scattered adjacent to the cell body, as marked in Figure 6.16g. This surface damage is similar to the disruption of microvilli structures on Caco-2 cells, a type of human intestinal epithelial cells, after exposure to hematite NPs *(21)*. Microvilli are external structures on the surface of the epithelium that aid in nutrient assimilation and structural integrity *(139)*. Similar to microvilli, flagella as well as other surface appendages (i.e. pili) play important roles in surface attachment, cellular stability, and mobility. Irreversible disruption of these surface structures may cause adverse consequences *(1, 8, 140)*. For example, losing these appendages, *E. coli* cells may lose mobility and stability *(141)*. Furthermore, the absence of such surface appendages may increase exposure of the *E. coli* cell membrane to NPs and may promote subsequent adverse effects, such as membrane lysis, permeation of NPs into the cells, and cellular deformation *(10)*. The drying process required for the KFM study did not harm the flagella because intact flagella were clearly observed on *E. coli* cells before exposure to hematite NPs, as shown in Figure 6.15. Thus, exposure to hematite NPs is assumed to induce the damage to the flagella.

Surface potential images provide a unique way to distinguish hematite NPs from

complex biological matrices (*E. coli* cells) based on their distinct surface potential, as discussed above. Hematite NPs are evident in the area surrounding the cell in Figure 6.16b, e, and h and are darker in color than the cell. As the exposure time increased, the cells became darker (compare the images in Figure 6.16b, e, and h). The surface potential of the cells dropped with exposure time largely because of the adsorption and accumulation of hematite NPs on their surface. The hematite NPs carry a negative potential of up to -800 mV, whereas the original *E. coli* cells have a surface potential of -40 to -100 mV. One potential implication of the accumulation of hematite NPs is reduced viability of *E. coli* cells because the respiratory chains on cell membranes may be disrupted or blocked, and reactive oxygen species (ROS) may be generated and present a oxidative stress on cells *(20)*. However, the surface potential changes could also alter the surface properties and lead to the release of surface energy as well as deactivation of functional groups *(73)*.

The phase images provide extraordinary contrast between the *E. coli* cell and its surrounding hematite NPs. Figure 6.16c shows the evident boundary of cellular envelope (serve as extracellular protection against various disruptive chemicals), marked by the red arrows, which is formed by EPS secreted by *E. coli* cells. Figure 6.16f and i show striking contrast between the adsorbed hematite NPs and the surface of the *E. coli* cell, as marked by the red arrows. In particular, Figure 6.16i provides compelling evidence that more small NPs than large ones accumulated on the cell surface and that the flagella were cut into pieces, as marked by the red arrows.

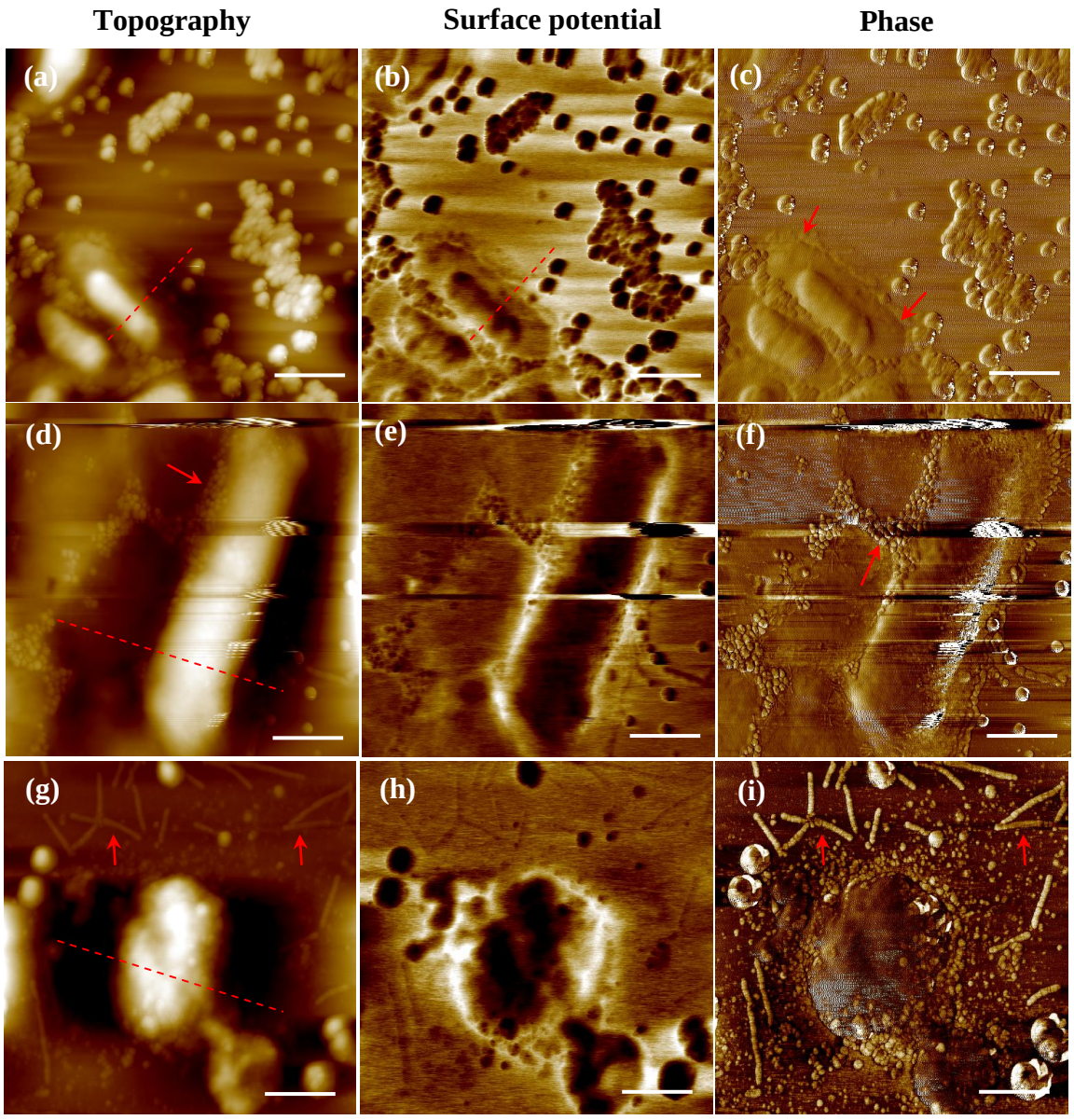

Figure 6.16. The topography (left column), surface potential (middle column), and phase images (right column) of live *E. coli* cells exposed to hematite NPs (98 nm). Exposure times were approximately (a)-(c) 3 min; (d)-(f) 10 min; and (g)-(i) 20 min. The white scale bars at the bottom right of (a) - (c) and (d) - (i) indicate lengths of 1 μm and 0.5 μm, respectively.

6.4.13. Dynamic changes in the surface potentials of E. coli cells after exposure to hematite NPs

To better understand the dynamic changes in surface potentials with the surface accumulation of hematite NPs and the surface potential of the cell are compared. The concentrations of hematite NPs in the buffered liquid of the test and control tubes were measured (see Figure 6.17a). The concentration of hematite NPs in the experimental tubes decreased rapidly within the initial 30 min, and after that adsorption equilibrium was achieved gradually. The concentration in the control tube was almost constant and thus the background adsorption to the plastic tube was negligible. It is possible to estimate the accumulated mass of hematite NPs on the cell surface using Figure 6.17a and knowing that a single *E. coli* cell has 2.52×10^{-13} g of wet mass and 6×10^{-12} m^2 of surface area *(135, 142)*. Thus, 0.1 mg/ml *E. coli* cells dispersed in a 50 ml test tube yields approximately 0.024 m^2 of surface area on which hematite NPs can accumulate.

Surface potentials were statistically determined by randomly selecting 10 positions in the center of the *E. coli* cells at each exposure time and then averaging the measured potentials. Figure 6.17b is a plot of mean surface potential versus accumulated mass of hematite NPs per *E. coli* surface area calculated as previously reported *(21)*. The two are considerably correlated. As the hematite NP mass on the cell surfaces increased, the mean surface potential dropped significantly in a non-linear fashion.

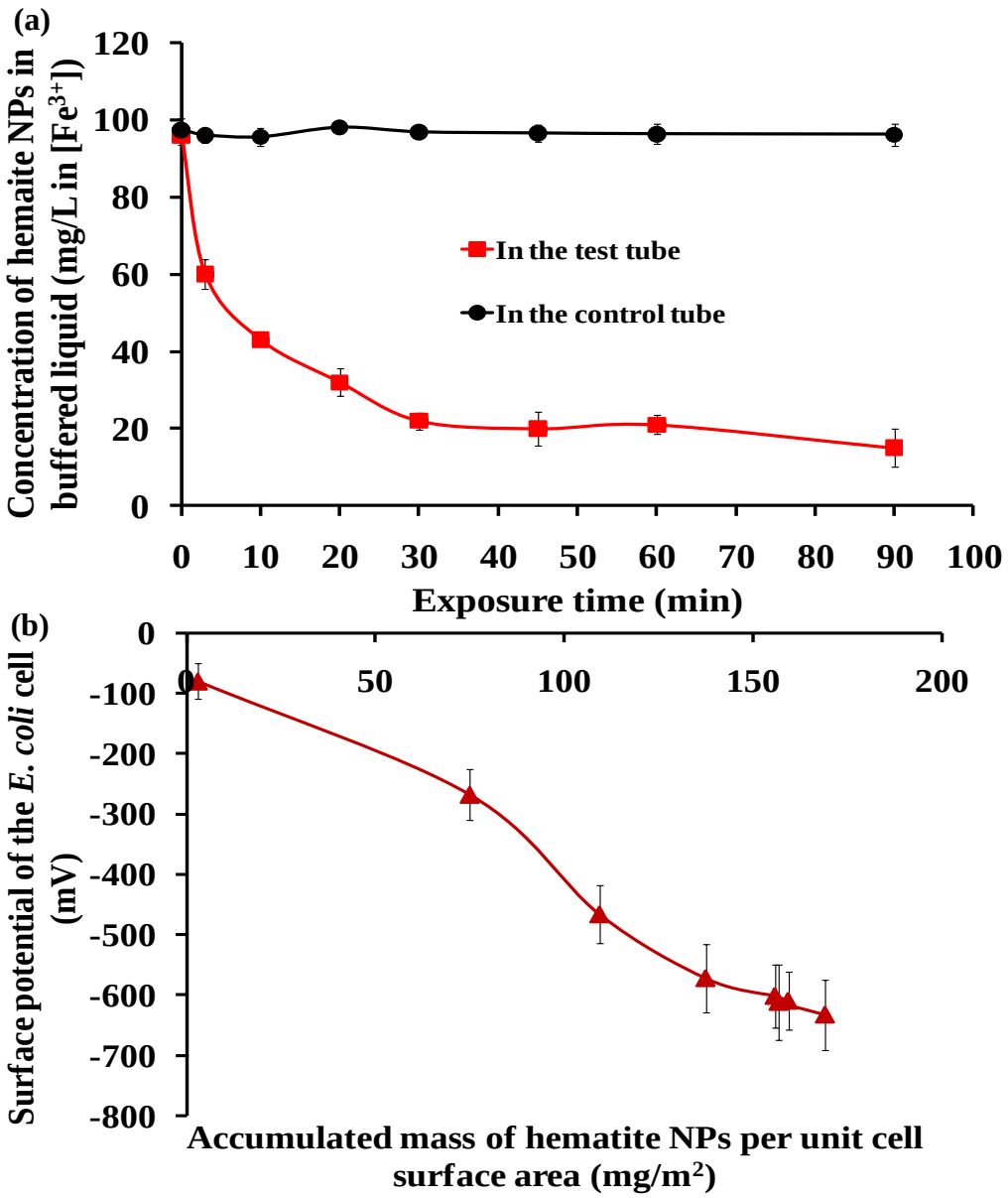

Figure 6.17. (a) The concentrations of hematite NPs in the test tube and control tube after different exposure times. (b) The accumulated mass of hematite NPs on the unit surface area of the cell versus the surface potentials of the *E. coli* cells at different exposure times. All data points in (a) are averages from triplicate experimental measurements, and error bars represent one standard deviation. When error bars are not visible, they are small and hidden behind the data symbols.

6.5. Research significance

This chapter systematically studied the interactions between hematite NPs and *E. coli* cells from different angles, including adsorption, surface interaction forces, and surface potential variations. For adsorption kinetics, I proposed a model based on EDLVO-IFBL theories that may lay out a mathematical framework to explain how size affects adsorption kinetics. The adsorption behavior of NPs may be linked to their fate, transport, and even biological impacts; thus, better prediction models are clearly needed for understanding their environmental behavior and bio-nano interactions. The results presented here demonstrate that the combination of EDLVO and IFBL theories provides a useful quantitative method to describe adsorption kinetics of hematite NPs onto bacterial surfaces. The results presented here lay the ground work for developing models to describe the thermodynamic and kinetics behavior of a range of NPs toward adsorption with microorganisms.

The size dependence not only applies to adsorption kinetics, but also found its role in surface interaction forces, particularly adhesion force between different sized NPs and *E. coli* cells. The size effect on interaction forces may arise from the effective contact area. The proposed model based on the effective contact area well explained the stronger adhesion to cells of surfaces composed of small NPs. This study may provide insightful information toward the understanding of surface interactions of NPs with biosystems and other interfacial phenomena at nanoscale.

As a versatile tool, the electric mode of AFM, KFM, was demonstrated its application in mapping surface morphology and surface potential for both NPs and *E. coli* cells. Surface potential plays an important role in interfacial forces such as electrostatic force *(23, 109),* and thus surface potential changes could influence particle-cell and cell-cell interactions *(143)* and change cellular mobility and viability. With this relation,

KFM can be used not only for local differentiation of NPs from cellular matrices but also for prediction of the accumulated mass of NPs on cell surfaces.

6.6. Reference

(1) Baun, A.; Hartmann, N. B.; Grieger, K.; Kusk, K. O. Ecotoxicity of engineered nanoparticles to aquatic invertebrates: a brief review and recommendations for future toxicity testing. *Ecotoxicology* **2008,** *17* (5), 387-395.

(2) Brunner, T. J.; Wick, P.; Manser, P.; Spohn, P.; Grass, R. N.; Limbach, L. K.; Bruinink, A.; Stark, W. J. In Vitro Cytotoxicity of Oxide Nanoparticles: Comparison to Asbestos, Silica, and the Effect of Particle Solubility. *Environ. Sci. Tech.* **2006,** *40* (14), 4374-4381.

(3) Geiser, M.; Rothen-Rutishauser, B.; Kapp, N.; Schurch, S.; Kreyling, W.; Schultz, H.; Im Hof, V.; Hyder, J.; Gehr, P. Ultrafine particles can cross cellular membranes by nonphagocytic mechanisms in lungs and cultured cell. *Environ Health Perspect* **2005,** *113* (11), 1555 - 1560.

(4) Gupta, A. K.; Gupta, M. Cytotoxicity suppression and cellular uptake enhancement of surface modified magnetic nanoparticles. *Biomaterials* **2005,** *26* (13), 1565-1573.

(5) Hussain, S. M.; Hess, K. L.; Gearhart, J. M.; Geiss, K. T.; Schlager, J. J. In vitro toxicity of nanoparticles in BRL 3A rat liver cells. *Toxicol. In Vitro* **2005,** *19* (7), 975-983.

(6) Zhu, X.; Chang, Y.; Chen, Y. Toxicity and bioaccumulation of TiO_2 nanoparticle aggregates in Daphnia magna. *Chemosphere* **2009,** *78* (3), 209-215.

(7) Schwegmann, H.; Feitz, A. J.; Frimmel, F. H. Influence of the zeta potential on the sorption and toxicity of iron oxide nanoparticles on *S. cerevisiae* and *E. coli*. *J. Colloid Interface Sci.* **2010,** *347* (1), 43-48.

(8) Baun, A.; Sørensen, S. N.; Rasmussen, R. F.; Hartmann, N. B.; Koch, C. B. Toxicity and bioaccumulation of xenobiotic organic compounds in the presence of aqueous suspensions of aggregates of nano-C60. *Aquat. Toxicol.* **2008,** *86* (3), 379-387.

(9) Jirasak, W.-E.; Svetlana, B.; Wannapong, T.; Tang, I.-M.; PeterTieleman, D.; Monticelli, L. Computer simulation study of fullerene translocation through lipid membranes. *Nature Nanotech* **2008,** *3*, 363-368.

(10) Geiser, M.; Rothen-Rutishauser, B.; Kapp, N.; Schurch, S.; Kreyling, W.; Schulz, H.; Semmler, M.; Hof, V. I.; Heyder, J.; Gehr, P. Ultrafine particles cross cellular membranes by nonphagocytic mechanisms in lungs and in cultured cells. *Environ. Health Perspect.* **2005,** *113* (11), 1555-1560.

(11) Trouiller, B.; Reliene, R.; Westbrook, A.; Solaimani, P.; Schiestl, R. H. Titanium Dioxide Nanoparticles Induce DNA Damage and Genetic Instability In vivo in Mice. *Cancer Res.* **2009,** *69* (22), 8784-8789.

(12) Bradford, A.; Handy, R. D.; Readman, J. W.; Atfield, A.; Mühling, M. Impact of Silver Nanoparticle Contamination on the Genetic Diversity of Natural Bacterial Assemblages in Estuarine Sediments. *Environ. Sci. Tech.* **2009,** *43* (12), 4530-4536.

(13) Zhang, W.; Yao, Y.; Chen, Y. Imaging and Quantifying the Morphology and Nanoelectrical Properties of Quantum Dot Nanoparticles Interacting with DNA. *J. Phys. Chem. C* **2010**, DOI:10.1021/jp107676h.
(14) Li, Z. Q.; Greden, K.; Alvarez, P. J. J.; Gregory, K. B.; Lowry, G. V. Adsorbed Polymer and NOM Limits Adhesion and Toxicity of Nano Scale Zerovalent Iron to *E. coli*. *Environ. Sci. Tech.* **2010,** *44* (9), 3462-3467.
(15) Brayner, R.; Ferrari-Iliou, R.; Brivois, N.; Djediat, S.; Benedetti, M. F.; Fievet, F. Toxicological impact studies based on *Escherichia* coli bacteria in ultrafine ZnO nanoparticles colloidal medium. *Nano Lett.* **2006,** *6* (4), 866-870.
(16) Kiser, M. A.; Westerhoff, P.; Benn, T.; Wang, Y.; Perez-Rivera, J.; Hristovski, K. Titanium Nanomaterial Removal and Release from Wastewater Treatment Plants. *Environ. Sci. Tech.* **2009,** *43* (17), 6757-6763.
(17) Kiser, M. A.; Ryu, H.; Jang, H. Y.; Hristovski, K.; Westerhoff, P. Biosorption of nanoparticles to heterotrophic wastewater biomass. *Water Res.* **2010,** *44* (14), 4105-4114.
(18) Zhang, H. S.; DiBaise, J. K.; Zuccolo, A.; Kudrna, D.; Braidotti, M.; Yu, Y. S.; Parameswaran, P.; Crowell, M. D.; Wing, R.; Rittmann, B. E.; Krajmalnik-Brown, R. Human gut microbiota in obesity and after gastric bypass. *Proc. Natl. Acad. Sci. U. S. A.* **2009,** *106* (7), 2365-2370.
(19) Oberdörster, G.; Oberdörster, E.; Oberdörster, J. Nanotoxicology: an emerging discipline evolving from studies of ultrafine particles. *Environ. Health. Perspect.* **2005,** *113* (7), 823-839.
(20) Nel, A.; Xia, T.; Madler, L.; Li, N. Toxic potential of materials at the nanolevel. *Science* **2006,** *311* (5761), 622-627.
(21) Zhang, W.; Kalive, M.; Capco, D. G.; Chen, Y. Adsorption of hematite nanoparticles onto Caco-2 cells and the cellular impairments: effect of particle size *Nanotechnology* **2010,** *21* (35), 355103.
(22) Ducker, W. A.; Grant, L. M. Effect of Substrate Hydrophobicity on Surfactant Surface aggregate Geometry. *J. Phys. Chem.* **1996,** *100* (28), 11507-11511.
(23) Hermansson, M. The DLVO theory in microbial adhesion. *Colloids Surf., B* **1999,** *14* (1-4), 105-119.
(24) He, Y. T.; Wan, J. M.; Tokunaga, T. Kinetic stability of hematite nanoparticles: the effect of particle sizes. *J. Nanopart. Res.* **2008,** *10* (2), 321-332.
(25) Snoswell, D. R. E.; Duan, J. M.; Fornasiero, D.; Ralston, J. Colloid stability of synthetic titania and the influence of surface roughness. *J. Colloid Interface Sci.* **2005,** *286* (2), 526-535.
(26) Schalow, T.; Brandt, B.; Starr, D. E.; Laurin, M.; Shaikhutdinov, S. K.; Schauermann, S.; Libuda, J.; Freund, H. J. Particle size dependent adsorption and reaction kinetics on reduced and partially oxidized Pd nanoparticles. *Phys Chem Chem Phys* **2007,** *9* (11), 1347-1361.
(27) Elimelech, M.; Gregory, J.; Jia, G.; Williams, R. *Surface interaction potentials*. Butterworth–Heinemann: Woburn, MA, USA., 1995.
(28) Gao, D.; Lin, D.-Q.; Yao, S.-J. Protein adsorption kinetics of mixed-mode adsorbent with benzylamine as functional ligand. *Chem. Eng. Sci.* **2006,** *61* (22), 7260-7268.

(29) Song, L.; Johnson, P. R.; Elimelech, M. Kinetics of Colloid Deposition onto Heterogeneously Charged Surfaces in Porous Media. *Environ. Sci. Tech.* **1994,** *28* (6), 1164-1171.
(30) Ryan, J. N.; Elimelech, M. Colloid mobilization and transport in groundwater. *Colloids Surf., A* **1996,** *107*, 1-56.
(31) Hammes, G. G. *Principles of Chemical Kinetics.* . Academic Press.: New York, 1978.
(32) Oss, C. J. v. Kinetics and Energetics of Specific Intermolecular Interactions. *J. Mol. Recogn.* **1997,** *10* (5), 203-216.
(33) Shen, C.; Li, B.; Huang, Y.; Jin, Y. Kinetics of Coupled Primary- and Secondary-Minimum Deposition of Colloids under Unfavorable Chemical Conditions. *Environ. Sci. Tech.* **2007,** *41* (20), 6976-6982.
(34) Hahn, M. W.; O'Melia, C. R. Deposition and Reentrainment of Brownian Particles in Porous Media under Unfavorable Chemical Conditions:Some Concepts and Applications. *Environ. Sci. Tech.* **2003,** *38* (1), 210-220.
(35) Franchi, A.; O'Melia, C. R. Effects of Natural Organic Matter and Solution Chemistry on the Deposition and Reentrainment of Colloids in Porous Media. *Environ. Sci. Tech.* **2003,** *37* (6), 1122-1129.
(36) Wilhelm, C.; Gazeau, F.; Roger, J.; Pons, J. N.; Bacri, J. C. Interaction of anionic superparamagnetic nanoparticles with cells: kinetic analyses of membrane adsorption and subsequent internalization. *langmuir* **2002,** *18* (21), 8148-8155.
(37) Cho, E. C.; Xie, J.; Wurm, P. A.; Xia, Y. Understanding the role of surface charges in cellular adsorption versus internalization by selectively removing gold nanoparticles on the cell surface with a I2/KI etchant. *Nano Lett.* **2009,** *9* (3), 1080-1084.
(38) Scarberry, K. E.; Dickerson, E. B.; McDonald, J. F.; Zhang, Z. J. Magnetic Nanoparticle-peptide Conjugates for in Vitro and in Vivo Targeting and Extraction of Cancer Cells. *J. Am. Chem. Soc.* **2008,** *130* (31), 10258-10262.
(39) Hong, Y.; Honda, R. J.; Myung, N. V.; Walker, S. L. Transport of Iron-Based Nanoparticles: Role of Magnetic Properties. *Environ. Sci. Tech.* **2009,** *43* (23), 8834-8839.
(40) Zhang, Y.; Chen, Y.; Westerhoff, P.; Hristovski, K.; Crittenden, J. C. Stability of commercial metal oxide nanoparticles in water. *Water Res.* **2008,** *42* (8-9), 2204-2212.
(41) Nowack, B.; Bucheli, T. D. Occurrence, behavior and effects of nanoparticles in the environment. *Environ. Pollut.* **2007,** *150* (1), 5-22.
(42) Zhang, W.; Stack, A. G.; Chen, Y. Interaction Force Measurement between *E. coli* Cells and Nanoparticles Immobilized Surfaces by Using AFM. *Colloids Surf., B* **2010,** *82* (2), 316-324
(43) Lu, F.; Wu, S. H.; Hung, Y.; Mou, C. Y. Size effect on cell uptake in well-suspended, uniform mesoporous silica nanoparticles. *Small* **2009,** *5* (12), 1408-1413.
(44) Napierska, D.; Thomassen, L. C.; Rabolli, V.; Lison, D.; Gonzalez, L.; Kirsch-Volders, M.; Martens, J. A.; Hoet, P. H. Size-dependent cytotoxicity of monodisperse silica nanoparticles in human endothelial cells. *Small* **2009,** *5*, 846-853.
(45) Shi, Z.; Huang, X.; Cai, Y.; Tang, R.; Yang, D. Size effect of hydroxyapatite nanoparticles on proliferation and apoptosis of osteoblast-like cells. *Acta. Biomater.* **2009,** *5* (1), 338-345.

(46) Watari, F.; Takashi, N.; Yokoyama, A.; Uo, M.; Akasaka, T.; Sato, Y.; Abe, S.; Totsuka, Y.; Tohji, K. Material nanosizing effect on living organisms: non-specific, biointeractive, physical size effects. *J. R. Soc. Interface* **2009,** *6*, 371-388.
(47) Hillyer, J. F.; Albrecht, R. M. Gastrointestinal persorption and tissue distribution of differently sized colloidal gold nanoparticles. *J. Pharm. Sci.* **2001,** *90* (12), 1927-1936.
(48) Leonenko, Z.; Finot, E.; Amrein, M. Adhesive interaction measured between AFM probe and lung epithelial type II cells. *Ultramicroscopy* **2007,** *107* (10-11), 948-953.
(49) McNamee, C. E.; Pyo, N.; Higashitani, K. Atomic force microscopy study of the specific adhesion between a colloid particle and a living melanoma cell: Effect of the charge and the hydrophobicity of the particle surface. *Biophys J* **2006,** *91* (5), 1960-9.
(50) Mougin, K.; Gnecco, E.; Rao, A.; Cuberes, M. T.; Jayararnan, S.; McFarland, E. W.; Haidara, H.; Meyer, E. Manipulation of gold nanoparticles: Influence of surface chemistry, temperature, and environment (vacuum versus ambient atmosphere). *langmuir* **2008,** *24* (4), 1577-1581.
(51) Lovern, S. B.; Strickler, J. R.; Klaper, R. Behavioral and physiological changes in Daphnia magna when exposed to nanoparticle suspensions (titanium dioxide, nano-C-60, and C(60)HxC(70)Hx). *Environ Sci Technol* **2007,** *41* (12), 4465-4470.
(52) Persson, B. N. J. On the mechanism of adhesion in biological systems. *J. Chem. Phys.* **2003,** *118* (16), 7614-7621.
(53) Butt, H.-J.; Cappella, B.; Kappl, M. Force measurements with the atomic force microscope: Technique, interpretation and applications. *Surf. Sci. Rep.* **2005,** *59* (1-6), 1-152.
(54) Janshoff, A.; Neitzert, M.; Oberdörfer, Y.; Fuchs, H., Force Spectroscopy of Molecular Systems - Single Molecule Spectroscopy of Polymers and Biomolecules. In 2000; Vol. 39, pp 3212-3237.
(55) Benoit, M.; Gaub, H. E. Measuring Cell Adhesion Forces with the Atomic Force Microscope at the Molecular Level. *Cells Tissues Organs* **2002,** *172*, 174-189.
(56) Puech, P.-H.; Poole, K.; Knebel, D.; Muller, D. J. A new technical approach to quantify cell-cell adhesion forces by AFM. *Ultramicroscopy* **2006,** *106* (8-9), 637-644.
(57) Sugimoto, Y.; Pou, P.; Abe, M.; Jelinek, P.; Perez, R.; Morita, S.; Custance, O. Chemical identification of individual surface atoms by atomic force microscopy. *Nature* **2007,** *446* (7131), 64-67.
(58) Boonaert, C. J. P.; Toniazzo, V.; Mustin, C.; Dufrene, Y. F.; Rouxhet, P. G. Deformation of Lactococcus lactis surface in atomic force microscopy study. *Colloids Surf., B: Biointerfaces* **2002,** *23* (2-3), 201-211.
(59) eacute; ndez-Vilas, A.; Gallardo-Moreno, A. M.; Gonz; aacute; lez-Mart; iacute; n, M. L. Atomic Force Microscopy of Mechanically Trapped Bacterial Cells. *Microsc. Microanal. Microsc. Microanal.* **2007,** *13* (01), 55-64.
(60) Mak, L. H.; Knoll, M.; Weiner, D.; Gorschluter, A.; Schirmeisen, A.; Fuchs, H. Reproducible attachment of micrometer sized particles to atomic force microscopy cantilevers. *Rev. Sci. Instrum.* **2006,** *77* (4), 046104-3.
(61) Bolshakova, A. V.; Kiselyova, O. I.; Filonov, A. S.; Frolova, O. Y.; Lyubchenko, Y. L.; Yaminsky, I. V. Comparative studies of bacteria with an atomic force microscopy operating in different modes. *Ultramicroscopy* **2001,** *86* (1-2), 121-128.

(62) Velegol, S. B.; Logan, B. E. Contributions of Bacterial Surface Polymers, Electrostatics, and Cell Elasticity to the Shape of AFM Force Curves. *langmuir* **2002,** *18* (13), 5256-5262.
(63) Camesano, T. A.; Natan, M. J.; Logan, B. E. Observation of Changes in Bacterial Cell Morphology Using Tapping Mode Atomic Force Microscopy. *langmuir* **2000,** *16* (10), 4563-4572.
(64) Doktycz, M. J.; Sullivan, C. J.; Hoyt, P. R.; Pelletier, D. A.; S. Wud; Allison, D. P. AFM imaging of bacteria in liquid media immobilized on gelatin coated mica surfaces. *Ultramicroscopy* **2003,** *97*, 209–216.
(65) RJ, D.; RE., M. Elastic, flexible peptidoglycan and bacterial cell wall properties. *Trends Microbiol.* **1994,** *2* (2), 57-60.
(66) Thwaites, J. J.; Mendelson, N. H. Mechanical behaviour of bacterial cell walls. *Adv Microb Physiol* **1991,** *32*, 173-222.
(67) Kang, S.; Elimelech, M. Bioinspired Single Bacterial Cell Force Spectroscopy. *langmuir* **2009,** *25* (17), 9656-9659.
(68) Sheng, X.; Ting, Y. P.; Pehkonen, S. O. Force measurements of bacterial adhesion on metals using a cell probe atomic force microscope. *J. Colloid Interface Sci.* **2007,** *310* (2), 661-669.
(69) Chernyshova, I. V.; Hochella, M. F., Jr.; Madden, A. S. Size-dependent structural transformations of hematite nanoparticles. 1. Phase transition. *Phys. Chem. Chem. Phys.* **2007,** *9* (14), 1736-1750.
(70) Kallay, N.; Zalac, S. Stability of nanodispersions: a model for kinetics of aggregation of nanoparticles. *J. Colloid Interface Sci.* **2002,** *253* (1), 70-76.
(71) Stack, A. G.; Higgins, S. R.; Eggleston, C. M. Point of zero charge of a corundum-water interface probed with optical Second Harmonic Generation (SHG) and Atomic Force Microscopy (AFM): New approaches to oxide surface charge. *Geochim. Cosmochim. Acta* **2001,** *65* (18), 3055-3063.
(72) Gaboriaud, F.; Dufrene, Y. F. Atomic force microscopy of microbial cells: Application to nanomechanical properties, surface forces and molecular recognition forces. *Colloids Surf., B: Biointerfaces* **2007,** *54* (1), 10-19.
(73) Nel, A. E.; Madler, L.; Velegol, D.; Xia, T.; Hoek, E. M. V.; Somasundaran, P.; Klaessig, F.; Castranova, V.; Thompson, M. Understanding biophysicochemical interactions at the nano-bio interface. *Nat. Mater.* **2009,** *8* (7), 543-557.
(74) Navrotsky, A.; Mazeina, L.; Majzlan, J. Size-driven structural and thermodynamic complexity in iron oxides. *Science* **2008,** *319*, 1635-1638.
(75) Lu, H. M.; Han, F. Q.; Meng, X. K. Size-dependent thermodynamic properties of metallic nanowires. *J. Phys. Chem. B* **2008,** *112*, 9444-9448.
(76) Colvin, V. L. The potential environmental impact of engineered nanomaterials. *Nat. Biotechnol.* **2003,** *21* (10), 1166-1170.
(77) Klaine, S. J.; Alvarez, P. J. J.; Batley, G. E.; Fernandes, T. F.; Handy, R. D.; Lyon, D. Y.; Mahendra, S.; McLaughlin, M. J.; Lead, J. R. Nanomaterials in the environment: behavior, fate, bioavailability, and effects. *Environ. Toxicol. Chem.* **2008,** *27* (9), 1825–1851
(78) Verma, A.; Stellacci, F. Effect of Surface Properties on Nanoparticle-Cell Interactions. *Small* **2010,** *6* (1), 12-21.

(79) Tiede, K.; Boxall, A. B. A.; Tear, S. P.; Lewis, J.; David, H.; Hassellov, M. Detection and characterization of engineered nanoparticles in food and the environment. *Food Addit. Contam.* **2008,** *25* (7), 795-821.
(80) Bernardes, J. S.; Rezende, C. A.; Galembeck, F. Morphology and Self-Arraying of SDS and DTAB Dried on Mica Surface. *langmuir* **2010,** *26* (11), 7824-7832.
(81) Gouveia, R. F.; Galembeck, F. Electrostatic Charging of Hydrophilic Particles Due to Water Adsorption. *J. Am. Chem. Soc.* **2009,** *131* (32), 11381-11386.
(82) Zhang, W.; Yao, Y.; Chen, Y. Imaging and Quantifying the Morphology and Nanoelectrical Properties of Quantum Dot Nanoparticles Interacting with DNA. *J. Phys. Chem. C* **2011,** *115* (3), 599–606.
(83) Jacobs, H. O.; Leuchtmann, P.; Homan, O. J.; Stemmer, A. Resolution and contrast in Kelvin probe force microscopy. *J. Appl. Phys.* **1998,** *84* (3), 1168-1173.
(84) Yotsumoto, H.; Yoon, R.-H. Application of Extended DLVO Theory: II. Stability of Silica Suspensions. *J. Colloid Interface Sci.* **1993,** *157* (2), 434-441.
(85) Butt, H.-J.; Jaschke, M.; Ducker, W. Measuring surface forces in aqueous electrolyte solution with the atomic force microscope. *Bioelectrochem. Bioenerg.* **1995,** *38* (1), 191-201.
(86) Ninham, B. W. On progress in forces since the DLVO theory. *Advances in Colloid and Interface Science* **1999,** *83* (1-3), 1-17.
(87) Oss, C. J. v. *Interfacial Forces in Aquaeous Media*. Second Edition ed.; Taylor & Francis Group: Boca Raton, Florida, 2006; p 81-83.
(88) Alexander, J.; Magonov, S.; Moeller, M. In *Topography and surface potential in Kelvin force microscopy of perfluoroalkyl alkanes self-assemblies*, 2009; AVS: pp 903-911.
(89) Evans, S. D.; Ulman, A. Surface potential studies of alkyl-thiol monolayers adsorbed on gold. *Chem. Phys. Lett.* **1990,** *170* (5-6), 462-466.
(90) Semenikhin, O. A.; Jiang, L.; Iyoda, T.; Hashimoto, K.; Fujishima, A. A Kelvin probe force microscopic study of the local dopant distribution in conducting polybithiophene. *Electrochim. Acta* **1997,** *42* (20-22), 3321-3326.
(91) Hayashi, K.; Saito, N.; Sugimura, H.; Takai, O.; Nakagiri, N. Regulation of the surface potential of silicon substrates in micrometer scale with organosilane self-assembled monolayers. *langmuir* **2002,** *18* (20), 7469-7472.
(92) Sun, L.; Wang, J. J.; Bonaccurso, E. Nanoelectronic Properties of a Model System and of a Conjugated Polymer: A Study by Kelvin Probe Force Microscopy and Scanning Conductive Torsion Mode Microscopy. *J. Phys. Chem. C* **2010,** *114* (15), 7161-7168.
(93) Rittmann, B. E.; McCarty, P. L. *Environmental Biotechnology: principles and application*. McGraw-Hill Companies, Inc.: 2002.
(94) Amihay Freeman, S. A. G. G. Fixation and stabilization of *Escherichia coli* cells displaying genetically engineered cell surface proteins. *Biotech.Bioeng.* **1996,** *52* (5), 625-630.
(95) Chen, K. L.; Mylon, S. E.; Elimelech, M. Aggregation kinetics of alginate-coated hematite nanoparticles in monovalent and divalent electrolytes. *Environ. Sci. Tech.* **2006,** *40* (5), 1516-1523.
(96) Balaev, A. E.; Dvoretski, K. N.; Doubrovski, V. A. In *Refractive index of escherichia coli cells*, 2002; Valery, V. T., Ed. SPIE: pp 253-260.

(97) Rekveld, S. Ellipsometric Studies of Protein Adsorption onto Hard Surfaces in a Flow Cell. University of Twente, Enschede, Netherlands, 1997.
(98) dos Santos Furtado, A. L.; Casper, P. Different methods for extracting bacteria from freshwater sediment and a simple method to measure bacterial production in sediment samples. *J. Microbiol. Methods* **2000,** *41* (3), 249-257.
(99) Petosa, A. R.; Jaisi, D. P.; Quevedo, I. R.; Elimelech, M.; Tufenkji, N. Aggregation and Deposition of Engineered Nanomaterials in Aquatic Environments: Role of Physicochemical Interactions. *Environ. Sci. Technol.* **2010,** *44* (17), 6532-6549.
(100) Elimelech, M. Particle Deposition on Ideal Collectors from Dilute Flowing Suspensions - Mathematical Formulation, Numerical-Solution, and Simulations. *Separ. Technol.* **1994,** *4* (4), 186-212.
(101) Balnois, E.; Wilkinson, K. J.; Lead, J. R.; Buffle, J. Atomic force microscopy of humic substances: effects of pH and ionic strength. *Environ. Sci. Technol.* **1999,** *33* (21), 3911-3917.
(102) Burnham, N. A.; Chen, X.; Hodges, C. S.; Matei, G. A.; Thoreson, E. J.; Roberts, C. J.; Davies, M. C.; Tendler, S. J. B. Comparison of calibration methods for atomic-force microscopy cantilevers. *Nanotechnol.* **2003,** *14* (1), 1-6.
(103) Gutierrez, L.; Mylon, S. E.; Nash, B.; Nguyen, T. H. Deposition and Aggregation Kinetics of Rotavirus in Divalent Cation Solutions. *Environ. Sci. Technol.* **2010,** *44* (12), 4552-4557.
(104) Limbach, L. K.; Li, Y.; Grass, R. N.; Brunner, T. J.; Hintermann, M. A.; Muller, M.; Gunther, D.; Stark, W. J. Oxide Nanoparticle Uptake in Human Lung Fibroblasts: Effects of Particle Size, Agglomeration, and Diffusion at Low Concentrations. *Environ. Sci. Technol.* **2005,** *39* (23), 9370-9376.
(105) Pan, Y.; Neuss, S.; Leifert, A.; Fischler, M.; Wen, F.; Simon, U.; Schmid, G.; Brandau, W.; Jahnen-Dechent, W. Size-dependent cytotoxicity of gold nanoparticles. *Small* **2007,** *3*, 1941-1949.
(106) Ong, Y. L.; Razatos, A.; Georgiou, G.; Sharma, M. M. Adhesion Forces between E. coli Bacteria and Biomaterial Surfaces. *langmuir* **1999,** *15* (8), 2719-2725.
(107) Adamczyk, Z.; Weronski, P. Application of the DLVO theory for particle deposition problems. *Adv. Colloid Interface Sci.* **1999,** *83* (1-3), 137-226.
(108) Bostrom, M.; Williams, D. R. M.; Ninham, B. W. Specific ion effects: Why DLVO theory fails for biology and colloid systems. *Phys. Rev. Lett.* **2001,** *8716* (16), -.
(109) Boström, M.; Deniz, V.; Franks, G. V.; Ninham, B. W. Extended DLVO theory: Electrostatic and non-electrostatic forces in oxide suspensions. *Adv. Colloid Interface Sci.* **2006,** *123-126*, 5-15.
(110) Cail, T. L.; Hochella, M. F. The effects of solution chemistry on the sticking efficiencies of viable Enterococcus faecalis: An atomic force microscopy and modeling study. *Geochim. Cosmochim. Acta* **2005,** *69* (12), 2959-2969.
(111) Vadillo-Rodriguez, V.; Busscher, H. J.; Norde, W.; de Vries, J.; Dijkstra, R. J. B.; Stokroos, I.; van der Mei, H. C. Comparison of Atomic Force Microscopy Interaction Forces between Bacteria and Silicon Nitride Substrata for Three Commonly Used Immobilization Methods. *Appl. Environ. Microb.* **2004,** *70* (9), 5441-5446.
(112) Razatos, A.; Ong, Y.-L.; Sharma, M. M.; Georgiou, G. Evaluating the interaction of bacteria with biomaterials using atomic force microscopy. *J. Biomater. Sci., Polym. Ed.* **1998,** *9* (12), 1361-1373.

(113) Razatos, A.; Ong, Y.-L.; Sharma, M. M.; Georgiou, G. Molecular determinants of bacterial adhesion monitored by atomic force microscopy. *Proc. Natl. Acad. Sci. USA* **1998,** *95* (19), 11059-11064.
(114) Razatos, A.; Ong, Y.-L.; Boulay, F.; Elbert, D. L.; Hubbell, J. A.; Sharma, M. M.; Georgiou, G. Force Measurements between Bacteria and Poly(ethylene glycol)-Coated Surfaces. *langmuir* **2000,** *16* (24), 9155-9158.
(115) Meine, K.; Klo?, K.; Schneider, T.; Spaltmann, D. The influence of surface roughness on the adhesion force. *Surf. Interface Anal.* **2004,** *36* (8), 694-697.
(116) Camesano, T. A.; Logan, B. E. Probing Bacterial Electrosteric Interactions Using Atomic Force Microscopy. *Environ. Sci. Tech.* **2000,** *34* (16), 3354-3362.
(117) Jucker, B. A.; Harms, H.; Hug, S. J.; Zehnder, A. J. B. Adsorption of bacterial surface polysaccharides on mineral oxides is mediated by hydrogen bonds. *Colloids Surf., B: Biointerfaces* **1997,** *9* (6), 331-343.
(118) Van Oss, C. J.; Good, R. J.; Chaudhury, M. K. The role of van der Waals forces and hydrogen bonds in "hydrophobic interactions" between biopolymers and low energy surfaces. *J. Colloid Interface Sci.* **1986,** *111* (2), 378-390.
(119) Lantz, M. A.; O'Shea, S. J.; Welland, M. E.; Johnson, K. L. Atomic-force-microscope study of contact area and friction on $NbSe_2$. *Phys. Rev. B* **1997,** *55* (16), 10776.
(120) Jaschke, M.; Butt, H.-J.; Manne, S.; Gaub, H. E.; Hasemann, O.; Krimphove, F.; Wolff, E. K. The atomic force microscope as a tool to study and manipulate local surface properties. *Biosens. Bioelectron.* **1996,** *11* (6-7), 601-612.
(121) Weisenhorn, A. L.; Maivald, P.; Butt, H. J.; Hansma, P. K. Measuring adhesion, attraction, and repulsion between surfaces in liquids with an atomic-force microscope. *Phys. Rev. B: Condens. Matter* **1992,** *45* (19), 11226.
(122) Johnson, K. L.; Kendall, K.; Roberts, A. D. Surface Energy and the Contact of Elastic Solids. *Proc. R. Soc. Lond. A* **1971,** *324* (1558), 301-313.
(123) Chu, Y.-S.; Dufour, S.; Thiery, J. P.; Perez, E.; Pincet, F. Johnson-Kendall-Roberts Theory Applied to Living Cells. *Phys. Rev. Lett.* **2005,** *94* (2), 028102.
(124) Hodges, C. S.; Looi, L.; Cleaver, J. A. S.; Ghadiri, M. Use of the JKR Model for Calculating Adhesion between Rough Surfaces. *langmuir* **2004,** *20* (22), 9571-9576.
(125) Radmacher, M.; Fritz, M.; Cleveland, J. P.; Walters, D. A.; Hansma, P. K. Imaging Adhesion Forces and Elasticity of Lysozyme Adsorbed on Mica with the Atomic-Force Microscope. *langmuir* **1994,** *10* (10), 3809-3814.
(126) Perry, C. C.; Weatherly, M.; Beale, T.; Randriamahefa, A. Atomic force microscopy study of the antimicrobial activity of aqueous garlic *versus* ampicillin against *Escherichia coli* and *Staphylococcus aureus*. *J. Sci. Food Agric.* **2009,** *89* (6), 958-964.
(127) Lan, G.; Wolgemuth, C. W.; Sun, S. X. Z-ring force and cell shape during division in rod-like bacteria. *PNAS* **2007,** *104* (41), 16110-16115.
(128) Kostoglou, M.; Karabelas, A. J. Effect of Roughness on Energy of Repulsion between Colloidal Surfaces. *J. Colloid Interface Sci.* **1995,** *171* (1), 187-199.
(129) Walz, J. Y. The effect of surface heterogeneities on colloidal forces. *Adv. Colloid Interface Sci.* **1998,** *74*, 119-168.
(130) Hoek, E. M. V.; Bhattacharjee, S.; Elimelech, M. Effect of Membrane Surface Roughness on Colloid-Membrane DLVO Interactions. *Langmuir* **2003,** *19* (11), 4836-4847.

(131) Xu, L.-C.; Vadillo-Rodriguez, V.; Logan, B. E. Residence Time, Loading Force, pH, and Ionic Strength Affect Adhesion Forces between Colloids and Biopolymer-Coated Surfaces. *langmuir* **2005,** *21* (16), 7491-7500.
(132) McNamee, C. E.; Pyo, N.; Tanaka, S.; Vakarelski, I. U.; Kanda, Y.; Higashitani, K. Parameters affecting the adhesion strength between a living cell and a colloid probe when measured by the atomic force microscope. *Colloids Surf., B: Biointerfaces* **2006,** *48* (2), 176-182.
(133) de Graaf, J.; Dijkstra, M.; van Roij, R. Adsorption trajectories and free-energy separatrices for colloidal particles in contact with a liquid-liquid interface. *J. Chem. Phys.* **2005,** *132* (16), 164902-14.
(134) Cao, T.; Tang, H.; Liang, X.; Wang, A.; Auner, G. W.; Salley, S. O.; Ng, K. Y. S. Nanoscale investigation on adhesion of *E. coli* to surface modified silicone using atomic force microscopy. *Biotech. Bioeng.* **2006,** *94* (1), 167-176.
(135) *E. coli* Statistics. Available at: http://gchelpdesk.ualberta.ca/CCDB/cgi-bin/STAT_NEW.cgi
(136) McMichael, J. C.; Ou, J. T. Structure of common pili from Escherichia coli. *J. Bacteriol.* **1979,** *138* (3), 969-975.
(137) Cheng, S. Y.; Bryant, R.; Doerr, S. H.; Wright, C. J.; Williams, P. R. Investigation of Surface Properties of Soil Particles and Model Materials with Contrasting Hydrophobicity Using Atomic Force Microscopy. *Environ. Sci. Tech.* **2009,** *43* (17), 6500-6506.
(138) Dong, R.; Yu, L. Y. E. Investigation of surface changes of nanoparticles using TM-AFM phase imaging. *Environ. Sci. Tech.* **2003,** *37* (12), 2813-2819.
(139) Koeneman, B. A.; Zhang, Y.; Westerhoff, P.; Chen, Y.; Crittenden, J. C.; Capco, D. G. Toxicity and cellular responses of intestinal cells exposed to titanium dioxide *Cell Biol. Toxicol.* **2009,** *26* (3), 225-238.
(140) Schilling, J. D.; Mulvey, M. A.; Hultgren, S. J. Structure and Function of Escherichia coli Type 1 Pili: New Insight into the Pathogenesis of Urinary Tract Infections. *J. Infect. Dis.* **2001,** *183* (S1), S36-S40.
(141) Das, M.; Hart-Van Tassell, A.; Urvil, P. T.; Lea, S.; Pettigrew, D.; Anderson, K. L.; Samet, A.; Kur, J.; Matthews, S.; Nowicki, S.; Popov, V.; Goluszko, P.; Nowicki, B. J. Hydrophilic Domain II of Escherichia coli Dr Fimbriae Facilitates Cell Invasion. *Infect. Immun.* **2005,** *73* (9), 6119-6126.
(142) Madigan, M. T.; Martinko, J. M.; Dunlap, P. V.; Clark, D. P. *Brock Biology of Microorganisms*. 9th ed.; Benjamin Cummings 2000.
(143) Prasher, R.; Bhattacharya, P.; Phelan, P. E. Brownian-motion-based convective-conductive model for the effective thermal conductivity of nanofluids. *J. Heat Transf.* **2006,** *128* (6), 588-595.

CHAPTER 7

PROBING THE NANOSCALE HYDROPHOBICITY

Work of this chapter is related to the publications or manuscripts:
Wen Zhang, Yongsheng Chen. Probing the nanoscale hydrophobicity using atomic force microscopy. In preparation.

7.1. Abstract

Innovative experimental approach was developed to resolve two important surface properties of nanomaterials, hydrophobicity and surface potential, at nanoscale. These two surface properties are two decisive factors in the fate, transport, and surface interactions of nanomaterials in the environment. A theoretical framework was first derived to correlate the adhesion force between the AFM cantilever tip and any surfaces of nanomaterials to the surface energy that are conventionally obtained from the contact angle measurement (CAM). Adhesion forces between the tip and surfaces of different NPs were acquired from the force mode of AFM, and the surface energy or hydrophobicity was then derived based on the adhesion forces. Finally, the surface hydrophobicity derived from adhesion force was found to be well comparable with those derived from contact angles measurement. However, the adhesion force measurement gives far high sensitivity and resolution than that of CAM in resolving the heterogeneity of surface hydrophobicity.

7.2. Introduction

Surface hydrophobicity (or hydrophilicity) plays key roles in surface interactions (e.g., partitioning), and largely determines environmental fate, transport and biological interactions of nanomaterials *(1)*. Manipulation of surface hydrophobicity has important applications. For example, hydrophobic NPs such as polymeric NPs are designed for bioremediation of hydrophobic contaminants *(2)*. Chitosan or chitosan-DNA NPs and functionalized gold NPs serve as vehicles for drug and gene deliveries *(3-6)*. However,

upon release into the environment, NPs are inevitably interacting with electrolyte ions, proteins (e.g., as albumin and fibronectin) *(7)*, and natural organic matter or NOM (e.g., humic acid and polysaccharides) *(8)*, which may alter surface hydrophobicity and morphology *(9)*, and thus result in different biavailability and biological consequences. For instance, the hydrophobic surfaces promote bacterial adhesion *(10, 11)*, placing high potential of particle accumulation on cellular surfaces *(13, 14)*.

Traditionally, partitioning affinity of environmental pollutants in polar or nonpolar solvents can be evaluated by octanol-water partitioning coefficient (K_{ow}) measurement. A high value of K_{ow} generally indicates a high potential to partition into the organic phase for chemicals, which thus may pose high risks of bioaccumulation, such as DDT (di(pflra-chlorophenyl)-trichloroethane) or dioxins. K_{ow} as an partitioning indicator for most nanomaterials has not been established *(12)*, largely because NPs are dramatically different heterogeneous properties as compared to conventional dissolvable pollutants *(13, 14)*. For instance, most NPs are insoluble and hardly maintained as stable dispersion due to aggregation and precipitation and this may result in inconsistency and artifacts in determination of K_{ow} *(12, 15)*. To assess material hydrophobicity, the contact angle measurement (CAM) is still the most appropriate, simple-to-adopt and widely used method *(16)*. Contact angles formed by static, macroscopic liquid droplets (e.g., water) at the surface of a flat solid in an inert atmosphere reflect an average surface properties of bulk materials. However, it might not be appropriate to extrapolate average or macroscopic hydrophobicity to the nanoscale properties *(17)*, because surface roughness*(10, 18, 19)*, heterogeneity *(20)*, and the presence of gas pockets (contained in the cavities or pores of the particle layer *(21)*) on material surfaces may vary the contact angles. For example, the gas confinement on the flat surface layer may make the liquid droplet float, shield the droplet adhesion to the substrate surface. As a result, the contact angle measurement may be unrepresentative of the average properties of the materials

and even erroneous. Furthermore, the nanoscale structure and surface chemistry ultimately may be more and more dependent on the specific crystallographic planes that are exposed to the bulk liquid *(22, 23)*. Thus, CAM is by no means sufficient to reflect the nanoscale hydrophobicity and novel approach is needed to overcome the shortcomings of K_{ow} or CAM in probing the hydrophobicity of NPs.

In line with this effort, previous studies have explored atomic force microscopy (AFM) for probing the surface characteristics. For the purpose of characterizing hydrophobicity, the force mode of AFM is often used to generate adhesion force, which is shown to be sensitive to the surface energies *(24)* and hydrophilic or hydrophobic characteristics of the interacting surfaces *(25)*. AFM utilizes a sharp tip to measure the adhesion force that arises from adhesive bonds between the two interacting surfaces. Adhesion force is also called rupture force that is used to break the adhesive bonds and the external energy applied in the rupture process is the work of adhesion or adhesion energy, which can be obtained from the force-distance curve, as illustrated previously in Figure 6.11. Based on the continuum thermodynamic approach (CTA), adhesion energy is related to the macroscopic observations of contact angles (e.g., the Young-Dupré equation) and potentially renders the nature of hydrophobicity of the probed sites of NPs *(26, 27)*. Work of adhesion between a Si_3N_4 AFM tip and methyl (CH_3), amine (NH_2), methyl fluoride (CF_3), and ester ($CO(OCH_3)$) end-group self-assembled monolayers (SAMs), as well as hydroxyl (OH) functionalized surfaces showed quantitative agreement with CAM of the surface energies *(28)*. For nanomaterials, it is largely unknown if such correlation or agreement between adhesion energy and CAM may also exist. Moreover, surface energy of nanomaterials is dependent on the size and shape *(29)*, surface structures *(27)*, and lattice parameters *(30)*. Clearly, a direct correlation between adhesion energy and CAM will allow us to better understand the nature of nanoscale surface hydrophobicity *(31)*, such as the effects of crystallographic orientation and

distribution on the surface energy variations of the exposure surfaces of nanocrystals *(32-35)*. Since nanomaterial surfaces also have typical surface functional groups such as OH^- as SAMs, it is worth studying whether the correlation between adhesion energy and surface energy may also exist.

In this regard, this study developed a generic model that correlates adhesion force to CAM and used this model to convert adhesion force to describe the nanoscale hydrophobicity. The generic model works for all kinds of surfaces (not limited to a certain surface groups), which is different from previous literature *(26, 27)*. Three types of SAMs with different surface functional groups ranging from hydrophilic to hydrophobic properties were examined to confirm the validity of the model. Finally, we measured the adhesion force between the Si_3N_4 tip and various surfaces of commercial NPs, including hematite (α-Fe_2O_3), TiO_2, CeO_2, ZnO, SiO_2, CuO, and Ag. The purpose of this chapter is to demonstrate a potentially useful tool with AFM in characterizing nanoscale hydrophobicity of materials and to provide insight into fundamental mechanisms of nanoscale processes.

7.3. Theoretical relationship between adhesion force and surface energy

The relationship between adhesion force and CAM was established on the basis of the free energy changes in the particle nucleation, mechanical contact model (e.g., JKR), and the continuum thermodynamic approach (CTA). If we assume the energistics during the adhesion force measurement (see Figure 7.1) follows the principle of the free energy change for a nucleation process, the free energy change (ΔG) of the whole system outlined by the red box is given by the sum of internal energy and surface energy *(36, 37)*:

$$\Delta G = \Delta G_i + \sigma \cdot \Delta S \quad (1)$$

where ΔG_i is the internal energy change, σ is the surface energy per unit surface area (mJ/m^2), and ΔS is the change of surface areas during the interactions between the tip and sample surface. This principle is enshrined in the concept of a critical nucleus of radius in the energetics of nucleation *(38)*. The internal energy is a function of temperature (T), so the free energy change is only related to the surface energy, which is the energy for reconstructing the solvent molecules at the solid-liquid interface.

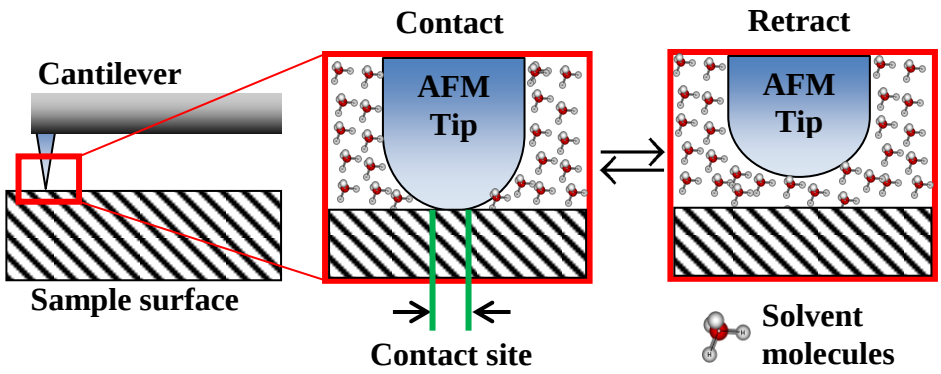

Figure 7.1. Scheme of adhesion force measurement with AFM and basis for the model employed to calculate the free energy changes between the contact and retraction states.

To engage the cantilever tip to contact the sample surface, a certain amount of external work is applied to the system to expel the solvent molecules adsorbed on both tip and samples surfaces. The contact site area between a spherical tip and a planar surface can be estimated through the Johnson-Kendall-Roberts (JKR) *(39)*, a classic contact mechanics model used to calculate the contact radius (the model assumes the contact is a circular and planar contact site) *(40)*. The contact radius (a) is a function of the loading force (F_L) as shown in Eq. (8) of chapter 6 and the F_L can be determined by aligning the initial laser deflection and the maximum limit of laser deflection *(41)*. To separate the contact, the tip will be dragged due to the adhesion force (F_{ad}) as shown in Figure 6.11c and certain adhesion energy (W_{ad}) is needed for the separation. W_{ad} can be obtained from the integration in the force-distance curve ($W_{ad} = \int F_{ad} dZ$, Z is the interaction distance; the triangle gray area in Figure 6.11c). W_{ad} is related to the JKR model by $W = \frac{W_{ad}}{\pi a^2}$, where W is the adhesion energy per unit contact area in the JKR equation. Thus, the adhesion energy increases the surface energy of the system in the red box after the tip is pulled up and the adhesion energy equals the surface energy variation *(42)*:

$$W_{ad} = \sigma \cdot \Delta S = (\gamma_{SL} + \gamma_{TL} - \gamma_{TS}) \cdot \pi \cdot a^2 \quad (2)$$

where γ_{SL}, γ_{TL}, and γ_{TS} are the interfacial energies between the sample surface and liquid interfaces, between the tip surface and liquid interfaces, and between the tip and sample surface, respectively (mJ/m^2). Eq. (2) is supported by the depletion attraction mechanism in Asakura–Oosawa theory *(43-45)*, which indicates that when the two surfaces contact, water molecules are stripped from the interspace and the water molecules outside the two surfaces will exert pressure on the two contact bodies, which enhances the attraction between the two surfaces, as shown in Figure 7.1. The free energy is released when the surfaces of two particles come into contact because of the surface energy changes *(43)*, so

to reconstruct the surface energy (solvation layers) before the contact, W_{ad} is needed. According to the Dupré equation, γ_{SL} and γ_{TL} can be further expressed as:

$$\gamma_{SL} = \gamma_S + \gamma_L - W_{SL} \tag{3}$$

$$\gamma_{TL} = \gamma_T + \gamma_L - W_{TL} \tag{4}$$

$$\gamma_{TS} = \gamma_T + \gamma_S - W_{TS} \tag{5}$$

Eqs. (3)~(4) indicate that the interfacial energies are directly linked to solid (sample and tip) and liquid solvent surface energies (γ_S, γ_T and γ_L) and the work of adhesion (W_{SL} W_{TL} and W_{TS}) *(27)*. W_{SL} can be deduced from the water contact angle using the Young equation:

$$W_{SL} = \gamma_{LV}(1+\cos\theta_{SL}) \approx \gamma_L(1+\cos\theta_{SL}) \tag{6}$$

where γ_{LV} is the interfacial energy between the liquid and vapor interface (mJ/m^2), θ_{SL} and θ_{TL} are the contact angles between the probe liquid and sample and tip surfaces. W_{TL} is equal to W_{TS} if the tip only involves London dispersion interactions with the solvent molecules or sample surfaces *(26)*. Combining Eq. (2)~(6) yields the relationship between W_{ad} and contact angles:

$$W_{ad} = (\gamma_S - \gamma_L \cdot \cos\theta_{SL} + \gamma_T - \gamma_L \cdot \cos\theta_{TL}) \cdot \pi \cdot a^2 \tag{7}$$

Eq. (7) can be converted to adhesion force-based form according to the JKR model:

$$\frac{W_{ad}}{\pi \cdot a^2} = \frac{F_{ad}}{1.5\pi \cdot R_C} = \gamma_L - \gamma_L \cdot \cos\theta_{SL} \tag{8}$$

where R_C is the radius of curvature for the cantilever tip (nm) and usually is reported by the manufacturer or determined by SEM. Eq. (8) indicates that adhesion force (F_{ad}) is

linearly related to the contact angle (θ_{SL}) and the surface tension of probe liquids (γ_L), which is known for water in our case. Thus, by measuring the adhesion force, we can indirectly determine the nanoscale contact angle (θ_{SL}) that potentially exits on the sample surface within a contact surface area of $\pi \cdot a^2$. Clearly, CAM is unable to capture this nanoscale contact angle. The following sections will experimentally verify the applicability of this linear model by testing different SAM surfaces with known contact angles and further used this method to examine the nanoscale surface hydrophobicity of a number of commercial nanomaterials.

7.4. Materials and Methods

7.4.1. Metal-based NPs

NPs and their relevant properties are shown in Table 7.1. All NPs were used as received without further purification. Water suspensions of different NPs were made by dispersing the power forms into deionized (DI) water with the mass concentration of approximately 100 mg/L, except that AgNPs with citrate acid as surface coating and stabilizer were purchased in a suspension form from vendor. After dispersal in DI water, the NP suspension was sonicated for 35-45 min (Misonix sonicator S-4000, Qsonica, LLC). The morphology and sizes were determined by transmission electron microscopy (TEM) on a Philips EM420 at 47~120 kV.

Table 7.1. List of the metal-based NPs used in this study.

NPs	Average particle diameter (nm)	pH of the suspension	Crystal type	Vendor
Fe_2O_3*	49	4.0	Alpha (hematite)	Lab-synthesized *(46)*
TiO_2	25	6.9	Anatase	Aldrich
CeO_2	25	4.5	Cubic (fluorite)	Aldrich
ZnO	50	6.8	--	Aldrich
SiO_2	33	5.9		Aldrich
CuO	42	7.0	Gamma and alpha	Nanostructured &AmorphousMaterials
Ag	80	5.0	Cubic	Ted Pella

7.4.2. Substrate surfaces

SAMs are well-ordered structures and allow homogenous interactions at different microscopic scales. In this study, four different SAMs including poly(ethyleneglycol) (PEG), hydrophobic silane, biotin, and biotin-streptavidin conjugates coated on 2×2 cm glass slides were purchased from MicroSurfaces Inc. USA. The gold substrate surfaces functionalized with different fractions of CH_3- and OH- groups were synthesized *(26)*. Briefly, gold (111) substrate surfaces (Agilent, USA) were modified by immersion for 14 h in ethanol solutions containing 1 mM $HS(CH_2)_{11}CH_3$ and $HS(CH_2)_{11}OH$ (11-Mercapto-1-undecanol, Sigma-Aldrich, USA) in various proportions (0:100, 25:75, 50:50, 75:25, and 100:0) and then rinsed with ethanol before use.

7.4.3. Cantilever tips

Two kinds of cantilever tips were used in the experiments, including silicon nitride (Si_3N_4) tip with Cr/Au (5/50) coating on the both reflex side and tip surface (RC800PB, Asylum Research, USA), and none-coated Si_3N_4 cantilevers (MCLT, Veeco, USA). Hydrophobic cantilevers were obtained by functionalizing the gold-coated Si_3N_4 cantilevers with CH_3 groups following the same method as described in section 3.4.1. All the cantilevers have V-shaped probes and other relevant properties are summarized in Table 7.2.

Table 7.2. Summary of the cantilever tip properties.

Cantilever type	Surface functionalization	Radius of curvature (R_C) of the tip (nm)	Spring constant (N/m)[c]	Frequency (kHz)	Water contact angle (^{o})
Gold-coated Si_3N_4 tip[a]	CH_3-terminated end group	42 ±12	0.06 ±0.03	17 ±4	105
Gold-coated Si_3N_4 tip[a]	None	42 ±12	0.06 ±0.03	17 ±4	0
Si_3N_4 tip[b]	None	20 ±5	0.07 ±0.05	22 ±7	15

[a,b] more information is available at http://www.asylumresearch.com/Probe/RC800PB,Olympus and http://www.brukerafmprobes.com/p-3444-mlct.aspx. [c] spring constants (K_{sp}) were determined by the Agilent Thermal K tuning modulus (see Agilent 5500 User's Guide for details) *(47)*.

7.4.4. Spin coating of nanomaterials

Before adhesion force measurement and CAM, NPs need to be immobilized on the clean and flat substrate surfaces. The spin coating procedures for different NPs were similar and have been introduced previously in section 3.4.5 of Chapter 3.

7.4.5. Contact angle measurement

Equilibrium advancing contact angles (θ_L) were measured on a Model 250 Ramé-hart goniometer at ambient conditions. Details of the operation can be found in section 3.4.5 of Chapter 3.

7.4.6. Adhesion force measurement with AFM

The immobilized NPs on the clean silicon wafer were rinsed with DI water to remove any loosely bonded NPs and then placed in liquid cells containing DI water. 10 locations at the NP layer were randomly selected to measure the adhesion force in force or contact mode, as shown in Figure 7.2. At least 10 force measurements were performed at each location. Based on the obtained adhesion forces, a histogram of adhesion force distribution was generated for each sample. Two kinds of cantilever tips (Si_3N_4 tip with and without gold coating) were used to repeat the adhesion force measurement. Detailed operation procedures of AFM in contact mode were introduced in section 6.3.9 of Chapter 6.

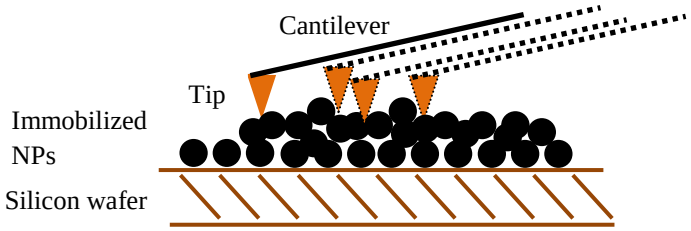

Figure 7.2. Schematics of adhesion force measurement with AFM at multiple locations with cantilever tips shown as dashed lines.

7.5. Results and discussion

7.5.1. Morphology of NPs

Figure 7.3a~d show TEM micrographs of the morphology of TiO_2, ZnO, SiO_2, and CuO, used in this study, while the TEM images of hematite (α-Fe_2O_3), CeO_2, and AgNPs can be found in previous Chapters 3~6. The four types of NPs (TiO_2, ZnO, SiO_2, and CuO) are close to spherical, and their diameters were 25.0 ± 5.9, 52.0 ± 9.1, 33.2 ± 0.8, and 42.1 ± 1.8 nm, which were consistent with the manufacturer-reported values. Figure 7.3e~h provide the particle size distribution histograms computed from TEM images via the image processing and analysis program ImageJ. TiO_2 and ZnO NPs had relatively broad size distribution, while SiO_2 and CuO NPs had much narrow size distribution.

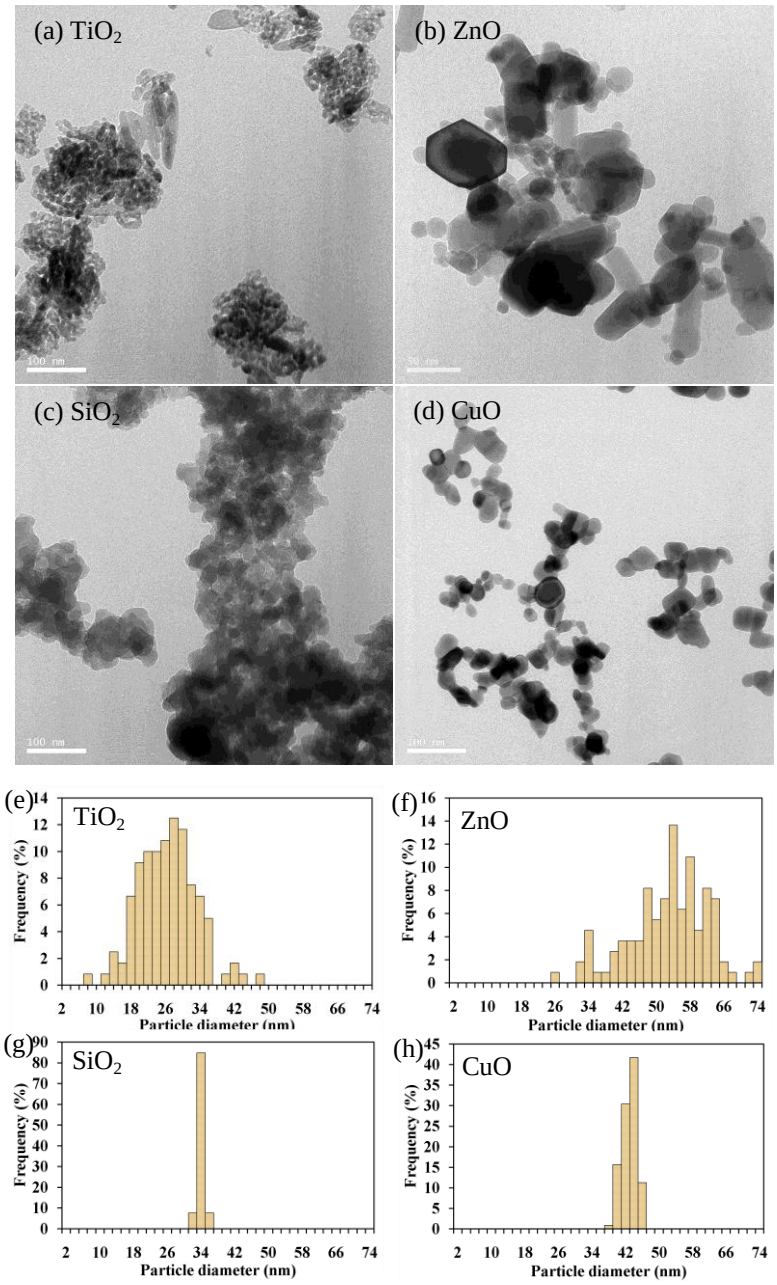

Figure 7.3. (a~c) TEM images of TiO_2, ZnO, SiO_2, and CuO, on a carbon-coated grid. All the white bars on the bottom left equals 100 nm, except the one in (b) that equals 50 nm. (e~h) Particle diameter distribution histrograms.

7.5.2. Contact angles of water on surfaces of NPs

Contact angle is a rapid measure of surface hydrophobicity with surface energy calculated from Young's relation. Hydrophilic surfaces usually have a water droplet that completely spreads out on the solid surface and the contact angle will be 0 ° to 30 °. If the surface is hydrophobic, the contact angle will be larger than 90 ° or as high as ~120 °. Based on the results of CAM for different NPs as shown in Table 7.3, the surface hydrophobicity is shifting from highly hydrophilic to hydrophobic in an order of TiO_2 > Fe_2O_3 > CuO > CeO_2 > SiO_2 > ZnO > AgNPs (coated with citrate acid). When the advancing water contact angle on the surface is less than 15^o, the hydration force becomes significant which may greatly stabilizes the colloidal suspension *(48)*, while the hydrophobic force becomes appreciable when θ_a>64^o which provides main driving force for particle coagulation *(49)*. The CAM for the same kinds of NPs may vary significantly from different literature, and this is because the contact angle or hydrophobicity is sensitive to many factors (to name a few, impurities or surface contamination, surface coating). One example is that a perfect pure gold surface is hydrophilic but with contamination of carbon in crystal lattice most gold surfaces appear slightly hydrophobic *(50)*. More examples on the surface functionalization effects on the surface hydrophobicity are reflected by the measurement of contact angle for different SAMs. As shown in Table 7.4, the hydrophobicity of the same substrate surfaces (i.e., gold and glass surfaces) is dramatically changed after being coated with different fractions of CH_3 groups or other protein molecules (e.g., biotin and streptavidin). These CAMs will be used to compare with and validate the model calculation of nanoscale contact angles based on the adhesion force measurement in the following sections.

Table 7.3. Water contact angles for various NP surfaces.

NPs	Contact angles (°)	Typical photos of the water droplet
Fe_2O_3	16.5 ± 0.6	
TiO_2	7.5 ± 4.3	
CeO_2	49.5 ± 0.5	
ZnO	69.0 ± 0.4	
SiO_2	63.4 ±9.5	
CuO	41.0 ± 0.6	
Ag	72 ± 3.2	

Table 7.4. Water contact angles for various substrate surfaces.

Gold surfaces coated with CH_3	Molar fractions of CH_3				
	0%	25%	50%	75%	100%
Contact angle (°)	30±1	60±2	82±2	100±3	105±5
SAMs	PEG-coated surface	Silane-coated surface	Biotin-coated surface	Biotin and streptavdin conjugated surface	
Contact angle (°)	10±2	96±2	18±3	23±1	

7.5.3. Adhesion force measurement between functionalized tips with different surface functionalization and CH_3-terminated surfaces

To verify the relationship between adhesion force and surface hydrophobicity, I also measured the adhesion force in DI water between different tips and the surfaces coated with different molar fractions of CH_3-terminated alkanethils according to the method of Alsteens, et al. *(26)*. With higher molar fractions of CH_3-alkanethiols, the surface tended to decrease the surface energy and became increasingly hydrophobic. Our results in Figure 7.4a indicated that adhesion forces for different tips all increased as the molar fraction of CH_3-alkanethils increased, which is consistent with previous literature *(26, 27)*. Compared to the gold tip coated with CH_3 ligands, the bare gold and Si_3N_4 tips also yielded similar dependence on surface functionalization for adhesion force. However, when adhesion forces is plotted versus the values of ($-\cos\theta_{SL}$), the sensitivity of adhesion forces over the change in contact angles is highest for CH_3-gold tip, followed by the Si_3N_4 and bare gold tips, which is indicated by the slopes of the linear regression equations. Moreover, from the fitting quality, the results for CH_3-gold tip reached the most excellent linear fitting with a correlation coefficient of 0.98, which is consistent with our model relation in Eq. (8). In contrast, the trend for the Si_3N_4 and bare gold tips appeared less linear with lower correlation coefficients. Thus, it is verified again that the adhesion force measurement using CH_3-gold tips can yield a good correlation with surface hydrophobicity.

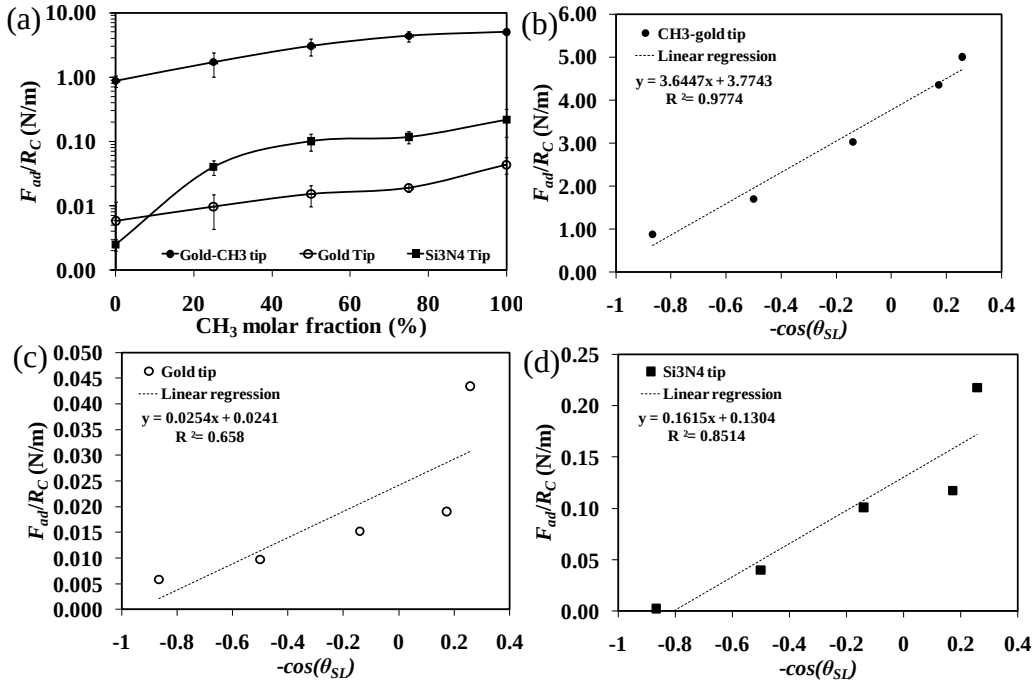

Figure 7.4. Adhesion force as a function of the surface fraction of CH_3-terminated alkanethils.

7.5.4. Adhesion force measurement between CH_3-coated gold tip and four types of SAMs

In addition to the above correlation on surfaces with CH_3-terminated alkanethils, it would be interesting to explore whether such a relationship exit on surfaces with other ligands or functional groups that are representative of environmentally relevant surface properties, because as mentioned previously the released NPs are most likely to interact with their surrounding environments (e.g., NOM) and thus dramatically changed their surface functionalization, making surface ligands of NPs rather complicated. Thus, to verify the correlation between adhesion forces and contact angles on multiple types of surfaces is necessary before applying the method to probe the surface characteristics of NPs. As indicated above, SAMs may serve as model surfaces with well-manipulated surface coatings of different functional groups and hydrophobicity. In this study, I measured the adhesion forces between the three types of tips and four different SAM surfaces and the results are shown in Figure 7.5a. Clearly, CH_3-gold tip yielded a clear trend over different SAM surfaces, while the other two tips had less apparent trend. This difference becomes more striking in Figure 7.5b~c, which plotted adhesion forces versus ($-\cos\theta_{SL}$). Visual inspection of the data fitting using linear regression reveals that only CH_3-gold tip presented a relatively good linear relationship that is anticipated by our model in Eq. (8), while the other two tips had some random changes in adhesion force on the hydrophic SAM surfaces (e.g., PEG, biotin, and streptavidin). Moreover, for CH_3-gold tip, the sensitivity of the adhesion force to the hydrophobicity of SAM surfaces seems lower as compared to the slope of the linear fitting equation in Figure 7.4b on CH_3-terminated surfaces. This matches the previous observations that the best agreement between the calculated surface energies based on adhesion force and experimental values is found for the $–CH_3/–CH_3$ system *(51)*, compared to other interacting systems (–COOH/–COOH, $–CH_3$/–COOH, $–CH_3$ or –COOH/octenyl-trichlorosilane). Because the

released metal-based NPs tend to interact with NOM (e.g., humic acid and fulvic acid), proteins and salts in the environment *(7, 52, 53)*, the typical surface groups found on metal-based NPs may include $–NH_2$, –OH and –COOH pairs as well as common cations and anions (e.g., Na^+, Ca^{2+}, Cl^- and SO_4^{2-}) in water. Thus, most metallic and metal oxide NPs in the environment should be close to hydrophilic, as supported by the contact angle results in Table 7.3, and the potential changes in surface hydrophobicity of NPs after entry into the environment may occur depending on the complexation with NOM or proteins. Thus, the results obtained for the four types of SAM surfaces may provide insight into the representative surface characteristics, especially for the hyphophilic surfaces.

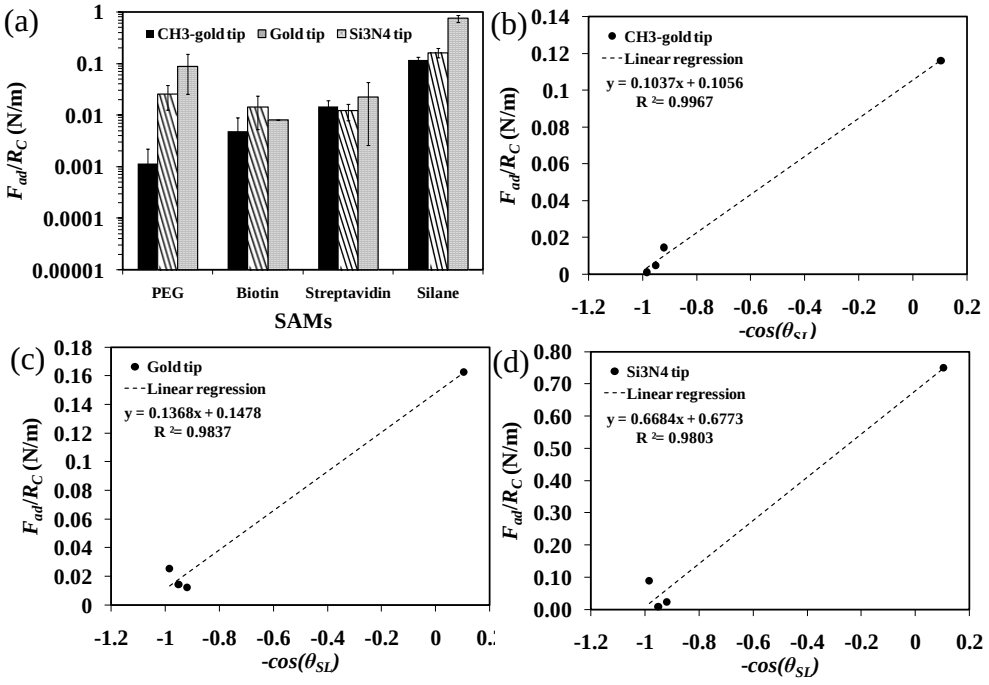

Figure 7.5. (a) Adhesion forces between three types of tips and different SAM surfaces. (b)~(d) Adhesion forces versus the value of ($-\cos\theta_{SL}$) for three types of tips.

7.5.5. Adhesion force measurement between the CH_3-coated gold tip and different NPs

In this section, I explored the applicability of the above method in evaluating the surface hydrophobicity of various metallic or metal oxide NPs using CH_3-coated gold tips that exhibit excellent correlation between adhesion force and contact angle. Theoretically, our model in Eq. (8) seems to be directly usable to calculate the contact angle based on adhesion force without any unknowns. However, one may also find that the slopes in the linear fitting equations in Figure 7.4b and Figure 7.5b are different by approximately one order of magnitude. The slope of Eq. (8) can theoretically be obtained knowing that the surface energy of water (γ_L) is 72.8 mJ/m^2 or 0.0728 N/m at 25 ^{o}C. Thus, the slope should be approximately 0.34 N/m at 25 ^{o}C, which is close to that (0.10 N/m) for SAM surfaces in Figure 7.5b. The discrepancies between the theoretical and the experimental values may be attributed to temperature fluctuation or other experimental artifacts caused by different cantilever tips *(54, 55)*. To avoid such potential artifacts and discrepancies, a "calibration curve" is needed for each CH_3-coated gold tip to obtain the actual slope in the linear curve of adhesion force versus contact angle using model surfaces such as SAMs. Here in this study, I used the "calibration equation" in Figure 7.5b to calculate the contact angles for different NPs based on adhesion forces and the results are shown in Figure 7.6. The model calculated contact angles are relatively consistent with the experimental measurements with good agreement obtained for CeO_2, ZnO, and AgNPs, as indicated by the low relative errors. In contrast, the calculated contact angles for the rest of NPs appear higher than those experimental values except ZnO and SiO_2 NPs. The difference between the model and experimental determinations of contact angles may be caused by experimental artifacts, but also largely represent a certain unique interfacial properties of NPs probably due to the effect of hydration on interfacial energy at nanoscale *(27, 56)*. According to Chiu et al. *(56)*, this effect arises from a geometrical effect caused by the curvature of the particle-water interface and consequently, the

surface hydrophobicity may shift from hydrophobic for ultrasmall NPs to hydrophilic properties for large particles. This may explains why the model calculated contact angles for most NPs are higher than those determined experimentally.

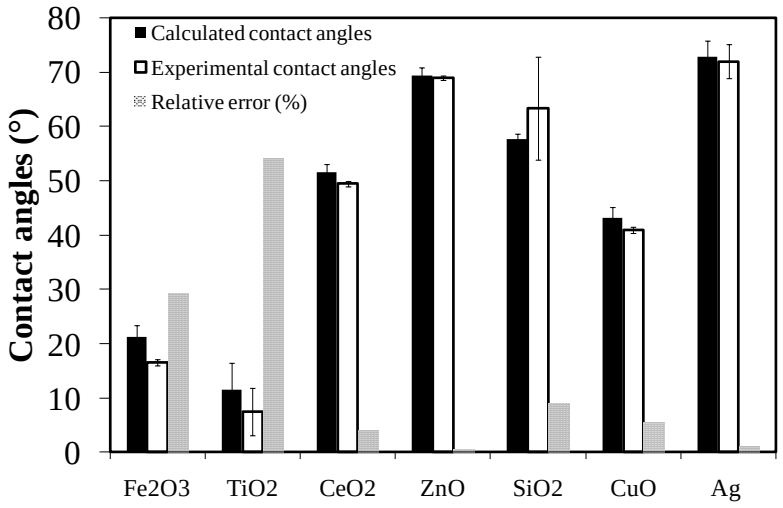

Figure 7.6. (a) Adhesion forces between three types of tips and different SAM surfaces. (b)~(d) Adhesion forces versus the value of (-cosθ_{SL}) for three types of tips.

7.5.6. Environmental applications

As stressed in the introduction, surface hydrophobicity dictates partitioning affinity of NPs between organic and inorganic phases and influences the fate and transport of NPs in aquatic systems. Knowledge of characterizing the surface hydrophobicity is essential for a complete understanding of more complicated self-assembly processes including aggregation, adsorption, deposition, and biological interactions, where surface interactions play a critical role determining the potential biological impacts (e.g., surface accumulation). Undoubtedly, our developed method provides a novel approach to evaluate nanoscale hydrophobicity of materials, especially nanomaterials, which are different to evaluate using conventional tools. This study only used pristine NPs without studying the effects of heterogeneity of NPs such as different particle size of the same materials and surface functionalizations or coatings of NOM and proteins, which would be more representative of environmental conditions and interesting to researchers. However, the pristine NPs provide simplistic surface characteristics that facilitate the method development, a focus of this study. The results of this study lay out groundwork toward the development of appropriate characterization tools for exploring the unique surface characteristics of materials at nanoscale.

7.6. Reference

(1) Chen, K. L.; Mylon, S. E.; Elimelech, M. Aggregation kinetics of alginate-coated hematite nanoparticles in monovalent and divalent electrolytes. *Environ. Sci. Tech.* **2006,** *40* (5), 1516-1523.
(2) Tungittiplakorn, W.; Cohen, C.; Lion, L. W. Engineered Polymeric Nanoparticles for Bioremediation of Hydrophobic Contaminants. *Environ. Sci. Technol.* **2004,** *39* (5), 1354-1358.
(3) De Campos, A. M.; Sánchez, A.; Alonso, M. a. J. Chitosan nanoparticles: a new vehicle for the improvement of the delivery of drugs to the ocular surface. Application to cyclosporin A. *International Journal of Pharmaceutics* **2001,** *224* (1-2), 159-168.
(4) Mao, H.-Q.; Roy, K.; Troung-Le, V. L.; Janes, K. A.; Lin, K. Y.; Wang, Y.; August, J. T.; Leong, K. W. Chitosan-DNA nanoparticles as gene carriers: synthesis, characterization and transfection efficiency. *J. Controlled Release* **2001,** *70* (3), 399-421.
(5) Ghosh, P.; Han, G.; De, M.; Kim, C. K.; Rotello, V. M. Gold nanoparticles in delivery applications. *Advanced Drug Delivery Reviews* **2008,** *60* (11), 1307-1315.

(6) Cheng, Y.; C. Samia, A.; Meyers, J. D.; Panagopoulos, I.; Fei, B.; Burda, C. Highly Efficient Drug Delivery with Gold Nanoparticle Vectors for in Vivo Photodynamic Therapy of Cancer. *JACS* **2008,** *130* (32), 10643-10647.
(7) Horie, M.; Nishio, K.; Fujita, K.; Endoh, S.; Miyauchi, A.; Saito, Y.; Iwahashi, H.; Yamamoto, K.; Murayama, H.; Nakano, H.; Nanashima, N.; Niki, E.; Yoshida, Y. Protein adsorption of ultrafine metal oxide and its influence on cytotoxicity toward cultured cells. *Chem. Res. Toxicol.* **2009,** *22* (3), 543-553.
(8) Xu, L. C.; Logan, B. E. Interaction forces between colloids and protein-coated surfaces measured using an atomic force microscope. *Environ. Sci. Technol.* **2005,** *39* (10), 3592-3600.
(9) Oss, C. J. v. *Interfacial Forces in Aquaeous Media*. Second Edition ed.; Taylor & Francis Group: Boca Raton, Florida, 2006; p 81-83.
(10) Gotzinger, M.; Weigl, B.; Peukert, W.; Sommer, K. Effect of roughness on particle adhesion in aqueous solutions: A study of Saccharomyces cerevisiae and a silica particle. *Colloids Surf., B: Biointerfaces* **2007,** *55* (1), 44-50.
(11) Yuehuei H. An, R. J. F., Concise review of mechanisms of bacterial adhesion to biomaterial surfaces. In 1998; Vol. 43, pp 338-348.
(12) Hoet, P. H. M.; Nemmar, A.; Nemery, B. Health impact of nanomaterials? *Nature Biotechnology* **2004,** *22* (1), 19-19.
(13) Oberdörster, G.; Oberdörster, E.; Oberdörster, J. Nanotoxicology: an emerging discipline evolving from studies of ultrafine particles. *Environ. Health. Perspect.* **2005,** *113* (7), 823-839.
(14) Tiede, K.; Boxall, A. B. A.; Tear, S. P.; Lewis, J.; David, H.; Hassellov, M. Detection and characterization of engineered nanoparticles in food and the environment. *Food Addit. Contam.* **2008,** *25* (7), 795-821.
(15) Darlington, T. K.; Neigh, A. M.; Spencer, M. T.; Nguyen, O. T.; Oldenburg, S. J. Nanoparticle characteristics affecting environmental fate and transport through soil. *Environ Toxicol Chem* **2009**, 1.
(16) Suzuki, S.; Nakajima, A.; Yoshida, N.; Sakai, M.; Hashimoto, A.; Kameshima, Y.; Okada, K. Hydrophobicity and Freezing of a Water Droplet on Fluoroalkylsilane Coatings with Different Roughnesses. *langmuir* **2007,** *23* (17), 8674-8677.
(17) Lehr, C.-M.; Bouwstra, J. A.; Boddé, H. E.; Junginger, H. E. A Surface Energy Analysis of Mucoadhesion: Contact Angle Measurements on Polycarbophil and Pig Intestinal Mucosa in Physiologically Relevant Fluids. *Pharm. Res.* **1992,** *9* (1), 70-75.
(18) Gavoille, J.; Takadoum, J.; Martin, N.; Durand, D. Wettability and surface forces measured by atomic force microscopy: the role of roughness. *European Physical Journal-Applied Physics* **2009,** *48* (1), -.
(19) Suresh, L.; Walz, J. Y. Direct measurement of the effect of surface roughness on the colloidal forces between a particle and flat plate. *J. Colloid Interface Sci.* **1997,** *196* (2), 177-190.
(20) Walz, J. Y. The effect of surface heterogeneities on colloidal forces. *Adv. Colloid Interface Sci.* **1998,** *74*, 119-168.
(21) Barthlott, W.; Neinhuis, C. Purity of the sacred lotus, or escape from contamination in biological surfaces. *Planta* **1997,** *202* (1), 1-8.
(22) Cheng, S. Y.; Bryant, R.; Doerr, S. H.; Wright, C. J.; Williams, P. R. Investigation of Surface Properties of Soil Particles and Model Materials with Contrasting

Hydrophobicity Using Atomic Force Microscopy. *Environ. Sci. Tech.* **2009,** *43* (17), 6500-6506.
(23) Stanek, C.; Tan, A.; Owens, S.; Grimes, R. Atomistic simulation of CeO_2 surface hydroxylation: implications for glass polishing. *J. Mater. Sci.* **2008,** *43* (12), 4157-4162.
(24) Eastman, T.; Zhu, D. M. Adhesion forces between surface-modified AFM tips and a mica surface. *langmuir* **1996,** *12* (11), 2859-2862.
(25) Binggeli, M.; Mate, C. M. Influence of capillary condensation of water on nanotribology studied by force microscopy. *Appl. Phys. Lett.* **1994,** *65* (4), 415-417.
(26) Alsteens, D.; Dague, E.; Rouxhet, P. G.; Baulard, A. R.; Dufrene, Y. F. Direct measurement of hydrophobic forces on cell surfaces using AFM. *langmuir* **2007,** *23* (24), 11977-11979.
(27) Kuna, J. J.; Voitchovsky, K.; Singh, C.; Jiang, H.; Mwenifumbo, S.; Ghorai, P. K.; Stevens, M. M.; Glotzer, S. C.; Stellacci, F. The effect of nanometre-scale structure on interfacial energy. *Nature Materials* **2009,** *8* (10), 837-842.
(28) Noel, O.; Brogly, M.; Castelein, G.; Schultz, J. In Situ Determination of the Thermodynamic Surface Properties of Chemically Modified Surfaces on a Local Scale: An Attempt with the Atomic Force Microscope. *langmuir* **2004,** *20* (7), 2707-2712.
(29) Magomedov, M. Dependence of the surface energy on the size and shape of a nanocrystal. *Phys. Solid State* **2004,** *46* (5), 954-968.
(30) Nanda, K. K.; Maisels, A.; Kruis, F. E. Surface Tension and Sintering of Free Gold Nanoparticles. *J. Phys. Chem. C* **2008,** *112* (35), 13488-13491.
(31) Burnham, N. A.; Dominguez, D. D.; Mowery, R. L.; Colton, R. J. Probing the surface forces of monolayer films with an atomic-force microscope. *Phys. Rev. Lett.* **1990,** *64* (16), 1931.
(32) Deshpande, S.; Patil, S.; Kuchibhatla, S. V. N. T.; Seal, S. Size dependency variation in lattice parameter and valency states in nanocrystalline cerium oxide. *Appl. Phys. Lett.* **2005,** *87* (13), -.
(33) Gao, Y.; Elder, S. A. TEM study of TiO_2 nanocrystals with different particle size and shape. *Mater. Lett.* **2000,** *44* (3-4), 228-232.
(34) Wiley, B.; Sun, Y. G.; Mayers, B.; Xia, Y. N. Shape-controlled synthesis of metal nanostructures: The case of silver. *Chem. Eur. J.* **2005,** *11* (2), 454-463.
(35) Si, R.; Flytzani-Stephanopoulos, M. Shape and crystal-plane effects of nanoscale ceria on the activity of Au-CeO_2 catalysts for the water-gas shift reaction. *Angewandte Chemie-International Edition* **2008,** *47* (15), 2884-2887.
(36) Yoreo, J. J. D.; Vekilov, P. G. *Principles of crystal nucleation and growth*. 2003; Vol. 54.
(37) Cundy, C. S.; Cox, P. A. The hydrothermal synthesis of zeolites: Precursors, intermediates and reaction mechanism. *Microporous Mesoporous Mater.* **2005,** *82* (1-2), 1-78.
(38) Mullin, J. W. *Crystallisation*. Fourth ed.; Butterworth Heinemann, Oxford, 2001.
(39) Gaboriaud, F.; Dufrene, Y. F. Atomic force microscopy of microbial cells: Application to nanomechanical properties, surface forces and molecular recognition forces. *Colloids Surf., B: Biointerfaces* **2007,** *54* (1), 10-19.
(40) Butt, H.-J.; Kappl, M. *surface and interfacial force*. WILEY-VCH Verlag GmbH & Co.: Weinheim, 2010.

(41) Xu, L.-C.; Vadillo-Rodriguez, V.; Logan, B. E. Residence Time, Loading Force, pH, and Ionic Strength Affect Adhesion Forces between Colloids and Biopolymer-Coated Surfaces. *langmuir* **2005,** *21* (16), 7491-7500.
(42) Dupont-Gillain, C. C.; Nysten, B.; Hlady, V.; Rouxhet, P. G. Atomic Force Microscopy and Wettability Study of Oxidized Patterns at the Surface of Polystyrene. *J. Colloid Interface Sci.* **1999,** *220* (1), 163-169.
(43) Marenduzzo, D.; Finan, K.; Cook, P. R. The depletion attraction: an underappreciated force driving cellular organization. *J. Cell Biol.* **2006,** *175* (5), 681-686.
(44) YODH, A. G.; LIN, K.; CROCKER, J. C.; DINSMORE, A. D.; VERMA, R.; KAPLAN, P. D. Entropically driven self-assembly and interaction in suspension. *Philos. Trans. R. Soc. London, Ser. A* **2001,** *359* (1782), 921-937.
(45) Asakura, S.; Oosawa, F. Interaction between Particles Suspended in Solutions of Macromolecules. *J. Polym. Sci.* **1958,** *33* (126), 183-192.
(46) Zhang, W.; Stack, A. G.; Chen, Y. Interaction Force Measurement between *E. coli* Cells and Nanoparticles Immobilized Surfaces by Using AFM. *Colloids Surf., B* **2010,** *82* (2), 316-324
(47) Burnham, N. A.; Chen, X.; Hodges, C. S.; Matei, G. A.; Thoreson, E. J.; Roberts, C. J.; Davies, M. C.; Tendler, S. J. B. Comparison of calibration methods for atomic-force microscopy cantilevers. *Nanotechnol.* **2003,** *14* (1), 1-6.
(48) Derjaguin, B. V.; Churaev, N. V. Structural component of disjoining pressure. *J. Colloid Interface Sci.* **1974,** *49* (2), 249-255.
(49) Ducker, W. A.; Grant, L. M. Effect of Substrate Hydrophobicity on Surfactant Surface aggregate Geometry. *J. Phys. Chem.* **1996,** *100* (28), 11507-11511.
(50) Smith, T. The hydrophilic nature of a clean gold surface. *J. Colloid Interface Sci.* **1980,** *75* (1), 51-55.
(51) Clear, S. C.; Nealey, P. F. Chemical Force Microscopy Study of Adhesion and Friction between Surfaces Functionalized with Self-Assembled Monolayers and Immersed in Solvents. *J. Colloid Interface Sci.* **1999,** *213* (1), 238-250.
(52) Stankus, D. P.; Lohse, S. E.; Hutchison, J. E.; Nason, J. A. Interactions between Natural Organic Matter and Gold Nanoparticles Stabilized with Different Organic Capping Agents. *Environ. Sci. Technol.* **2011,** *45* (8), 3238-3244.
(53) Aiken, G. R.; Hsu-Kim, H.; Ryan, J. N. Influence of Dissolved Organic Matter on the Environmental Fate of Metals, Nanoparticles, and Colloids. *Environ. Sci. Technol.* **2011,** *45* (8), 3196-3201.
(54) Noy, A.; Zepeda, S.; Orme, C. A.; Yeh, Y.; De Yoreo, J. J. Entropic Barriers in Nanoscale Adhesion Studied by Variable Temperature Chemical Force Microscopy. *JACS* **2003,** *125* (5), 1356-1362.
(55) Park, J. H.; Aluru, N. R. Temperature-dependent wettability on a titanium dioxide surface. *Molecular Simulation* **2009,** *35* (1-2), 31-37.
(56) Chiu, C. C.; Moore, P. B.; Shinoda, W.; Nielsen, S. O. Size-dependent hydrophobic to hydrophilic transition for nanoparticles: A molecular dynamics study. *J. Chem. Phys.* **2009,** *131* (24), -.

CHAPTER 8

PROBING THE NANOSCALE SURFACE POTENTIAL

Work of this chapter is related to the publications or manuscripts:
Wen Zhang, Yongsheng Chen. Probing the nanoscale electric properties of metal-based nanoparticles using zeta potential measurement and Kelvin probe force microscopy. In preparation.

8.1. Abstract

Surface potential or surface charge strongly influences the surface interactions, resulting in deposition, adsorption and aggregation behavior of natural colloids and engineered NPs. Therefore, the understanding of NP environment fate, transport, and biological interactions must include a fundamental framework for quantifying the surface potential. Our results show that the measured zeta potential based on electrophoresis has particle size dependence for NPs and the measurement accuracy may also be affected factors like concentrations of particles. The particle size effect on zeta potential was well explained by the Poisson-Boltzmann equation under Debye-Hückel approximation. Interestingly, this particle size effect was also observed from the surface potential measured by Kelvin force microscopy (KFM), another useful tool for quantifying surface potential at nanoscale. Based on the principle of KFM operation, the size effect may be interpreted by the Coulomb's Law, a "first-principle" theory that describes the electric field of point charge in vacuum. The good agreement between the proposed model and the experimental results demonstrated that KFM could serve as alternative approach for the surface potential measurement of NPs that is potentially correlated with and compliment the zeta potential measurement that was found to be strongly affected by the heterogeneity of NPs in aqueous phase.

8.2. Introduction

Anthropogenic nanomaterials and NPs can inevitably be released into the environment with the broad applications of nano-enable products *(1, 2)*. Most of them

may end up in soil, sediments, and other aquatic environments (lakes or rivers) *(3-7)*. Stability of NPs significantly affects the fate and transport as well as bioavailability *(8-10)*. As chapter 7 introduced a novel method for quantifying nanoscale hydrophobicity of NPs, which is a key parameter associated with surface interactions, specifically affecting van der Waals and acid-base forces according to the DLVO theory *(11)*, this chapter discusses surface potential or surface charge of NPs, another important parameter for particle stability in aqueous phase, which is usually represented by zeta (ζ) potential *(12, 13)*. ζ potential measures electric potentials at the slipping layer of the electric double layer (EDL) of a colloidal particle, which is related to both surface charge and the local environment of the particle *(14)*. ζ potential is either directly used to represent surface potential (ψ_0) *(15)*, or used to calculate ψ_0, which is situated at the precise particle-liquid interface *(14)*. ζ potential is commonly obtained by laser Doppler electrophoresis, which measures the net electrophoretic mobility (μ_E) of particles in the liquid under an electric field. Then μ_E is converted to ζ potential using Henry's approximation *(16)*. In the DLVO theory, ζ potential is commonly used to calculate the electrostatic interaction energy *(17, 18)*. Positive electrostatic energy indicates the presence of electric repulsion between particles that greatly stablizes the particle dispersion. Increasing the electrolyte concentration or ionic strength leads to screening of surface charge and shrinking of the EDL. Consequently, the particle dispersion becomes less stable and aggregation may occur.

Although ζ potential is widely used as a rapid and convenient indicator of the stability of colloids, it may be less accurate to reveal the accurate surface charge of NPs. The classical electrokinetic measurement relies on microelectrophoresis, where the electrophoretic mobility of colloidal particles and the movement of NPs can be tracked with conventional microscopes. Moreover, when particle sizes shrink smaller and smaller, the heterogeneity (e.g., surface roughness, shape, and radius of curvature) of NPs

may have an increasing effect on the mobility of particles during electrophoresis. This is probably because the interfacial energy becomes more dependent on surface structures such as size and shape of NPs *(19, 20)*, which in turn changes the thickness of EDL and affects the electric properties of particle surfaces due to hydration effects. Moreover, the influence of environmental factors (e.g., ionic strength, pH, temperature) on the measurement accuracy and reproducibility may become more significant *(21-23)*. For instance, particle mobility may be more affected by Brownian movement than large particles as indicated by the Stokes-Einstein equation. High temperature leads to high random kinetic energy of particles and for small particles, the diffusivity is higher than that of large NPs. However, to date, there has been very little systematic research designed to assess the temperature effect on ζ potential measurement for NPs *(24)* as well as other potential factors such as particle size and concentrations, and their effects on the reproducibility of zeta-potential measurements of dispersed NPs *(25, 26)*.

Because nanomaterials or NPs are categorized as new materials that show extraordinary electronic and structural properties, fundamental work to develop appropriate characterization tools is clearly needed. As one of the powerful functions integrated in atomic force microscopy (AFM), Kelvin probe force microscopy (KPFM) or KFM provides us a unique opportunity specifically for quantifying and mapping surface potential distributions of nanomaterials *(27-30)*. KFM is an adaption of an AFM in the electric force mode *(31, 32)*, which is sensitive to electrostatic potential difference between two contact surfaces. The contact potential difference (CPD) between two surfaces brought into close proximity is measured in KFM by using vibrating capacitor method (or Kelvin method). Instead of measuring the AC current, electrostatic forces acting on the cantilever are measured in KFM. Electrostatic forces between the probe and various regions of the sample arise due to the local mechanical and electromagnetic properties *(33)*, such as surface charges, doping levels, or dielectric constants. The

cantilever tip is applied with an alternating current (AC) to vibrate at sinusoidal voltage signal at a frequency of ω, while a direct current (DC) bias is adjusted to nullify the CPD *(28, 29)*. When the electrostatic force at the first harmonic resonance frequency (F_ω) becomes zero, the DC bias voltage equals the CPD, which makes it possible to obtain a quantitative measurement of the surface potential of nanostructures both in air and in vacuum *(34)*.

Recent work has demonstrated the capability of KFM in measuring the surface potential of nanostructures, including semiconductors *(35)*, inorganic films *(36)*, organosilane self-assembled monolayers (SAMs) terminated with different functional groups *(37)*, conjugated polymer thin films *(30)*, and other organic materials (e.g., perfluoroalkyl alkanes) *(33)*. Eun Ji Yoo, et al. investigated flocculation behavior of colloidal AuNPs modified with various biomolecules (amino acids, glutathione, oligopeptides, and proteins) and employed KFM to investigate the effects of surface modifications on flocculation behavior *(38)*. In addition, KFM provides surface potential distribution that is complementary to the topography and phase images that conventional AFM provides *(27, 39, 40)*.

In this work, I explored the applicability of KFM in studying nanoelectrical properties of various commercial metallic and metal oxide NPs (Fe_2O_3, CeO_2, Al_2O_3, CuO, TiO_2, ZnO, AuNPs, PtNPs, and AgNPs). To better understand the potential connections between the ζ potential and surface potential from KFM, I symmetrically analyzed the principles of ζ potential and the Kelvin probe method, discussed the potential factors, weakness or artifacts associated with these measurements, and finally I attempted to correlated the two descriptors of surface potential with a proposed model based on the Coulomb's law and Debye-Hückel approximation. The over-arching goal of this study is to develop appropriate analytical approach for quantifying the nanoscale

electrical properties of NPs, to cast light into the experimental artifacts, and to ultimately avoid these artifacts to obtain accurate measurement of surface potential.

8.3. Principles about zeta potential measurement and Kelvin probe method

8.3.1. Zeta potential theory

The fundamental quantity measured is the net electrophoretic mobility (μ_E) of the particles, which is then converted to the ζ potential using Henry's approximation *(16)*:

$$\mu_E = \frac{2\zeta\varepsilon f(\kappa r)}{3\eta} \quad (1)$$

where ε is the dielectric constant (or permittivity); η is the medium's viscosity (i.e., the viscosity of water); κr is the ratio of particle radius to Debye double layer thickness; and $f(\kappa r)$ refers to Henry's function, which is 1.5 under the Smoluchowski approximation and 1 under the Hückel approximation. In aqueous media with moderate electrolyte concentrations, 1.5 is most commonly applied *(41)*.

8.3.2. Kelvin probe method

The Kelvin method, also called the vibrating capacitor method, is a well-known technique for determining the contact potential difference between different materials. Figure 8.1a shows that the tip and sample are in close proximity, but without electrical contact between them. Their Fermi levels align at the vacuum level energies corresponding to the respective work functions (Φ). As the two surfaces are in contact as indicated by the connection via a wire (Figure 8.1b), electrons flow from the tip with the smaller work function to the sample with the larger work function. This causes the smaller work function tip to charge positively while the sample charges negatively. This creates an electric potential between the two surfaces, shifting their electronic states relative to each other. The electron transfer process stops once the electric field between them compensates for the work function difference. In this equilibrated state, the

potential associated with the electric field exactly equals the work function difference or the CPD between the tip and sample. In AFM, where the tip usually has a very small tip radius of curvature (~10 nm), the capacitance of the tip-substrate capacitor becomes too low to measure a significant electrical current change. However, the AFM provides a sensitive tool for measuring the electrostatic forces (~pN) that are induced by the charges accumulating on the tip and at the sample surface. A force (F) can be derived from the total energy of the tip-substrate capacitor ($E = 1/2C(V_{bias} + V_{CPD})^2$) resulting in:

$$F = \frac{1}{2}\frac{dC}{dz_0}(V_{bias} + V_{CPD})^2 \tag{2}$$

where C is the capacitance of the system formed by the tip and the sample, dC/dz_0 is the change in capacitance for the given geometry and V_{bias} is the additional applied constant potential. Since the actual electrostatic force owing to the V_{CPD} is low in magnitude (~pN) and thus the tip deflection is hardly measurable (~picometer), the practical KFM is operated by vibrating the tip at a certain frequency ω and amplitude V_0 (see Figure 1c) to amplify the signal. The resulting oscillating electrostatic force is then expressed as:

$$F = \frac{1}{2}\frac{dC}{dz_0}(V_{bias} + V_{CPD} + V_0 \sin(\omega t))^2 \tag{3}$$

Separating the frequency components into F_{DC}, F_{ω}, and $F_{2\omega}$ leads to

$$F_{DC} = \frac{1}{2}\frac{dC}{dz_0}(V_{bias} + V_{CPD})^2 + \frac{V_0^2}{2}) \tag{4}$$

$$F_{\omega} = \frac{dC}{dz_0}V_0 \sin(\omega t)\cdot(V_{bias} + V_{CPD}) \tag{5}$$

$$F_{2\omega} = \frac{dC}{4dz_0}V_0^2 \cos(2\omega t) \tag{6}$$

Gradual application of a counter potential to the CPD and monitoring the force at the angular resonance frequency F_{ω}, which will become zero when (V_{bias} +V_{CPD}) = 0. Using a lock-in amplifier (LIA), the F_{ω} component is used as the input to a feedback loop which adjusts the DC bias (V_{bias}) to nullify V_{CPD} *(28, 29)*. Ideally, the feedback loop will minimize the electrostatic forces on the tip resulting in an accurate measure of surface potential (V_{CPD}). However, the electrostatic forces can be varied by electromagnetic properties and heterogeneity of sample surfaces *(33)*, such as surface charges, doping levels, dielectric constants, shape and roughness, which in fact is related to the local variations in the work function of materials. In metals, the work function is considered to be the energy difference between the vacuum level and the Fermi energy. In other types of materials, such as semiconductors or insulators, the work function may arise from the difference in energy between the vacuum level and the most loosely bound electron inside the sample. The work function depends on the specific material, adsorption layers (e.g., water), oxide layer thickness, dopant concentration, electrostatic charges, surface dipole moments and temperature. Thus, the KFM mode is useful for the study of surfaces made from different materials, such as polymer blends and composite materials. However, the surface coating, modifications, water adsorption (relative humidity) and other variations in work functions of materials may lead to errors in surface potential measurement. For instance, the work function difference estimated from Eq. (5) is independent both on the tip-sample distance and on the applied V_{bias}. However, the suitable tip-sample distance was shown to be 200 nm or greater to extract correct electronic information of the sample *(34)*.

It is also worth mentioning that KFM measures the CPD and the absolute measurement of local potential is achievable through calibrating the work function of the tip surface (usually with gold or platinum coating). The calibration is conducted against a surface with known work function such as a highly oriented pyrolytic graphite (HOPG)

(42). It was shown to be a reliable work function standard (approximately 4.6~4.7 eV.) for measurement in air because HOPG is chemically very inert, it does not form significant interface dipoles with typical ambient contaminants (e.g., hydrocarbons and water) found on surfaces *(34, 43)*. By comparing the measured asymptotic CPD of sample surfaces with the HOPG work function reference, we can estimate the absolute surface potentials that are considered as "not measurable" in aquatic chemistry *(14)*. The relation between work function of the conductive tip (Φ_{tip}) and the sample (Φ_{sample}) is expressed as *(44)*, $\phi_{sample} = \phi_{tip} - eV_{CPD}$, where *e* is the elementary charge (1.602×10^{-19} C).

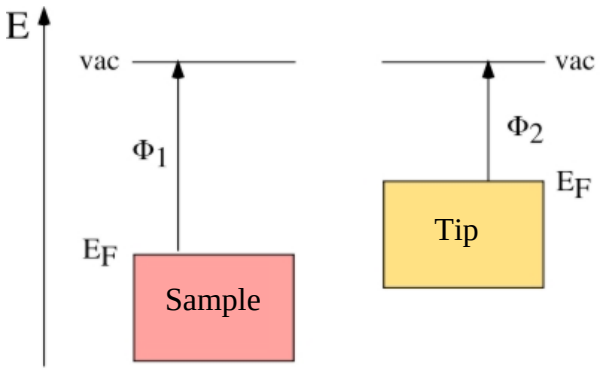

(a) Tip and sample are separated.

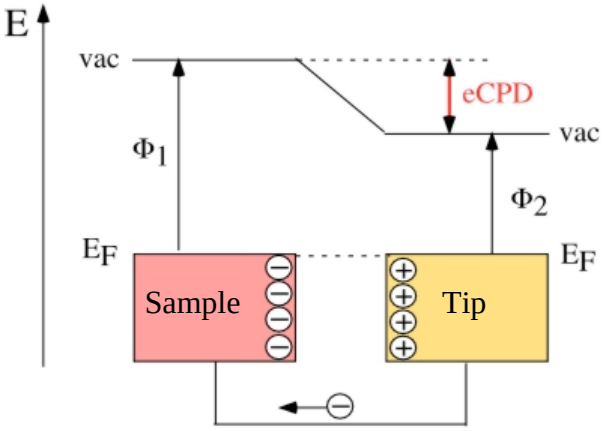

(b) Tip and sample are in contact.

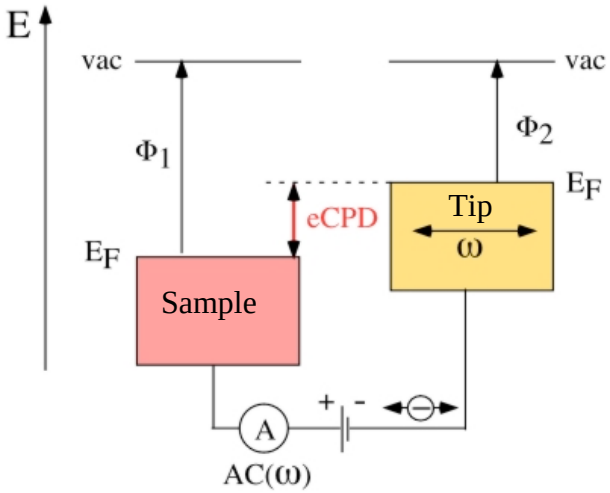

(c) Upon applying an additional external potential, where $V_{bias}=V_{CPD}$.

Figure 8.1. Schematic of the Kelvin probe method.

8.4. Materials and Methods

8.4.1. NPs

All pristine NPs are used as samples and their properties are previously mentioned in section 7.4.1 of chapter 7.

8.4.2. Zeta potential measurement

Instrumental settings associate with zeta potential measurement of the suspensions of various NPs can be found in previous chapters. The specific aqueous conditions (e.g., ionic strength and pH) are mentioned in the result discussion.

8.4.3. KFM

The KFM was operated on an Agilent 5500 AFM (Molecular Imaging) equipped with MAC III unit, which has three lock-in amplifiers (LIA) enabling multifrequency measurements. LIA 1 was used for topography imaging in the intermittent contact mode, which was performed at the first flexural resonance of the probes ω_{mech} and LIA 2 was used for KFM, providing AC and DC voltages to the probe and detecting the electrostatic response either from the photodetector (AM-AM) directly or from the LIA 1 employed for the topography servo (AM-FM). Pt-coated silicon cantilever probes (Olympus AC240TM, Japan) with a force constant of approximately 2~5 N/m and a nominal resonance frequency of 70 kHz were used and operated with an offset of 0.6 V below the measured resonance frequency. An AC bias voltage of 2 V at a frequency of 70 kHz was applied between the probe and sample and a DC bias was set at a frequency of 5 kHz with the bias voltage provided from the LIA 2 servo. The work function of the conductive tip was calibrated with respective to freshely cleaved HOPG (0001). In KFM, the whole microscope was fully contained in an environmental chamber that was used to

control ambient pressure, temperature (25 ± 2 ^{o}C), and humidity (less than 10%) measured by VWR humidity/temperature thermometer.

The water suspensions of NPs was spread out and deposited on a clean silicon wafer purchased from Sigma-Aldrich that was cleaved to a small piece of approximately 3 mm × 8 mm and air-dried for 1 min. The silicon wafer was finally fixed on a small piece (1 cm × 1 cm) of conductive double-sided tape (Ted Pella), which was placed on a grounded microscope stage. Topography, phase, and surface potential images were obtained simultaneously.

8.5. Results and discussion

This section first discussed the effects of particle size and concentrations on the ζ potential measurement based on literature and the representative experimental data of hematite and AgNPs. Other factors such as shape, ionic strength, ph, and temperature are likely to contribute to the ζ potential measurement precision as indicated above. However, these factors are not covered in this study because previous research has addressed the importance for some of these factors in the ζ potential measurement whereas the particle shape effect will be considered as my future research. The second part of this section is showed the typical results of surface potential (i.e., CPD) of NPs, analyzed the particle size dependence of the KFM-surface potential, and finally combined experimental evidence and proposed models to establish a potential connection between ζ potential and KFM-surface potential, which aims at elucidating the fundamental mechanisms of the nanoscale surface potential.

8.5.1. Influences of particle size on ζ potential measurement

The particle size effect on the ζ potential measurement has rarely been discussed although a great number of recent studies employ ζ potential as an indicator for surface

potential or surface charge. Here the results of AgNPs and hematite are shown and discussed because these two NPs are synthesized with distinct sizes and have stable dispersions in water without aggregation. Figure 8.2 clearly show the size-dependence of ζ potential: the ζ potentials of small NPs were lower than those of large ones, which is commonly found at different pHs and ionic strengths. One exception is found for AgNPs when the ionic strength was higher than 100 mM, ζ potential of 20 nm AgNPs shifted to more negative values, while the other two sizes had a positive shift. This is probably an artifact caused by aggregation because small NPs due to high local particle density have a much higher tendency of aggregation in the presence of electrolytes *(18)*. In contrast, hematite NPs have a relatively stable hydrodynamic size distribution over a broad ionic strength range as shown in Figure 8.2d, and thus the size dependence of ζ potential of hematite NPs is fairly consistent in Figure 8.2c.

The particle size effect on the ζ potential measurement is actually embedded into the term of $f(\kappa r)$ in Eq. (1). The Smoluchowski approximation applies if the extent of the diffuse layer is small relative to the curvature of the particles *(45)*, while the Hückel approximation applies when the diffuse layer is larger than the curvature of the particles (e.g., altrasmall NPs). In addition, according to Eq. (10), ζ potential is directly related to the electrophoretic mobility, which is apparently related to particle properties, such as shape and cross-sectional area. These properties are likely to influence the mobility of NPs via changing the friction force during the electrophoresis.

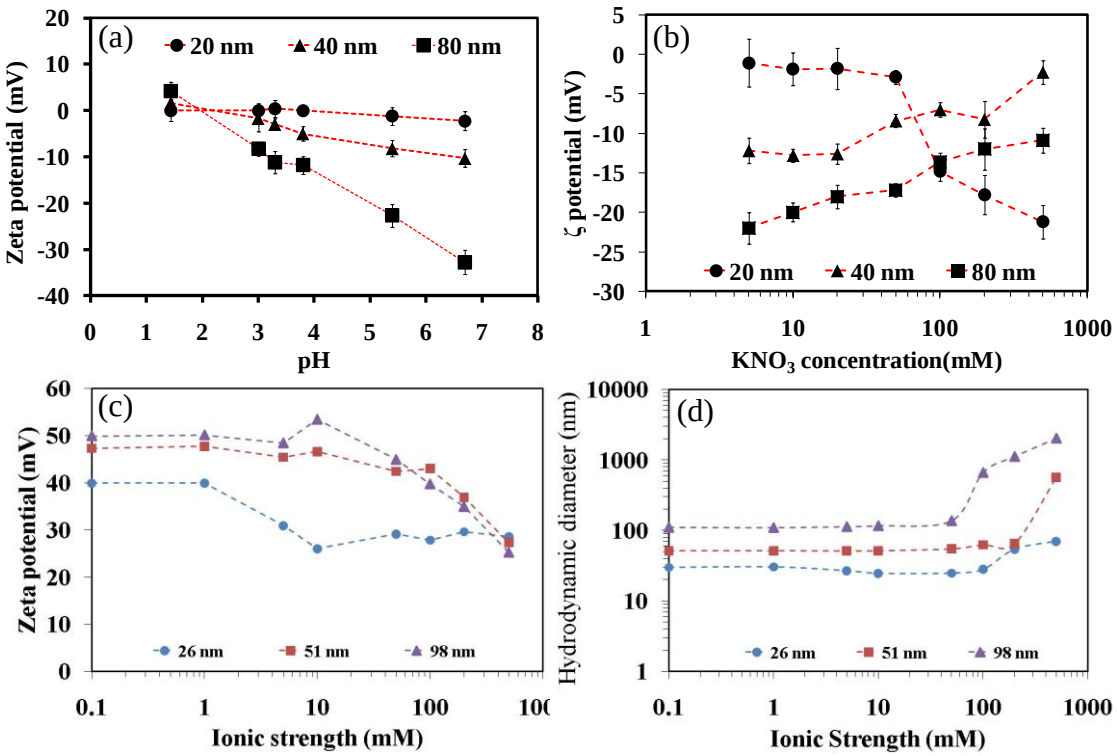

Figure 8.2. (a~b) ζ potential of AgNPs versus pHs (the ionic strength is less than 10 mM) and different concentrations of KNO_3 (pH was approximately 5.7). (c) ζ potential of hematite NPs versus different ionic strengths contributed by NaCl (pH was approxiamtely 5.6). (d) Hydrodynamic diameters of differnet sized hematite NPs at different ionic strengths (the dashed lines are a guide to the eye).

Previously, Jailani et al. proposed that the reduction in ζ potential by the decrease in particle size could be explained by the increasing total surface area of solid increases with the decreasing size, which results in an increased solution electrolyte concentration due to dissociation of ionizable surface sites and dissolution of the particles *(25)*. This interpretation is quite possible for surface-reactive particles and the interpretation here I propose is based on the theoretical relationship between the absolute surface potential (ψ_0) and ζ potential, which is connected by the Poisson-Boltzmann equation under Debye-Hückel approximation *(46)*:

$$\psi_0 = \zeta (1 + z / R) \exp(\kappa z) \tag{7}$$

where *z* is the distance from the particle's surface to the slipping plane, a distance that is generally of the order of ≈3 to 5 Å *(47)*, *R* is the Stokes radius of the particle (nm), κ^{-1} is the Debye length (nm) ($\kappa^{-1} = \sqrt{\frac{\varepsilon\varepsilon_0 k_B T}{2 N_A I e^2}}$) and other related parameters were previously defined in section 3.4.7 of chapter 3. Eq. (7) can easily be converted to the form of ζ potential as a function of ionic strength (*I*):

$$\zeta = \frac{\psi_0}{(1 + z / R)} \exp(\kappa z) = \frac{\psi_0}{(1 + z / R)} \exp(-\sqrt{\frac{2 N_A I e^2}{\varepsilon\varepsilon_0 k_B T}} z) \tag{8}$$

Surface potential (ψ_0) is the potential at the exact interface between the charged surface and the polar liquid that is independent on ionic strength according to classic electrochemistry. For the same particle size, ζ potential is an exponential function of -$(I)^{0.5}$, indicating that as the ionic strength (*I*) increases, the thickness of Debye length (κ^{-1}) will be compressed and the magnitude of ζ potential will decrease, which is consistent with the experimental observations for hematite and AgNPs. For the particle effect, if we neglect the variation of ψ_0 over particle sizes, we can see that with particle radius increasing the magnitude of ζ potential should be increasing. But the sensitivity of ζ

potential to the variation of particle sizes depends on the magnitude of *z/R*. For example, when $R \gg z$, the value of ζ potential will not sensitively vary with *R*, which may partially interpret the reason why the ζ potential measurement of colloids is often not observed and why large or aggregated NPs do not show size dependence. On the contrary, when *R* is decreasing (e.g., ultrasmall NPs), the sensitivity of ζ potential over the variation of *R* may be high.

Therefore, size effects on the ζ potential measurement were not appreciable largely because the aggregation during the preparations of particle dispersions rapidly increases the particle size of NPs *(48)*. Therefore, it is extremely important to provide sufficient descriptions for the ζ potential measurement conditions (e.g., particle preparation procedures, measurement time, ionic strength, or pH) because these conditions may dramatically change the aggregation state of NPs and lead to the variations of the results *(49, 50)*.

8.5.2. Influences of concentrations on zeta potential measurement

It was previously reported that concentrations of particles affected the ζ potential measurement *(11, 25)*. As shown in Figure 8.3, when the concentration of TiO_2 NPs is lower than 0.1% (w/v), the measurement of the ζ potential is relatively stable and reproducible. When the concentration is high, there is an apparent shift to positive the ζ potentials. Interestingly, another recent study found that when the concentrations of multi-walled carbon nanotubes (MWCNTs) and gold NPs are too low, their ζ potentials strongly depend on concentration, and low concentrations result in a shift to positive ζ potentials *(11)*. The shift in ζ potential was attributed to an increase in contribution of the signal from extraneous particulate matter. Other than this possible experimental artifact, more important potential causes may include (1) the high local particle density that results in particle agglomeration and the increase in the hydrodynamics sizes; (2) the high concentration also possibly alters the medium viscosity (η); and (3) The high

concentration leads to higher turbidity resulting in obscuration of light transmission. The low concentrations also lead to erroneous measurement of ζ potential due to the unstable refracted light intensity. Appropriate concentrations for ζ potential measurements are dependent on specific compositions of particles, particle size, and the relative refractive index of the particles *(51)*. The larger the particle size, the more scattered light it produces and hence the lower the concentration that can be measured. The relative refractive index becomes lower, such as with proteins, the minimum concentration will be much higher.

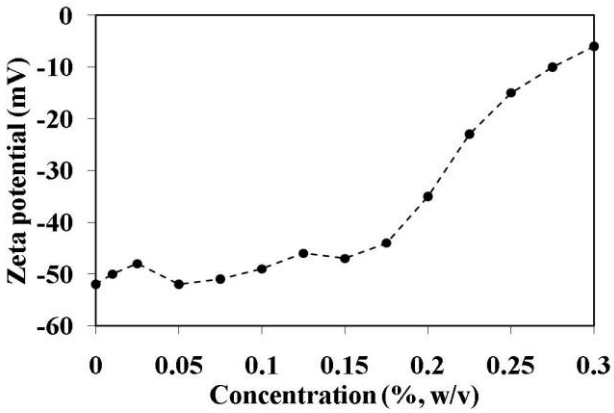

Figure 8.3. ζ potential as a function of sample concentration (% w/v) of TiO_2 dispersed in 10 mM NaCl. Data reproduced from ref. *(51)*.

8.5.3. Surface potential measurement by KFM

Figure 8.4 shows the typical images of topography and surface potential of hematite NPs deposited on the silicon substrate by KFM. Most hematite NPs were close to spherical with relatively uniform shape and size distributions, which is consistent with TEM results shown in Chapters 3 and 6. The primary particle size is around 50 nm but the images from KFM revealed relatively larger sizes probably due to particle aggregation as indicated by the red arrows in Figure 8.4a. The height profiles of individual NPs that correspond to the red dashed lines across the images in Figure 8.4a can be further extracted.

In Figure 8.4c, hematite NPs appeared darker in color than the bare silicon substrate background, indicating that hematite NPs were negatively charged relative to the substrate (grounded to 0 V). To determine the surface potential of individual NPs, similarly, we can draw a red dashed line across the surface potential image and the resulting cross-section profile can reveal the exact quantity of surface potential as shown in Figure 8.4d. Surface potential varied greatly, from -400 mV to -800 mV, for hematite NPs.

More surface potential images are provided in Figure 8.5 for Al_2O_3, CuO, TiO_2, ZnO, AuNPs, and PtNPs (platinum NPs obtained from Professor John Crittenden's lab in school of chemical and biomolecular engineering at Georgia Tech). Clearly, different NPs exhibit different extent of surface potentials, with the average potential of -45 mV (CeO_2), -100 mV (TiO_2), -250 mV (ZnO), -300 mV (PtNPs), -350 mV (CuO), -400 mV (AuNPs), and -800 mV (Al_2O_3). All the surface potentials were found negative, which is reasonable according to the theory of electric double layer (EDL) *(14)*.

We can see that KFM provides versatile functions that not merely yield morphology information of NPs, but also quantify surface potentials. For that reason,

KFM can potentially be used to identify individual NPs or areas with specific surface potentials as discussed in our previous study *(52)*.

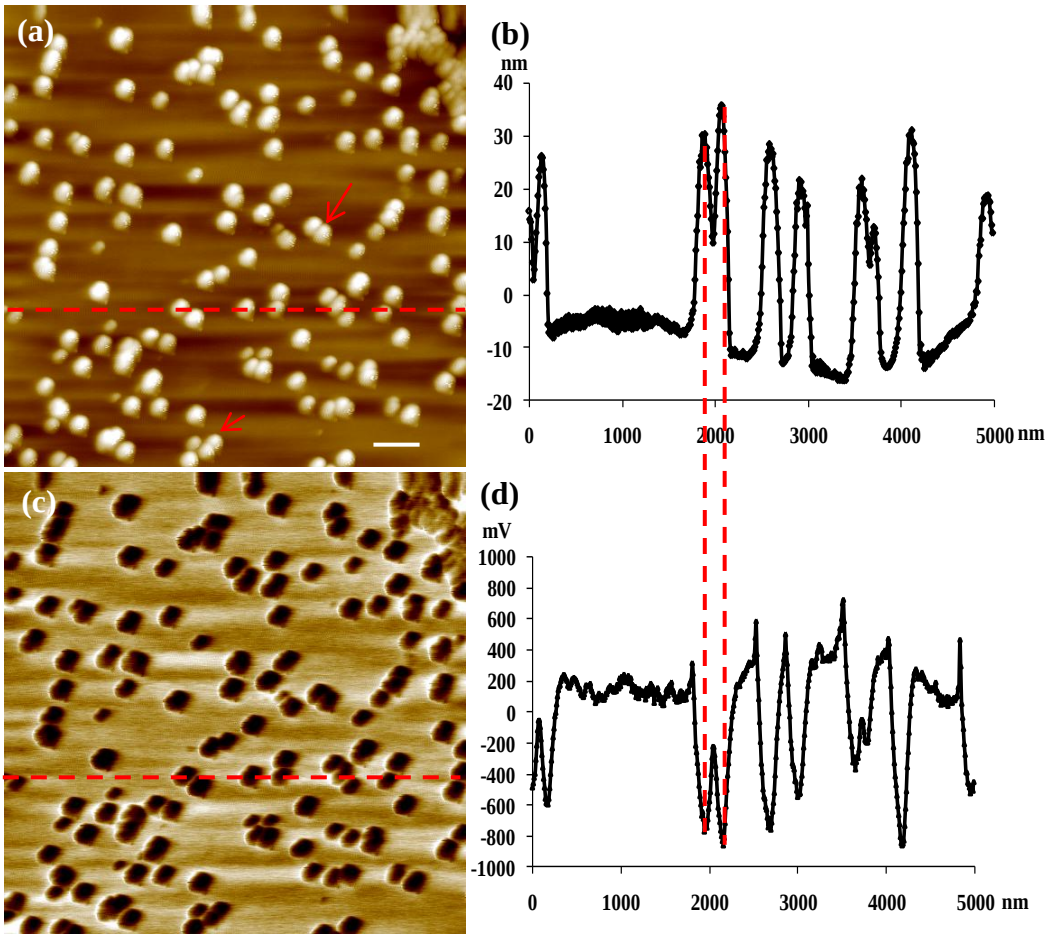

Figure 8.4. Typical images of the topography (a) and surface potential (c) for 49-nm Hematite NPs from KFM (b) and (d) show the cross-section profiles taken along the directions marked with the dashed red lines in the images of (a) and (c), respectively. The scan area of (a) and (c) is 5 μm × 5 μm and the white solid lines at the bottom right in (a) is a scale bar of 500 nm.

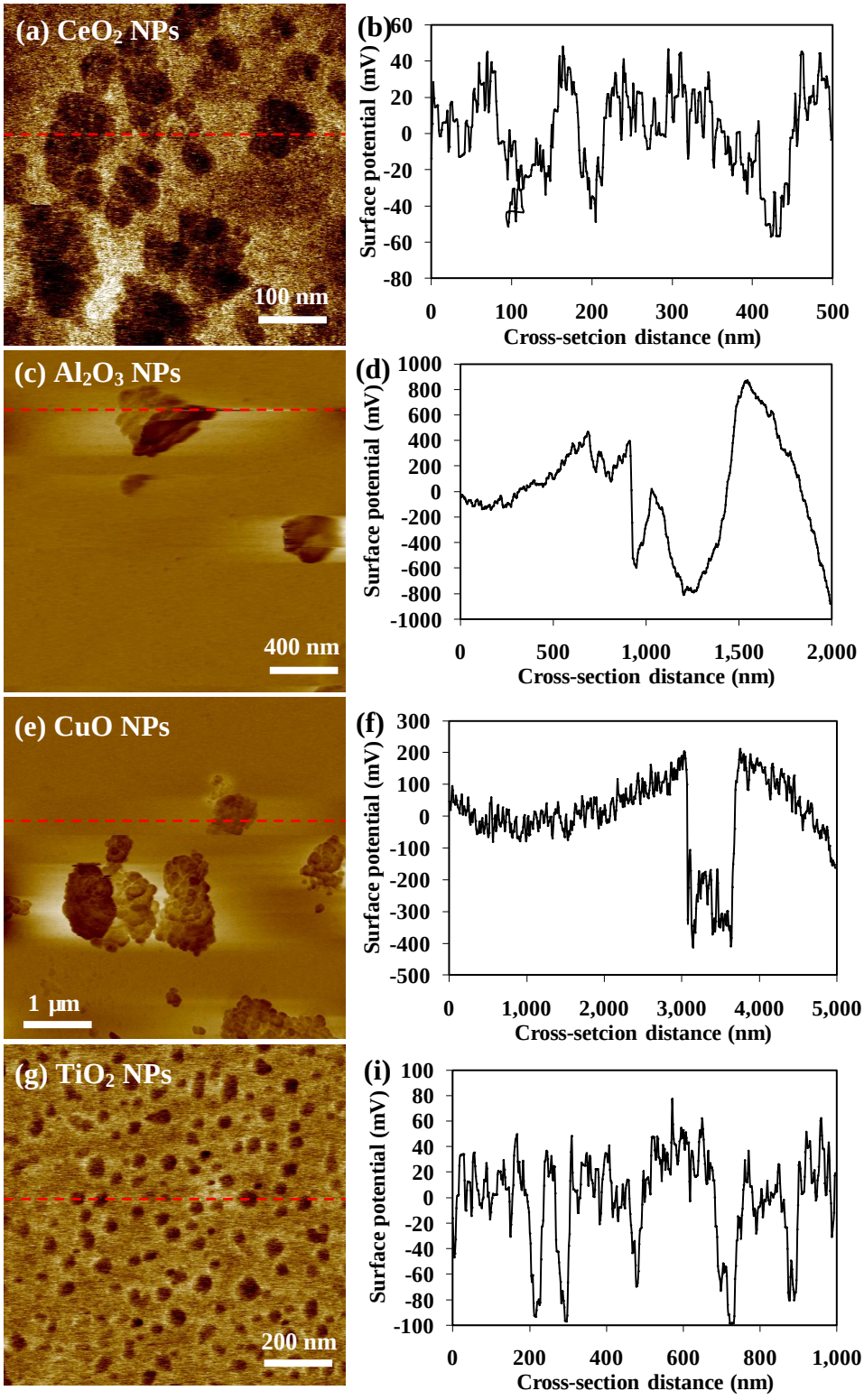

Continued in next page.

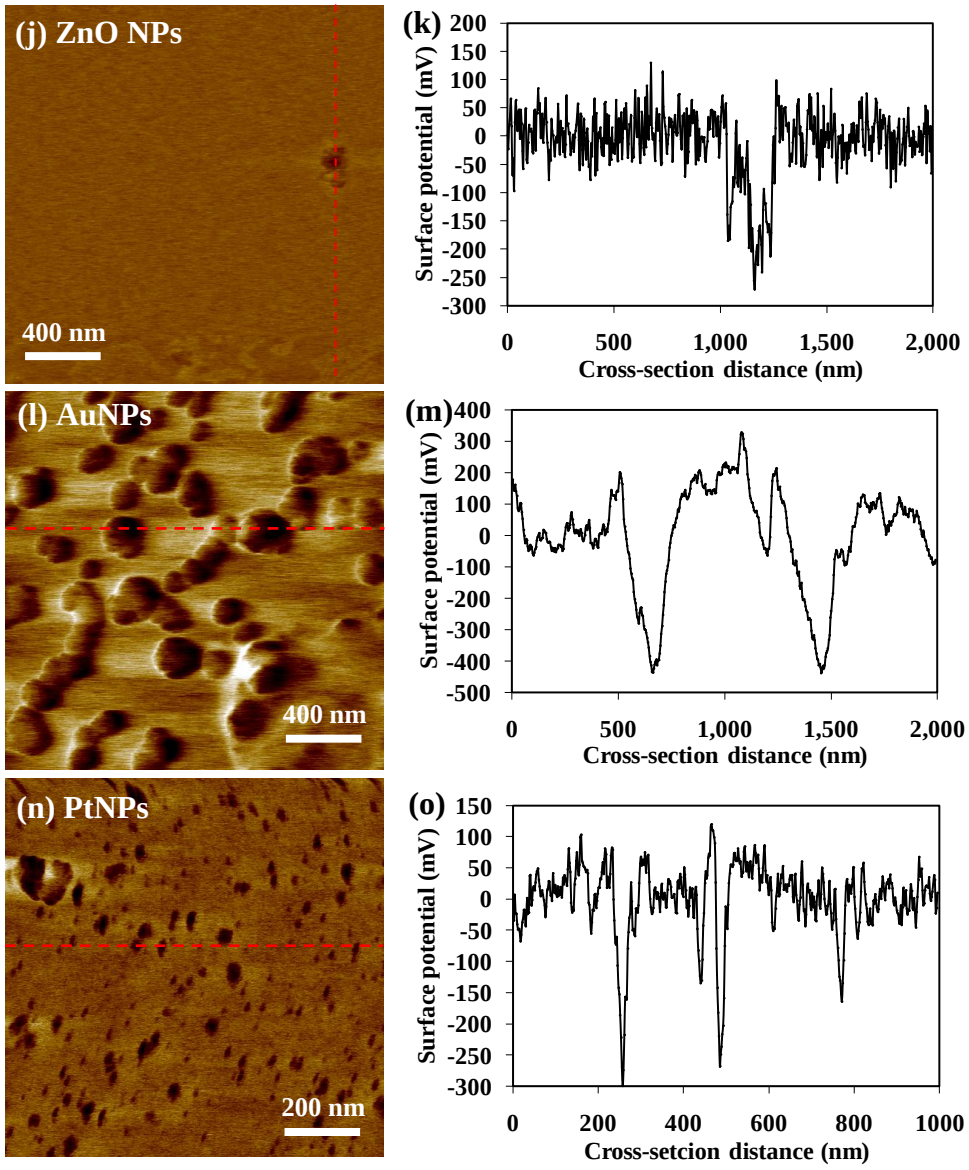

Figure 8.5. Surface potential images of various metallic and metal oxide NPs and the cross-sectional profiles taken along the directions marked with the dashed red lines in the surface potential images.

8.5.4. Particle size effect on surface potentials obtained from KFM

To show the particle size effect on surface potential of NPs measured from KFM, a certain different sized NPs were randomly selected from the images as shown by the red dotted circles in Figure 8.6a,c. Here the surface potentials for different sizes of hematite and AgNPs shown in Figure 8.6b,d indicate that small NPs tend to have less negative surface potentials, whereas large ones have more negative surface potentials. Good curve fits were obtained for both hematite and AgNPs with fitting equations shown as insets. This size dependence is widely found in all other NPs that have been discussed above (the detailed results are not shown here). For example, I previously studied the interactions between QDs and *E. coli* cells and found that small QDs penetrated into the cells and bound with DNA molecules, resulting in the transformation of polymeric DNA into pearl-like spheres *(52)*. In this study, the surface potentials of QDs also had apparent dependence on particle size (this dependence is shown in Figure 1f of this published article).

Although KFM has been employed for many years, this pronounced size effect on surface potential measurement has not been discussed, and let alone the fundamental mechanisms behind the size effect. Here I attempt to use the "first-principle" theories to interpret the potential causes of the size effect. Based on the principle of KFM in section 8.3.2, we may consider a single NP as a point charge (q) and according to the Coulomb's Law, the magnitude of the electric field (ψ_0):

$$\psi_0 = \frac{1}{4\pi\varepsilon_0}\frac{q}{r^2} = \frac{1}{4\pi\varepsilon_0}\frac{\sigma\left(4\pi R^2\right)}{r^2} \tag{9}$$

where ψ_0 is the absolute surface potential (in vacuum), ε_0 is the dielectric permittivity of a vacuum, 8.854×10^{-12} C/(V m), q is the point charge (C), r is the distance from the particle surface (nm), σ is surface charge density (C/m^2), and R is the particle radius (nm). For a

homogeneous point charge (surface charge distributed evenly), the surface charge density (σ) is constant and the electric potential at a specific distance (r) away from the surface of the point charge should be proportional to R^2. As indicated above, KFM measures CPD when the tip and sample are in close proximity, but without electrical contact between them. Thus, the surface potential obtained from KFM could be the electric potential at a very small distance ($r \rightarrow 0$) and because the second-order polynomial fitting equations in Figure 8.6b,d further match the theoretical relationship between surface potential and particle size in Eq. (9), the Coulomb's Law may be used to interpret the size effects on the surface potential measurement from KFM. Moreover, a recent study discussed the effect of the distance between the tip and sample surface on the magnitude of surface potential *(34)* and the results are shown here in Figure 8.7, where there is clear distance dependence (r) for surface potential. According to the theoretical relationship in Eq. (9), surface potential is inversely proportional to r^2, which is consistent with the experimental observations of Figure 8.7. This example further supports the application of Coulomb's Law in interpretation of the origin of the surface potential from KFM.

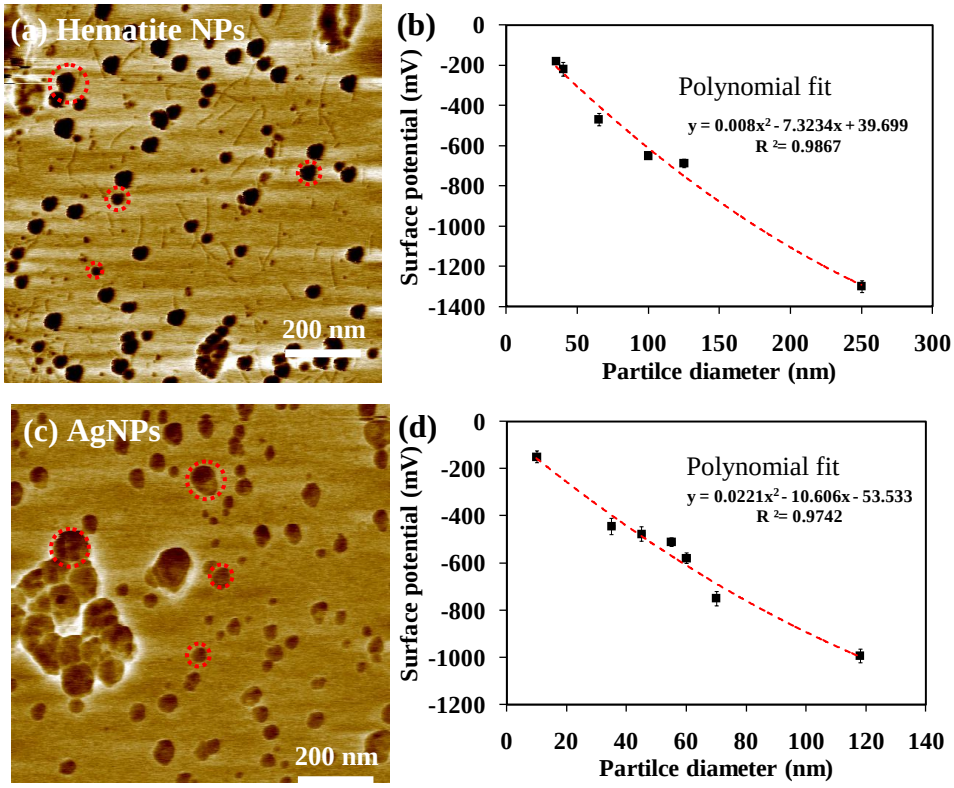

Figure 8.6. Size dependence of surface potentials of hematite and AgNPs obtained from KFM.

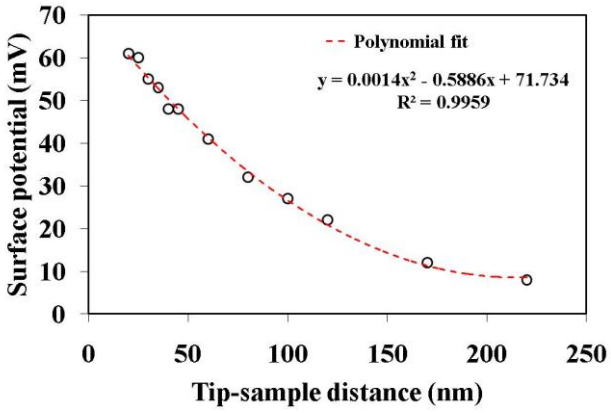

Figure 8.7. Tip-sample distance dependence of the measured surface potential of the HOPG surface at V_{AC} of 2V with the relatively humidity of zero. Data reproduced from ref. *(34)*.

8.5.5. Potential connections between ζ potential and KFM-surface potential

Based on the common observation of size effect on ζ potential and KFM-surface potential, we might be able to find connections between them, which are important for understanding the origin of surface potentials of nanostructures. Although it is hard to draw a direct connection between them, clearly, as mentioned previously, KFM is capable of estimating the absolute surface potentials that are considered as "not measurable" in aquatic chemistry *(14)*, by calibrating the measured asymptotic CPD of sample surfaces with the HOPG work function reference. In water chemistry, ζ potential is well related to the absolute surface potential (ψ_0) by the Poisson-Boltzmann equation in Eq. (7) on the basis of the Gouy-Chapman model of the diffuse double layer *(53, 54)*, which delineates the exponential decay of ζ potential over the distance away from the solid surface and the magnitude of ζ potential is much lower than ψ_0. On the basis of my experimental results, the measured surface potentials for various NPs are generally greater than their ζ potentials by several orders of magnitude, which is in agreement with the analysis with the Poisson-Boltzmann equation. This suggests that ζ potential could strongly be correlated with KFM-surface potential and if the KFM-surface potential is or close to ψ_0 we may be able to use KFM as alternative tools to measure ψ_0 and then calculate ζ potential via Eq. (7). Furthermore, we can use this calculated ζ potential to verify the measurement of ζ potential obtained from electrophoresis that is frequently found to carry a certain experimental artifacts associated with the dynamic and heterogeneous properties of NPs in aqueous phase. Of course, the accurate correlations may require future research, which will largely bring a physical insight into the understandings of aquatic electrochemical potentials. Thus, the knowledge obtained from these preliminary results laid out groundwork toward better understanding of the accurate surface potential measurement.

8.6. Reference

(1) Klaine, S. J.; Alvarez, P. J. J.; Batley, G. E.; Fernandes, T. F.; Handy, R. D.; Lyon, D. Y.; Mahendra, S.; McLaughlin, M. J.; Lead, J. R. Nanomaterials in the environment: behavior, fate, bioavailability, and effects. *Environ. Toxicol. Chem.* **2008,** *27* (9), 1825–1851

(2) Nel, A.; Xia, T.; Madler, L.; Li, N. Toxic potential of materials at the nanolevel. *Science* **2006,** *311* (5761), 622-627.

(3) Brunner, T. J.; Wick, P.; Manser, P.; Spohn, P.; Grass, R. N.; Limbach, L. K.; Bruinink, A.; Stark, W. J. In Vitro Cytotoxicity of Oxide Nanoparticles: Comparison to Asbestos, Silica, and the Effect of Particle Solubility. *Environ. Sci. Tech.* **2006,** *40* (14), 4374-4381.

(4) Geiser, M.; Rothen-Rutishauser, B.; Kapp, N.; Schurch, S.; Kreyling, W.; Schultz, H.; Im Hof, V.; Hyder, J.; Gehr, P. Ultrafine particles can cross cellular membranes by nonphagocytic mechanisms in lungs and cultured cell. *Environ Health Perspect* **2005,** *113* (11), 1555 - 1560.

(5) Gupta, A. K.; Gupta, M. Cytotoxicity suppression and cellular uptake enhancement of surface modified magnetic nanoparticles. *Biomaterials* **2005,** *26* (13), 1565-1573.

(6) Hussain, S. M.; Hess, K. L.; Gearhart, J. M.; Geiss, K. T.; Schlager, J. J. In vitro toxicity of nanoparticles in BRL 3A rat liver cells. *Toxicol. In Vitro* **2005,** *19* (7), 975-983.

(7) Farré, M.; Gajda-Schrantz, K.; Kantiani, L.; Barceló, D. Ecotoxicity and analysis of nanomaterials in the aquatic environment. *Anal. Bioanal. Chem.* **2009,** *393* (1), 81-95.

(8) Zhu, X.; Wang, J.; Zhang, X.; Chang, Y.; Chen, Y. The impact of ZnO nanoparticle aggregates on the embryonic development of zebrafish (Danio rerio). *Nanotechnology* **2009,** *20*, 9.

(9) Baun, A.; Hartmann, N. B.; Grieger, K.; Kusk, K. O. Ecotoxicity of engineered nanoparticles to aquatic invertebrates: a brief review and recommendations for future toxicity testing. *Ecotoxicology* **2008,** *17* (5), 387-395.

(10) Persson, B. N. J. On the mechanism of adhesion in biological systems. *J. Chem. Phys.* **2003,** *118* (16), 7614-7621.

(11) Tantra, R.; Schulze, P.; Quincey, P. Effect of nanoparticle concentration on zeta-potential measurement results and reproducibility. *Particuology* **2010,** *8* (3), 279-285.

(12) Guzman, K. A. D.; Finnegan, M. P.; Banfield, J. F. Influence of surface potential on aggregation and transport of titania nanoparticles. *Environ. Sci. Technol.* **2006,** *40* (24), 7688-7693.

(13) Zhang, Y.; Chen, Y.; Westerhoff, P.; Crittenden, J. C. Stability and Removal of Water Soluble CdTe Quantum Dots in Water. *Environ. Sci. Technol.* **2007,** *42* (1), 321-325.

(14) Stumm, W.; Morgan, J. J. *Aquatic chemistry*. 3rd ed.; John Wiley & Sons, Inc.: New York, 1996.

(15) Phenrat, T.; Saleh, N.; Sirk, K.; Tilton, R. D.; Lowry, G. V. Aggregation and sedimentation of aqueous nanoscale zerovalent iron dispersions. *Environ. Sci. Technol.* **2007,** *41* (1), 284-290.

(16) Hunter, R. J. *Foundations of colloid science*. 2nd ed.; Clarendon Press: Oxford, 2001.
(17) Buettner, K. M.; Rinciog, C. I.; E.Mylon, S. Aggregation Kinetics of Cerium Oxide Nanoparticles in Monovalent and Divalent Electrolytes. *Colloids Surf., A* **2010,** *366* (1-3), 74-79.
(18) He, Y. T.; Wan, J. M.; Tokunaga, T. Kinetic stability of hematite nanoparticles: the effect of particle sizes. *J. Nanopart. Res.* **2008,** *10* (2), 321-332.
(19) Kuna, J. J.; Voitchovsky, K.; Singh, C.; Jiang, H.; Mwenifumbo, S.; Ghorai, P. K.; Stevens, M. M.; Glotzer, S. C.; Stellacci, F. The effect of nanometre-scale structure on interfacial energy. *Nature Materials* **2009,** *8* (10), 837-842.
(20) Magomedov, M. Dependence of the surface energy on the size and shape of a nanocrystal. *Phys. Solid State* **2004,** *46* (5), 954-968.
(21) Rodriguez, K.; Araujo, M. Temperature and pressure effects on zeta potential values of reservoir minerals. *J. Colloid Interface Sci.* **2006,** *300* (2), 788-794.
(22) Jayaweera, P.; Hettiarachchi, S.; Ocken, H. Determination of the high temperature zeta potential and pH of zero charge of some transition metal oxides. *Colloids Surf., A* **1994,** *85* (1), 19-27.
(23) Evenhuis, C. J.; Guijt, R. M.; Macka, M.; Marriott, P. J.; Haddad, P. R. Variation of zeta-potential with temperature in fused-silica capillaries used for capillary electrophoresis. *Electrophoresis* **2006,** *27* (3), 672-676.
(24) Freitas, C.; Müller, R. H. Effect of light and temperature on zeta potential and physical stability in solid lipid nanoparticle (SLN(TM)) dispersions. *International Journal of Pharmaceutics* **1998,** *168* (2), 221-229.
(25) Jailani, S.; Franks, G. V.; Healy, T. W. zeta potential of nanoparticle suspensions: Effect of electrolyte concentration, particle size, and volume fraction. *J. Am. Ceram. Soc.* **2008,** *91* (4), 1141-1147.
(26) Medrzycka, K. B. The Effect of Particle Concentration on Zeta-Potential in Extremely Dilute-Solutions. *Colloid. Polym. Sci.* **1991,** *269* (1), 85-90.
(27) Berger, R.; Butt, H.-J.; Retschke, M. B.; Weber, S. A. L. Electrical Modes in Scanning Probe Microscopy. *Macromol. Rapid Commun.* **2009,** *30* (14), 1167-1178.
(28) Evans, S. D.; Ulman, A. Surface potential studies of alkyl-thiol monolayers adsorbed on gold. *Chem. Phys. Lett.* **1990,** *170* (5-6), 462-466.
(29) Semenikhin, O. A.; Jiang, L.; Iyoda, T.; Hashimoto, K.; Fujishima, A. A Kelvin probe force microscopic study of the local dopant distribution in conducting polybithiophene. *Electrochim. Acta* **1997,** *42* (20-22), 3321-3326.
(30) Sun, L.; Wang, J. J.; Bonaccurso, E. Nanoelectronic Properties of a Model System and of a Conjugated Polymer: A Study by Kelvin Probe Force Microscopy and Scanning Conductive Torsion Mode Microscopy. *J. Phys. Chem. C* **2010,** *114* (15), 7161-7168.
(31) Magonov, S.; Alexander, J., Application Note "Exploring measurements of local electric properties". In Agilent Technologies: Chandler, 2008.
(32) Sugimura, H.; Ishida, Y.; Hayashi, K.; Takai, O.; Nakagiri, N. Potential shielding by the surface water layer in Kelvin probe force microscopy. *Appl. Phys. Lett.* **2002,** *80* (8), 1459-1461.
(33) Alexander, J.; Magonov, S.; Moeller, M. In *Topography and surface potential in Kelvin force microscopy of perfluoroalkyl alkanes self-assemblies*, 2009; AVS: pp 903-911.

(34) Liscio, A.; Palermo, V.; Mullen, K.; Samori, P. Tip-Sample Interactions in Kelvin Probe Force Microscopy: Quantitative Measurement of the Local Surface Potential. *J. Phys. Chem. C* **2008,** *112* (44), 17368-17377.
(35) Shikler, R.; Fried, N.; Meoded, T.; Rosenwaks, Y. Measuring minority-carrier diffusion length using a Kelvin probe force microscope. *Phys. Rev. B: Condens. Matter* **2000,** *61* (16), 11041.
(36) Palermo, V.; Palma, M.; Tomović, Ž.; Watson, M. D.; Friedlein, R.; Müllen, K.; Samorì, P. Influence of Molecular Order on the Local Work Function of Nanographene Architectures: A Kelvin-Probe Force Microscopy Study. *Chemphyschem* **2005,** *6* (11), 2371-2375.
(37) Hayashi, K.; Saito, N.; Sugimura, H.; Takai, O.; Nakagiri, N. Regulation of the surface potential of silicon substrates in micrometer scale with organosilane self-assembled monolayers. *langmuir* **2002,** *18* (20), 7469-7472.
(38) Yoo, E. J.; Li, T.; Park, H. G.; Chang, Y. K. Size-dependent flocculation behavior of colloidal Au nanoparticles modified with various biomolecules. *Ultramicroscopy* **2008,** *108* (10), 1273-7.
(39) Yagi, K.; Fujihira, M. Study of mixed Langmuir-Blodgett films of hydrocarbon and fluorocarbon amphiphilic compounds by scanning surface potential microscopy and friction force microscopy. *Appl. Surf. Sci.* **2000,** *157* (4), 405-411.
(40) MacLeod, B. A.; Ginger, D. S. The Changing Face of PEDOT:PSS Films: Substrate, Bias, and Processing Effects on Vertical Charge Transport. *J. Phys. Chem. C* **2008,** *112* (21), 7922-7927.
(41) Elimelech, M.; Gregory, J.; Jia, G.; Williams, R. *Surface interaction potentials*. Butterworth–Heinemann: Woburn, MA, USA., 1995.
(42) Hansen, W. N.; Hansen, G. J. Standard reference surfaces for work function measurements in air. *Surf. Sci.* **2001,** *481* (1-3), 172-184.
(43) Liscio, A.; Palermo, V.; Samorì, P. Nanoscale Quantitative Measurement of the Potential of Charged Nanostructures by Electrostatic and Kelvin Probe Force Microscopy: Unraveling Electronic Processes in Complex Materials. *Acc. Chem. Res.* **2010,** *43* (4), 541-550.
(44) Palermo, V.; Palma, M.; Samori, P. Electronic characterization of organic thin films by Kelvin probe force microscopy. *Adv. Mater.* **2006,** *18* (2), 145-164.
(45) Crittenden, J. *Water Treatment: Principles and Design* Wiley; 2 edition: 2005.
(46) Oss, C. J. v. *Interfacial Forces in Aquaeous Media*. Second Edition ed.; Taylor & Francis Group: Boca Raton, Florida, 2006; p 81-83.
(47) Wu, W. J.; Nancollas, G. H. Application of the extended DLVO theory - the stability of alatrofloxacin mesylate solutions. *Colloids Surf., B* **1999,** *14* (1-4), 57-66.
(48) Zhang, Y.; Chen, Y.; Westerhoff, P.; Hristovski, K.; Crittenden, J. C. Stability of commercial metal oxide nanoparticles in water. *Water Res.* **2008,** *42* (8-9), 2204-2212.
(49) French, R. A.; Jacobson, A. R.; Kim, B.; Isley, S. L.; Penn, R. L.; Baveye, P. C. Influence of Ionic Strength, pH, and Cation Valence on Aggregation Kinetics of Titanium Dioxide Nanoparticles. *Environ. Sci. Technol.* **2009,** *43* (5), 1354-1359.
(50) Keller, A. A.; Wang, H.; Zhou, D.; Lenihan, H. S.; Cherr, G.; Cardinale, B. J.; Miller, R.; Ji, Z. Stability and Aggregation of Metal Oxide Nanoparticles in Natural Aqueous Matrices. *Environ. Sci. Technol.* **2010,** *44* (6), 1962-1967.

(51) Zetasizer Nano application note from Malvern Instruments. Available at: http://www.malvern.com/LabEng/industry/colloids/colloid_application_notes.htm
(52) Zhang, W.; Yao, Y.; Chen, Y. Imaging and Quantifying the Morphology and Nanoelectrical Properties of Quantum Dot Nanoparticles Interacting with DNA. *J. Phys. Chem. C* **2011,** *115* (3), 599–606.
(53) Larson, I.; Drummond, C. J.; Chan, D. Y. C.; Grieser, F. Direct force measurements between titanium dioxide surfaces. *J. Am. Chem. Soc.* **1993,** *115* (25), 11885-11890.
(54) Oberhauser, A. F.; Marszalek, P. E.; Erickson, H. P.; Fernandez, J. M. The molecular elasticity of the extracellular matrix protein tenascin. *Nature* **1998,** *393* (6681), 181-185.

CHAPTER 9

MAJOR CONCLUSIONS

The key findings of this work are briefly outlined below:

1. NP properties such as size, shape, surface charge, and hydrophobicity are interconnected. These interconnections may complicate the evaluation of the environmental behavior and biological effects.

2. Most NP properties (e.g., size) are dynamically changing after NPs are dispersed in aqueous environments.

3. The dynamical changes in NP properties and environmental behavior (e.g., aggregation) will greatly influence the subsequent fate, transport, and biological effects.

4. Aggregation of metal oxide NPs is influenced by size, pH, ionic strength, temperature, and many more environmental factors (e.g., NOM). To quantitatively describe aggregation kinetics, I established kinetics models based on Arrhenius and Smoluchowski equations, which give us better understandings of relationships between particle properties and aggregation kinetics.

5. In contrast to most metal oxide NPs, metallic NPs such as AgNPs are chemically reactive and assessing the stability of reactive NPs requires considerations of environmental components such as oxygen and carbon dioxide, which may interfere the aggregation process by introducing oxidation, speciation, and precipitation to AgNPs.

6. In exploration of the exposure effects of NPs on human cells, adsorption kinetics of hematite NPs on Caco-2 cells was found to be size dependent and surface accumulation of NPs induced disruption of microvillus structures and adhesin adjunctions, which are used to assimilate nutrients and to support the cellular integrity.

7. In the exposure experiments with bacteria (*E. coli*), adsorption kinetics of hematite NPs was again found to be size dependent, which was successfully interpreted by the IFBL theory. Exposure of hematite NPs to *E. coli* cells showed significant disruption on cell surface structures, leading to deformation of cells, damages of surface appendages (i.e., flagella), and changes to the surface potential.

8. Interfacial force measurement between NPs and *E. coli* cells provides insight into the adsorption mechanisms and the results show that small particle size had greater adhesion forces than large particle size.

9. Nanoscale hydrophobicity was theoretically and experimentally explored using AFM and the measurement of adhesion forces was linked to and converted to contact angles at nanoscale. AFM probes hydrophobicity at localized and nanoscale surfaces rather than the bulk scale material surfaces. Nanoscale hydrophobicity was found to be slightly different from the contact angle measurements at bulk scale materials for some NPs.

10. Nanoscale surface potential was probed using KFM and was found to be potentially connected with zeta potential, which is commonly used to indicate the surface potential characteristics of NPs. However, KFM reveals surface potential at local and nanoscale surfaces compared to the average electric properties revealed by zeta potential.

FUTURE WORK

Based on the current knowledge and challenges, future work on the bio-nano interactions may start with addressing the following critical issues associated with unique nanoparticle characteristics and their toxicological significance:

1. Shape effects on surface energy and electrical properties of NPs;
2. Shape effect on aggregation and other environmental behavior (e.g., ion release and partitioning);
3. Transport characteristics of NPs within different phases (air, water, abiotic and biotic solids).
4. Correlation between dynamic aggregation, disaggregation, ion release kinetics and toxicokinetics;
5. Exploration of non-ROS mediated nanotoxicological mechanisms of metal-based NPs in low redox environments, where low oxidative conditions should dramatically reduce the formation of oxidative radicals and thus ROS-mediated nanotoxicity could be minimized.
6. Ultramicroscopic methodology development for evaluating the surface damages of cellular systems *in situ*, *in vivo* and *in vitro*.

APPENDIX A

MASS TRANSFER RATES OF DISSOLVED OXYGEN IN QUARTER-STRENGTH HOAGLAND MEDIUM

The overall mass transfer coefficient (K_La) for oxygen in Hoagland medium was determined according to the clean water test *(1, 2)*. Before conducting the DO measurement, the medium was purged with high purity (99.999%) nitrogen (Airgas, GA) for 30 min to remove the initial DO. The DO concentration of the medium was measured by a DO meter (VWR® sympHony® Dissolved Oxygen Meter) over approximately 20 h. Table A1 summarizes important parameters and calculation equations for K_La.

Table A1. Parameters and equations for calculating K_La.

	Equation	Value
Medium depth, d, (m)	--	0.08
Henry constant, K_H (mol L^{-1} atm^{-1})	--	0.00139
Temperature (K)	--	298
Oxygen pressure at depth of d (atm)	$P_d=(P_{atm}+0.0965d)\times 21\%$	0.0016
Partial pressure of oxygen at the liquid-gas interface (atm)	$P_{ex} = \frac{P_{atm}\cdot(1-f)\cdot 21\%}{1-f\cdot 21\%}$ (f=0.1)	0.193
Saturated oxygen concentration, C_s, (mg L^{-1})	$C_s = K_H^T \frac{(Pd + Pex)}{2}$	8.9627
Oxygen concentration, C_{DO}, (mg L^{-1})	Measured by DO meter	--

Figure A1 shows the DO concentration changes in Hoagland medium. Clearly, the DO concentration follows pseudo first-order kinetics *(2)*:

$$\frac{dC_{DO}}{dt} = K_L a (C_S - C_{DO}) \quad \text{(A1)}$$

Rearranging Eq. (A1) yields:

$$\ln\left(\frac{(C_S - C_{DO,t})}{(C_S - C_{DO,t=0})}\right) = K_L a \cdot t \qquad \text{(A2)}$$

Because $(C_S - C_{DO,t=0})$ is constant, $\log_{10}(C_S - C_{DO,t})$ has a linear relationship with time *t*, as shown in the inset in Figure A1. The slope is equal to $K_L a$ /2.303, and on the basis of the linear fit equation, $K_L a$ is 0.3309 h^{-1}. Knowing $K_L a$, we can estimate the oxygen mass transfer rate in the cuvettes in which Ag^+ release occurred. For example, we measured the initial DO concentration in Hoagland medium before conducting the Ag^+ release experiments to be approximately 7.8 mg/L (slightly below C_S). According to Eq. (A1), the overall mass transfer rate of oxygen is equal to 6.01 μmol L^{-1} h^{-1}, which is much larger than the oxygen consumption rates shown in Table 4.2. Furthermore, the transfer rate may increase further as DO is depleted as a result of the oxidation reaction. Thus, DO is not a rate-limiting factor for the ion release kinetics.

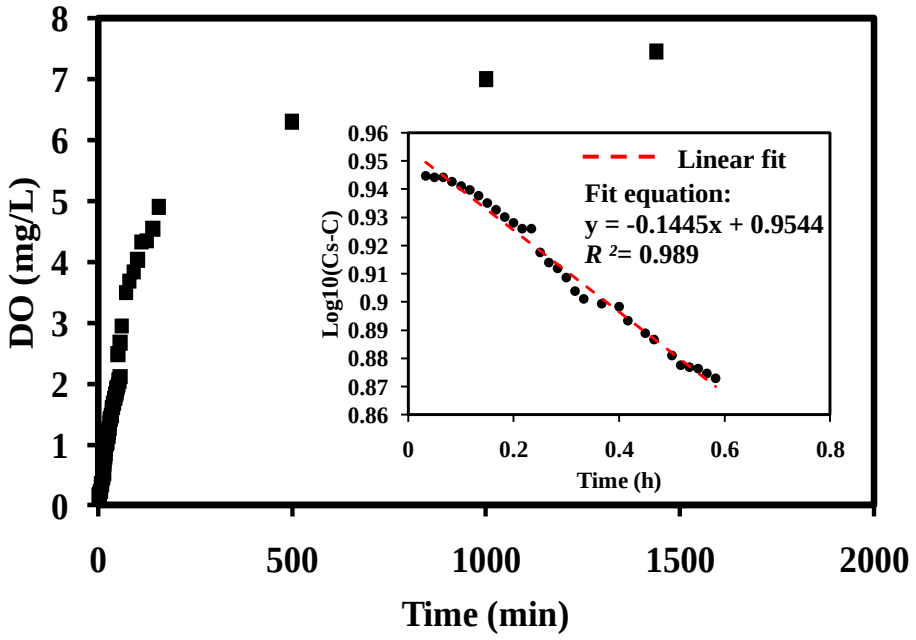

Figure A1. DO curve for Hoagland medium after nitrogen purging. The inset shows the plot of $\log_{10}(C_S - C_{DO,t})$ versus *t*.

Reference

(1) Käppeli, O.; Fiechter, A. On the methodology of oxygen transfer coefficient measurments. *Biotechnology Letters* **1981,** *3* (10), 541-546.
(2) Tchobanoglous, G.; Burton, F. *Wastewater engineering treatment, disposal, and reuse*. Third edition ed.; Metcalf & Eddy: 1991.

APPENDIX B

MODEL DEVELOPMENT FOR SIZE EFFECT OF NPS ON ADHESION FORCE BETWEEN CELL SURFACE AND NP ARRAY

The mathematical modeling for the particle size effect on adhesion force is derived based on the possible effective contact areas. The *E. coli* cell surface was treated as an infinitely large and plain surface. Obviously, in reality it is not the true because of surface structure like pili and flagella. However, considering the contact between the cell surface and NPs in nano-scale, these surface structures are infinitely huge. Fig. B1 presents the conceptual model we used to illustrate the subtle changes in interfacial contact areas resulting from particle size change. As calculated by the JKR model, the same loading force by the cantilever tip would result in a constant contact site area ($\pi \cdot a^2$). However, for contact conditions of the deformable surfaces like *E. coli* cells, it is possible that the deformed surfaces have more contact with NPs when compressed into the local nano-scale void spaces between NPs as shown in Fig. B1. It is assumed that the projected contact areas for NPs are the same ($=\pi \cdot r^2$, see the pink area in Fig. B1-A) and the total area of these contact areas is equal to $\pi \cdot a^2$ and $\pi \cdot a^2 = \sum_i^N \pi r_i^2$, where a is the radius of contact site area in the JKR model and N is the number of contact sites. The effective contact areas between the *E. coli* cells and different sized NPs are different, as illustrated by the blue cambered surface area on the sphere of NPs in Fig. B1-A due to the compression of the soft *E. coli* cell surface against the rigid body of NPs. Obviously, the smaller particles have more blue effective contact areas than large ones. Since the adhesion force is proportional to the effective contact area between the two interacting surfaces *(1, 2)*, the adhesion force can be related to particle size by this expression:

$$F_{ad} \propto N \int_0^{R-\sqrt{R^2-r^2}} 2\pi \sqrt{R^2 - (\sqrt{R^2 - r^2} + x)^2}\, dx \tag{B1}$$

where N is the number of NPs interacting with *E. coli* cell surfaces; R is the NP radius, nm; and r is the projected contact area radius, nm.

However, the interspaces between particles can weaken the adhesion force by reducing the effective contact and thus adhesion force is inversely proportional to the volume of the void space in the interspaces. In Fig. B1B, for a control area ($dS=L\times L$), the hollow space, highlighted by the black dotted circles, varies with particle size. This can be expressed mathematically as:

$$V = N \times \left[(2R)^3 - (4\pi R^3 / 3) \right] / 2 \tag{B2}$$

where R is particle radius, nm; and N is the number of particles in the control area ($L\times L$). To make the void space volume comparable between different particle sizes, the volume expression in Eq. (B2) needs to be normalized by dividing the particle size, R. Thus, V_{norm} represents the normalized void space volume per unit size of particle:

$$V_{norm} = V / R \tag{B3}$$

Adhesion force is inversely proportional to the normalized void space volume as we assumed above that adhesion force is inversely proportional to the volume of void space in the interspaces:

$$F_{ad} \propto 1 / V_{norm} \tag{B4}$$

By integrating the two proposed mechanisms (Eq. B1 ~ B4) for NP size to affect adhesion force, the adhesion force Eq. can be expressed as:

$$F_{ad} = K\int_{0}^{R-\sqrt{R^2-r^2}} 2\pi\sqrt{R^2-(\sqrt{R^2-r^2}+x)^2}\,dx / V_{norm} \tag{B5}$$

The theoretical form can be derived as:

$$F_{ad} = K\int_{0}^{R-\sqrt{R^2-r^2}} \frac{\sqrt{R^2-(\sqrt{R^2-r^2}+x)^2}}{R^2}\,dx \approx \frac{K(R-\sqrt{R^2-r^2})r}{R^2} \tag{B6}$$

where K is a constant for two specific engaging surfaces, nN; R is the NP radius; and r is the radius of the projected contact area between one NP and *E. coli* cell surface, $\pi a^2 = N\cdot\pi r^2$. Dimensional analysis of Eq. B6 reveals that adhesion force (F_{ad}) is proportional to a simple form, $\frac{Kr}{R}$.

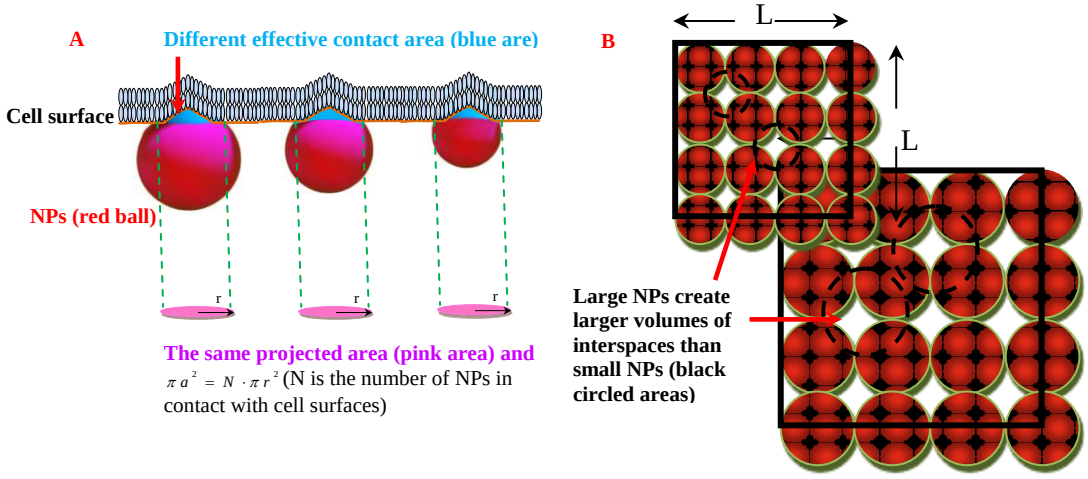

Figure. B1. Schematics of modeling the size effect of NPs on adhesion force.

We fitted our experimental data for hematite NPs with the Eq. (B6), and the fitting parameters of K and r are 2550 nN and 5.0 nm respectively. The fit was evaluated by calculating the standard deviation as the Objective Function (*OF*) required to reach the minimum:

$$O.F = \sqrt{\frac{1}{N-1}\sum\left(\frac{C_{data}-C_{model}}{C_{data}}\right)^2} \tag{B7}$$

where N is the data number; C_{data} is the experimental data point; and C_{model} is the simulated data point. For our fit, OF is equal to 0.67. The squared correlation coefficient, R^2, between the experimental data and simulated data is 0.71. The fit with the adhesion force data for corundum NPs yields OF of 0.540 and R^2 of 0.997. The fitting parameters of K and r are 2550 nN and 5.6 nm respectively. It is interesting that corundum and hematite NPs share the same value of K which can be a characteristic adhesion force for the specific interactions and indicates the potential maximal adhesion force when the radius of the projected contact area (r) is equal to the particle radius (R). The difference in the values of r between corundum and hematite NPs was probably caused by the contact site number (N) because according to the JKR model the radius of total contact site area (a) under a constant the initial loading force will be the same so that values of (r) should be depending on N due to the relation of $\pi a^2 = N \cdot \pi r^2$ and N is considerably affected by the surface topographical properties of NPs, (e.g., number of the protruding peaks of the surface may determine contact sites with the cell surface). This model is by no means a precise relationship between adhesion force and sizes of NPs but an approximation based on the feature of force measurement with AFM. In order to improve the applicability of the model, we are still working on measuring other NPs of different sizes and calibrating the model parameters.

Reference:

(1) Spalla, O.; eacute; kicheff, P. Adhesion between Oxide Nanoparticles: Influence of Surface Complexation. *J Colloid Interface Sci* **1997,** *192* (1), 43-65.
(2) Yuehuei H. An, R. J. F., Concise review of mechanisms of bacterial adhesion to biomaterial surfaces. In 1998; Vol. 43, pp 338-348.

VITA

Wen Zhang

Ph.D. Student

School of Civil and Environmental Engineering

Georgia Institute of Technology

200 Bobby Dodd Way, Atlanta, GA 30332

Tel: +1-(480)294-9782; Fax: 404-385-7087; e-mail: wzhang76@gatech.edu

EDUCATION

Ph.D. student, School of Civil and Environmental Engineering, Georgia Institute of Technology, 08/2011 (anticipated), GPA 4.0/4.0

M.S. with honor (top 1%), *Environmental Science and Engineering*, Tongji University, 2007, GPA 3.7/4.0

B.S., *Environmental Science and Engineering*, Tsinghua University, 2004, GPA 3.6/4.0

EXPERIENCES

Georgia Institute of Technology, Atlanta, GA (07/2009 - present)
Arizona State University, Tempe, Az (06/2007 - 06/2009)
Research assistant, Ph.D. student

- Specialized in nanomaterial surface analysis, imaging techniques (topography, roughness, and surface potential), and interfacial interaction force measurement with atomic force microscopy (AFM);
- Skilled in using scanning electron microscopy (SEM) and transmission electron microscopy (TEM), metal element analysis (X-ray Energy-Dispersive spectroscopy), high resolution TEM, and crystal characterization;
- Analyze metal or metal oxide concentrations in complicated matrix (i.e. food, plants) by ICP-MS/OES (PerkinElmer), and perform QA/QC, statistical analysis and error analysis;
- Proposal writing and journal publication;

Tongji University, Shanghai, China (9/2004 - 3/2007)
Research assistant, M.S. student

- Established and operated expanded granular sludge bioreactor (EGSB) to remove 2,4-dichlorophenol from wastewater;
- HPLC (Agilent/HP) analysis of chlorophenol degradation products and perform QA/QC;
- Characterize anaerobic sludge and microbial communities using molecular biotechnological methods (PCR, DGGE, and molecular cloning);

Tsinghua University, Beijing, China (9/2004 - 3/2007)
Research assistant, B.S. student

- Established and operated upflow anaerobic sludge bioreactor (UASB) to remove high-strength organic wastewater;
- Analyze Carbon dioxide, and methane by GC (Shimadzu), test nitrate, nitrite and chloride by IC (Shimadzu), and perform QA/QC;

HONOR AND REWARDS OBTAINED IN THE US

2008 Travel Grant recipient, Division of Graduate Studies (DGS), Arizona State University

2011 Recipient of 2011 Simon Karecki Award, SRC/SEMATECH

2011 Certificate of Merit for Presentation at ACS 242th National Meeting-ENVR

JOURNAL PUBLICATIONS IN THE US

1. Wen Zhang, Madhavi Kalive, David G Capco, and Yongsheng Chen, Adsorption of hematite nanoparticles onto Caco-2 cells and the cellular impairments: effect of particle size. ***Nanotechnology*** **21 355103.**
2. Wen Zhang and Yongsheng Chen, Interaction force measurement between *E. coli* cells and nanoparticles immobilized surfaces by using AFM. ***Colloids and Surfaces B: Biointerfaces,*** 2011, 316-324
3. Wen Zhang, Ying Yao, and Yongsheng Chen Quantifying and Imaging the Morphology and Nanoelectric Properties of Soluble Quantum Dot Nanoparticles Interacting with DNA. ***Journal of Physical Chemistry C***, 2011, 115 (3), 599-606.
4. Wen Zhang, Bruce Rittmann, and Yongsheng Chen. Size effects on adsorption kinetics of hematite NPs on *E. coli* cells. ***Environmental Science and Technology***, 2011, 45 (6), 2172-2178.

5. Wen Zhang, Ying Yao, Nicole Sullivan, Yongsheng Chen. Modeling the primary size effects of citrate-coated silver nanoparticles on their ion release kinetics. ***Environmental Science and Technology***, DOI: 10.1021/es104205a.

6. Wen Zhang, Ying Yao, Kungang Li, Ying Huang, Yongsheng Cheṇ. Influence of Dissolved Oxygen on Aggregation Kinetics of Citrate-coated Silver Nanoparticles. ***Environmental pollution***. Under review.

7. Wen Zhang, Yongsheng Chen. Probing the nanoscale hydrophobicity using atomic force microscopy. In preparation.

8. Wen Zhang, Yongsheng Chen. Probing the nanoscale electric properties of metal-based nanoparticles using zeta potential measurement and Kelvin probe force microscopy. (***Langmuir letter***), In preparation.

9. Wen Zhang, Kungang Li, and Yongsheng Chen. Aggregation kinetics of metal oxide NPs and kinetics modeling. ***Environmental Science and Technology***, In preparation.

10. Wen Zhang, Joseph B Hughes, and Yongsheng Chen. Changes of mechanical and nanoelectric properties of *E. coli* cells after exposure to hematite NPs. (***Applied environmental microbiology***), In preparation.

11. Wen Zhang, Ying Yao, Ching-Hua Huang, and Yongsheng Chen. Measurement of trace level metal based nanoparticles by ICP-MS without sample digestion. In preparation.

12. Liwen Zhang, Elijah J. Petersen, Wen Zhang, Yongsheng Chen, Miguel Cabrera, Qingguo Huang. Phase Distribution of 14C-labeled Multi-walled Carbon Nanotubes in Aqueous Systems Containing Model Solids: Clay. ***Environmental Science and Technology***, In preparation.

13. Yang Li, Wen Zhang, Ying Yao, Kungang Li, Yongsheng Cheṇ. Oxidative Dissolution of CdSe/ZnS quantum dots under UV irradiation: A Kinetic and Mechanistic Study. ***Environmental Science and Technology***, In preparation.

ORAL PRESENTATIONS

1. Wen Zhang, Yongsheng Chen, and Bruce Rittmann. Methodology Development for Adhesion Force Measurement between Nanomaterials and Cells Using AFM. 48th Annual Arizona-Southern Nevada ASM Branch Meeting. Arizona State University, Tempe, Arizona, April, 12, 2008

2. Wen Zhang, Xiaoshan Zhu, Xuezhi Zhang, Yongsheng Chen. Potential Toxicity of Nanomaterials and their Removal. International Environmental Nanotechnology conference. Chicago, Michigan, October, 2008

3. Wen Zhang, Yongsheng Chen, et.al., Methodology Development for Adhesion Force Measurement between Nanomaterials and Cells Using AFM. 237th American Chemical Society National Meeting & Exposition, March 22 - 26, 2009 Salt Lake City, UT

4. Wen Zhang, Yongsheng Chen, et.al., Development of Quantitative Structure-Activity Relationship for Prediction of Biological Effects of Nanoparticles Associated with Semiconductor Industries. GRC SEMATECH Engineering Research Center for Environmentally Benign Semiconductor Manufacturing Review, February 17-19, 2010. University of Arizona. Tucson, Arizona

5. Wen Zhang, Yongsheng Chen, et.al., Development of Quantitative Structure-Activity Relationship for Prediction of Biological Effects of Nanoparticles Associated with Semiconductor Industries. ICEIN 2010: International Conference on the Environmental Implications of Nanotechnology May 11 - 13, 2010. University of California Los Angeles (UCLA), Los Angeles, California.

6. Wen Zhang, and Yongsheng Chen. Effect of Nanoparticle Size on Adhesion Force with *E. coli* Cells. TECHCON 2010 Technology and Talent for the 21st Century conference Proceedings. Sep, 13-14, 2010, Austin, Texas

7. Wen Zhang and Yongsheng Chen. Development of an In Vitro Test and a Prototype Model to Predict Cellular Penetration of Nanoparticles. 2010 U.S. EPA Nanotechnology Grantees Meeting. Portland, Oregon, In Conjunction with the SETAC North America 31st Annual Meeting Bridging Science with Communities. November 8~9, 2010

8. Wen Zhang, and Yongsheng Chen. SRC annual review and grantees meeting. GRC SEMATECH Engineering Research Center for Environmentally Benign Semiconductor Manufacturing Review, March 8-11, 2011. University of Arizona. Tucson, Arizona

9. Wen Zhang and Yongsheng Chen. Aggregation and ion release kinetics of citrate-coated silver nanoparticles, ACS 241st National Meeting & Exhibition in Anaheim, California, March 27-31, 2011.